



**HAL**  
open science

## Differential exhumation of the Eastern Cordillera in the Central Andes

Benjamin Gérard, Xavier Robert, Laurence Audin, Pierre G Valla, Matthias Bernet, Cécile Gautheron

► **To cite this version:**

Benjamin Gérard, Xavier Robert, Laurence Audin, Pierre G Valla, Matthias Bernet, et al.. Differential exhumation of the Eastern Cordillera in the Central Andes. *Tectonics*, 2021, 40 (4), 10.1029/2020TC006314 . hal-03388206v1

**HAL Id: hal-03388206**

**<https://hal.science/hal-03388206v1>**

Submitted on 20 Oct 2021 (v1), last revised 14 Dec 2021 (v2)

**HAL** is a multi-disciplinary open access archive for the deposit and dissemination of scientific research documents, whether they are published or not. The documents may come from teaching and research institutions in France or abroad, or from public or private research centers.

L'archive ouverte pluridisciplinaire **HAL**, est destinée au dépôt et à la diffusion de documents scientifiques de niveau recherche, publiés ou non, émanant des établissements d'enseignement et de recherche français ou étrangers, des laboratoires publics ou privés.

1     **Differential exhumation of the Eastern Cordillera in the Central Andes:**  
2     **Evidence for south-verging backthrusting (Abancay Deflection, Peru)**

3

4     **Benjamin Gérard<sup>1\*</sup>, Xavier Robert<sup>1</sup>, Laurence Audin<sup>1</sup>, Pierre G. Valla<sup>1,2</sup>, Matthias**  
5     **Bernet<sup>1</sup>, Cécile Gautheron<sup>3</sup>**

6

7     <sup>1</sup>Univ. Grenoble Alpes, IRD, ISTERRE, CNRS, 38000 Grenoble, France

8     <sup>2</sup>Institut of Geological Sciences, University of Bern, Baltzerstrasse 3, 3012 Bern, Switzerland

9     <sup>3</sup>Université Paris-Saclay, CNRS, GEOPS, 91405, Orsay, France

10    \**Now at GET, Université de Toulouse, CNRS, IRD, UPS, (Toulouse), France*

11

12    Corresponding author: Benjamin Gérard ([benjamin.gerard.alpes@gmail.com](mailto:benjamin.gerard.alpes@gmail.com))

13

14    **Key Points:**

- 15     • Thermochronological data quantifying the tectonic history of the undocumented  
16       northern edge of the Peruvian Altiplano (Abancay Deflection)
- 17     • 3-D thermo-kinematic models unravel the evolution of the Eastern Cordillera & the  
18       Altiplano
- 19     • Steady and uniform exhumation between 40 and 5 Ma, followed by tectonically-  
20       driven tilting of the Eastern Cordillera

21

22

23

24

25

26 **Abstract**

27        Located at the northern tip of the Altiplano, the Abancay Deflection marks abruptly  
28 the latitudinal segmentation of the Central Andes spreading over the Altiplano to the south  
29 and the Eastern Cordillera northward. The striking morphological contrast between the low-  
30 relief Altiplano and the high-relief Eastern Cordillera makes this area a well-suited place to  
31 determine spatio-temporal variations in surface and/or rock uplift and discuss the latest phase  
32 of the formation of the Central Andes. Here, we aim to quantify exhumation and uplift  
33 patterns in the Abancay Deflection since 40 Ma, and present new apatite (U-Th)/He and  
34 fission-track data from four altitudinal profiles and additional individual samples. Age-  
35 elevation relationships and thermal modeling both document that the Abancay Deflection  
36 experienced a moderate, spatially-uniform and steady exhumation at  $0.2\pm 0.1$  km/m.y.  
37 between 40 Ma and  $\sim 5$  Ma implying common large-scale exhumation mechanism(s). From  
38  $\sim 5$  Ma, while the northern part of the Eastern Cordillera and the Altiplano registered similar  
39 ongoing slow exhumation, the southern part of the Eastern Cordillera experienced one order-  
40 of-magnitude of exhumation acceleration ( $1.2\pm 0.4$  km/m.y). This differential exhumation  
41 since  $\sim 5$  Ma implies active tectonics, river capture and incision affecting the southern Eastern  
42 Cordillera. 3D thermo-kinematic modeling favors a tectonic decoupling between the  
43 Altiplano and the Eastern Cordillera through backthrusting activity of the Apurimac fault. We  
44 speculate that the Abancay Deflection, with its “bull’s-eye” structure and significant  
45 exhumation rate since 5 Ma, may represent an Andean proto-syntaxis, similar to the syntaxes  
46 described in the Himalaya or Alaska.

47

48 **Keywords:** Central Andes, Abancay Deflection, Thermochronology, Differential  
49 exhumation, Tectonic decoupling, Apurimac fault

50

51 **1 Introduction**

52         The Central Andes contain the second-highest and widest plateau on Earth: the  
53 Altiplano. This wide morphologic domain spreading over 350-400 km of maximum width is  
54 characterized by low relief sustained by an over-thickened crust of ~60 km (Allmendinger et  
55 al., 1997; James, 1971). Andean topography building started during the Cretaceous (~120-  
56 110 Ma; Jaillard & Soler, 1996). Tectonic, climatic and erosional interactions affecting the  
57 Altiplano and its eastward border, the Eastern Cordillera (Figure 1), have been extensively  
58 studied in the southern Central Andes (Bolivia, Argentina; Strecker et al., 2007). The  
59 northern edge of the Altiplano, namely the Abancay Deflection (Southern Peru; Marocco,  
60 1971; Dalmayrac et al., 1980; Gérard et al., 2021), however, has been poorly documented,  
61 although its relief and structural organization reveals uncommon features with curved faults,  
62 deflected drainage basins and rivers, and deeply-incised landforms. The Abancay Deflection  
63 occupies a part of the Altiplano to the south and the Eastern Cordillera northward (Figures 1  
64 & 2), and is limited to the north by the Subandes. Morphologically, the Altiplano and the  
65 Eastern Cordillera acquired their respective modern mean elevation of ~4 km and ~4.5 km  
66 before 5 Ma (Sundell et al., 2019). Although having experienced similar timing and  
67 magnitude of surface uplift, the Altiplano and the Eastern Cordillera are quite different in  
68 terms of morphology and geology. In comparison, the Eastern Cordillera presents prominent  
69 landscape relief enhanced by deep incision and much older bedrock lithologies (Paleozoic for  
70 the Eastern Cordillera vs. Meso-Cenozoic for the Altiplano; Figure 2a). The Subandes  
71 represent the most recent domain in terms of orogen building and corresponds to the eastward  
72 propagation of Andean deformation through successive fold and thrust fronts since the  
73 Miocene (Espurt et al., 2011), tectonically involving Paleozoic and Cenozoic deposits in thin  
74 and thick-skinned mode (Figure 2a; Gautheron et al., 2013).

75 Mechanisms for exhumation of the Bolivian and southern Peruvian Eastern Cordillera  
76 are debated and imply either east-verging thrusting along a ramp connected to the Subandean  
77 zone (Gotberg et al., 2010; Rak et al., 2017), or reactivation of inherited faults as west-  
78 verging backthrusts (Perez et al., 2016), both with subsequent erosion of the built topography.  
79 All these geometries and kinematics are nonetheless not mutually exclusive. In Bolivia, the  
80 Eastern Cordillera experienced exhumation between 50 and 15 Ma with transfer of tectonic  
81 deformation to the Subandean zone at ca. 15 Ma (Barnes et al., 2012). From  
82 thermochronological records, the northern Altiplano has been suggested to have experienced  
83 a steady exhumation of  $\sim 0.2$  km/m.y. between around 40 and 15 Ma (Ruiz et al., 2009).  
84 However, the limited records before 38 Ma and after 14 Ma for this area prevent deciphering  
85 and/or speculating between different exhumation dynamics and drivers. Quantification of the  
86 exhumation history could give insights regarding surface uplift under specific geological  
87 conditions (England & Molnar, 1990), the lack of exhumation data does not allow to discuss  
88 surface-uplift scenarios such as slow and continuous surface uplift associated with (lower)  
89 crustal deformation since 40 Ma (Barnes & Ehlers, 2009; Husson & Sempere, 2003; Ouimet  
90 & Cook, 2010), versus potential surface-uplift acceleration during the Miocene triggered by  
91 lithospheric delamination event(s) (Garzzone et al., 2017). The high-relief Eastern Cordillera  
92 seems to register a more recent and complex exhumation history ( $< 5$  Ma) with both  
93 topographic incision and regressive erosion (Lease and Ehlers, 2013; Gérard et al., 2021).  
94 Regarding the climatic imprint on the Eastern Cordillera, major canyon carving is supposedly  
95 related to Pliocene global climate cooling (Lease & Ehlers, 2013). Nonetheless, increased  
96 orographic precipitation in such a rising orogen (Insel et al., 2010) could explain also canyon  
97 incision events earlier than the Pliocene (Poulsen et al., 2010).

98 Although the timing of surface uplift and mechanisms of exhumation are debated, a  
99 clear contrast and decoupling in terms of vertical motion between the Altiplano, the Eastern

100 Cordillera and the Subandes has emerged (Garzzone et al., 2017). Our aims is to provide  
101 further quantitative constraints to unravel the mechanisms triggering the Abancay Deflection  
102 exhumation since 40 Ma and discuss exhumation rates and timing in relation to large-scale  
103 surface-uplift information. The deeply-incised Abancay Deflection is the ideal target to  
104 unravel the long-term evolution of the northern edge of the Altiplano (Figure 1). Here we  
105 present new apatite (U-Th)/He (AHe) and fission-track (AFT) data, targeting Permo-Triassic  
106 (Mišković et al., 2009) and Paleogene (Carlier et al., 1996; Mamani et al., 2010) plutonic  
107 bedrock along high-relief valleys. We interpret the thermochronological data using age-  
108 elevation relationships (AER; Glotzbach et al., 2011), thermal (2D; QTQt; Gallagher, 2012)  
109 and thermo-kinematic (3D; Pecube; Braun, 2003; Braun et al., 2012) modeling to determine  
110 the late-Eocene to modern exhumation history of the Abancay Deflection and discuss  
111 potential exhumation mechanisms.

112

## 113 **2 Geological setting**

114 The Abancay Deflection connects the Central and Northern Andes in Peru; its hinge-like  
115 character is emphasized by the  $>45^\circ$  deflection of its fault pattern from the overall NNW-SSE  
116 axis of the range (Figure 2a; Marocco, 1971). This region is directly located above the slab  
117 dip transition of the Nazca oceanic plate (Figure 1) from “flat” (northward) to “normal”  
118 (southward) subduction (Barazangi & Isacks, 1976). The study area encompasses the distinct  
119 morpho-tectonic regions of the Altiplano to the south and the Eastern Cordillera to the north,  
120 separated by the regional crustal-scale Apurimac fault system (Figure 2; Carlier et al., 2005).  
121 This fault system marks the northern limit of the Arequipa terrane accreted to South America  
122 at 1 Ga (Loewy et al., 2004; Ramos, 2008). In the Eastern Cordillera, the existing  
123 relationships between lithospheric thinning and magmatism suggest that the Apurimac fault  
124 system seems to affect the study area since at least the Late Permian (by a strike slip fault in

125 an extensional context; Sempere et al., 2002) which remarkably shows the long-term tectonic  
126 inheritance of the region. Eocene-early Oligocene plutons (50-30 Ma; Mamani et al., 2010)  
127 emplaced into Meso-Cenozoic sedimentary rocks (Carlier et al., 1996) crop out in the high-  
128 elevation and low-relief Altiplano. This domain was exhumed steadily at moderate rates  
129 ( $\sim 0.2$  km/m.y.), at least between 38 and 14 Ma (Ruiz et al., 2009). In contrast, Permo-Triassic  
130 batholiths are dominant in the higher and deeply-incised Eastern Cordillera and intruded into  
131 lower Paleozoic rocks (Figure 2; Mišković et al., 2009). Preliminary thermochronological  
132 data (AFT ages of  $\sim 2$  Ma; Kennan, 2008) of two samples, from the core of the Abancay  
133 region, suggest rapid and recent exhumation for the Eastern Cordillera. Thermal perturbation  
134 linked to magmatic arc activity ceased after ca. 30 Ma and the latest local and sporadic  
135 volcanic events (from 7 to 0.5 Ma; Bonhomme et al., 1988; Carlier et al., 1996) focused  
136 along the Apurimac fault system mostly south east of Cuzco (Bonhomme et al., 1988).  
137 Inherited deflected faults and arched-captured rivers characterize the Abancay Deflection on  
138 the northern edge of the Altiplano. The Abancay Deflection records high-magnitude  
139 counterclockwise tectonic rotation of up to  $65^\circ$  during the late Eocene-early Miocene ( $\sim 40$ -20  
140 Ma; Butler et al., 1995; Richards et al., 2004; Roperch et al., 2006, 2011) and possibly more  
141 recently (since  $\sim 12$  Ma; Rouse et al., 2005) in a Bolivian Orocline bending context (Müller  
142 et al., 2002). In such context, according to the single study available with micro-structural  
143 analysis (Dalmayrac et al., 1980), it appears that the Abancay Deflection mainly recorded  
144 left-lateral tectonic deformation since the late Eocene, possibly associated with a limited  
145 vertical component. This sinistral shear behavior is also supported by paleomagnetic data  
146 obtained close to Cuzco (Gilder et al., 2003). In addition, it appears that the Eastern  
147 Cordillera did not experience any burial during the Eocene, since it acted like a long-lived  
148 structural high as suggested by the lack of a Meso-Cenozoic sedimentary cover (except for  
149 Quaternary fluvial and landslide deposits of limited spatial extent; Figure 2a; Perez et al.,

150 2016). Finally, at least since the early Cenozoic, the Eastern Cordillera was high enough to  
151 prevent sediment transfer from the Western Cordillera to the Amazonian basin and was also  
152 an eroding area, representing a sediment source toward both the Altiplano to the southwest  
153 and the Amazonian basin to the northeast (Perez et al., 2016).

154         The Subandean zone and the Altiplano are documented as tectonically active; with  
155 shortening since ~14 Ma in the Subandes (Espurt et al., 2011; Gautheron et al., 2013; Figure  
156 3) and extension since ~5 Ma in the Altiplano (Cabrera et al., 1991; Figure 3). In between,  
157 the Eastern Cordillera, limited southward by the Apurimac fault system presents nowadays a  
158 low-magnitude crustal seismicity, which mainly focuses along the Altiplano-Eastern  
159 Cordillera limit (Figure 3a). It is however, too low to determine any specific tectonic  
160 behavior (Figure 3b). Preliminary thermochronological investigation in the core of the  
161 Eastern Cordillera (Machu Picchu; Figure 2b), nonetheless, favors a post ~4 Ma acceleration  
162 of incision-driven exhumation with the capture of a northern-extended paleo-Altiplano along  
163 with potential tectonic activity of the Apurimac fault system (Gérard et al., 2021). However,  
164 this inference has been restricted to the area of Machu Picchu and cannot be extended yet for  
165 the entire Abancay Deflection. Also, this preliminary study can neither validate nor invalidate  
166 potential tectonic-driven exhumation. The observed seismicity for the Apurimac fault system  
167 area could be linked and/or connected with either Subandean flat-ramp thrust systems or  
168 undocumented active internal backthrusts, or even normal faulting as currently occurring in  
169 the Altiplano (Wimpenny et al., 2020). Potential tectonic drivers responsible for building the  
170 Abancay Deflection and particularly the Eastern Cordillera area remain unknown.  
171 Quantitative thermochronology and modeling are ideal tools that enable us to explore  
172 exhumation patterns over the whole area and to discuss the possible exhumation mechanisms.

173

### 174 **3 Methods**



175 AHe and AFT thermochronology are based on He and fission-track production during  
176 alpha decay of  $^{238}\text{U}$ ,  $^{235}\text{U}$ ,  $^{232}\text{Th}$  and  $^{147}\text{Sm}$  and fission decay of  $^{238}\text{U}$ , respectively, with  
177 associated  $^4\text{He}$  and fission-track accumulation within apatite crystals. Using a rate of He  
178 diffusion out of the crystals or fission-track annealing with temperature, those methods can  
179 be used to record the thermal evolution of the upper crust, given their thermal sensitivity  
180 ranges spanning from  $\sim 80\text{-}40^\circ\text{C}$  (Ault et al., 2019) and  $\sim 75\text{-}125^\circ\text{C}$  (Reiners & Brandon,  
181 2006) respectively, for active mountain ranges, depending on cooling rate and/or holding  
182 time within the respective partial retention or annealing zones. Thus, low-temperature  
183 thermochronology records the thermal evolution of the upper crust ( $< 5\text{ km}$ ) and is a key to  
184 decipher between different exhumation mechanisms through time-evolving rock uplift and  
185 landscape evolution (Ault et al., 2019; Reiners & Shuster, 2009). Quantitative interpretation  
186 with three different types of models (*i.e.* geometric, thermal and thermo-kinematic, sections  
187 3.2-3.4) with increasing complexity makes it possible to test model robustness and propose  
188 consistent scenarios for the exhumation of the Abancay Deflection.

189

### 190 **3.1 Low-temperature thermochronological data**

191 We collected 33 samples from igneous bedrock along four altitude profiles  
192 (Ocobamba, Lucma, Abancay and Limatambo) complemented by 6 individual samples across  
193 the Abancay Deflection, in order to get an optimal coverage of the study area (Figures 2 & 4;  
194 Table 1). Granite samples were crushed and sieved at the Géode laboratory (Lyon, France) to  
195 extract the 100-160  $\mu\text{m}$  grain size fractions. Apatite crystals were concentrated using  
196 standard magnetic and heavy-liquid separation techniques at the GeoThermoChronology  
197 (GTC) platform within the ISTerre laboratory (Université Grenoble Alpes, France).

198 For AHe dating, single euhedral apatite crystals were carefully selected under a  
199 binocular microscope to identify minerals without fractures and/or inclusions that would

200 skew the AHe age (diffusion artifacts and/or additional  $^4\text{He}$  sources; Farley, 2002). We  
201 determined the individual grain geometry and calculated the alpha-ejection correction factor  
202 using the Qt\_FT program (Gautheron and Tassan-Got, 2010; Ketcham et al., 2011).  
203 Individual apatites were encapsulated in platinum tubes allowing apatite heating and  
204 manipulation. Each apatite in its platinum tube was then heated under high vacuum  
205 conditions at high temperature ( $1050\pm 50^\circ\text{C}$  using an infrared diode laser) twice for 5 min at  
206 GEOPS laboratory (Université Paris Saclay, France). The released  $^4\text{He}$  gas was mixed with a  
207 known amount of  $^3\text{He}$ , purified and the gas was analyzed using a Prisma Quadrupole.  
208 The  $^4\text{He}$  content was determined by isotope dilution method. Subsequently, apatite crystals  
209 were dissolved in 100  $\mu\text{l}$  of  $\text{HNO}_3$  5N solution containing known amount of  $^{235}\text{U}$ ,  $^{230}\text{Th}$ ,  
210  $^{149}\text{Sm}$  and  $^{42}\text{Ca}$ . The solution was heated at  $70^\circ\text{C}$  during 3 h and after a cooling time, 900  $\mu\text{l}$   
211 of distilled water was added. The final solution was analyzed using an ELEMENT XR ICP-  
212 MS and the  $^{238}\text{U}$ ,  $^{230}\text{Th}$  and  $^{147}\text{Sm}$  concentrations and apatite weight (using the Ca content)  
213 were determined following the methodology proposed by Evans et al. (2005). Durango  
214 apatite crystals were also analyzed during the same period to ensure the data quality. The  
215 one-sigma error on each AHe age amounts to 8%, reflecting the analytical error and the  
216 uncertainty on the  $F_T$  ejection factor correction. More details about the analytical procedure  
217 can be found in Recanati et al. (2017).

218 For AFT dating at the GTC laboratory (ISterre, Grenoble, France), apatites were  
219 mounted in epoxy resin, polished, and etched for 20 s at  $21^\circ\text{C}$  using a 5.5 M  $\text{HNO}_3$  solution  
220 to reveal spontaneous fission tracks. Using the external detector method, all samples were  
221 irradiated together with Durango and Fish Canyon Tuff age standards and IRMM540R  
222 dosimeter glasses at the FRM II reactor (Munich, Germany). Tracks were counted and  
223 horizontally confined track lengths were measured dry at 1250x magnification under an  
224 Olympus BX51 optical microscope, using the FTStage 4.04 program at ISterre. We used the

225 BINOMFIT program (Ehlers et al., 2005) to calculate the AFT central ages (Figures S1 to  
226 S27).

227

### 228 **3.2 Age-elevation relationships (AER)**

229 For AER modeling, single- or multi-tier age-elevation relationships (AER) to the AFT  
230 and AHe data from an altitudinal profile data were fitted using a Bayesian approach to obtain  
231 a first-order estimate of apparent exhumation rates and to possibly evidence any potential  
232 break-in-slope in AERs by minimization of the Bayesian Information Criterion (BIC;  
233 Glotzbach et al., 2011; Schwarz, 1978). The BIC provides a statistical way to assess the  
234 appropriate model complexity (Schwarz, 1978) by computing the ratio between likelihood  
235 (fitting) and the model complexity (number of break-in-slope; Glotzbach et al., 2011). This  
236 statistical approach implies that the lower the BIC value is for different scenarios (i.e. one  
237 single or multiple segment(s) for a given AER), statistically the more robust is the inferred  
238 slope of the AER in terms of apparent exhumation rate. In our study, we only present and  
239 interpret the outcome scenarios that minimize the BIC criterion. This approach provides first-  
240 order constraints on the exhumation rates and potential exhumation changes through time for  
241 each altitudinal profile. These apparent exhumation rates are, nonetheless, not incorporating  
242 any consideration regarding the inter-sample AHe/AFT kinetic variability, the thermal crustal  
243 regime, the relief evolution and the isostasy assuming a quasi-vertical profile (Stüwe et al.,  
244 1994). These modeling biases will be considered with 2D thermal and 3D thermo-kinematic  
245 modeling described hereafter.

246

### 247 **3.3 Time-temperature modeling (QTQt)**

248 Time-temperature modeling with QTQt (Bayesian transdimensional and MCMC  
249 sampling; Gallagher, 2012) gives quantitative constraints regarding thermal histories for

250 individual samples, with the possibility to combine multi-samples from pseudo-vertical  
251 profiles. We processed 300,000 iterations for both individual sample and profiles exploring  
252 predicted T-t paths with their respective likelihood to extract best-fitting thermal histories  
253 (Figures S28 to S37). We used the implemented annealing model of Ketcham et al. (2007)  
254 and the radiation damage model of Gautheron et al. (2009) for AFT and AHe data  
255 respectively. We allowed the geothermal gradient to vary over time between 10 and 40°C/km  
256 which are common for the non-volcanic Central Andes (Barnes et al., 2008). The total  
257 timespan explored considers two times the older thermochronological age for each profile to  
258 eliminate any potential temporal bias.

259         Assessing the geothermal gradient is a crucial point for exhumation rate computation,  
260 and the Abancay Deflection is devoid of any direct measurement. We computed a geothermal  
261 gradient according to the nearest thermal parameter measurements and/or accepted values.  
262 Using heat flow and thermal conductivity measurements at the Tintaya mine 100 km south-  
263 east of Cuzco in the Altiplano (40 mW/m<sup>2</sup> and 2.9 W/m/°C respectively; Figure 1b; Henry &  
264 Pollack, 1988), crustal average heat production (~0.9 μW/m<sup>3</sup>; Springer, 1999), thermal  
265 diffusivity for granitic bedrock (~40 km<sup>2</sup>/m.y.; Arndt et al., 1997; Whittington et al., 2009)  
266 and a 25°C surface temperature (Gonfiantini et al., 2001), we obtained a geothermal gradient  
267 of 18±4°C/km (Text S1). This computed value is consistent with direct measurements  
268 inferred from the Camisea area (~17°C/km; Figure 1b; Espurt et al., 2011) and the Tintaya  
269 mine (~14°C/km; Henry & Pollack, 1988). Moreover, this value overlaps with compiled  
270 geothermal gradients for the Eastern Cordillera in Bolivia (26±8°C/km; Barnes et al., 2008).

271         Following QTQt modeling, we thus convert cooling histories derived from QTQt  
272 expected models into exhumation rates, using an assumed constant and spatially-uniform  
273 geothermal gradient of 18±4°C/km. We report the 95% confidence interval around the

274 expected models. This method leads to averaging and smoothing of the predicted cooling  
275 histories but is a conservative approach. With these estimates, in addition to the AER and  
276 Pecube outcomes, we can compare exhumation rates between these different and independent  
277 approaches to identify consistency in model predictions or any potential impact of different  
278 assumptions in the modeling approaches. Magmatic arc activity at the Abancay Deflection  
279 and its potential thermal perturbation ceased after ~30 Ma (Mamani et al., 2010). It appears  
280 that the Eastern Cordillera did not experience any burial during the Eocene, because it acted  
281 like a long-lived structural high (Perez et al., 2016), as mentioned earlier. Furthermore,  
282 Cenozoic basins only occurred in the Altiplano domain (Figure 2a), which prevented  
283 potential sedimentary burial in our study area. For the Altiplano, most of the sedimentary  
284 cover was deposited synchronously with the magmatic arc activity prior to 30 Ma (Figure 2a;  
285 Mamani et al., 2010) and even prior to ~40 Ma considering the crystallization age of the  
286 Cotabamba pluton we sampled (Limatambo profile; Table 1; Perello et al., 2003). We  
287 consequently assumed that all samples in the Altiplano were at temperatures higher than the  
288 closure temperature before the onset of cooling in our QTQt models (interpreted from 40  
289 Ma). For the surface, we implemented an atmospheric lapse rate of 6°C/km according to  
290 Gonfiantini et al. (2001) for the eastern flank of the inter-tropical Andes. Parameters used for  
291 QTQt data inversion are displayed in Table S1.

292

### 293 **3.4 Thermo-kinematic modeling (Pecube)**

#### 294 **3.4.1 Pecube model**

295 Pecube modeling allows to quantify thermal histories for rock particles at depth in  
296 exhumation or burial contexts, considering landscape evolution (topography, relief), the  
297 thermal regime of the crust, the tectonic setting (faults, uplift or subsidence) and isostasy  
298 (Braun, 2003; Braun et al., 2012). Pecube modeling offers the possibility to simultaneously

299 test numerous tectonic or incision scenarios in 3D, computing associated thermal histories,  
300 and to subsequently compare numerical predictions to observed thermochronological data  
301 (punctual or along altitudinal profiles). By solving the 3D heat equation in the crust, the  
302 thermo-kinematic program Pecube v4.2 (Braun, 2003; Braun et al., 2012) predicts the spatial  
303 distribution of thermochronological ages for specific samples considering exhumation  
304 through lateral and vertical rock kinetics and relief evolution. We used Pecube in inverse  
305 mode (Neighborhood Algorithm - NA; Sambridge, 1999a,b) to determine optimal value  
306 ranges for tested parameters by minimizing the misfit function between predictions and  
307 observations (Text S2).

308

### 309 **3.4.2 Input data and fixed parameters**

310 We implemented into Pecube thermochronological data including AFT and AHe  
311 thermochronometric systems. We used 33 AHe ages (AHe mean grain ages, 28 new data and  
312 5 from Gérard et al., 2021) and 42 AFT ages (AFT central ages, 32 new data, 2 from Kennan,  
313 2008, and 8 from Ruiz et al., 2009). We implemented the present-day topography extracted  
314 from the global elevation database GTOPO30 (Figure 5). The He diffusion coefficient and  
315 the AFT annealing model from Farley (2000) and Ketcham et al. (1999) have been used,  
316 respectively. For AHe data, we chose the Farley (2000) model for He diffusion as it presents  
317 mean values for the diffusion coefficient for low-damaged apatites. In our case, as  
318 exhumation histories are simple without identified reheating, damage influence may play a  
319 minor role in the He diffusion process and is nearly identical to the Gautheron et al. (2009)  
320 diffusion model in such a case. It is not possible with Pecube to reproduce the AHe age  
321 dispersion between crystals due to damage impact on He diffusion (Gautheron et al., 2009;  
322 Shuster et al., 2006). So, we here decided to implement the AHe mean ages and standard  
323 deviation errors (Table S2). Regarding the AFT data, we also implemented track-length

324 measurements when available. Finally, we also subsequently compared the Pecube model T-t  
325 outcomes (best-fitting scenarios) to T-t paths derived from QTQt modeling.

326 In order to optimize computation time, we divided the Abancay Deflection into two  
327 crustal blocks (Altiplano and Eastern Cordillera; Figure 2) that we modeled independently.  
328 Each of these crustal blocks represents the natural tectono-morphic boundary of the Abancay  
329 Deflection. The timespan explored starts at 50 Ma for all the simulations to eliminate any  
330 potential temporal bias. We subsequently divided the explored timespan into six time slices:  
331 50, 25, 15, 10, 5 and 0 Ma. For each time boundary, we fit the modeled mean paleo-elevation  
332 according to Sundell et al. (2019). We do not have, however, any information regarding the  
333 relief evolution of the Abancay Deflection, which sits in a remote location with no existing  
334 information about relief evolution (Text S4). Finally, for exhumation rate quantification from  
335 thermochronological data, we fixed the crustal thermal and rheological parameters in space  
336 and time (Figure 5; Table S3). For these parameters, we finally explored the basal  
337 temperature of the crustal block and the thermal diffusivity to test our chosen geothermal  
338 gradient (Table S4).

339

### 340 **3.4.3 Neighborhood Algorithm inversions and explored parameters**

341 We used Pecube in inverse mode to quantitatively constrain parameter values (i.e.  
342 tectono-morphic scenarios) that best reproduce the input thermochronological data. We  
343 extracted the best-fitting parameter values for each inversion computing probability density  
344 functions (Sambridge, 1999a;b). When the inversion clearly converges toward a unique  
345 parameter solution (one peak for the probability density function), we extracted the parameter  
346 value applying the  $2\sigma$  standard deviation. We consequently used forward Pecube modeling to  
347 present the best-fitting scenarios (T-t paths) and data reproducibility using inversion-derived  
348 parameters as input data (Supporting Information).

349           Because of computing time issues with the global model, and as the Altiplano and the  
350 Eastern Cordillera present opposite morphologies (flat vs. deeply incised; Gérard et al.,  
351 2021), and different exhumation trends according to local studies (slow and continuous (Ruiz  
352 et al., 2009) vs. recent acceleration (Kennan, 2008; Gérard et al., 2021)), we explored these  
353 areas separately with the ultimate goal to unravel their respective exhumation pattern. For the  
354 Altiplano model, we explored the basal crustal temperature (proxy for the geothermal  
355 gradient; Figure 5), the exhumation history for the entire crustal block (Figure 5), and  
356 landscape evolution through time (topography offset and relief amplification factor; Figure  
357 S38). Inverting topography offset and relief amplification factor can also be used to identify  
358 any potential reheating through sedimentary burial. If a complex cooling history with sample  
359 burial/reheating would be needed to explain the thermochronological data, we would expect  
360 the inversion outcomes to converge toward lowering of the relief amplification factor,  
361 implying valley filling and sample burial.

362           For the Eastern Cordillera model, we explored the exhumation history for the entire  
363 crustal block (Figure 5), relief and topographic evolution (Figure S38), and the kinematics of  
364 the Apurimac fault system (fault dip, timing of initiation and fault velocity; Figure 5).  
365 Because of the code architecture, block exhumation and fault kinematics parameters were  
366 treated independently, which allows to explore both regional exhumation (spatially constant)  
367 and additional exhumation along the fault (spatially variable). For instance, the regional  
368 background exhumation (block exhumation) should imply deep-crustal/lithospheric  
369 mechanisms affecting equally the entire crustal block. The fault kinematics would imply a  
370 localized structure on which an additional source of exhumation could exist. Finally, the  
371 landscape dynamics through incision and deposition (relief and topographic evolution) could  
372 generate an additional source of exhumation or burial. Basal temperature for the Eastern  
373 Cordillera has been fixed in order to limit the number of inverted parameters and any



374 modeling convergence issue. We fixed the basal temperature at 560°C (geothermal gradient  
375 of 18°C/km and surface temperature of 20°C) following previous studies (Barnes et al., 2008;  
376 Espurt et al., 2011; Henry & Pollack, 1988). This corresponds to an unperturbed geothermal  
377 gradient, which is then modified by rock advection. The detailed list of the explored Pecube  
378 parameters is available in Table S4.

379

## 380 **4 Results**

### 381 **4.1 New thermochronological data and AERs**

382 For the entire Abancay Deflection area, new 108 single-crystal AHe ages (from 28  
383 samples) and 27 AFT central ages range from  $0.7\pm 0.1$  to  $35.8\pm 2.9$  Ma and from  $2.6\pm 1.9$  to  
384  $38.2\pm 4.4$  Ma respectively (Figure 4 & 6; Tables 2 and 3). Reproducibility of single-crystal  
385 AHe ages is satisfactory with averaged dispersion <10% for the whole dataset. For AFT  
386 central ages, all samples passed the  $\chi^2$  test (>5%; Table 3; Figures S1 to S27), meaning that  
387 we can consider single-age populations for each sample (Green, 1981). Thermochronological  
388 ages ranging up to 40 Ma are characteristic of the northern Eastern Cordillera and the  
389 Altiplano, as shown for the Lucma, Abancay and Limatambo altitudinal profiles and  
390 individual data (AB-17-19 and AB-17-18; Figure 4 & 6). The southern Eastern Cordillera  
391 presents much younger thermochronological ages, all <10 Ma (Ocobamba profile and  
392 Incahuasi zone, AB-17-13 and AB-17-15; Figure 4 & 6).

393 For all altitudinal profiles, both AHe and AFT ages best fit a single AER statistically,  
394 but they reveal different rates and timing of exhumation (Figure 6). The Lucma profile  
395 presents apparent exhumation rates of  $0.07^{+0.01}_{-0.01}$  and  $0.08^{+0.04}_{-0.02}$  km/m.y since 40 Ma, based on  
396 AHe and AFT data, respectively (Figure 6), while the Abancay and Limatambo profiles give  
397 apparent exhumation rates between 0.1 to 0.2 km/m.y, with a possible increase in exhumation  
398 since 10-15 Ma (Figure 6). In the case of the Abancay profile, even if the three lowest

399 samples appear aligned vertically (suggesting a potential acceleration in exhumation; Figure  
400 6), our AER approach statistically favors a single linear trend, reconciled by the 95%  
401 confidence interval driven by data resolution and uncertainties. The Ocobamba profile  
402 presents much higher apparent exhumation rates for the last 6 Ma, with  $0.5_{-0.1}^{+0.2}$  km/m.y based  
403 on AHe and  $0.9_{-0.4}^{+3.7}$  km/m.y, based on AFT. These exhumation rates estimates correspond to  
404 the lowest computed BIC, and consequently to the best-fitting solutions according our  
405 Bayesian approach for interpreting AERs (Glotzbach et al., 2011).

406

#### 407 **4.2 Numerical thermo(-kinematic) modeling**

408 Modeled time-temperature (T-t) paths with QTQt show for the entire study area a  
409 moderate and continuous cooling history with a cooling rate of  $\sim 2.5^{\circ}\text{C}/\text{m.y.}$  between 40 (~38  
410 Ma for the Limatambo profile due to the intrusion emplacement constraint; Figure 7c) and ca.  
411 5 Ma (Figure 7; note that the rapid cooling for the Limatambo profile is due to the  
412 Cotabamba pluton crystallization, and has not been taking into account because it has a very  
413 limited effect over time). Whereas cooling trends are relatively similar for the northern  
414 Eastern Cordillera and the Altiplano (Figures 7a,c; Figures S31 to S35), T-t paths for the  
415 southern Eastern Cordillera (Ocobamba profile and individual data) suggest an increase in  
416 cooling rate with values of  $\sim 17^{\circ}\text{C}/\text{m.y.}$  between 7 and 3 Ma (Figure 7b; Figures S28 to S30  
417 & S36), in agreement with AERs (Figure 6). It appears, however, that the timing for cooling  
418 acceleration in the Incahuasi zone (Figures 4 and S36) occurred slightly later (2-3 Ma). This  
419 signal could correspond to the same cooling acceleration identified for the southern Eastern  
420 Cordillera (7-3 Ma) with a short time-lag, or, could represent a local trend due to unidentified  
421 fault and/or exhumation process. Individual QTQt-derived cooling paths (Figure S28 to S36)  
422 exhibit short-term variations and more complex possible thermal histories. For a conservative  
423 approach, we chose to extract the statistically most robust signal for each profile or individual

424 sample, by considering the 95% confidence interval around the expected T-t path (Figure 7).  
425 This method prevents from potential over-interpretation of model outcomes, by focusing on  
426 well-constrained T-t paths. The apparent cooling increase at <2 Ma observed for Lucma and  
427 Limatambo profiles (Figures S33 and S34) represents a modeling bias. Indeed, all samples  
428 are colder than the closure temperature. The present-day surface temperature imposed in  
429 QTQt drives this apparent cooling acceleration, not supported by the thermochronological  
430 data. These modeling biases are not further considered in the following.

431 For Pecube modeling, we display results from our thermo-kinematic inversions in 2D  
432 graphs, where the explored parameter space is illustrated and each forward model is colored  
433 by its respective misfit value (Figures 8 and 9). We present thereafter the best-fitting value  
434 for explored parameters within each modeled crustal block. For the Altiplano model,  
435 parameter exploration through data inversion reveals a clear inversion convergence for the  
436 output background exhumation rate at  $0.2\pm 0.1$  km/m.y (Figure 8a) with high reproducibility  
437 of observed thermochronological ages and time-temperature paths (Figure 8b; Figure S41).  
438 The basal temperature does not converge but presents four peaks at  $420\pm 15^\circ\text{C}$ ,  $480\pm 20^\circ\text{C}$ ,  
439  $525\pm 10^\circ\text{C}$  and  $675\pm 30^\circ\text{C}$  (Figure 8a) corresponding, respectively, to geothermal gradients of  
440  $14\pm 1$ ,  $16\pm 1$ ,  $17\pm 1$  and  $22\pm 1^\circ\text{C}/\text{km}$  (Text S1). Relief amplification factors do not converge  
441 neither and are non-determinative or not discriminating (Figure S39). For the Eastern  
442 Cordillera model, the well-constrained value for background exhumation is converging to  
443  $0.2\pm 0.1$  km/m.y (Figure 9a), similarly to the Altiplano results. The lateral (north-south)  
444 position of the Apurimac fault system at 25 km depth (x fault parameter) is constrained to -  
445  $34\pm 5$  km (the negative sign corresponds to the northward exploration of this parameter).  
446 According to the approximate surface trace of the Apurimac fault system and to the output  
447 value for x fault, we estimated a fault dip ranging between  $28^\circ$  to  $47^\circ$  toward the north  
448 (Figures 9a and 9d). Regarding the fault kinematics, Pecube models favor fault activation at

449 5.3±1.5 Ma with an associated fault velocity of 2.9±0.6 km/m.y (Figure 9b). By taking into  
450 account the fault dip and velocity predictions, fault-induced exhumation rate is ~1 km/m.y.  
451 By adding background exhumation to the previous results, net exhumation rates of 1.2±0.4  
452 km/m.y are predicted for the southern Eastern Cordillera since ~5 Ma (Figure 9e). For the  
453 same time period, the northern Eastern Cordillera and the Altiplano underwent steady  
454 exhumation rates (Figure 10). Finally, and similarly to the Altiplano crustal-block model,  
455 relief amplification factor through time does not converge for the Eastern Cordillera model  
456 (Figure S40). The thermochronological data reproducibility is, however, robust (Figure S42).

457

## 458 **5 Discussion**

### 459 **5.1 From cooling rate to exhumation rate**

460 Our three different and independent modeling approaches are based on the statistically  
461 most robust scenarios for cooling and exhumation. As a result, they may not entirely reflect  
462 the variability of raw thermochronological data. Such an approach is, however, conservative  
463 to interpret models without over-interpreting the outcomes. Because the landscape parameters  
464 (topography offset & relief amplification factor) did not converge for Pecube inversions, the  
465 landscape evolution through time cannot be quantitatively assessed by our modeling. The  
466 relief amplification factor (Figure S38) can be used as a proxy for burial *i.e.* reheating of the  
467 upper crust. As shown by the non-convergence toward a minimization of the relief  
468 amplification factor at any time step explored (Figures S39 & S40), Pecube inversions  
469 confirm that no burial/reheating are required to accurately reproduce the thermochronological  
470 dataset. This result implies that the thermal perturbation supposedly associated with the  
471 magmatic arc activity between 50 and 30 Ma (Mamani et al., 2010) is not registered in our  
472 local thermochronological record (except maybe for the highest and oldest AFT data from the  
473 Limatambo profile). This can be explained by three reasons: 1) present-day outcropping

474 rocks were at that time still at depth and thus at temperatures above the PRZ/PAZ, i.e. not  
475 impacted by this reheating event; 2) for the southern Eastern Cordillera, the high exhumation  
476 rates since ~5 Ma, have removed the upper crustal section that could have potentially  
477 registered older thermal perturbations; and 3) the thermal perturbation was potentially  
478 spatially and/or temporally localized and did not affect our sampled sites. This last point also  
479 applies for the 7-0.5 Ma volcanism along the Apurimac fault system described south of  
480 Cuzco and in northern Bolivia by Bonhomme et al. (1988). The volcanism was spatially  
481 localized, and spread out sporadically over time. The thermal perturbation induced was thus  
482 restricted to the Apurimac fault zone, limited in time, and did not affect our sample sites. The  
483 same reasoning applies to a potential sediment burial that could have affected the Altiplano.  
484 We consequently assumed that our samples did not experienced reheating after 40 Ma.  
485 Modeled thermal histories obtained from the Abancay Deflection area present only a  
486 monotonic cooling phase with variable cooling rates (Figure 7). This simplifies our modeling  
487 approach regarding the crustal thermal structure.

488         Because we did not detect any perturbation of thermal histories by reheating or  
489 potential isotherm relaxation (sampled rocks were deep and hot enough before the modeled  
490 onset time for rock cooling), we convert the inferred cooling scenario into simple exhumation  
491 histories. Exhumation rates estimated from QTQt-derived cooling rates and using a steady  
492 and spatially-uniform geothermal gradient ( $18\pm 4^\circ\text{C}/\text{km}$ ), apparent exhumation rates from  
493 AERs (Glotzbach et al., 2011) and Pecube inversions results are all consistent with high data  
494 reproducibility between three independent approaches (Figure S43). This confirms that the  
495 assumed geothermal gradients for QTQt and Pecube models are satisfactory, even if we  
496 cannot tightly constrain the basal crustal temperature from Pecube inversion (Figure 8a). This  
497 non-convergence issue is frequently encountered in this type of modeling (*e.g.* Robert et al.,  
498 2011; Valla et al., 2012) and can be bypassed only by imposing thermal parameter values

499 from regional estimates. In detail, we identified four temperature peaks (probability density  
500 function for the Altiplano model; Figure 8a), corresponding to geothermal gradients spanning  
501 from 13°C/km to 23°C/km, compatible with our chosen value of  $18\pm 4^\circ\text{C}/\text{km}$  for the  
502 uppermost 5 km of the crust, using a basal temperature of 560°C. We furthermore performed  
503 inversion for each crustal model (Altiplano and Eastern Cordillera blocks; Table S4; Text  
504 S5), imposing a “warmer” geothermal gradient (30°C/km; Text S5). It clearly appears that the  
505  $\sim 20^\circ\text{C}/\text{km}$  geothermal gradient seems to be the most likely option for the Abancay Deflection  
506 at the scale of our study, with better thermochronological data reproducibility (Text S5;  
507 Figures S45 and S46).

508 We separated the study area into three zones derived from the patterns in output  
509 exhumation rate (QTQt; Figures 4 and 7). Using Pecube outcomes, the Altiplano and the  
510 northern Eastern Cordillera experienced similar exhumation histories since 40 Ma with  
511 exhumation rates of  $0.15\pm 0.10$  km/m.y. (Figure 10). The southern Eastern Cordillera  
512 experienced the same exhumation rate from  $\sim 20$  to  $5.3\pm 1.5$  Ma, followed by an acceleration  
513 of exhumation to  $1.2\pm 0.4$  km/m.y. (Figure 10). Even though the thermochronological data  
514 modeling and output time-temperature paths from QTQt are limited to the last 20 Ma for the  
515 southern Abancay Deflection (Figures 7b and 9c), we propose by temporal extrapolation that  
516 the southern Eastern Cordillera underwent similar exhumation rates as its neighboring areas  
517 (*i.e.* Altiplano and northern Eastern Cordillera) between 40 and 20 Ma. We proposed this  
518 hypothesis because no data corroborate any incision and/or tectonic activity pulses that would  
519 modify the exhumation dynamics affecting the southern Eastern Cordillera, punched between  
520 the northern Eastern Cordillera and the Altiplano. Over the last  $\sim 5$  Ma, the exhumation  
521 acceleration is spatially framed southward by the Apurimac fault system, pointing towards a  
522 differential exhumation pattern in the Abancay Deflection that we attribute to tectonically-  
523 driven rock uplift along the Apurimac fault system with rock removal by efficient erosion.

524

## 525 **5.2 Exhumation of the Abancay Deflection between 40 and 5 Ma**

526         The whole Abancay Deflection region experienced steady, moderate ( $0.2\pm 0.1$   
527 km/m.y.) and apparently spatially-uniform exhumation between 40 and 5 Ma (Figures 10 and  
528 11). This exhumation rate is highly consistent with those inferred between 40 and 15 Ma  
529 from the only thermochronological data available in the area (0.17 km/m.y.; Ruiz et al.,  
530 2009). Even if the Peruvian Altiplano experienced Miocene faulting delimitating intra-  
531 mountainous basins (Tinajani, Punacancha, and Paruro basins; Carlotto, 2013; Horton et al.,  
532 2014), there is no evidence for any acceleration of exhumation nor sedimentary burial related  
533 to these crustal processes according to our three independent modeling approaches.  
534 Surprisingly, although the Bolivian Eastern Cordillera registered peaks of exhumation  
535 through tectonic and erosional processes between 50 and 15 Ma (Barnes et al., 2012; ~500  
536 km to the south-east of our study area), our data and inverse models rather favor a large-scale  
537 uniform exhumation history during that period.

538         Consequently, we interpret the steady and uniform exhumation rates as the record of  
539 low-magnitude surface denudation affecting the Abancay Deflection in an internally-drained  
540 environment (Figure 11; Gérard et al., 2021). Furthermore, contemporaneously to the  
541 Bolivian Orocline bending during Miocene (Roperch et al., 2006), the Abancay Deflection  
542 was built in a left-lateral transpressional context (Dalmayrac et al., 1980) associated to lateral  
543 rock advection from the south (Figures 11c and 11d) with limited rock uplift as shown by  
544 QTQt and Pecube inversions (Figure 9c); *i.e.* data reproducibility is overall good without  
545 implying any additional earlier rock uplift due to the transpressional context. The crustal  
546 tectonic regime, dominated by horizontal motion, cannot be registered by the  
547 thermochronological data, nor easily-modeled by balanced cross-section that encompass only  
548 2D processes (Gotberg et al., 2010). Moreover, our outcomes, pointing towards a low-

549 magnitude exhumation rate of  $\sim 0.2$  km/m.y. between 40 and 5 Ma, are comparable in terms  
550 of magnitude with the large-scale and steady surface uplift (at  $\sim 0.1$  km/m.y) of the Eastern  
551 Cordillera and the Altiplano modeled by Sundell et al. (2019). The output exhumation rates  
552 are the part of rock uplift accommodated by erosion, while the remaining part (unconstrained  
553 by our thermochronological record) is the surface uplift.

554         The low-exhumation and surface-uplift rates are compatible with large-scale tectonic  
555 shortening (Lamb, 2011; Phillips et al., 2012) and/or lower crustal flow (Husson and  
556 Sempere, 2003; Tassara, 2005; Ouimet and Cook, 2010). Kar et al. (2016) suggested more  
557 rapid surface uplift of the northern Altiplano between 10 and 5 Ma (0.4 km/m.y). Indeed, one  
558 or multiple lithospheric delamination event(s) implying pulses of rapid surface uplift have  
559 been proposed during the Miocene (Garzione et al., 2017). Consequently, the Altiplano may  
560 have risen rapidly without prominent incision and thus recorded limited exhumation (*i.e.*  
561 steady low exhumation rates despite rapid surface uplift). In a potentially endorheic context  
562 (Gérard et al., 2021), sediment evacuation and thus large-scale erosion rates are low. Such an  
563 acceleration of surface uplift should have induced an increase in erosion/exhumation via  
564 enhanced erosion due to orographic precipitation, at the edge of the plateau between 10 and 5  
565 Ma. Nevertheless, it has been also demonstrated from regional-climate numerical modeling  
566 that such a surface-uplift acceleration can be an artifact driven by climatic variability (Ehlers  
567 & Poulsen, 2009). Considering our data and modeling outcomes, as well as the timing of the  
568 exhumation acceleration from our data ( $5 \pm 2$  Ma), we cannot discard nor validate any of these  
569 surface-uplift models (slow and steady vs. acceleration of surface uplift between 10 and 5  
570 Ma).

571

### 572 **5.3 Southern Eastern Cordillera – 5 Ma exhumation rate increase**



573           The southern Eastern Cordillera, framed southward by the Apurimac fault system, has  
574 registered an order-of-magnitude acceleration in exhumation since ca. 5 Ma, driven by both  
575 topographic incision and tectonic uplift. The capture of an endorheic high-elevation paleo-  
576 Altiplano and subsequent pulse of incision could partly explain the exhumation acceleration  
577 for the southern Eastern Cordillera, although not enough to explain the total amount of  
578 exhumation since 5 Ma (Gérard et al., 2021). This timing is consistent with the inferred  
579 initiation of canyon carving (Pliocene) further south in the Bolivian Eastern Cordillera (Lease  
580 & Ehlers, 2013). Pecube modeling, however, does not allow quantitatively constraining relief  
581 and topographic evolution through time (Text S4).

582           The local 5-Ma exhumation event affecting the southern Eastern Cordillera (Figure  
583 11e) cannot be explained by large-scale phenomenon such as lithospheric delamination,  
584 neither in terms of spatial extent nor timing (Garzzone et al., 2006; Sobolev and Babeyko,  
585 2005). Tectonic uplift along local structures associated with enhanced erosion could be a  
586 potential trigger for our observed pattern of thermochronological ages and exhumation  
587 (Figures 4, 6 and 7). Pecube inverse outcomes show that the inherited crustal-scale Apurimac  
588 fault system can reproduce the 3D thermochronological-data pattern, with significant tilting  
589 of the southern Eastern Cordillera (Figure 9). Regionally, the fault system is curved around  
590 the Abancay Deflection. In such a deflected thrusting pattern, it is geometrically difficult to  
591 link the southern Eastern Cordillera to a south-dipping ramp located beneath and connected  
592 to the main Subandean front without implying an unlikely and complex structural geometry.  
593 Furthermore, the Subandean front has been active since 14 Ma (Espurt et al., 2011), which  
594 clearly predates the 5-Ma exhumation signal we observed in the Eastern Cordillera. The  
595 Apurimac fault system appears to be the most likely structure tilting the Eastern Cordillera  
596 (Figure 9) associated with backthrusting activity with a relatively low north-dipping angle of  
597 30-40° (Figure 9d). This tectonic signal is added to the large-scale and long-term exhumation

598 signal affecting the whole area since 40 Ma ( $0.2\pm 0.1$  km/m.y.) and generates the differential  
599 exhumation pattern observed in Figure 9e.

600         Considering end-member values of best-fitting Pecube parameters (*i.e.* fault dipping  
601 angle, timing for fault activation and fault velocity), we estimated a first-order total  
602 horizontal crustal shortening ranging between 6 and 21 km (mean shortening rate of  $2.8\pm 1.5$   
603 km/m.y.). The total amount of vertical rock uplift ranges between 4 and 17 km (mean rock  
604 uplift rate of  $2.2\pm 1.3$  km/m.y.) since 5 Ma. However, given our thermochronometric dataset  
605 and the lack of high-temperature thermochronometers to further constrain the pre-5-Ma  
606 exhumation in the area, we considered that highest rock-uplift estimated from Pecube  
607 modeling are unrealistic and rather should be  $\sim 7$  km maximum for the last 5 Ma. The  
608 parameter ranges derived from our approach do not allow to constrain precisely the tectonic  
609 deformation (nor vertical or horizontal) rates and thus to further discriminate the tectonic  
610 balance and the respective importance of different rock-uplift drivers for the southern Eastern  
611 Cordillera. On the other hand, rock-uplift rates overlap with exhumation rates over the last 5  
612 Ma ( $2.2\pm 1.3$  km/m.y. vs.  $1.2\pm 0.4$  km/m.y. respectively; Figure 10), which highlights the  
613 consistency between 2D and 3D modeling approaches. Furthermore, constrained 5-Ma  
614 horizontal shortening rates for the southern Eastern Cordillera ( $2.8\pm 1.5$  km/m.y.) are also  
615 consistent with balanced cross-section reconstructions and derived shortening rates in the  
616 Subandean area ( $\sim 3.8$  km/m.y.; Espurt et al., 2011), directly located to the north of the  
617 Abancay Deflection (Figure 1).

618         Although thick-skinned backthrusts have been reported as active since the Late  
619 Miocene to the north of the Abancay Deflection (Shira mountains; Gautheron et al., 2013;  
620 Huaytapallana fault, in the continuity of the Apurimac fault system; Dorbath et al., 1990;  
621 Figure 3b), we document for the first time the recent tectonic activity (*i.e.*  $< 5$  Ma) for the  
622 Abancay region itself, with significant but local exhumation along the Apurimac fault system

623 south-verging backthrusting. The low-magnitude earthquake cluster in this zone (Figure 3a)  
624 strongly corroborates our interpretation, also supporting the hypothesis that such fault activity  
625 and observed exhumation pattern on million-year timescales is still ongoing today.

626

#### 627 **5.4 Potential drivers for the Apurimac fault system re-activation**

628 The Abancay Deflection is framed northward by the Subandean zone, which has been  
629 tectonically active since ca. 14 Ma (Espurt et al., 2011). To the south, the Altiplano is  
630 characterized by extensional faulting since the Quaternary (Sébrier et al., 1985; Wimpenny et  
631 al., 2018). Our results show that the Eastern Cordillera was tilted through the south-verging  
632 backthrust of the Apurimac fault system, which has been active since 8 to 2 Ma and  
633 statistically more likely since ca. 5 Ma (Figures 7b, 9b, 11e and 12). Considering the  
634 orogenic-prism balance theory (Whipple & Meade, 2004; Willett et al., 1993), the tectonic-  
635 shortening transfer from the Altiplano to the Subandes (since ca. 15 Ma in Bolivian Andes;  
636 Horton, 2005; Norton and Schlunegger, 2011; Anderson et al., 2018) was triggered by  
637 sediment accumulation in the foreland basin (i.e. paleo-Subandean zone; Mosolf et al., 2011)  
638 following the late-Miocene South-American monsoon intensification (Poulsen et al., 2010).  
639 Sediment accumulation in the foreland coming from more internal part of the mountain range  
640 (which implies mass removal) created a regional stress pattern reorganization that probably  
641 triggered eastward propagation of deformation. Thus, the question of the out-of-sequence  
642 Apurimac back thrust activity needs to be addressed.

643 From a morphologic viewpoint, the peculiarity of the Abancay Deflection makes it the  
644 only region at the scale of the northern Altiplano where the hydrographic network is reaching  
645 the core of the orogen after crossing the entire Eastern Cordillera (Apurimac and Urubamba  
646 Rivers; Figures 1 and 11). The river capture, incision and subsequent increased erosion were  
647 probably triggered and enhanced by wetter conditions during the late-Miocene (Poulsen et

648 al., 2010) and Pliocene climate variability (Lease & Ehlers, 2013; Peizhen et al., 2001).  
649 Given the initiation of reverse faulting at ca. 5 Ma, the Apurimac fault system has played as  
650 an out-of-sequence thrust. We thus conceptually interpret in the following the tectonic  
651 evolution of the Abancay Deflection (Figures 11 and 12), linking the climate evolution and  
652 the tectonic transfer regarding the orogenic prism re-balancing and geodynamic settings:

653 (1) Late-Miocene precipitation intensification (Poulsen et al., 2010) on the eastern  
654 flank of the Peruvian Andes favored the regressive erosion through the proto-Apurimac and -  
655 Urubamba Rivers. These paleo-drainage systems captured and incised the internally-drained  
656 paleo-Abancay Deflection (Figures 11d and 11e).

657 (2) In consequence to this drainage capture, river incision subsequently enhanced  
658 erosional processes over the large-scale Abancay Deflection. Rivers deeply carved the  
659 Eastern Cordillera, and sediments were exported toward the foreland basin and trapped  
660 within it (in the paleo-Subandes).

661 (3) By orogenic prism rebalancing, the Subandean deformation propagated northward  
662 at ca. 5 Ma (Mosolf et al., 2011; Gautheron et al., 2013). In the core of the orogen, mass  
663 removal decreased the taper angle and thus favored tectonically-driven rock uplift of the  
664 eroding southern Eastern Cordillera through the internal Apurimac fault system (Figures 11e  
665 and 12; DeCelles et al., 2009). Concurrently, the generated sediments accumulated in the  
666 Subandes have maintained the activity and the propagation of the Subandean front  
667 (Gautheron et al., 2013; Mosolf et al., 2011).

668 (4) Focused deformation localized on the Apurimac fault system may be explained by  
669 its specific position and geographic organization, bounding the northern edge of the Arequipa  
670 terrane (Figure 12; Loewy et al., 2004). The Arequipa terrane could play the role of a buttress  
671 and the deformation could focus on the south-verging lithospheric-scale Apurimac fault  
672 system, with the Brazilian shield northward (Figure 12). The northward advance of the

673 Arequipa terrane is still an ongoing process according to GPS measurements that support the  
674 current Bolivian Orocline bending (Allmendinger et al., 2005; Villegas-Lanza et al., 2016). In  
675 addition, the Apurimac fault system is a lithospheric-scale inherited structure (Carlier et al.,  
676 2005; Dalmayrac et al., 1980; Sempere et al., 2002) and constitutes a mechanical weak zone  
677 promoting the localization and accumulation of deformation.

678         Although the Andes present numerous deflected zones (*i.e.* Cajamarca, Huancabamba  
679 in Peru; Dalmayrac et al., 1980), the Abancay Deflection is exceptional with respect to its  
680 size, highly-rotated fault systems and its peculiar location at the northern tip of the Altiplano.  
681 It marks abruptly the along-strike segmentation of the Central Andes facing the Amazon  
682 basin with E-W topographic high. Although backthrusting activity through reactivated  
683 Cretaceous crustal normal-fault tilting in the Eastern Cordillera has been already documented  
684 in southern Peru (Perez et al., 2016), the Apurimac fault system backthrusting is a singularity  
685 for this region by its size and inheritance, and appears to be one of the main structure  
686 articulating the northern narrow Andes vs. the southern Bolivian Orocline. This fault system  
687 acted as a suture between the eastern Altiplano and the Eastern Cordillera (Jaillard & Soler,  
688 1996) and was reactivated as a backthrust within the last 5 Ma providing stronger uplift in the  
689 Eastern Cordillera. The relative position of the Arequipa terrane (Figure 11) acting as a rigid  
690 indenter could explain the accumulation of horizontal and vertical deformation in such  
691 limited-extend area and the subsequent orthogonal direction of the topography in comparison  
692 to the main orogen elongation axis. This could furthermore explain this undocumented  
693 tectonic behavior and probable higher erosion rates with an E-W topography facing the  
694 Amazonian moisture flux enhancing orographic updraft.

695

696 **5.5 Is the Abancay Deflection a Tectonic syntaxis?**

697           According to the geodynamic context with an oblique subduction, as well as the slab  
698 dip transition (flat northward vs. steep southward of the Abancay region; Barazangi & Isacks,  
699 1976), the Apurimac fault system could be a contractional duplex developed at bends or a  
700 stepover of crustal-scale strike-slip faulting. The Abancay Deflection presents however,  
701 numerous geomorphic, tectonic and geodynamic features at the origin of the theory of the  
702 tectonic syntaxes (Table 4) already documented in the Himalaya (Namche Barwa; Nanga  
703 Parbat; *e.g.* Zeitler et al., 2001) and Alaska (Saint Elias mount; *e.g.* Enkelmann et al., 2017).  
704 Focusing on the Abancay Deflection, high exhumation rates appear concentrated in the core  
705 of a distorted zone of limited-extend and framed by deflected active faults, promoting the  
706 classification of the Abancay Deflection as a tectonic syntaxis (This study; Table 4). In this  
707 case, the Arequipa terrane could play the role of the indenter in response to counterclockwise  
708 rotation (Roperch et al., 2006) of the northern limb of the Bolivian Orocline since the  
709 Miocene (Allmendinger et al., 2005; Müller et al., 2002).

710           The Himalayan syntaxes are characterized by heat advection, subsequent upward  
711 deflection of isotherms inducing a brittle-ductile rheological limit to the ascent (Koons et al.,  
712 2013). These peculiar thermal and rheological parameters associated to high geothermal  
713 gradients ( $\sim 60^{\circ}\text{C}/\text{km}$ ; Craw et al., 1994) and shallow seismicity ( $\sim 2\text{-}5$  km depth; Meltzer et  
714 al., 1998) are defining tectonic aneurisms (Koons et al., 2013). The Abancay Deflection,  
715 however, seems to be relatively “cold” ( $\sim 20^{\circ}\text{C}/\text{km}$ ; this study) and brittle at depth, consistent  
716 with geothermal gradient that do not exceed  $30^{\circ}\text{C}/\text{km}$  (Eastern Cordillera far south in  
717 Bolivia; Barnes et al., 2008; Henry & Pollack, 1988), and crustal seismicity up to 30 km  
718 depth, respectively (Figure 3a). Thus, the Abancay Deflection cannot be defined as a tectonic  
719 aneurism.

720           The similarity in structural and geomorphic setting between the Abancay Deflection  
721 and the Himalayan/Alaskan syntaxes, leads us to speculate that the Abancay Deflection may

722 reflect an incipient Andean syntaxis, where drainage capture and ensuing rapid incision of the  
723 plateau edge led to focused exhumation and tectonic uplift along a deflected fault pattern. In  
724 such a geodynamic context, associated to ocean – continent convergence, the closest  
725 comparison can be done with the Denali syntaxis in Alaska (Figure 13). The Abancay  
726 Deflection, however, has not reached yet (and maybe will never do) a mature stage of  
727 tectonic aneurism.

**Table 4.** Compilation of observations and comparison of documented tectonic syntaxes with the Abancay Deflection

Observation	Himalayan syntaxis	Alaskan syntaxis	Abancay Deflection
<u>Morphology</u>			
Positive anomaly of topography	<b>YES</b> Nanga Parbat mountains (NP) Namche Barwa mountains (NB) (Zeitler et al., 2001)	<b>YES</b> Denali mountains St Elias mount (Enkelmann et al., 2017)	<b>YES</b> Cordillera Vilcabamba (Salcantay, southern Eastern Cordillera) (Gérard et al. 2021)
High relief and incision	<b>YES</b> Indus River (NP) / Tsangpo River (NB) (Zeitler et al., 2001)	<b>YES</b> Seward et Logan glaciers (Enkelmann et al., 2017)	<b>YES</b> Urubamba River (Gérard et al. 2021)
Major crossing-orogens rivers	<b>YES</b> Indus River (NP) / Tsangpo River (NB) (Zeitler et al., 2001)	<b>NA*</b> Glaciated area	<b>YES</b> Urubamba River (This study; Gérard et al. 2021)
Captured high elevation plateau upstream	<b>YES</b> Tibetan plateau	<b>NO</b> No plateau	<b>YES</b> Altiplano



Observation	Himalayan syntaxis	Alaskan syntaxis	Abancay Deflection
Tightened and aligned rivers along active faults	<b>YES</b> Salween, Mekong / Yangtze Rivers (NB; Hallet & Molnar, 2001); Hari, Murgab et Helmand Rivers (NP; Brookfield, 1998)	<b>NA*</b> Glaciated area	<b>YES</b> Urubamba and Apurimac Rivers along the Apurimac fault system (This study; Gérard et al. 2021)
Knickpoints	<b>YES</b> Tsangpo River crossing the NB (Zeitler et al., 2001)	<b>NA*</b> Masked bedrock beneath the glaciers	<b>YES</b> Urubamba River crossing the Eastern Cordillera (Gérard et al. 2021)
<b><u>Tectonics and Geodynamic</u></b>			
Tectonic rotation and strike-slip faulting	<b>YES</b> Crustal folding through orogen-parallel compression (Royden et al., 1997) Jiali-Parlung fault (NB; Burg et al., 1998) Karakorum fault (NP; Bossart et al., 1988)	<b>YES</b> Fairweather fault (Chapman et al., 2012)	<b>YES</b> Counterclockwise rotation and left-lateral component of the Apurimac fault during Miocene (Dalmayrac et al., 1980; Roperch et al., 2006)
Thick-skinned tectonic	<b>YES</b> (Zeitler et al., 2001)	<b>YES</b> (Chapman et al., 2012)	<b>YES</b> Apurimac fault delimiting 2 crustal blocks (This study; Carlier et al., 2005)

Observation	Himalayan syntaxis	Alaskan syntaxis	Abancay Deflection
Localized deformation	<b>YES</b>	<b>YES</b>	<b>YES</b>
along crustal-scale faults and magmatic fluid circulation	(NP; Edwards et al., 2000; Schneider et al., 1999; Seeber & Pêcher, 1998)	Except for fluids circulation (Koons et al., 2010, 2013)	Apurimac fault and volcanic fluids circulation since ~7 Ma (Carlier et al., 1996; Carlier et al., 2005)
Indenter	<b>YES</b>	<b>YES</b>	<b>YES</b>
	Indian plate (Burtman & Molnar, 1993)	Yakutat terrane (Koons et al., 2010; Marechal et al., 2015)	Arequipa terrane (Ramos, 2010; Villegas-Lanza et al., 2016)
Higher exhumation rates into the core of the syntaxis	<b>YES</b>	<b>YES</b>	<b>YES</b>
	~10 km/m.y. since ~1 Ma (King et al., 2016)	~2 to ~5 km/m.y. since ~2 Ma (Enkelmann et al., 2009; Enkelmann et al., 2017; Falkowski et al., 2014)	~1,2 km/m.y. since ~5 Ma (This study)
<u>Conclusion</u>			
Tectonic syntaxis	<b>YES</b>	<b>YES</b>	<b>YES</b>
*Not applicable			

9

0

731 **6 Conclusions**

732 Our new thermochronological data and inverse thermo(-kinematic) modeling from the  
733 Abancay Deflection reveal steady and spatially-uniform exhumation for the whole study area  
734 between 40 and 5 Ma, at a moderate rate of  $\sim 0.2$  km/m.y. We interpret such slow and steady  
735 exhumation as evidence for large-scale crustal shortening and/or lower crustal flow  
736 associated to low-magnitude erosion rates in an internally-drained area. The differential  
737 exhumation of the Abancay Deflection area initiated at ca. 5 Ma, characterized by around  
738 500% increase in exhumation rate for the southern Eastern Cordillera ( $\sim 1.2$  km/m.y). This 5-  
739 Ma exhumation signal has been driven by incision (capture of the paleo-endoreic  
740 environment) and enhanced by tectonically-driven rock uplift along the Apurimac fault  
741 system activation as a south-verging backthrust. For the first time, we document the recent  
742 ( $< 5$  Ma) and ongoing tectonic activity of this fault system. Finally, we propose the late-  
743 Miocene precipitation intensification and the Arequipa terrane underplating as potential  
744 triggers for the re-activation of this out-of-sequence inherited crustal-scale thrust.  
745 Considering such a geomorphic and structural setting together with rapid and focused  
746 exhumation, in a region of anomalously high relief and topography, we speculate that the  
747 Abancay Deflection may represent the first identified incipient Andean syntaxis.

748

749 **Acknowledgements**

750 This work was supported by the IRD (Institut de Recherche pour le Développement),  
751 ISTERre, the INSU (Institut National des Sciences de l'Univers), and the ANR-12-NS06-  
752 0005-01 project for the AHe analysis. We are grateful to the SERNANP, the INGEMMET  
753 (Cusco-PATA convenio 006-2016-Fondecyt) and the National Archaeological Park of Machu  
754 Picchu, for the provided facilities. We thank P.H. Leloup and G. Mahéo (Géode laboratory,  
755 Lyon) and the GTC platform (F. Coeur & F. Sénebier, ISTERre, Grenoble) for sample

756 processing, as well as M. Balvay, R. Pinna-Jamme & F. Haurine for assistance during AFT  
757 and AHe dating. Datasets for this research are included in this paper (and its supplementary  
758 information files). We thank Mauricio Parra, Joel Saylor and an anonymous reviewer for  
759 instructive feedbacks on this manuscript. Datasets for this research are available at  
760 PANGAEA® - Data Publisher for Earth & Environmental Science doi:XXX), [Creative  
761 Commons Attribution License].

762

### 763 **Figure captions**

764

765 **Figure 1.** Abancay Deflection location. a) Location within South America of the study area  
766 at the northern tip of the Altiplano in Peru (P). b) Zoom-in on the Abancay Deflection area  
767 (black square in panel a). Double black arrows highlight the topography elongation axis. Note  
768 the pronounced incision within the study area through the iso-elevation line (black) at 3.8 km  
769 elevation via the Urubamba and Apurimac rivers (blue) canyons. Black thin lines framed by  
770 white triangles highlight the latitudinal range width variation with the Abancay Deflection as  
771 the transition zone between the northern narrow Peruvian Andes and the southern wide  
772 Bolivian Orocline. Black squares with red borders are the places where thermal parameters  
773 were measured.

774

775 **Figure 2.** Geology and morphology of the Abancay Deflection. a) Geological map of the  
776 study area. The crustal scale Apurimac fault system marks the tectonic limit between the  
777 Altiplano and the Eastern Cordillera. (INGEMMET geological map database - 1:100,000).  
778 White rectangles refer to previous thermochronological studies; references are provided in  
779 the method and results sections. b) Simplified map (from a) with major litho-tectonic  
780 domains: the Altiplano in blue and the Eastern Cordillera framed in red. c) 3D DEM of the

781 Abancay Deflection. On panels, red stars are the thermochronological sample location  
782 (vertical profiles and individual data; this study). 2D colored area (b) and corresponding 3D  
783 views (c) are crustal block locations processed with 3D thermo-kinematics modeling using  
784 Pecube for the Altiplano (blue) and the Eastern Cordillera (red) blocks.

785

786 **Figure 3.** Crustal seismic map of the Abancay Deflection (Dashed squares; hypocenters < 60  
787 km;  $M_w > 2$ ). a) Mapped earthquakes come from the USGS, IGP and ISC databases. Regions  
788 included into black ellipses emphasize positive anomalous cluster of seismicity in  
789 comparison with the quiescent Abancay core of the Eastern Cordillera. Black lines represent  
790 the major thrusts of the studied area. b) Moment tensors (CMT) for earthquakes (1969-2019)  
791 for the Abancay Deflection region (Dziewonski et al., 1981; Ekström et al., 2012). Focal  
792 mechanisms (transpressional) for the two 1969 Huaytapallana events are framed by the black  
793 rectangle (Dorbath et al., 1990; Suarez et al., 1983). There are no CMT data for  $M_w < 5.5$   
794 earthquakes. Tectonic shortening characterizes the Subandean front whereas extensional  
795 mechanisms affect the Altiplano. The question mark refers to the unknown tectonic behavior  
796 for the Eastern Cordillera.

797

798 **Figure 4.** Sample locations of the new thermochronological ages within the Abancay  
799 Deflection. Red and pink polygons are, respectively, Permo-Triassic and Eocene plutons.  
800 Previous studies are: 1: Gérard et al. (2021) and Kennan (2008); 2: Ruiz et al. (2009); 3:  
801 Espurt et al. (2011) and Gautheron et al. (2013). Blue and red numbers below sample names  
802 refer to AHe mean ages and AFT central ages for individual samples and the two-sampled-  
803 point Incahuasi vertical profile. Red capital letters refer to the other sampled vertical profiles  
804 (A: Ocobamba profile; B: Lucma profile; C: Limatambo profile & D: Abancay profile).  
805 Profiles results are displayed in Figure 6. Green, red and black contours mark the latitudinal

806 segmentation of the Abancay Deflection defining three areas according to thermal histories  
807 modeled with QTQt (*i.e.* Northern EC, Southern EC and Altiplano respectively). The black  
808 dashed square frames the Abancay Deflection. AFT: Apurimac fault system; EC: Eastern  
809 Cordillera.

810

811 **Figure 5.** Parameters implemented and/or explored in Pecube through time. Example for the  
812 Eastern Cordillera crustal block (see Figure 2 for location). For the Altiplano block we only  
813 explored the crustal block exhumation (1). Red dots mark the location of the  
814 thermochronological data. Numbers and question marks refer to explored parameters. 1:  
815 Crustal block exhumation (km/Ma); 2: Fault velocity (km/Ma); 3: Timing of fault activation  
816 (Ma); 4:  $x$  fault (km), proxy for the fault geometry (fault dip). AFS: Apurimac fault system.  
817 Additional details are given in Table S4 & Figure S38.

818

819 **Figure 6.** Age-Elevation plots (AHe & AFT ages) for the vertical profiles of Ocobamba (A;  
820 Oco.), Lucma (B), Limatambo (C) and Abancay (D) (see Figure 4 for profiles location). Blue  
821 diamonds are single-grain AHe ages, open diamonds are mean AHe (blue) and central AFT  
822 (red) ages. Blue and red numbers on the graphics refer to AER apparent exhumation rates  
823 (km/m.y.), respectively, for AHe and AFT ages. Blue and red dashed lines correspond to  
824 minimum and maximum values for exhumation rates (AER; 95% confidence interval).

825

826 **Figure 7.** Time-temperature paths derived from QTQt inverse modeling of  
827 thermochronological data (Gallagher, 2012). a, b and c: Synthesis of time-temperature paths  
828 (colored lines) derived from QTQt (95 % confidence interval around the expected model; see  
829 the Supporting information for detailed inverse modeling outcomes). For profiles, because  
830 cooling dynamics are similar for top and bottom samples we plotted here the minimum and

831 maximum confidence envelopes. Colored numbers in legend refer to the output cooling rates.  
832 See the Supporting information for details regarding the data reproducibility (observed vs.  
833 predicted data). a, b and c, respectively, correspond to samples in the northern Eastern  
834 Cordillera (EC), the southern Eastern Cordillera and the Altiplano (see Figure 4 for location).  
835 In b, number 1 (Machu Picchu profile) refers to Gérard et al. 2021 and the black dotted  
836 rectangle correspond to the cooling acceleration timing at  $5\pm 2$  Ma.

837

838 **Figure 8.** 3D Pecube inversion results for the Altiplano crustal block. a) 2D parameter space  
839 and inversion results for crustal-block exhumation vs. basal temperature. Each colored point  
840 corresponds to one forward model. Blue curves (up and right subpanels) are the probability  
841 density for each parameter. The yellow star is the best-fitting model. b) Direct comparison of  
842 time-temperature paths derived from QTQt and ones computed with Pecube best-fitting  
843 model. c) Crustal-block model for the Altiplano (see Figure 2 for location) with locations of  
844 thermochronological data.

845

846 **Figure 9.** 3D Pecube inversion results for the Eastern Cordillera crustal block. a) 2D  
847 parameter space and inversion results for crustal-block exhumation vs. position of the fault at  
848 25 km-depth (x fault parameter). b) 2D parameter space and inversion results for the fault  
849 velocity vs. activation timing of the Apurimac fault system. Each colored point corresponds  
850 to one forward model. Blue curves (up and right subpanels) are the probability density for  
851 each parameter. The yellow stars in panels a and b are the best-fitting model. c) Direct  
852 comparison of time-temperature paths derived from QTQt and ones computed with Pecube  
853 best-fitting model. d) Crustal-block model for the Eastern Cordillera with locations of  
854 thermochronological data (see Figure 2 for location). e) Surface exhumation pattern for the

855 Eastern Cordillera since ~5 Ma predicted from Pecube best-fitting model. AFS is the  
856 Apurimac fault system.

857

858 **Figure 10.** Exhumation rates derived from Pecube for the Abancay Deflection through time.  
859 Each color corresponds to the three exhumation areas identified in this study. Details  
860 regarding the computed values for exhumation rates according to AERs, QTQt and Pecube  
861 are available in the Figure S43.

862

863 **Figure 11.** Tectonomorphic evolution of the Abancay Deflection since 40 Ma. Left panels  
864 represent the large-scale schematic map views of the study area (black dashed square). Right  
865 panels are 3D Abancay Deflection schematic crustal blocks corresponding to the surface to  
866 the square defined in the left panels. a, b, c, d and e refer, respectively, to the situation at 40  
867 Ma, between 40 and 25 Ma, between 25 and 10 Ma, between 10 and 5 Ma and finally since 5  
868 Ma to present day. AFS: Apurimac fault system; EC: Eastern Cordillera; AP: Altiplano.

869

870 **Figure 12.** Andean orogenic model (South-North cross section) crossing through the  
871 Abancay Deflection since ca. 5 Ma. Modified after the double-verging prism orogenic model  
872 of Armijo et al. (2015). Green numbers refer to the initiation timing of the associated crustal  
873 deformation. Black circled numbers refer to the compiled previous and present studies: 1:  
874 Loewy et al. (2004); Ramos (2008, 2010); 2 : Armijo et al. (2015); 3: Sébrier et al. (1985);  
875 Mercier et al. (1992); Wimpenny et al. (2018); 4: This study; 5: Espurt et al. (2011);  
876 Gautheron et al. (2013). AFS refers to Apurimac Fault System.

877

878 **Figure 13.** Geodynamic comparison between the Abancay Deflection and the St Elias  
879 syntaxis of Alaska. a) The Abancay Deflection case; the bulls-eye structure and morphology



880 of the Abancay Deflection (red circle) suggests that it is an incipient syntaxis, with the  
881 Arequipa terrane acting as the indenter. b) The St Elias case from Falkowski et al. (2014).  
882 The Yakutat microplate plays the role of the indenter for this Alaskan syntaxis.

883

884 **Table 1**

885 *Note:* The Geologic unit and pluton period columns refer to the studies of Egeler & De Booy  
886 (1961), Lancelot et al. (1978), Mišković et al. (2009), Perello et al. (2003), Reitsma (2012)  
887 and the INGEMMET geological database.

888

889 **Table 2**

890 *Note:* Morphology refers to the apatite geometry. 2py: 2 hexagonal pyramids; 2b: 2 broken  
891 faces; 1b + 1py: 1 broken face & 1 hexagonal pyramid (Brown et al., 2013).  $F_T$  is the alpha  
892 ejection correction factor and  $R_s$  is the sphere equivalent radius of hexagonal crystal  
893 (Gautheron et al., 2012; Ketcham et al., 2011).

894

895 **Table 3**

896 *Note:* Fission-track age is given as Central Age (Galbraith & Laslett, 1993). Tracks were  
897 counted and horizontally confined track lengths were measured dry at 1250x magnification  
898 under an Olympus BX51 optical microscope, using the FTStage 4.04 program at ISTERre.  
899 Ages were calculated with the BINOMFIT program (Ehlers et al., 2005), using a zeta value  
900 of  $275.18 \pm 11.53$  and the IRMM 540 uranium glass standard (15 ppm U). MDpar = mean  
901 Dpar value, MTL = mean track lengths of horizontally confined tracks.

902 \*N.D. = no data

903 †Previous data (Kennan, 2008). For samples LK95/200 and LK95/202, elevations are  
904 respectively 3.1 and 2.1 km.

905 §N.R. = not reported

906 # Previous data from Ruiz et al. (2009) for samples Pi6.1 (3.87 km); Pi6.2 (3.80 km); Pi6.3  
907 (3.65 km); Pi6.4 (3.45 km); Pi6.5 (3.25 km); Pi6.6 (3.10 km); Pi6.7 (3.00 km); and Pi6.8  
908 (2.85 km).

909

## 910 **References**

911 Allmendinger, R. W., Jordan, T. E., Kay, S. M., & Isacks, B. L. (1997). the Evolution of the  
912 Altiplano-Puna Plateau of the Central Andes. *Annual Review of Earth and Planetary*  
913 *Sciences*, 25(1), 139–174. <https://doi.org/10.1146/annurev.earth.25.1.139>

914 Allmendinger, R. W., Smalley, R., Bevis, M., Caprio, H., & Brooks, B. (2005). Bending the  
915 Bolivian orocline in real time. *Geology*, 33(11), 905–908.  
916 <https://doi.org/10.1130/G21779.1>

917 Anderson, R. B., Long, S. P., Horton, B. K., Thomson, S. N., Calle, A. Z., & Stockli, D. F.  
918 (2018). Orogenic Wedge Evolution of the Central Andes, Bolivia (21°S): Implications  
919 for Cordilleran Cyclicity. *Tectonics*, 37(10), 3577–3609.  
920 <https://doi.org/10.1029/2018TC005132>

921 Armijo, R., Lacassin, R., Coudurier-Curveur, A., & Carrizo, D. (2015). Coupled tectonic  
922 evolution of Andean orogeny and global climate. *Earth-Science Reviews*. Elsevier B.V.  
923 <https://doi.org/10.1016/j.earscirev.2015.01.005>

924 Arndt, J., Bartel, T., Scheuber, E., & Schilling, F. (1997). Thermal and rheological properties  
925 of granodioritic rocks from the Central Andes, North Chile. *Tectonophysics*, 271(1–2),  
926 75–88. [https://doi.org/10.1016/S0040-1951\(96\)00218-1](https://doi.org/10.1016/S0040-1951(96)00218-1)

927 Ault, A. K., Gautheron, C., & King, G. E. (2019). Innovations in (U Th)/He, fission track,  
928 and trapped charge thermochronometry with applications to earthquakes, weathering,  
929 surface mantle connections, and the growth and decay of mountains. *Tectonics*.

- 930 <https://doi.org/10.1029/2018tc005312>
- 931 Barazangi, M., & Isacks, B. L. (1976). Spatial distribution of earthquakes and subduction of  
932 the Nazca plate beneath South America. *Geology*, (4), 686–692.
- 933 Barnes, J B, & Ehlers, T. A. (2009). End member models for Andean Plateau uplift. *Earth-*  
934 *Science Reviews*. Elsevier B.V. <https://doi.org/10.1016/j.earscirev.2009.08.003>
- 935 Barnes, Jason B., Ehlers, T. A., Insel, N., McQuarrie, N., & Poulsen, C. J. (2012). Linking  
936 orography, climate, and exhumation across the central Andes. *Geology*, 40(12), 1135–  
937 1138. <https://doi.org/10.1130/G33229.1>
- 938 Barnes, Jason B, Ehlers, T. A., McQuarrie, N., O’Sullivan, P. B., & Tawackoli, S. (2008).  
939 Thermochronometer record of central Andean Plateau growth, Bolivia (19.5°S).  
940 *Tectonics*, 27(3). <https://doi.org/10.1029/2007TC002174>
- 941 Bonhomme, M., Fornari, M., Laubacher, G., Sébrier, M., & Vivier, G. (1988). New Cenozoic  
942 K-Ar ages on volcanic rocks from the eastern High Andes, southern Peru. *Journal of*  
943 *South American Earth Sciences*, 1(2), 179–183.
- 944 Bossart, P., Dietrich, D., Greco, A., Ottiger, R., & Ramsay, J. (1988). The Tectonic Structure  
945 of the Hazara-Kashmir Syntaxis, Southern Himalayas, Pakistan. *Tectonics*, 7(2), 273–  
946 297.
- 947 Braun, J. (2003). Pecube: A new finite-element code to solve the 3D heat transport equation  
948 including the effects of a time-varying, finite amplitude surface topography. *Computers*  
949 *and Geosciences*, 29(6), 787–794. [https://doi.org/10.1016/S0098-3004\(03\)00052-9](https://doi.org/10.1016/S0098-3004(03)00052-9)
- 950 Braun, J., van der Beek, P., Valla, P., Robert, X., Herman, F., Glotzbach, C., et al. (2012).  
951 Quantifying rates of landscape evolution and tectonic processes by thermochronology  
952 and numerical modeling of crustal heat transport using PECUBE. *Tectonophysics*, 524–  
953 525, 1–28. <https://doi.org/10.1016/j.tecto.2011.12.035>
- 954 Brookfield, M. E. (1998). The evolution of the great river systems of southern Asia during

- 955 the Cenozoic India-Asia collision: rivers draining southwards. *Geomorphology*, 22(3–4),  
956 285–312. [https://doi.org/10.1016/S0169-555X\(97\)00082-2](https://doi.org/10.1016/S0169-555X(97)00082-2)
- 957 Brown, R. W., Beucher, R., Roper, S., Persano, C., Stuart, F., & Fitzgerald, P. (2013).  
958 Natural age dispersion arising from the analysis of broken crystals. Part I: Theoretical  
959 basis and implications for the apatite (U-Th)/He thermochronometer. *Geochimica et*  
960 *Cosmochimica Acta*, 122(120), 478–497. <https://doi.org/10.1016/j.gca.2013.05.041>
- 961 Burg, J. P., Nievergelt, P., Oberli, F., Seward, D., Davy, P., Maurin, J. C., et al. (1998). The  
962 Namche Barwa syntaxis: Evidence for exhumation related to compressional crustal  
963 folding. *Journal of Asian Earth Sciences*, 16(2–3), 239–252.  
964 [https://doi.org/10.1016/S0743-9547\(98\)00002-6](https://doi.org/10.1016/S0743-9547(98)00002-6)
- 965 Burtman, V., & Molnar, P. (1993). Geological and geophysical evidence for deep subduction  
966 of continental crust beneath the Pamir. *Geological Society of America Special Paper*,  
967 281, 1–76.
- 968 Butler, R. F., Richards, D., Sempere, T., & Marshall, L. (1995). Paleomagnetic  
969 determinations of vertical-axis tectonic rotations from Late Cretaceous and Paleocene  
970 strata of Bolivia. *Geology*, (9), 799–802.
- 971 Cabrera, J., Sébrier, M., & Mercier, J. L. (1991). Plio-Quaternary geodynamic evolution of a  
972 segment of the Peruvian Andean Cordillera located above the change in the subduction  
973 geometry: the Cuzco region. *Tectonophysics*, 190(2–4), 331–362.  
974 [https://doi.org/10.1016/0040-1951\(91\)90437-W](https://doi.org/10.1016/0040-1951(91)90437-W)
- 975 Carlier, G, Lorand, J. P., Bonhomme, M., & Carlotto, V. (1996). A reappraisal of the  
976 cenozoic inner arc magmatism in southern Peru: consequences for the evolution of the  
977 central Andes for the past 50 Ma. In *Third International Symposium on Andean*  
978 *Geodynamics (ISAG)* (pp. 551–554). Saint Malo.
- 979 Carlier, Gabi, Lorand, J. P., Liégeois, J. P., Fornari, M., Soler, P., Carlotto, V., & Cárdenas, J.

- 980 (2005). Potassic-ultrapotassic mafic rocks delineate two lithospheric mantle blocks  
981 beneath the southern Peruvian Altiplano. *Geology*, 33(7), 601–604.  
982 <https://doi.org/10.1130/G21643.1>
- 983 Carlotto, V. (2013). Paleogeographic and tectonic controls on the evolution of Cenozoic  
984 basins in the Altiplano and Western Cordillera of southern Peru. *Tectonophysics*, 589,  
985 195–219. <https://doi.org/10.1016/j.tecto.2013.01.002>
- 986 Chapman, J. B., Pavlis, T. L., Bruhn, R. L., Worthington, L. L., Gulick, S. P. S., & Berger, A.  
987 L. (2012). Structural relationships in the eastern syntaxis of the St. Elias orogen, Alaska.  
988 *Geosphere*, 8(1), 105–126. <https://doi.org/10.1130/GES00677.1>
- 989 Clark, M. K., Schoenbohm, L. M., Royden, L. H., Whipple, K. X., Burchfiel, B. C., Zhang,  
990 X., et al. (2004). Surface uplift, tectonics, and erosion of eastern Tibet from large-scale  
991 drainage patterns. *Tectonics*, 23(1), 1–21. <https://doi.org/10.1029/2002TC001402>
- 992 Craw, D., Koons, P. O., Winslow, D., Chamberlain, C. P., & Zeitler, P. (1994). Boiling fluids  
993 in a region of rapid uplift, Nanga Parbat Massif, Pakistan. *Earth and Planetary Science*  
994 *Letters*, 128(3–4), 169–182. [https://doi.org/10.1016/0012-821X\(94\)90143-0](https://doi.org/10.1016/0012-821X(94)90143-0)
- 995 Dalmayrac, B., Laubacher, G., & Marocco, R. (1980). *Géologie des Andes péruviennes*  
996 (ORSTOM). Paris.
- 997 DeCelles, P., Ducea, M., Kapp, P., & Zandt, G. (2009). Cyclicity in Cordilleran orogenic  
998 systems. *Nature Geoscience*, 2, 251–257.  
999 <https://doi.org/https://doi.org/10.1038/ngeo469>
- 1000 Dorbath, C., Dorbath, L., Cisternas, A., Deverchére, J., & Sebrier, M. (1990). Seismicity of  
1001 the huancayo basin (central Peru) and the huaytapallana fault. *Journal of South*  
1002 *American Earth Sciences*, 3(1), 21–29. [https://doi.org/10.1016/0895-9811\(90\)90015-S](https://doi.org/10.1016/0895-9811(90)90015-S)
- 1003 Dziewonski, A. M., Chou, T. A., & Woodhouse, J. H. (1981). Determination of earthquake  
1004 source parameters from waveform data for studies of global and regional seismicity.

- 1005 *Journal of Geophysical Research*, 86(B4), 2825–2852.
- 1006 <https://doi.org/10.1029/JB086iB04p02825>
- 1007 Edwards, M. A., Kidd, W. S. F., Khan, M. A., & Schneider, D. A. (2000). Tectonics of the  
1008 SW margin of the Nanga Parbat-Haramosh massif. *Geological Society, London, Special  
1009 Publications*, (170), 77–100.
- 1010 Egeler, C., & De Booy, T. (1961). Preliminary Note on the Geology of the Cordillera  
1011 Vilcabamba (SE Peru), with Emphasis on the... *Geologie & Mijnbouw*, 40(3), 319–325.
- 1012 Ehlers, T. A., Chaudhri, T., Kumar, S., Fuller, C. W., Willett, S. D., Ketcham, R. A., &  
1013 Brandon, M. T. (2005). Computational Tools for Low-Temperature Thermochronometer  
1014 Interpretation. *Reviews in Mineralogy and Geochemistry*, 58(1), 589–622.  
1015 <https://doi.org/10.2138/rmg.2005.58.22>
- 1016 Ehlers, Todd A, & Poulsen, C. J. (2009). Influence of Andean uplift on climate and  
1017 paleoaltimetry estimates. *Earth and Planetary Science Letters*, 281(3–4), 238–248.  
1018 <https://doi.org/10.1016/j.epsl.2009.02.026>
- 1019 Ekström, G., Nettles, M., & Dziewoński, A. M. (2012). The global CMT project 2004-2010:  
1020 Centroid-moment tensors for 13,017 earthquakes. *Physics of the Earth and Planetary  
1021 Interiors*, 200–201, 1–9. <https://doi.org/10.1016/j.pepi.2012.04.002>
- 1022 England, P., & Molnar, P. (1990). Surface uplift, uplift of rocks, and exhumation of rocks.  
1023 *Geology*, 18, 1173–1177. [https://doi.org/10.1130/0091-7613\(1990\)018<1173](https://doi.org/10.1130/0091-7613(1990)018<1173)
- 1024 Enkelmann, E., Zeitler, P. K., Pavlis, T. L., Garver, J. I., & Ridgway, K. D. (2009). Intense  
1025 localized rock uplift and erosion in the StElias orogen of Alaska. *Nature Geoscience*,  
1026 2(5), 360–363. <https://doi.org/10.1038/ngeo502>
- 1027 Enkelmann, Eva, Piestrzeniewicz, A., Falkowski, S., Stübner, K., & Ehlers, T. A. (2017).  
1028 Thermochronology in southeast Alaska and southwest Yukon: Implications for North  
1029 American Plate response to terrane accretion. *Earth and Planetary Science Letters*, 457,

- 1030 348–358. <https://doi.org/10.1016/j.epsl.2016.10.032>
- 1031 Espurt, N., Barbarand, J., Roddaz, M., Brusset, S., Baby, P., Saillard, M., & Hermoza, W.  
1032 (2011). A scenario for late Neogene Andean shortening transfer in the Camisea  
1033 Subandean zone (Peru, 12°S): Implications for growth of the northern Andean Plateau.  
1034 *Bulletin of the Geological Society of America*, 123(9–10), 2050–2068.  
1035 <https://doi.org/10.1130/B30165.1>
- 1036 Evans, N. J., Byrne, J. P., Keegan, J. T., & Dotter, L. E. (2005). Determination of Uranium  
1037 and Thorium in Zircon, Apatite, and Fluorite: Application to Laser (U–Th)/He  
1038 Thermochronology. *Journal of Analytical Chemistry*, 60(12), 1159–1165.
- 1039 Falkowski, S., Enkelmann, E., & Ehlers, T. A. (2014). Constraining the area of rapid and  
1040 deep-seated exhumation at the St. Elias syntaxis, Southeast Alaska, with detrital zircon  
1041 fission-track analysis. *Tectonics*, 33(5), 597–616.  
1042 <https://doi.org/10.1002/2013TC003408>
- 1043 Farley, K. A. (2000). Helium diffusion from apatite: General behavior as illustrated by  
1044 Durango fluorapatite. *Journal of Geophysical Research: Solid Earth*, 105(B2), 2903–  
1045 2914. <https://doi.org/10.1029/1999jb900348>
- 1046 Farley, Kenneth A. (2002). (U–Th)/He Dating: Techniques, Calibrations, and Applications.  
1047 *Reviews in Mineralogy and Geochemistry*, 47, 819–844.  
1048 <https://doi.org/10.2138/rmg.2002.47.18>
- 1049 Galbraith, R. F., & Laslett, G. M. (1993). Statistical models for mixed fission track ages.  
1050 *International Journal of Radiation Applications and Instrumentation. Part, 21(4)*, 459–  
1051 470. [https://doi.org/10.1016/1359-0189\(93\)90185-C](https://doi.org/10.1016/1359-0189(93)90185-C)
- 1052 Gallagher, K. (2012). Transdimensional inverse thermal history modeling for quantitative  
1053 thermochronology. *Journal of Geophysical Research: Solid Earth*, 117(2), 1–16.  
1054 <https://doi.org/10.1029/2011JB008825>

- 1055 Garzione, C. N., Molnar, P., Libarkin, J. C., & MacFadden, B. J. (2006). Rapid late Miocene  
1056 rise of the Bolivian Altiplano: Evidence for removal of mantle lithosphere. *Earth and*  
1057 *Planetary Science Letters*, 241(3–4), 543–556.  
1058 <https://doi.org/10.1016/j.epsl.2005.11.026>
- 1059 Garzione, C. N., McQuarrie, N., Perez, N. D., Ehlers, T. A., Beck, S. L., Kar, N., et al.  
1060 (2017). Tectonic Evolution of the Central Andean Plateau and Implications for the  
1061 Growth of Plateaus. *Annual Review of Earth and Planetary Sciences*, 45(1), 529–559.  
1062 <https://doi.org/10.1146/annurev-earth-063016-020612>
- 1063 Gautheron, C., & Tassan-Got, L. (2010). A Monte Carlo approach to diffusion applied to  
1064 noble gas/helium thermochronology. *Chemical Geology*, 273(3–4), 212–224.  
1065 <https://doi.org/10.1016/j.chemgeo.2010.02.023>
- 1066 Gautheron, C., Tassan-Got, L., Barbarand, J., & Pagel, M. (2009). Effect of alpha-damage  
1067 annealing on apatite (U-Th)/He thermochronology. *Chemical Geology*, 266(3–4), 166–  
1068 179. <https://doi.org/10.1016/j.chemgeo.2009.06.001>
- 1069 Gautheron, C., Tassan-Got, L., Ketcham, R. A., & Dobson, K. J. (2012). Accounting for long  
1070 alpha-particle stopping distances in (U-Th-Sm)/He geochronology: 3D modeling of  
1071 diffusion, zoning, implantation, and abrasion. *Geochimica et Cosmochimica Acta*, 96,  
1072 44–56. <https://doi.org/10.1016/j.gca.2012.08.016>
- 1073 Gautheron, C., Espurt, N., Barbarand, J., Roddaz, M., Baby, P., Brusset, S., et al. (2013).  
1074 Direct dating of thick- and thin-skin thrusts in the Peruvian Subandean zone through  
1075 apatite (U-Th)/He and fission track thermochronometry. *Basin Research*, 25(4), 419–  
1076 435. <https://doi.org/10.1111/bre.12012>
- 1077 Gérard, B., Audin, L., Robert, X., Gautheron, C., van der Beek, P., Bernet, M., et al. (2021).  
1078 Pliocene river capture and incision of the northern Altiplano: Machu Picchu, Peru.  
1079 *Journal of the Geological Society*, 178. <https://doi.org/https://doi.org/10.1144/jgs2020->



- 1080 100
- 1081 Gilder, S., Rouse, S., Farber, D., McNulty, B., Sempere, T., Torres, V., & Palacios, O.  
1082 (2003). Post-Middle Oligocene origin of paleomagnetic rotations in Upper Permian to  
1083 Lower Jurassic rocks from northern and southern Peru. *Earth and Planetary Science  
1084 Letters*, 210(1–2), 233–248. [https://doi.org/10.1016/S0012-821X\(03\)00102-X](https://doi.org/10.1016/S0012-821X(03)00102-X)
- 1085 Glotzbach, C., van der Beek, P. A., & Spiegel, C. (2011). Episodic exhumation and relief  
1086 growth in the Mont Blanc massif, Western Alps from numerical modelling of  
1087 thermochronology data. *Earth and Planetary Science Letters*, 304(3–4), 417–430.  
1088 <https://doi.org/10.1016/j.epsl.2011.02.020>
- 1089 Gonfiantini, R., Roche, M.-A., Olivry, J.-C., Fontes, J.-C., & Zuppi, G. M. (2001). The  
1090 altitude effect on the isotopic composition of tropical rains. *Chemical Geology*, (181),  
1091 147–167.
- 1092 Gotberg, N., McQuarrie, N., & Caillaux, V. C. (2010). Comparison of crustal thickening  
1093 budget and shortening estimates in southern Peru (12–14°S): Implications for mass  
1094 balance and rotations in the “Bolivian orocline.” *Bulletin of the Geological Society of  
1095 America*, 122(5–6), 727–742. <https://doi.org/10.1130/B26477.1>
- 1096 Green, P. F. (1981). A new look at statistics in fission-track dating. *Nuclear Tracks*, 5, 77–86.
- 1097 Hallet, B., & Molnar, P. (2001). Distorted drainage basins as markers of crustal strain east of  
1098 the Himalaya. *Journal of Geophysical Research: Solid Earth*, 106(B7), 13697–13709.  
1099 <https://doi.org/10.1029/2000jb900335>
- 1100 Henry, S., & Pollack, H. (1988). Terrestrial Heat Flow Above the Andean Subduction Zone  
1101 in Bolivia and Peru. *Journal of Geophysical Research*, 93(B12), 153–162.  
1102 <https://doi.org/10.1029/JB093iB12p15153>
- 1103 Horton, B. K. (2005). Revised deformation history of the central Andes: Inferences from  
1104 Cenozoic foredeep and intermontane basins of the Eastern Cordillera, Bolivia.

- 1105 *Tectonics*. <https://doi.org/10.1029/2003TC001619>
- 1106 Horton, B. K., Perez, N. D., Fitch, J. D., & Saylor, J. E. (2014). Punctuated shortening and  
1107 subsidence in the Altiplano Plateau of southern Peru: Implications for early Andean  
1108 mountain building. *Lithosphere*, 7(2), 117–137. <https://doi.org/10.1130/L397.1>
- 1109 Husson, L., & Sempere, T. (2003). Thickening the Altiplano crust by gravity-driven crustal  
1110 channel flow. *Geophysical Research Letters*, 30(5), 1–4.  
1111 <https://doi.org/10.1029/2002GL016877>
- 1112 Insel, N., Poulsen, C. J., & Ehlers, T. A. (2010). Influence of the Andes Mountains on South  
1113 American moisture transport, convection, and precipitation. *Climate Dynamics*, 35(7),  
1114 1477–1492. <https://doi.org/10.1007/s00382-009-0637-1>
- 1115 Jaillard, E., & Soler, P. (1996). Cretaceous to early Paleogene tectonic evolution of the  
1116 northern Central Andes (0–18 degrees S) and its relations to geodynamics.  
1117 *Tectonophysics*, 259(2), 41–53. [https://doi.org/10.1016/0040-1951\(95\)00107-7](https://doi.org/10.1016/0040-1951(95)00107-7)
- 1118 James, D. (1971). Plate tectonic model for the evolution of the central andes: Discussion.  
1119 *Bulletin of the Geological Society of America*, 82, 3325–3346.  
1120 [https://doi.org/10.1130/0016-7606\(1973\)84<1493:PTMFTE>2.0.CO;2](https://doi.org/10.1130/0016-7606(1973)84<1493:PTMFTE>2.0.CO;2)
- 1121 Kar, N., Garziona, C. N., Jaramillo, C., Shanahan, T., Carlotto, V., Pullen, A., et al. (2016).  
1122 Rapid regional surface uplift of the northern Altiplano plateau revealed by multiproxy  
1123 paleoclimate reconstruction. *Earth and Planetary Science Letters*, 447, 33–47.  
1124 <https://doi.org/10.1016/j.epsl.2016.04.025>
- 1125 Kennan, L. (2008). Fission track ages and sedimentary provenance studies in Peru, and their  
1126 implications for andean paleogeographic evolution, stratigraphy and hydrocarbon  
1127 systems. In *VI INGEPEP, 13–17 October 2008* (p. 13). Lima, Peru. Retrieved from  
1128 <http://www.agu.org/pubs/crossref/1988/JB093iB12p15153.shtml>
- 1129 Ketcham, R. A., Donelick, R. A., & Carlson, W. D. (1999). Variability of apatite fission-

- 1130 track annealing kinetics: III. Crystallographic orientation effects. *American*  
1131 *Mineralogist*, 84, 1235–1255. <https://doi.org/10.2138/am-1999-0902>
- 1132 Ketcham, R. A., Carter, A., Donelick, R. A., Barbarand, J., & Hurford, A. J. (2007).  
1133 Improved modeling of fission-track annealing in apatite. *American Mineralogist*, 92(5–  
1134 6), 799–810. <https://doi.org/10.2138/am.2007.2281>
- 1135 Ketcham, R. A., Gautheron, C., & Tassan-Got, L. (2011). Accounting for long alpha-particle  
1136 stopping distances in (U-Th-Sm)/He geochronology: Refinement of the baseline case.  
1137 *Geochimica et Cosmochimica Acta*, 75(24), 7779–7791.  
1138 <https://doi.org/10.1016/j.gca.2011.10.011>
- 1139 King, G. E., Herman, F., & Guralnik, B. (2016). Northward migration of the eastern  
1140 Himalayan syntaxis revealed by OSL thermochronometry. *Science*, 353(6301), 800–  
1141 804. <https://doi.org/10.1126/science.aaf2637>
- 1142 Koons, P. O., Hooks, B. P., Pavlis, T., Upton, P., & Barker, A. D. (2010). Three-dimensional  
1143 mechanics of Yakutat convergence in the southern Alaskan plate corner. *Tectonics*,  
1144 29(4), 1–17. <https://doi.org/10.1029/2009TC002463>
- 1145 Koons, P. O., Zeitler, P. K., & Hallet, B. (2013). Tectonic Aneurysms and Mountain  
1146 Building. In *Treatise on Geomorphology* (Vol. 5, pp. 318–349).  
1147 <https://doi.org/10.1016/B978-0-12-374739-6.00094-4>
- 1148 Lamb, S. (2011). Did shortening in thick crust cause rapid Late Cenozoic uplift in the  
1149 northern Bolivian Andes? *Journal of the Geological Society*, 168(5), 1079–1092.  
1150 <https://doi.org/10.1144/0016-76492011-008>
- 1151 Lancelot, J. R., Laubacher, G., Marocco, R., & Renaud, U. (1978). U/Pb radiochronology of  
1152 two granitic plutons from the eastern Cordillera (Peru) - Extent of Permian magmatic  
1153 activity and consequences. *Geologische Rundschau*, 67(1), 236–243.  
1154 <https://doi.org/10.1007/BF01803263>

- 1155 Lease, R. O., & Ehlers, T. A. (2013). Incision into the eastern Andean Plateau during  
1156 Pliocene cooling. *Science*, *341*(6147), 774–776. <https://doi.org/10.1126/science.1239132>
- 1157 Loewy, S. L., Connelly, J. N., & Dalziel, I. W. D. (2004). An orphaned basement block: The  
1158 Arequipa-Antofalla Basement of the central Andean margin of South America. *Bulletin*  
1159 *of the Geological Society of America*, *116*(1–2), 171–187.  
1160 <https://doi.org/10.1130/B25226.1>
- 1161 Mamani, M., Wörner, G., & Sempere, T. (2010). Geochemical variations in igneous rocks of  
1162 the Central Andean orocline (13°S to 18°S): Tracing crustal thickening and magma  
1163 generation through time and space. *Bulletin of the Geological Society of America*,  
1164 *122*(1–2), 162–182. <https://doi.org/10.1130/B26538.1>
- 1165 Marechal, A., Mazzotti, S., Elliott, J., Freymueller, J., & Schmidt, M. (2015). Indentor-corner  
1166 tectonics in the Yakutat-St. Elias collision constrained by GPS. *Journal of Geophysical*  
1167 *Research: Solid Earth*, *120*, 3897–3908.  
1168 <https://doi.org/10.1002/2015JB012608>.Received
- 1169 Marocco, R. (1971). Etude géologique de la chaîne andine au niveau de la déflexion  
1170 d'Abancay (Pérou). *Cah. ORSTOM*, *3*(1971), 45–58.
- 1171 Meltzer, A. S., Sarker, G. L., Seeber, L., & Armbruster, J. (1998). Snap, crackle, pop!  
1172 Seismicity and crustal structure at Nanga Parbat, Pakistan, Himalaya. *Eos (Transactions,*  
1173 *American Geophysical Union*, *79*(F909).
- 1174 Mercier, L., Sébrier, M., Lavenu, A., Cabrera, J., Bellier, O., Dumont, J. ., & Machare, J.  
1175 (1992). Changes in the Tectonic Regime Above a Subduction Zone of Andean Type:  
1176 The Andes of Peru and Bolivia During the Pliocene-Pleistocene. *Journal of Geophysical*  
1177 *Research*, *97*(B8), 945–982.
- 1178 Mišković, A., Spikings, R. A., Chew, D. M., Košler, J., Ulianov, A., & Schaltegger, U.  
1179 (2009). Tectonomagmatic evolution of Western Amazonia: Geochemical

- 1180 characterization and zircon U-Pb geochronologic constraints from the Peruvian Eastern  
1181 Cordilleran granitoids. *Bulletin of the Geological Society of America*, 121(9–10), 1298–  
1182 1324. <https://doi.org/10.1130/B26488.1>
- 1183 Mosolf, J. G., Horton, B. K., Heizler, M. T., & Matos, R. (2011). Unroofing the core of the  
1184 central Andean fold-thrust belt during focused late Miocene exhumation: Evidence from  
1185 the Tipuani-Mapiri wedge-top basin, Bolivia. *Basin Research*, 23(3), 346–360.  
1186 <https://doi.org/10.1111/j.1365-2117.2010.00491.x>
- 1187 Müller, J. P., Kley, J., & Jacobshagen, V. (2002). Structure and Cenozoic kinematics of the  
1188 Eastern Cordillera, southern Bolivia (21°S). *Tectonics*, 21(5), 1-1-1–24.  
1189 <https://doi.org/10.1029/2001tc001340>
- 1190 Norton, K., & Schlunegger, F. (2011). Migrating deformation in the Central Andes from  
1191 enhanced orographic rainfall. *Nature Communications*, 2(1).  
1192 <https://doi.org/10.1038/ncomms1590>
- 1193 Ouimet, W. B., & Cook, K. L. (2010). Building the central Andes through axial lower crustal  
1194 flow. *Tectonics*, 29(3), 1–15. <https://doi.org/10.1029/2009TC002460>
- 1195 Peizhen, Z., Molnar, P., & Downs, W. R. (2001). Increased sedimentation rates and grain  
1196 sizes 2-4 Ma ago due to the influence of climate change on erosion rates. *Nature*,  
1197 410(April), 891–897.  
1198 [https://doi.org/http://www.nature.com/nature/journal/v410/n6831/supinfo/410891a0\\_S](https://doi.org/http://www.nature.com/nature/journal/v410/n6831/supinfo/410891a0_S1.html)  
1199 1.html
- 1200 Perello, J., Carlotto, V., Zarate, A., Ramos, P., Posso, H., Neyra, C., et al. (2003). Porphyry-  
1201 Style Alteration and Mineralization of the Middle Eocene to Early Oligocene  
1202 Andahuaylas-Yauri Belt , Cuzco Region , Peru. *Economic Geology*, 98, 1575–1605.
- 1203 Perez, N. D., Horton, B. K., Mcquarrie, N., Stubner, K., & Ehlers, T. A. (2016). Andean  
1204 shortening , inversion and exhumation associated with thin- and thick-skinned

- 1205 deformation in southern Peru. *Geological Magazine*, 153, 1013–1041.
- 1206 <https://doi.org/10.1017/S0016756816000121>
- 1207 Perez, N. D., Horton, B. K., & Carlotto, V. (2016). Structural inheritance and selective  
1208 reactivation in the central Andes: Cenozoic deformation guided by pre-Andean  
1209 structures in southern Peru. *Tectonophysics*, 671, 264–280.
- 1210 <https://doi.org/10.1016/j.tecto.2015.12.031>
- 1211 Phillips, K., Clayton, R. W., Davis, P., Tavera, H., Guy, R., Skinner, S., et al. (2012).  
1212 Structure of the subduction system in southern Peru from seismic array data. *Journal of*  
1213 *Geophysical Research*, 117(11), 1–17. <https://doi.org/10.1029/2012JB009540>
- 1214 Poulsen, C. J., Ehlers, T. A., & Insel, N. (2010). Onset of Convective Rainfall During  
1215 Gradual Late Miocene Rise of the Central Andes. *Science*, 328(April), 490–494.
- 1216 <https://doi.org/10.1126/science.1185078>
- 1217 Rak, A. J., McQuarrie, N., & Ehlers, T. A. (2017). Kinematics, Exhumation, and  
1218 Sedimentation of the North Central Andes (Bolivia): An Integrated Thermochronometer  
1219 and Thermokinematic Modeling Approach. *Tectonics*, 36(11), 2524–2554.
- 1220 <https://doi.org/10.1002/2016TC004440>
- 1221 Ramos, V. A. (2008). The Basement of the Central Andes: The Arequipa and Related  
1222 Terranes. *Annual Review of Earth and Planetary Sciences*, 36(1), 289–324.
- 1223 <https://doi.org/10.1146/annurev.earth.36.031207.124304>
- 1224 Ramos, V. A. (2010). The Grenville-age basement of the Andes. *Journal of South American*  
1225 *Earth Sciences*, 29(1), 77–91. <https://doi.org/10.1016/j.jsames.2009.09.004>
- 1226 Recanati, A., Gautheron, C., Barbarand, J., Missenard, Y., Pinna-Jamme, R., Tassan-Got, L.,  
1227 et al. (2017). Helium trapping in apatite damage: Insights from (U-Th-Sm)/He dating of  
1228 different granitoid lithologies. *Chemical Geology*, 470(September), 116–131.
- 1229 <https://doi.org/10.1016/j.chemgeo.2017.09.002>

- 1230 Reiners, P. W., & Brandon, M. T. (2006). Using Thermochronology To Understand Orogenic  
1231 Erosion. *Annual Review of Earth and Planetary Sciences*, 34(1), 419–466.  
1232 <https://doi.org/10.1146/annurev.earth.34.031405.125202>
- 1233 Reiners, P. W., & Shuster, D. L. (2009). Thermochronology and landscape evolution. *Physics*  
1234 *Today*, (September), 31–36.
- 1235 Reitsma, M. J. (2012). *Reconstructing the Late Paleozoic - Early Mesozoic plutonic and*  
1236 *sedimentary record of south-east Peru : Orphaned back-arcs along the western margin*  
1237 *of Gondwana*.
- 1238 Richards, D. R., Butler, R. F., & Sempere, T. (2004). Vertical-axis rotations determined from  
1239 paleomagnetism of Mesozoic and Cenozoic strata of the Bolivian Andes. *Journal of*  
1240 *Geophysical Research: Solid Earth*, 109(7), 1–21.  
1241 <https://doi.org/10.1029/2004JB002977>
- 1242 Robert, X., Van Der Beek, P., Braun, J., Perry, C., & Mugnier, J. L. (2011). Control of  
1243 detachment geometry on lateral variations in exhumation rates in the Himalaya: Insights  
1244 from low-temperature thermochronology and numerical modeling. *Journal of*  
1245 *Geophysical Research: Solid Earth*, 116(5), 1–22.  
1246 <https://doi.org/10.1029/2010JB007893>
- 1247 Roperch, P., Sempere, T., Macedo, O., Arriagada, C., Fornari, M., Tapia, C., et al. (2006).  
1248 Counterclockwise rotation of late Eocene-Oligocene fore-arc deposits in southern Peru  
1249 and its significance for oroclinal bending in the central Andes. *Tectonics*, 25(3).  
1250 <https://doi.org/10.1029/2005TC001882>
- 1251 Roperch, P., Carlotto, V., Ruffet, G., & Fornari, M. (2011). Tectonic rotations and  
1252 transcurrent deformation south of the Abancay deflection in the Andes of southern Peru.  
1253 *Tectonics*, 30(2). <https://doi.org/10.1029/2010TC002725>
- 1254 Rouse, S., Gilder, S., Fornari, M., & Sempere, T. (2005). Insight into the Neogene tectonic

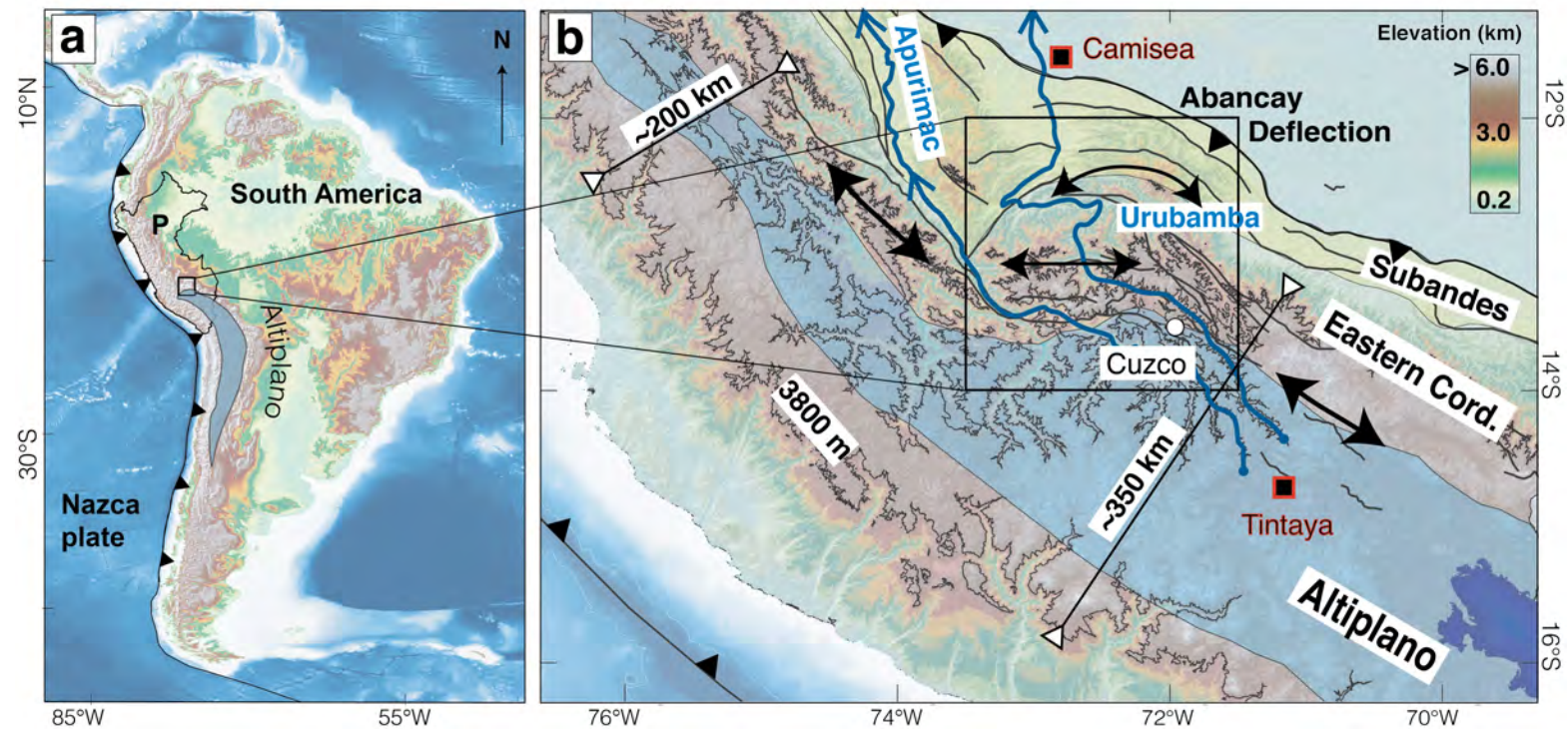
- 1255 history of the northern Bolivian Orocline from new paleomagnetic and geochronologic  
1256 data. *Tectonics*, 24(6), 1–23. <https://doi.org/10.1029/2004TC001760>
- 1257 Royden, L. H., Burchfiel, B. C., King, R. W., Wang, E., Chen, Z., Shen, F., & Liu, Y. (1997).  
1258 Surface deformation and lower crustal flow in eastern Tibet. *Science*, 276(5313), 788–  
1259 790. <https://doi.org/10.1126/science.276.5313.788>
- 1260 Ruiz, G. M. H., Carlotto, V., Van Heiningen, P. V., & Andriessen, P. A. M. (2009). Steady-  
1261 state exhumation pattern in the Central Andes – SE Peru. *Geological Society, London,*  
1262 *Special Publications*, 324(1), 307–316. <https://doi.org/10.1144/SP324.20>
- 1263 Sambridge, M. (1999). Geophysical inversion with a neighbourhood algorithm –II.  
1264 Appraising the ensemble. *Geophys. J. Int.*, 138, 727–746.
- 1265 Sambridge, Malcolm. (1999). Geophysical inversion with a neighbourhood algorithm - I.  
1266 Searching a parameter space. *Geophysical Journal International*, 138(2), 479–494.  
1267 <https://doi.org/10.1046/j.1365-246X.1999.00876.x>
- 1268 Schneider, D. A., Edwards, M. A., Kidd, W. S. F., Asif Khan, M., Seeber, L., & Zeitler, P. K.  
1269 (1999). Tectonics of Nanga Parbat, western Himalaya: Synkinematic plutonism within  
1270 the doubly vergent shear zones of a crustal-scale pop-up structure. *Geology*, 27(11),  
1271 999–1002. [https://doi.org/10.1130/0091-7613\(1999\)027<0999:TONPWH>2.3.CO;2](https://doi.org/10.1130/0091-7613(1999)027<0999:TONPWH>2.3.CO;2)
- 1272 Schwarz, G. E. (1978). Estimating the dimension of a model. *Annu. Stat.*, 6, 461–464.
- 1273 Sébrier, M., Mercier, L., Francois, M., Laubacher, G., & Carey-Gailhardis, E. (1985).  
1274 Quaternary Normal and Reverse Faulting and the State of Stress in the Central Andes of  
1275 South Peru. *Tectonics*, 4(7), 739–780.
- 1276 Seeber, L., & Pêcher, A. (1998). Strain partitioning along the Himalayan arc and the Nanga  
1277 Parbat antiform. *Geology*, 26(9), 791–794. [https://doi.org/10.1130/0091-](https://doi.org/10.1130/0091-7613(1998)026<0791:SPATHA>2.3.CO;2)  
1278 [7613\(1998\)026<0791:SPATHA>2.3.CO;2](https://doi.org/10.1130/0091-7613(1998)026<0791:SPATHA>2.3.CO;2)
- 1279 Sempere, T., Carlier, G., Soler, P., Fornari, M., Carlotto, V., Jacay, J., et al. (2002). Late



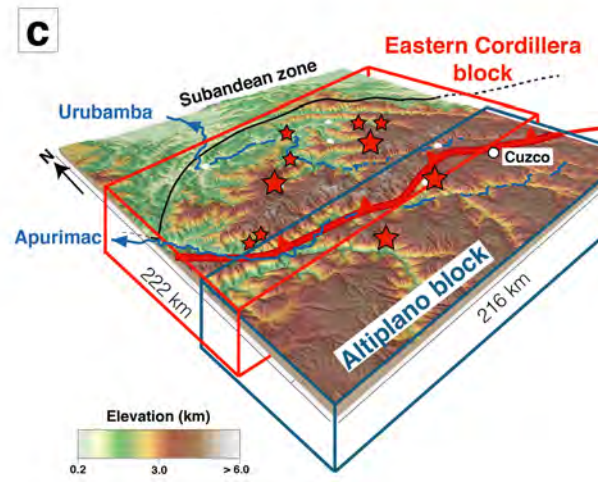
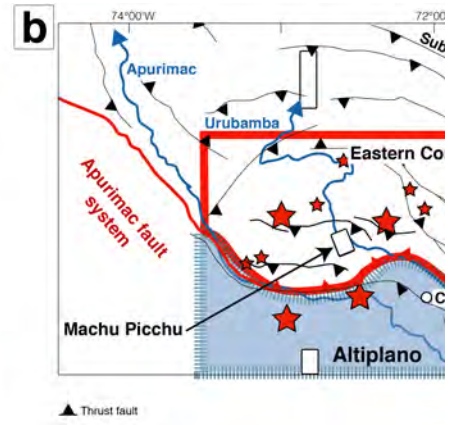
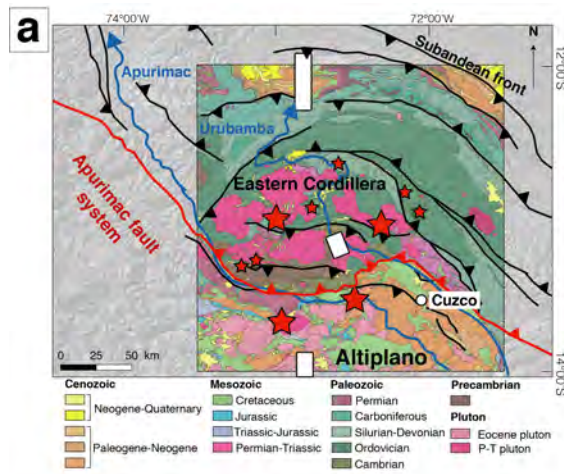
- 1280 Permian-Middle Jurassic lithospheric thinning in Peru and Bolivia, and its bearing on  
1281 Andean-age tectonics. *Tectonophysics*, 345(1–4), 153–181.  
1282 [https://doi.org/10.1016/S0040-1951\(01\)00211-6](https://doi.org/10.1016/S0040-1951(01)00211-6)
- 1283 Shuster, D. L., Flowers, R. M., & Farley, K. A. (2006). The influence of natural radiation  
1284 damage on helium diffusion kinetics in apatite. *Earth and Planetary Science Letters*,  
1285 249(3–4), 148–161. <https://doi.org/10.1016/j.epsl.2006.07.028>
- 1286 Sobolev, S. V., & Babeyko, A. Y. (2005). What drives orogeny in the Andes? *Geology*,  
1287 33(8), 617–620. <https://doi.org/10.1130/G21557.1>
- 1288 Springer, M. (1999). Interpretation of heat-flow density in the Central Andes. In  
1289 *Tectonophysics* (Vol. 306, pp. 377–395). [https://doi.org/10.1016/S0040-1951\(99\)00067-](https://doi.org/10.1016/S0040-1951(99)00067-0)  
1290 0
- 1291 Strecker, M. R., Alonso, R. N., Bookhagen, B., Carrapa, B., Hilley, G. E., Sobel, E. R., &  
1292 Trauth, M. H. (2007). Tectonics and Climate of the Southern Central Andes. *Annual*  
1293 *Review of Earth and Planetary Sciences*, 35(1), 747–787.  
1294 <https://doi.org/10.1146/annurev.earth.35.031306.140158>
- 1295 Stüwe, K., White, L., & Brown, R. (1994). The influence of eroding topography on steady-  
1296 state isotherms. Application to fission track analysis. *Earth and Planetary Science*  
1297 *Letters*, 124, 63–74.
- 1298 Suarez, G., Molnar, P., & Burchfiel, B. C. (1983). Seismicity, fault plane solutions, depth of  
1299 faulting, and active tectonics of the Andes of Peru, Ecuador, and southern Colombia.  
1300 *Journal of Geophysical Research*, 88(B12), 10403–10428.  
1301 <https://doi.org/10.1029/JB088iB12p10403>
- 1302 Sundell, K. E., Saylor, J. E., Lapen, T. J., & Horton, B. K. (2019). Implications of variable  
1303 late Cenozoic surface uplift across the Peruvian central Andes. *Scientific Reports*, 9(1),  
1304 1–12. <https://doi.org/10.1038/s41598-019-41257-3>

- 1305 Tassara, A. (2005). Interaction between the Nazca and South American plates and formation  
1306 of the Altiplano-Puna plateau: Review of a flexural analysis along the Andean margin  
1307 (15°-34°S). *Tectonophysics*, 399(1-4 SPEC. ISS.), 39–57.  
1308 <https://doi.org/10.1016/j.tecto.2004.12.014>
- 1309 Valla, P. G., Van Der Beek, P. A., Shuster, D. L., Braun, J., Herman, F., Tassan-Got, L., &  
1310 Gautheron, C. (2012). Late Neogene exhumation and relief development of the Aar and  
1311 Aiguilles Rouges massifs (Swiss Alps) from low-temperature thermochronology  
1312 modeling and 4He/3He thermochronometry. *Journal of Geophysical Research: Earth*  
1313 *Surface*, 117(1), 1–23. <https://doi.org/10.1029/2011JF002043>
- 1314 Villegas-Lanza, J., Chlieh, M., Cavalié, O., Tavera, H., Baby, P., Chire-Chira, J., & Nocquet,  
1315 J.-M. (2016). Active tectonics of Peru: Heterogeneous interseismic coupling along the  
1316 Nazca megathrust, rigid motion of the Peruvian Sliver, and Subandean shortening  
1317 accommodation. *Journal of Geophysical Research: Solid Earth*, 121, 7371–7394.  
1318 <https://doi.org/10.1002/2015JB012608>.Received
- 1319 Whipple, K. X., & Meade, B. J. (2004). Controls on the strength of coupling among climate,  
1320 erosion, and deformation in two-sided, frictional orogenic wedges at steady state.  
1321 *Journal of Geophysical Research: Earth Surface*, 109(F1), 1–24.  
1322 <https://doi.org/10.1029/2003jf000019>
- 1323 Whittington, A. G., Hofmeister, A. M., & Nabelek, P. I. (2009). Temperature-dependent  
1324 thermal diffusivity of the Earth's crust and implications for magmatism. *Nature*,  
1325 458(7236), 319–321. <https://doi.org/10.1038/nature07818>
- 1326 Willett, S., Beaumont, C., & Fullsack, P. (1993). Mechanical model for the tectonics of  
1327 doubly vergent compressional orogens. *Geology*, 21(4), 371–374.  
1328 [https://doi.org/10.1130/0091-7613\(1993\)021<0371:MMFTTO>2.3.CO;2](https://doi.org/10.1130/0091-7613(1993)021<0371:MMFTTO>2.3.CO;2)
- 1329 Wimpenny, S., Copley, A., Benavente, C., & Aguirre, E. (2018). Extension and Dynamics of

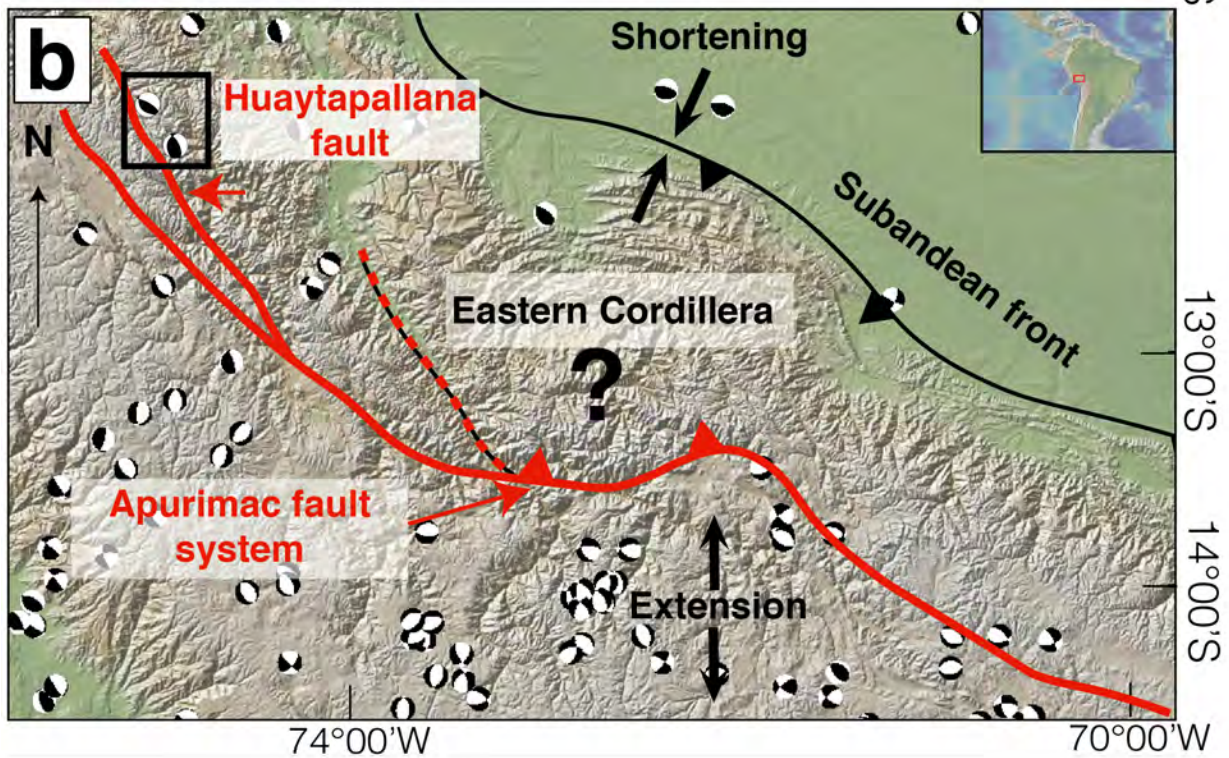
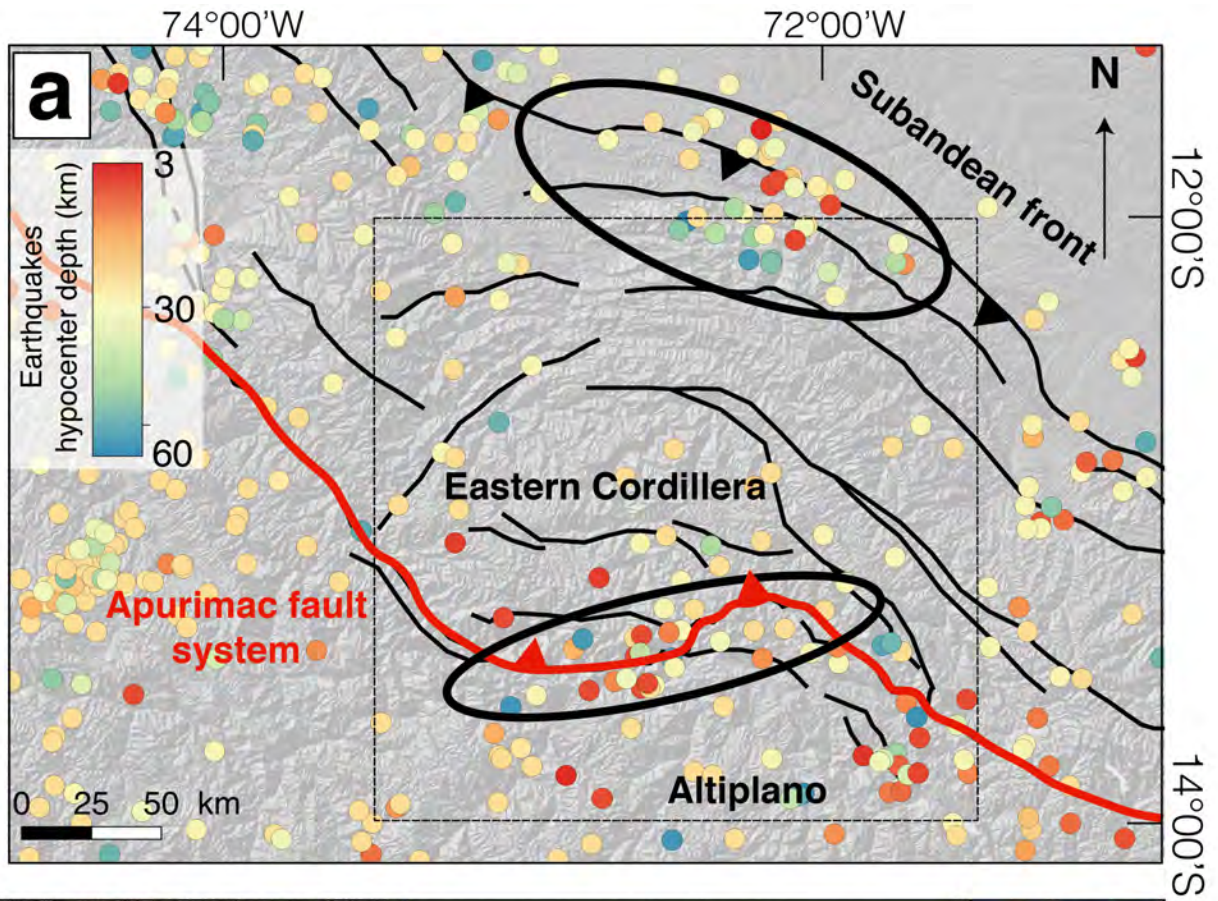
- 1330 the Andes Inferred From the 2016 Parina (Huarichancara) Earthquake. *Journal of*  
1331 *Geophysical Research: Solid Earth*, 123(9), 8198–8228.  
1332 <https://doi.org/10.1029/2018JB015588>
- 1333 Wimpenny, S., Benavente, C., Copley, A., Garcia, B., Rosell, L., O’Kane, A., & Aguirre, E.  
1334 (2020). Observations and dynamical implications of active normal faulting in South  
1335 Peru. *Geophysical Journal International*, 222(1), 27–53.  
1336 <https://doi.org/10.1093/gji/ggaa144>
- 1337 Yang, R., Fellin, M. G., Herman, F., Willett, S. D., Wang, W., & Maden, C. (2016). Spatial  
1338 and temporal pattern of erosion in the Three Rivers Region, southeastern Tibet. *Earth*  
1339 *and Planetary Science Letters*, 433, 10–20. <https://doi.org/10.1016/j.epsl.2015.10.032>
- 1340 Zeitler, P. K., Meltzer, A. S., Koons, P. O., Craw, D., Hallet, B., Chamberlain, C. P., et al.  
1341 (2001). Erosion, Himalayan Geodynamics, and the Geomorphology of Metamorphism.  
1342 *GSA Today*, 11(January), 4–9.  
1343



1  
 2 **Figure 1.** Abancay Deflection location. a) Location within South America of the study area at the northern tip of the Altiplano in Peru (P). b)  
 3 Zoom-in on the Abancay Deflection area (black square in panel a). Double black arrows highlight the topography elongation axis. Note the  
 4 pronounced incision within the study area through the iso-elevation line (black) at 3.8 km elevation via the Urubamba and Apurimac rivers  
 5 (blue) canyons. Black thin lines framed by white triangles highlight the latitudinal range width variation with the Abancay Deflection as the  
 6 transition zone between the northern narrow Peruvian Andes and the southern wide Bolivian Orocline. Black squares with red borders are the  
 7 places where thermal parameters were measured.



17 **Figure 2.** Geology and morphology of the Abancay Deflection. a) Geological map of the  
18 study area. The crustal scale Apurimac fault system marks the tectonic limit between the  
19 Altiplano and the Eastern Cordillera. (INGEMMET geological map database - 1:100,000).  
20 White rectangles refer to previous thermochronological studies; references are provided in  
21 the method and results sections. b) Simplified map (from a) with major litho-tectonic  
22 domains: the Altiplano in blue and the Eastern Cordillera framed in red. c) 3D DEM of the  
23 Abancay Deflection. On panels, red stars are the thermochronological sample location  
24 (vertical profiles and individual data; this study). 2D colored area (b) and corresponding 3D  
25 views (c) are crustal block locations processed with 3D thermo-kinematics modeling using  
26 Pecube for the Altiplano (blue) and the Eastern Cordillera (red) blocks.



27

28

29

30 **Figure 3.** Crustal seismic map of the Abancay Deflection (Dashed squares; hypocenters < 60  
31 km;  $M_w > 2$ ). a) Mapped earthquakes come from the USGS, IGP and ISC databases. Regions  
32 included into black ellipses emphasize positive anomalous cluster of seismicity in  
33 comparison with the quiescent Abancay core of the Eastern Cordillera. Black lines represent  
34 the major thrusts of the studied area. b) Moment tensors (CMT) for earthquakes (1969-2019)  
35 for the Abancay Deflection region (Dziewonski et al., 1981; Ekström et al., 2012). Focal  
36 mechanisms (transpressional) for the two 1969 Huaytapallana events are framed by the black  
37 rectangle (Dorbath et al., 1990; Suarez et al., 1983). There are no CMT data for  $M_w < 5.5$   
38 earthquakes. Tectonic shortening characterizes the Subandean front whereas extensional  
39 mechanisms affect the Altiplano. [The question mark refers to the unknown tectonic behavior](#)  
40 [for the Eastern Cordillera.](#)

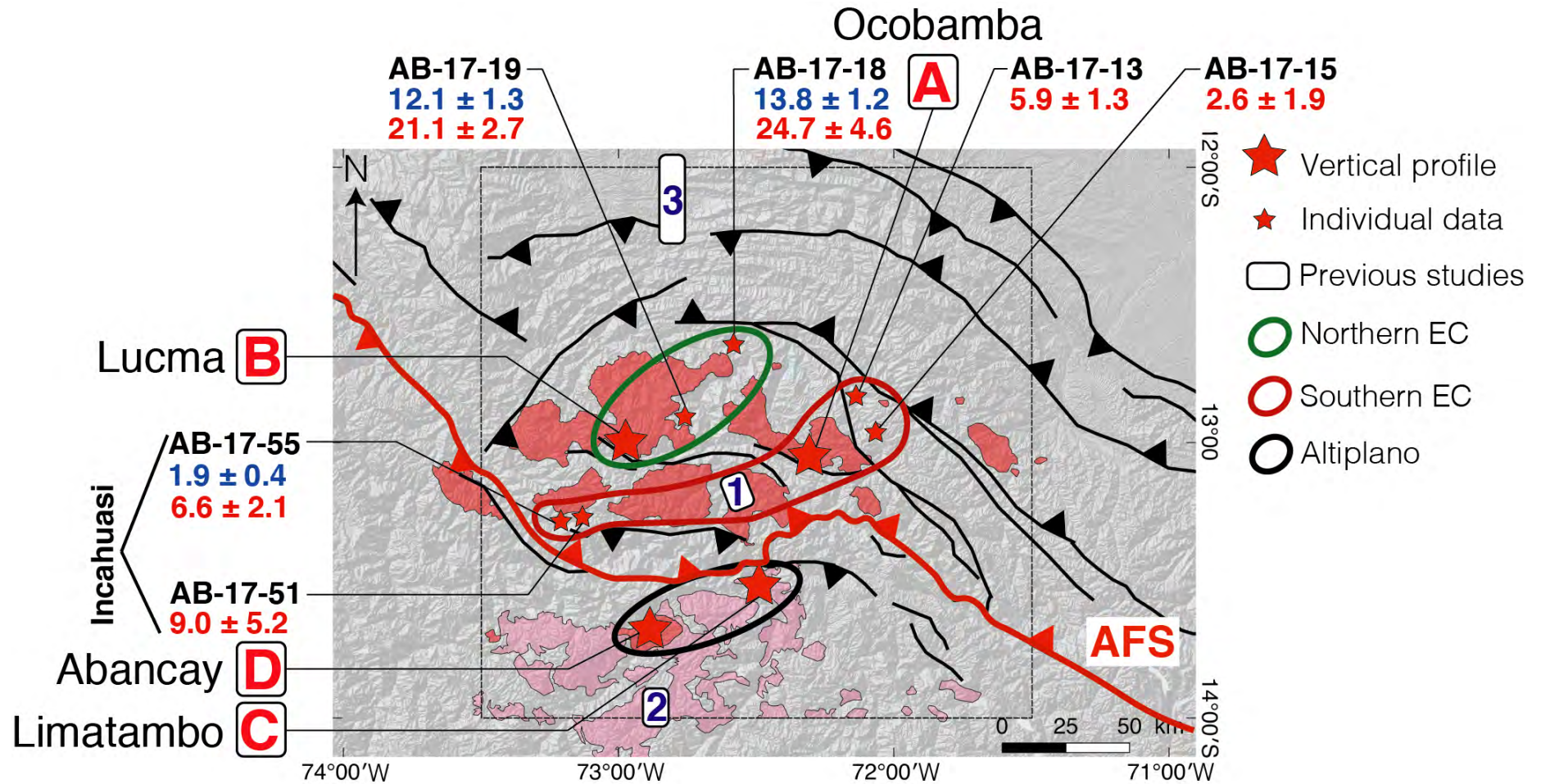
41

42

43

44

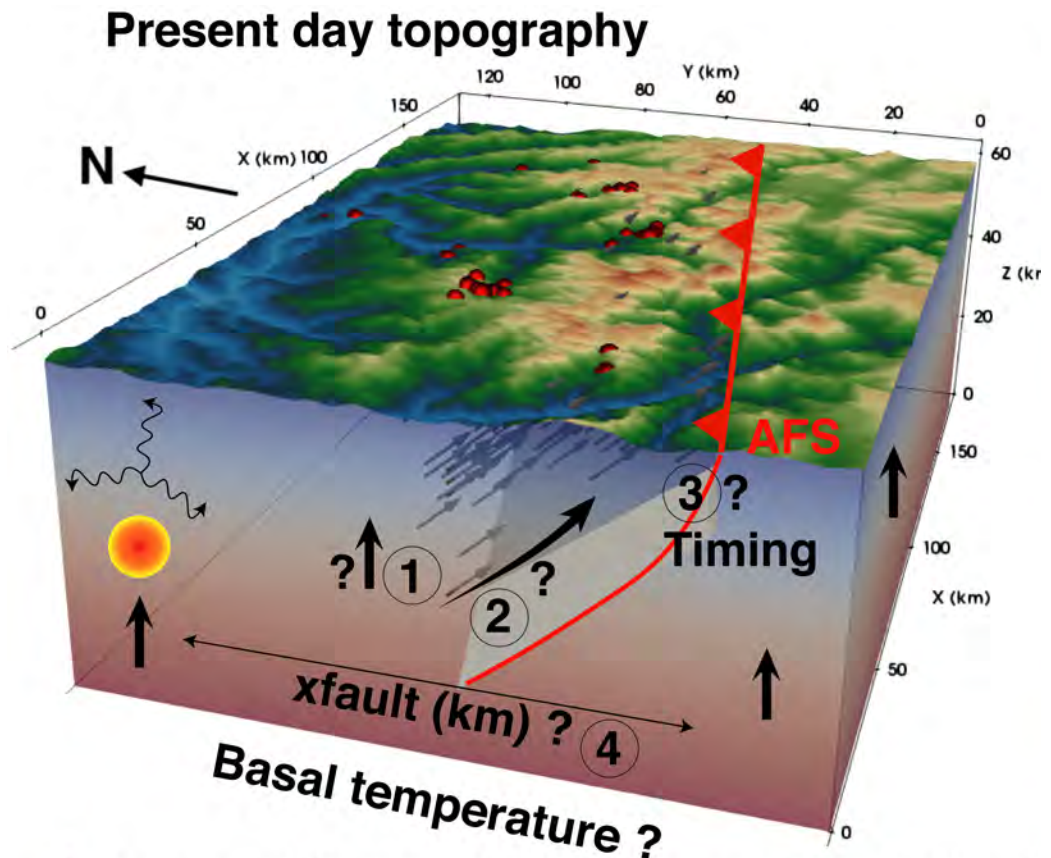






46

47 **Figure 4.** Sample locations of the new thermochronological ages within the Abancay Deflection. Red and pink polygons are respectively Permo-  
 48 Triassic and Eocene plutons. Previous studies are: 1: Gérard et al. (in press) and Kennan (2008); 2: Ruiz et al. (2009); 3: Espurt et al. (2011) and

49 Gautheron et al. (2013). Blue and red numbers below sample names refer to AHe mean ages and AFT central ages for individual samples and the  
50 two-sampled-point Incahuasi vertical profile. Red capital letters refer to the other sampled vertical profiles (A: Ocobamba profile; B: Lucma  
51 profile; C: Limatambo profile & D: Abancay profile). Profiles results are displayed in [Figure 6](#). Green, red and black contours mark the  
52 latitudinal segmentation of the Abancay Deflection defining three areas according to thermal histories modeled with QTQt (*i.e.* Northern EC,  
53 Southern EC and Altiplano respectively). The black dashed square frames the Abancay Deflection. AFT: Apurimac fault system; EC: Eastern  
54 Cordillera.



-  Thermal diffusivity - fixed      Crustal / Mantle density - fixed
-  Heat production - fixed      Lapse rate - fixed

56

57 **Figure 5.** Parameters implemented and/or explored in Pecube through time. Exa

58 Eastern Cordillera crustal block (see Figure 2 for location). For the Altiplano b

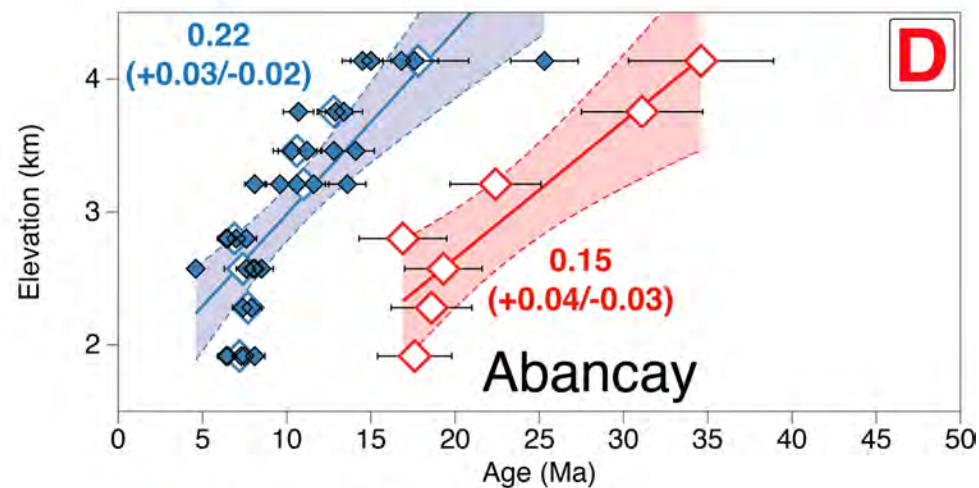
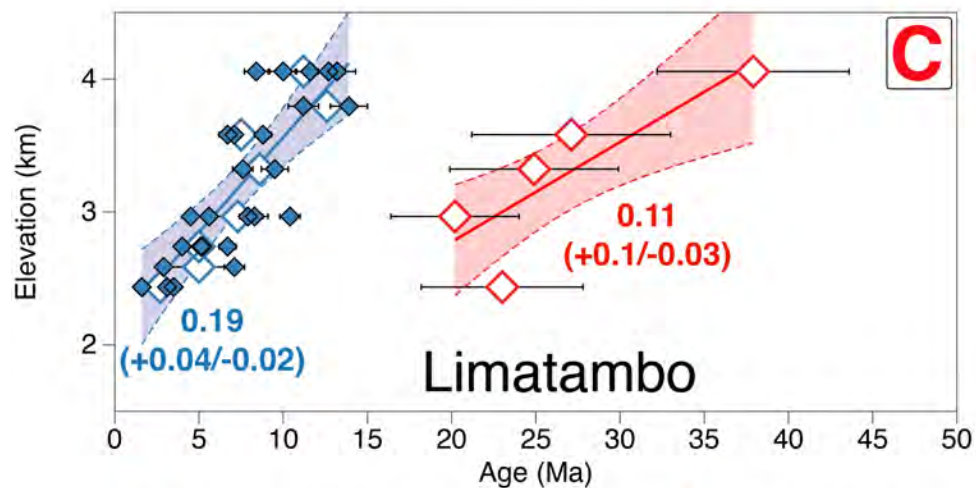
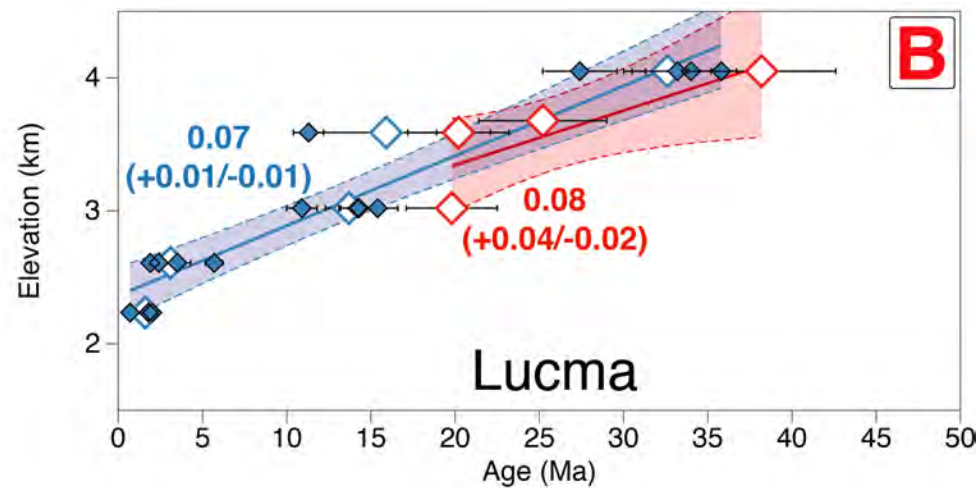
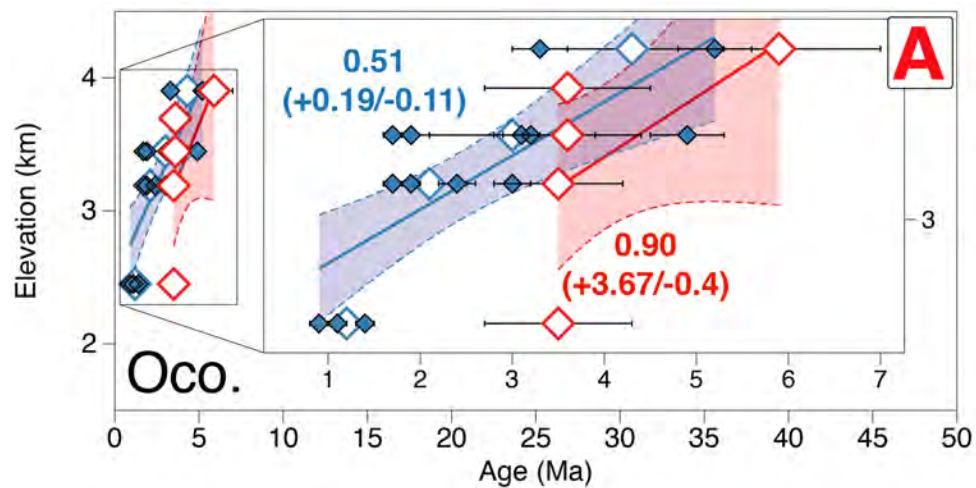
59 explored the crustal block exhumation (1). Red dots mark the loca

60 thermochronological data. Numbers and question marks refer to explored p

61 Crustal block exhumation (km/Ma); 2: Fault velocity (km/Ma); 3: Timing of fa

62 (Ma); 4: x fault (km), proxy for the fault geometry (fault dip). AFS: Apurimac

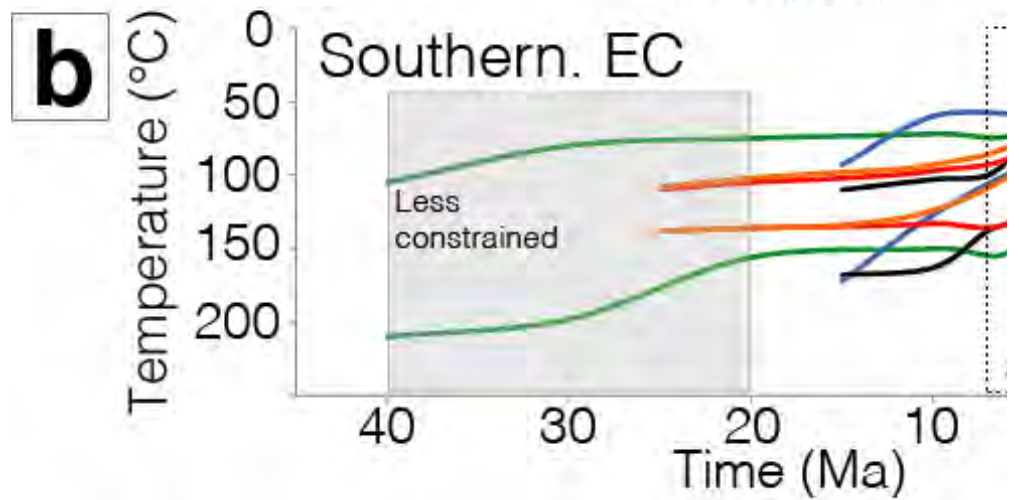
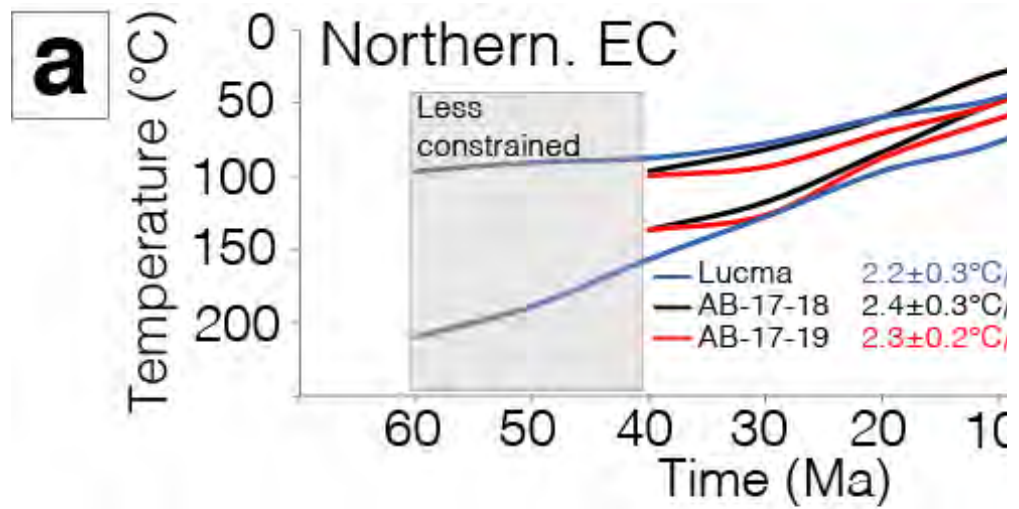
63 Additional details are given in Table S4 &amp; Figure S38.



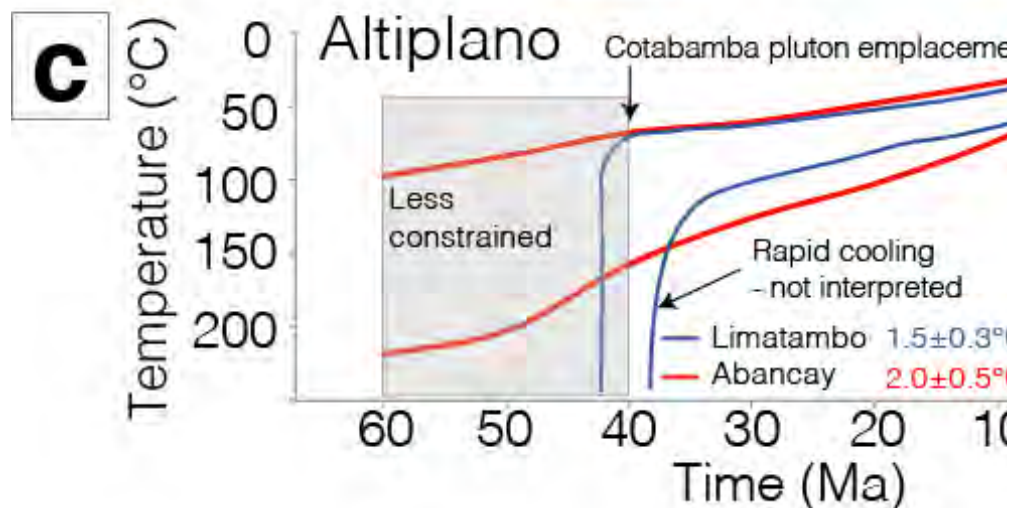
◆ Single-crystal AHe age      ◇ AHe mean age

◇ AFT central age

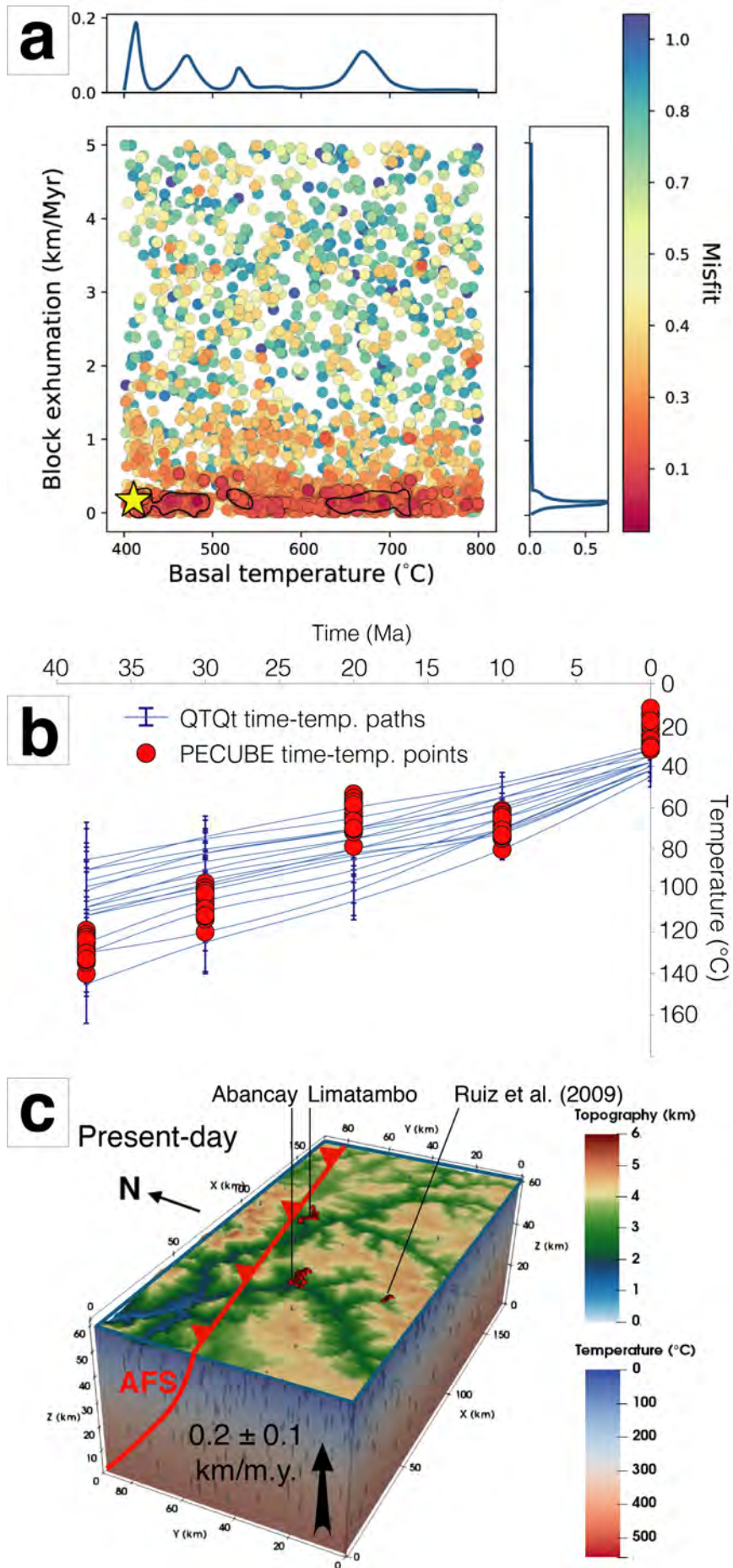
66 **Figure 6.** Age-Elevation plots (AHe & AFT ages) for the vertical profiles of Ocobamba (A; Oco.), Lucma (B), Limatambo (C) and Abancay (D)  
67 (see Figure 4 for profiles location). Blue diamonds are single-grain AHe ages, open diamonds are mean AHe (blue) and central AFT (red) ages.  
68 Blue and red numbers on the graphics refer to AER apparent exhumation rates (km/m.y.) respectively for AHe and AFT ages. Blue and red  
69 dashed lines correspond to minimum and maximum values for exhumation rates (AER; 95% confidence interval).  
70



	Ante ~5 Ma	Cooling rates increasing	Pos
Incahuasi	$4.3 \pm 3.3^\circ\text{C/m.y.}$		22±
Ocobamba	$2.8 \pm 1.8^\circ\text{C/m.y.}$		13±
AB-17-15	$2.2 \pm 0.4^\circ\text{C/m.y.}$		16±
Machu Picchu (1)	$0.7 \pm 0.2^\circ\text{C/m.y.}$		21±
AB-17-13	$4.7 \pm 1.5^\circ\text{C/m.y.}$		12±

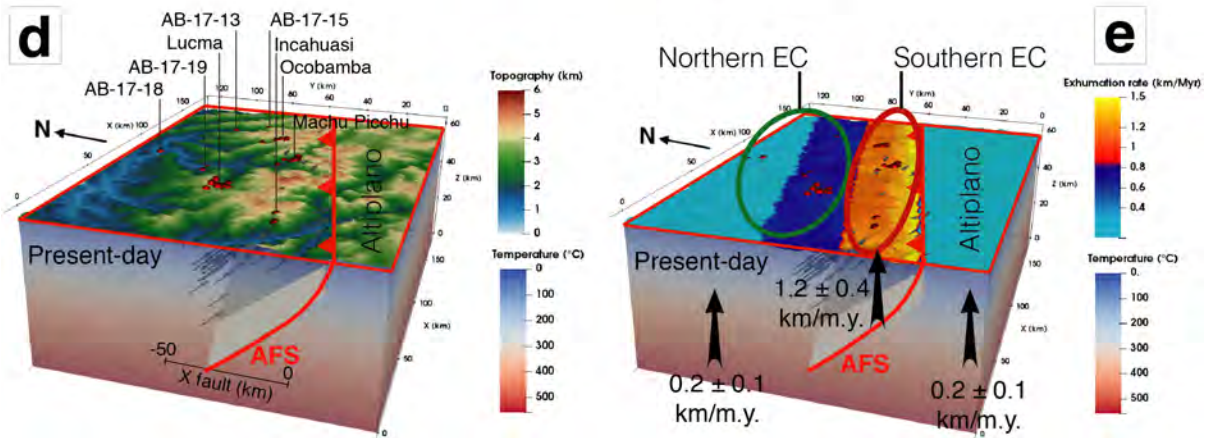
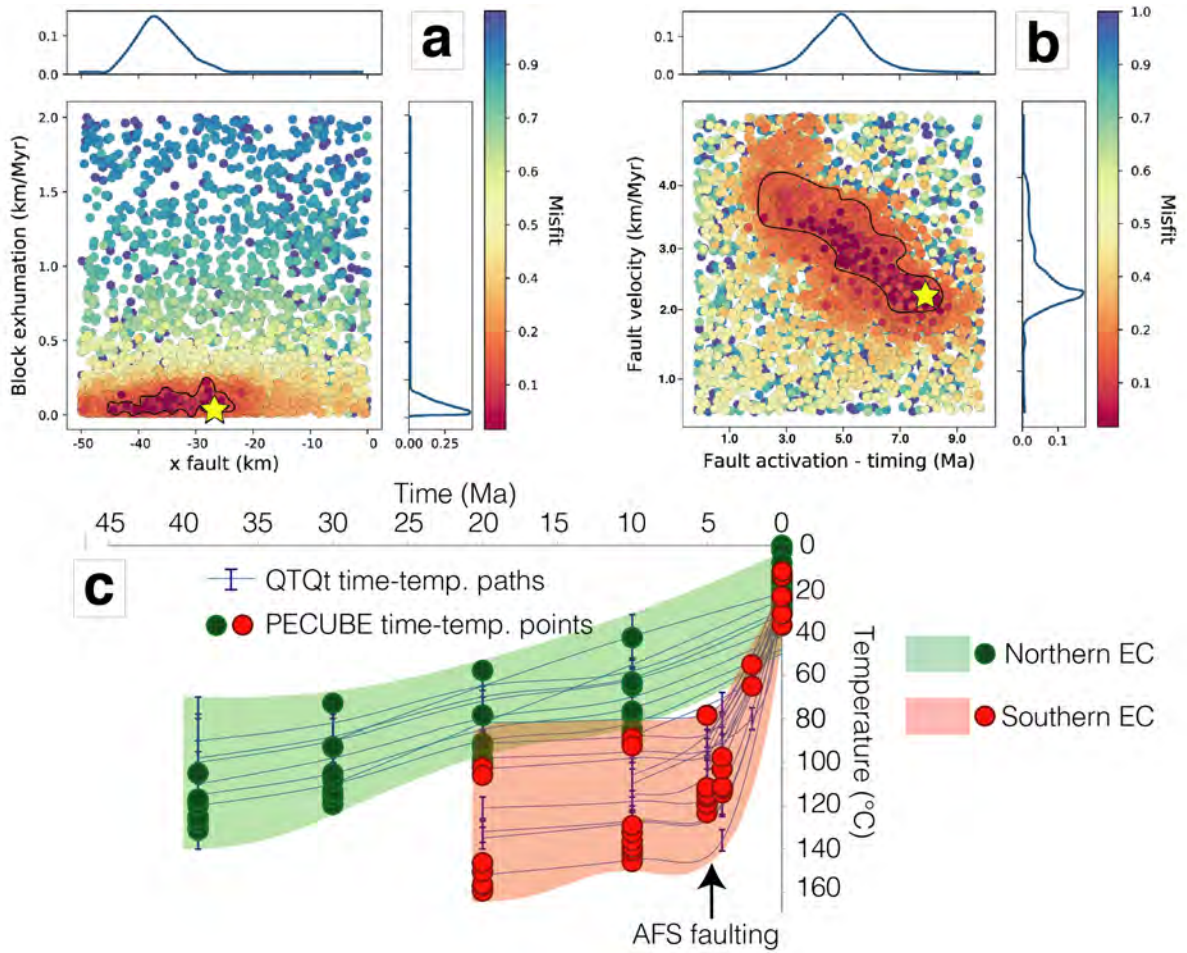


73 **Figure 7.** Time-temperature paths derived from QTQt inverse modeling of  
74 thermochronological data (Gallagher, 2012). a, b and c: Synthesis of time-temperature paths  
75 (colored lines) derived from QTQt (95 % confidence interval around the expected model; see  
76 the Supporting information for detailed inverse modeling outcomes). For profiles, because  
77 cooling dynamics are similar for top and bottom samples we plotted here the minimum and  
78 maximum confidence envelopes. Colored numbers in legend refer to the output cooling rates.  
79 See the Supporting information for details regarding the data reproducibility (observed vs.  
80 predicted data). a, b and c respectively correspond to samples in the northern Eastern  
81 Cordillera (EC), the southern Eastern Cordillera and the Altiplano (see Figure 4 for location).  
82 In b, number 1 (Machu Picchu profile) refers to Gérard et al. in press and the black dotted  
83 rectangle correspond to the cooling acceleration timing at  $5\pm 2$  Ma.  
84





86 **Figure 8.** 3D Pecube inversion results for the Altiplano crustal block. a) 2D parameter space  
87 and inversion results for crustal-block exhumation vs. basal temperature. Each colored point  
88 corresponds to one forward model. Blue curves (up and right subpanels) are the probability  
89 density for each parameter. The yellow star is the best-fitting model. b) Direct comparison of  
90 time-temperature paths derived from QTQt and ones computed with Pecube best-fitting  
91 model. c) Crustal-block model for the Altiplano (see Figure 2 for location) with locations of  
92 thermochronological data.



93

94

95

96

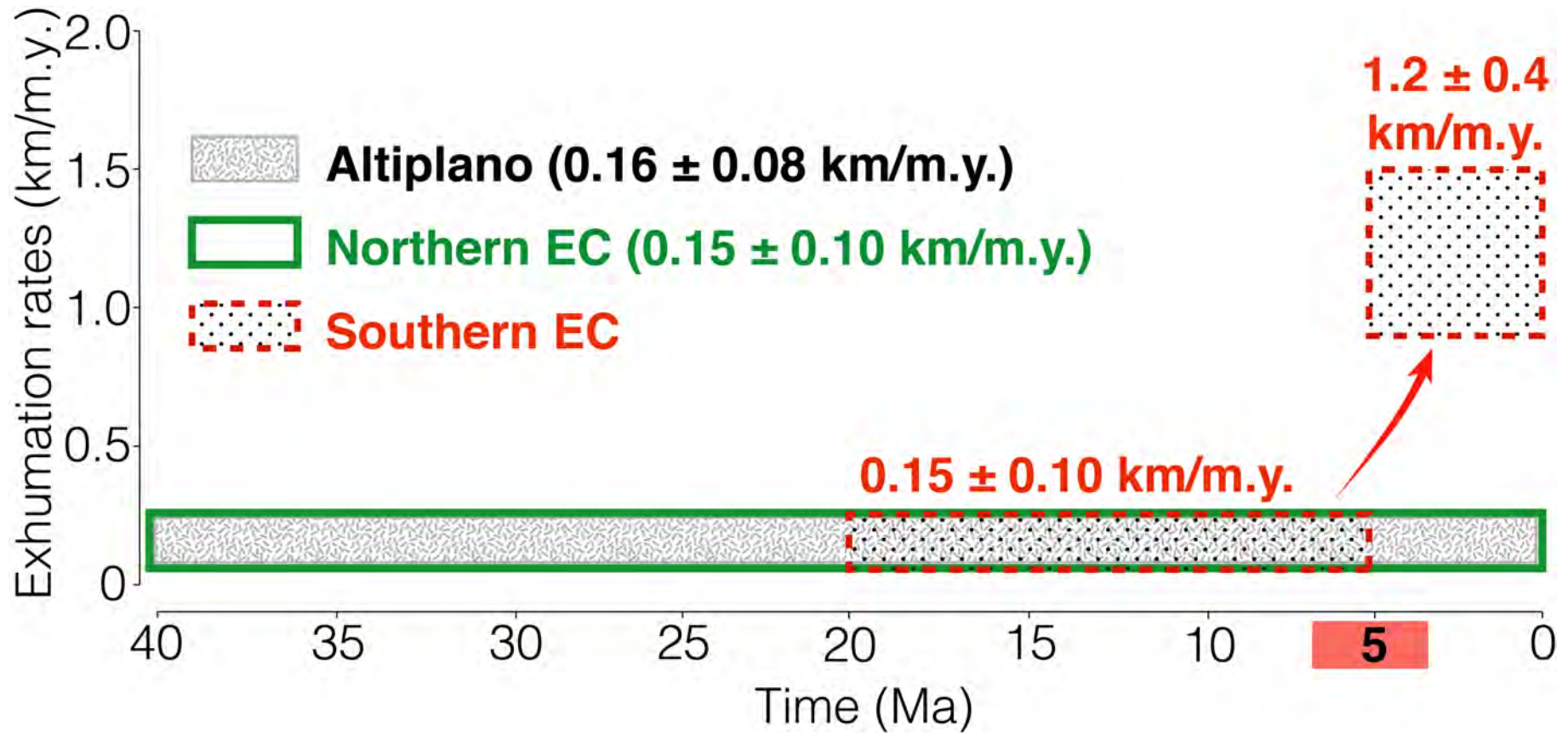
97

98

99

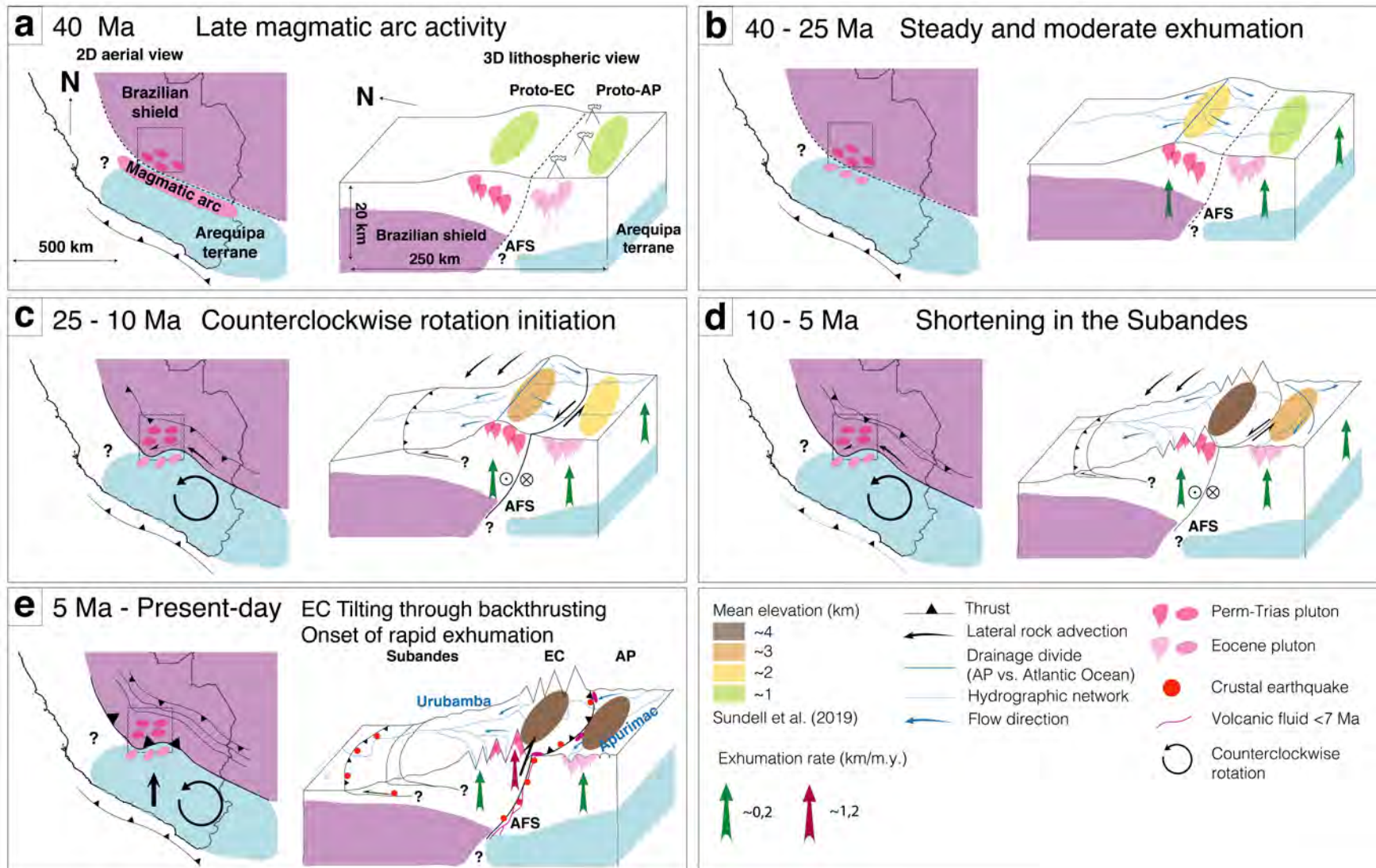
100 **Figure 9.** 3D Pecube inversion results for the Eastern Cordillera crustal block. a) 2D  
101 parameter space and inversion results for crustal-block exhumation vs. position of the fault at  
102 25 km-depth (x fault parameter). b) 2D parameter space and inversion results for the fault  
103 velocity vs. activation timing of the Apurimac fault system. Each colored point corresponds  
104 to one forward model. Blue curves (up and right subpanels) are the probability density for  
105 each parameter. The yellow stars in panels a and b are the best-fitting model. c) Direct  
106 comparison of time-temperature paths derived from QTQt and ones computed with Pecube  
107 best-fitting model. d) Crustal-block model for the Eastern Cordillera with locations of  
108 thermochronological data (see Figure 2 for location). e) Surface exhumation pattern for the  
109 Eastern Cordillera since ~5 Ma predicted from Pecube best-fitting model. AFS is the  
110 Apurimac fault system.  
111

112



113

114 **Figure 10.** Exhumation rates derived from Pecube for the Abancay Deflection through time. Each color corresponds to the three exhumation  
115 areas identified in this study. Details regarding the computed values for exhumation rates according to AERs, QTQt and Pecube are available in  
116 the Figure S43.



118 **Figure 11.** Tectonomorphic evolution of the Abancay Deflection since 40 Ma. Left panels represent the large-scale schematic map views of the  
119 study area (black dashed square). Right panels are 3D Abancay Deflection schematic crustal blocks corresponding to the surface to the square  
120 defined in the left panels. a, b, c, d and e refer respectively to the situation at 40 Ma, between 40 and 25 Ma, between 25 and 10 Ma, between 10  
121 and 5 Ma and finally since 5 Ma to present day. AFS: Apurimac fault system; EC: Eastern Cordillera; AP: Altiplano.

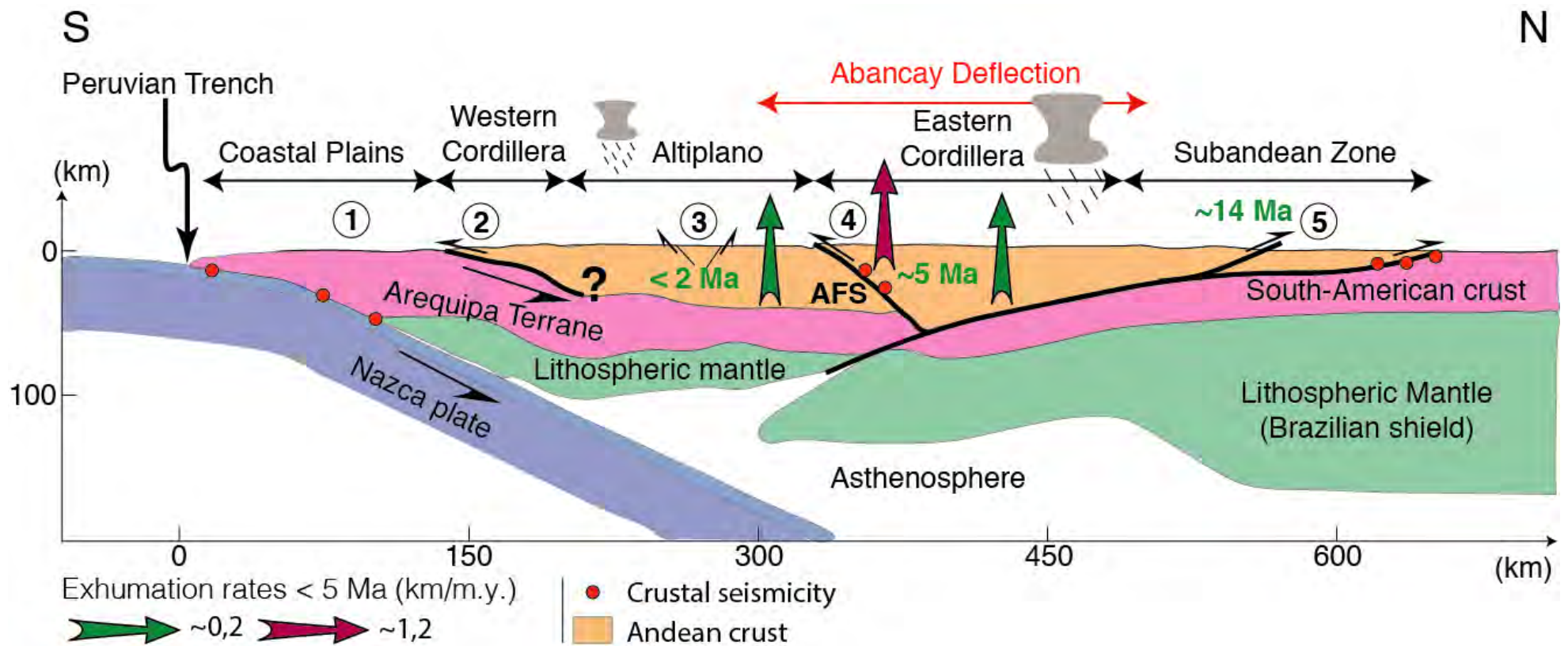


**Figure 12.** Andean orogenic model (South-North cross section) crossing through the Abancay Deflection since ca. 5 Ma. Modified after the double-verging prism orogenic model of Armijo et al. (2015). Green numbers refer to the initiation timing of the associated crustal deformation. Black circled numbers refer to the compiled previous and present studies: 1: Loewy et al. (2004); Ramos (2008, 2010); 2 : Armijo et al. (2015); 3: Sébrier et al. (1985); Mercier et al. (1992); Wimpenny et al. (2018); 4: This study; 5: Espurt et al. (2011); Gautheron et al. (2013). AFS refers to Apurimac Fault System.

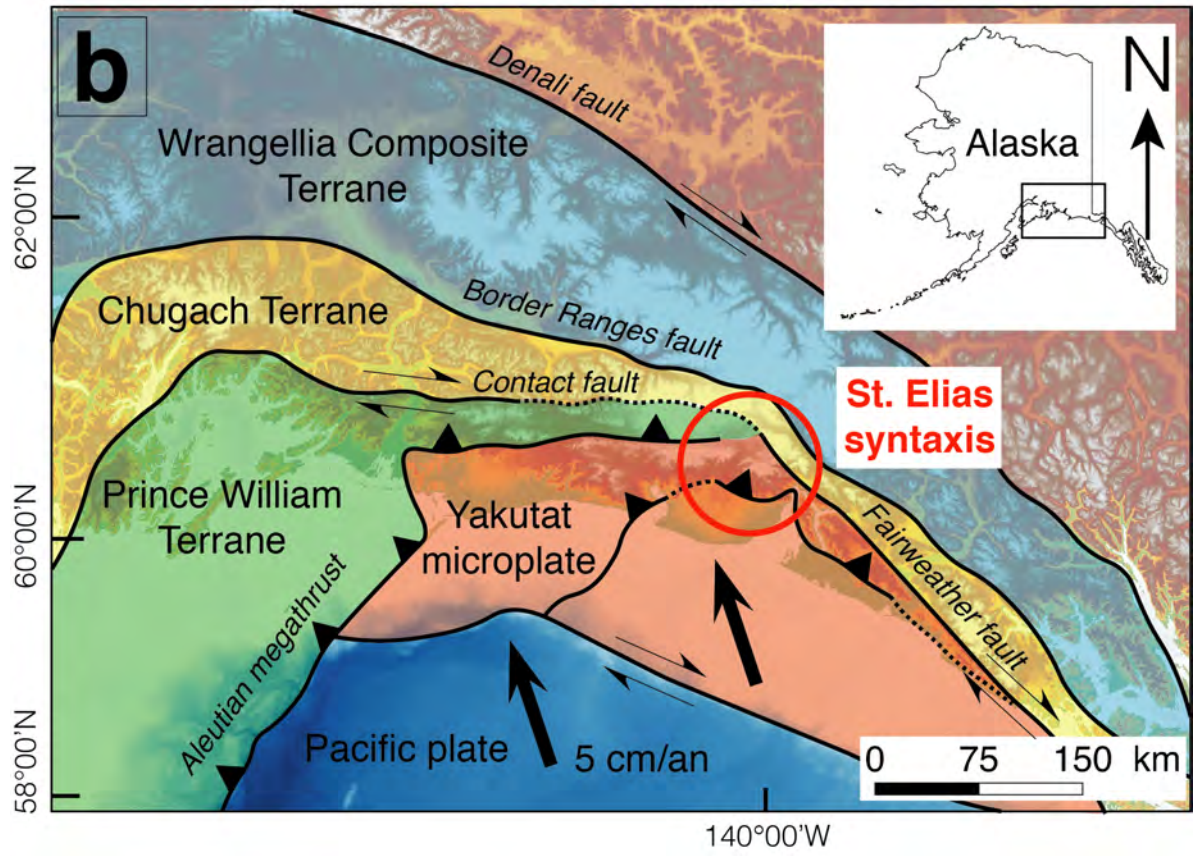
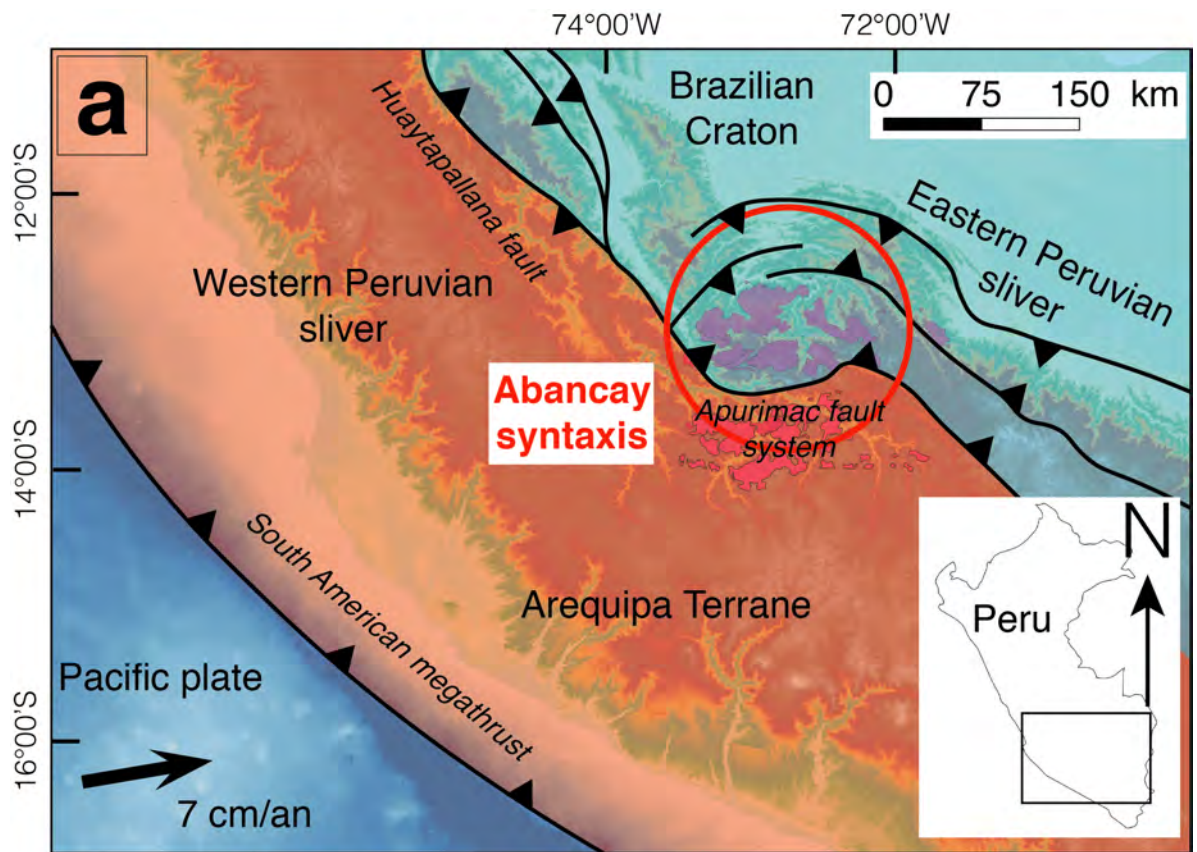




**Figure 13.** Geodynamic comparison between the Abancay Deflection and the St Elias syntaxis of Alaska. a) The Abancay Deflection case; the bulls-eye structure and morphology of the Abancay Deflection (red circle) suggests that it is an incipient syntaxis, with the Arequipa terrane acting as the indenter. b) The St Elias case from Falkowski et al. (2014). The Yakutat microplate plays the role of the indenter for this Alaskan syntaxis.

**Differential exhumation of the Eastern Cordillera in the Central Andes:**

**Evidence for south-verging backthrusting (Abancay Deflection, Peru)**

Benjamin Gérard<sup>1\*</sup>, Xavier Robert<sup>1</sup>, Laurence Audin<sup>1</sup>, Pierre G. Valla<sup>1,2</sup>, Matthias Bernet<sup>1</sup>,  
Cécile Gautheron<sup>3</sup>

<sup>1</sup> *Univ. Grenoble Alpes, IRD, ISTERRE, CNRS, 38000 Grenoble, France*

<sup>2</sup> *Institut of Geological Sciences, University of Bern, Baltzerstrasse 3, 3012 Bern, Switzerland*

<sup>3</sup> *Université Paris-Saclay, CNRS, GEOPS, 91405, Orsay, France*

*\*Now at GET, Université de Toulouse, CNRS, IRD, UPS, (Toulouse), France.*

**Contents of this file**

- Text S1: Present-day geothermal gradient computation for the Abancay Deflection
- Text S2: Neighborhood Algorithm (NA) inversions with Pecube
- Text S3: Limitation for fault geometry at the surface with Pecube
- Text S4: Topography / relief inversed with Pecube – non convergent parameters
- Text S5: Pecube outcomes imposing a warmer geothermal gradient (30°C/km)
- Figure S1: AFT single-grain data (a) and radial plots (b) for sample AB-17-05
- Figure S2: AFT single-grain data (a) and radial plots (b) for sample AB-17-06
- Figure S3: AFT single-grain data (a) and radial plots (b) for sample AB-17-07
- Figure S4: AFT single-grain data (a) and radial plots (b) for sample AB-17-08
- Figure S5: AFT single-grain data (a) and radial plots (b) for sample AB-17-11
- Figure S6: AFT single-grain data (a) and radial plots (b) for sample AB-17-13
- Figure S7: AFT single-grain data (a) and radial plots (b) for sample AB-17-15
- Figure S8: AFT single-grain data (a) and radial plots (b) for sample AB-17-18
- Figure S9: AFT single-grain data (a) and radial plots (b) for sample AB-17-19
- Figure S10: AFT single-grain data (a) and radial plots (b) for sample AB-17-22
- Figure S11: AFT single-grain data (a) and radial plots (b) for sample AB-17-23
- Figure S12: AFT single-grain data (a) and radial plots (b) for sample AB-17-25
- Figure S13: AFT single-grain data (a) and radial plots (b) for sample AB-17-26
- Figure S14: AFT single-grain data (a) and radial plots (b) for sample AB-17-29
- Figure S15: AFT single-grain data (a) and radial plots (b) for sample AB-17-31
- Figure S16: AFT single-grain data (a) and radial plots (b) for sample AB-17-32
- Figure S17: AFT single-grain data (a) and radial plots (b) for sample AB-17-33
- Figure S18: AFT single-grain data (a) and radial plots (b) for sample AB-17-36
- Figure S19: AFT single-grain data (a) and radial plots (b) for sample AB-17-37
- Figure S20: AFT single-grain data (a) and radial plots (b) for sample AB-17-38

- Figure S21: AFT single-grain data (a) and radial plots (b) for sample AB-17-39
- Figure S22: AFT single-grain data (a) and radial plots (b) for sample AB-17-40
- Figure S23: AFT single-grain data (a) and radial plots (b) for sample AB-17-41
- Figure S24: AFT single-grain data (a) and radial plots (b) for sample AB-17-42
- Figure S25: AFT single-grain data (a) and radial plots (b) for sample AB-17-44
- Figure S26: AFT single-grain data (a) and radial plots (b) for sample AB-17-51
- Figure S27: AFT single-grain data (a) and radial plots (b) for sample AB-17-55
- Figure S28: QTQt inversion results for the Ocobamba high-altitudinal profile
- Figure S29: QTQt inversion results for the AB-17-13 sample
- Figure S30: QTQt inversion results for the AB-17-15 sample
- Figure S31: QTQt inversion results for the AB-17-18 sample
- Figure S32: QTQt inversion results for the AB-17-19 sample
- Figure S33: QTQt inversion results for the Lucma high-altitudinal profile
- Figure S34: QTQt inversion results for the Limatambo high-altitudinal profile
- Figure S35: QTQt inversion results for the Abancay high-altitudinal profile
- Figure S36: QTQt inversion results for the Incahuasi high-altitudinal profile
- Figure S37: Observed vs. predicted thermochronological ages (AFT & AHe) modeled with QTQt
- Figure S38: Parameters implemented and/or explored in Pecube through time
- Figure S39: Pecube inversion results for landscape evolution parameters through time for the Altiplano block
- Figure S40: Pecube inversion results for landscape evolution parameters through time for the Eastern Cordillera block
- Figure S41: Observed data vs. predicted ones from Pecube for the Altiplano crustal block
- Figure S42: Observed data vs. predicted ones from Pecube for the Eastern Cordillera crustal block
- Figure S43: Exhumation rates derived from AER, QTQt and Pecube
- Figure S44: Sample locations within the Abancay Deflection
- Figure S45: 3D Pecube inversion results for the Altiplano crustal block imposing a geothermal gradient of 30°C/km
- Figure S46: 3D Pecube inversion results for the Eastern Cordillera crustal block imposing a geothermal gradient of 30°C/km
- Table S1: QTQt parameters for thermochronological data modeling
- Table S2: Apatite (U-Th-Sm)/He data – Computed values for Pecube modeling
- Table S3. Thermal and rheological parameters for Pecube modeling
- Table S4: Explored parameters and ranges for thermochronological data inversion (Pecube modeling)

### **Additional Supporting Information (Files uploaded separately)**

- Movie S1: Tectono-morphic evolution of the southern Abancay Deflection (Altiplano block) since 50 Ma (Topography, relief)
- Movie S2: Tectono-morphic evolution of the southern Abancay Deflection (Altiplano block) since 50 Ma (Exhumation rates)
- Movie S3: Tectono-morphic evolution of the southern Abancay Deflection (Altiplano block) since 50 Ma (AHe surface ages)
- Movie S4: Tectono-morphic evolution of the southern Abancay Deflection (Altiplano block) since 50 Ma (AFT surface ages)

- Movie S5: Tectono-morphic evolution of the northern Abancay Deflection (Eastern Cordillera block) since 50 Ma (Exhumation rates)
- Movie S6: Tectono-morphic evolution of the northern Abancay Deflection (Eastern Cordillera block) since 50 Ma (Topography, relief)
- Movie S7: Tectono-morphic evolution of the northern Abancay Deflection (Eastern Cordillera block) since 50 Ma (AHe surface ages)
- Movie S8: Tectono-morphic evolution of the northern Abancay Deflection (Eastern Cordillera block) since 50 Ma (AFT surface ages)

## Introduction

This document includes extra-information regarding thermochronological ages (AHe & AFT) computation and details about the 2D and 3D modeling (2D time-temperature modeling outputs (QTQt; Gallagher, 2012) and 3D thermo-kinematic modeling results (Pecube; Braun, 2003; Braun et al., 2012)). We collected 33 samples into crystalline bedrock through five high-altitudinal profiles (Ocobamba, Lucma, Incahuasi, Abancay and Limatambo) and 4 individual samples over the Abancay Deflection (Figure S44). The field trip took place between April and June 2016. The AHe (Table S2) and AFT (Figures S1-S27) analyses were performed respectively at GEOPS laboratory (Université Paris Saclay, France) and ISTerre laboratory (University Grenoble Alpes, France). Computed age uncertainties are available in the data tables (main article text). Additionally, we provide 8 videos (Movies S1-S8) presenting the tectono-morphic evolution (topography, exhumation rates and surface thermochronological ages evolution) of the southern and northern Abancay Deflection according to the best-fitting Pecube modeling outcomes (discussion in the main article text). For each modeled crustal blocks, we provide graphics exhibiting observed data vs. predicted ones for validation of Pecube 3D modeling (Figures S41-S42). Modeling outcomes are all compared to age-elevation relationships and QTQt modeling (Table S1 and Figures S28-S37) to derive the exhumation histories of studied areas (Figure S43).

### Text S1. Present-day geothermal gradient computation for the Abancay Deflection

Using the simplified heat equation from Braun et al. (2006), we estimated the geothermal gradient for the Abancay Deflection.

List of parameters:

$T_{\text{surface}}$ : Temperature at the surface (K; °C)

$T_{\text{bottom}}$ : Temperature at the base of the crust (K; °C)

zc: Crustal depth (km)

$\kappa$ : Thermal diffusivity ( $\text{km}^2/\text{Ma}$ )

H: Heat production for the crust (K/Ma)

$\rho$ : Density of the crust ( $\text{kg}/\text{m}^3$ )

c: Specific heat capacity ( $\text{J}/\text{kg}/\text{K}$ )

Processed values for these parameters are displayed in the Table S3.

We firstly computed the thermal conductivity ( $k$ ; Equation 1) and the heat production rate ( $A$ ; Equation 2):

$$k = \kappa \times \rho \times c \quad (1)$$

$$A = (H \times \rho \times c) \times 10^6 \quad (2)$$

k: Thermal conductivity ( $\text{W}/\text{m}/\text{K}$ )

A: Heat production rate ( $\mu\text{W}/\text{m}^3$ )

We then obtained the heat flow ( $q_0$ ; Equation 3;  $\text{mW}/\text{m}^2$ ).

$$q_0 = \left( \left( \frac{(T_{\text{bottom}} - T_{\text{surface}}) \times k}{z \times 10^3} \right) + \left( A \times (z \times 10^3) \right) \right) \times 10^3 \quad (3)$$

From this computed heat flow, we computed a temperature at  $z$  km-depth ( $T_z$ ; Equation 4;  $^\circ\text{C}$ ):

$$T_z = T_{\text{surface}} + \left( \frac{q_0 \times z \times 10^3}{k} \right) - \left( \left( \frac{A}{2 \times k} \right) \times (z \times 10^3)^2 \right) \quad (4)$$

We finally approximate the geothermal gradient ( $G$ ;  $^\circ\text{C}/\text{km}$ ) performing the following average (Equation 5):

$$G = \frac{(T_z - T_{\text{surface}})}{z} \quad (5)$$

For example using these values:

$T_{\text{surface}} = 298,15 \text{ K (} 25^\circ\text{C)}$

$T_{\text{bottom}} = 833,15 \text{ K (} 560^\circ\text{C)}$

$z = 56 \text{ km}$

$\kappa = 40 \text{ km}^2/\text{Ma} \rightarrow 1.26 \times 10^{-6} \text{ m}^2/\text{s}$

$H = 279,15 \text{ K/Ma} \rightarrow 2.04 \times 10^{-13} \text{ }^\circ\text{C}/\text{s}$

$\rho = 2750 \text{ kg}/\text{m}^3$

$c = 800 \text{ J}/\text{kg}/\text{K}$

$$k = 1.26 \times 10^{-6} \times 2750 \times 800 = 2.79 \text{ W}/\text{m}/\text{K}$$

$$A = (2.04 \times 10^{-13} \times 2750 \times 800) \times 10^6 = 0.45 \text{ } \mu\text{W}/\text{m}^3$$

$$A = 4.48 \times 10^{-7} \text{ W}/\text{m}^3$$

$$q_0 = \left( \left( \frac{(560 - 25) \times 2.79}{56 \times 1000} \right) + (4.48 \times 10^{-7} \times (56 \times 1000)) \right) \times 1000 = 51.74 \text{ mW}/\text{m}^2$$

$$q_0 = 5.17 \times 10^{-2} \text{ W}/\text{m}^2$$

$$T_5 = 25 + \left( \frac{5.17 \times 10^{-2} \times 5 \times 1000}{2.79} \right) - \left( \left( \frac{4.48 \times 10^{-7}}{2 \times 2.79} \right) \times (5 \times 1000)^2 \right) = 115.76^\circ\text{C}$$

$$G = \frac{(115.76 - 25)}{5} = \mathbf{18^\circ\text{C}/\text{km}}$$

**Text S2.** Neighborhood Algorithm (NA) inversions with Pecube

We used Pecube in inverse mode to quantitatively constrain parameter values (tectono-morphic scenarios; Figures S38 and Tables S3-S4) that best reproduce the input thermochronological data. Pecube uses the implemented Neighborhood Algorithm (NA; Sambridge, 1999a;b), which explores the parameter space by progressive misfit minimization and permits to rapidly converge toward a best-fitting tectono-morphic scenario. The Misfit function (Equations 6 and 7) measures the difference between

observed and predicted data, with three different parts: the thermochronological ages (M1; Equation 6), the fission track-length distributions (Kuiper test for comparison between observed and predicted track-length distributions) and the thermal history (M2: Equation 7):

$$M1 = \sqrt{\frac{\sum_{i=0}^{N1} (A_o^i - A_p^i)^2 / dA_i^2}{N1}} \quad (6)$$

With  $A_o$ , the observed thermochronological ages,  $dA$ , the analytical error,  $A_p$ , the predicted ages from Pecube and  $N1$  the total number of implemented ages.

$$M2 = \sqrt{\frac{\sum_{i=0}^{N2} (T_o^i - T_p^i)^2 / dT_i^2}{N2}} \quad (7)$$

For the thermal histories,  $T_o$  is the implemented temperature derived from QTQt,  $dT$  is the error of these temperatures (95% reliability; QTQt; Gallagher, 2012),  $T_p$  is the predicted temperature by Pecube and  $N2$  is the total number of steps defining the thermal history. More details regarding the misfit functions are available in the Pecube user guide on GitHub following this link: <https://github.com/jeanbraun/Pecube>.

**Text S3.** Limitation for fault geometry at the surface with Pecube

Implementation of complex fault systems cannot be modeled with Pecube because of geometrical and fault-velocity computational issues. Although the Apurimac fault system trace at the surface is curved (x/y axis; Figure 2), we approximate it in Pecube by a straight and oblique fault separating the Altiplano from the Eastern Cordillera. The geometry of the fault at depth (z axis) is explored with PECUBE and discussed in the manuscript.

**Text S4.** Topography / relief inversed with Pecube – non convergent parameters

The relief amplification factor did not converge during PECUBE inverse modeling and cannot be quantified for the Altiplano and the Eastern Cordillera (Figures S39 and S40). We notwithstanding further explored this parameter through forward modeling to assess to what extent it is needed for our thermochronological data. Trial-and-error approach using PECUBE forward models suggests an increase in topographic relief between 10 and 0 Ma to reproduce accurately the observed thermochronological data (although this parameter is not a first order control on the exhumation history). Since the relief-amplification factor can be interpreted as a proxy for incision, we linked this needed relief increase to the large-scale capture of the Abancay Deflection system by the Urubamba and Apurimac drainage network (Gérard et al. in press) and subsequent incision since ~10 Ma. From our thermochronological record and literature data interpretation (van Heiningen et al., 2005; Gérard et al., in press), we further propose that the capture of the Abancay Deflection likely occurred during the late Miocene/early Pliocene around ~5 Ma and that associated erosion started slightly after.

**Text S5.** Pecube outcomes imposing a warmer geothermal gradient (30°C/km)

To test the robustness of our computed geothermal gradient for the Abancay Deflection (~20°C/km), which is crucial for exhumation computation, we performed the same inversion as presented in the manuscript for both the Altiplano and the Eastern Cordillera model with identical parameters except for the geotherm, imposing a warmer geothermal gradient of 30°C/km as compiled and accepted for the Bolivian Eastern Cordillera (Barnes et al., 2008).

For the Altiplano block model, we explored exhumation rates for the entire crustal block between 40 Ma to present-day for values ranging from -10 to 10 km/m.y (subsidence vs. exhumation). This parameter nicely converge to  $0.45 \pm 0.10$  km/m.y. (Figure S45a). Processing this best-fitting rate into forward modeling we observed that, counter intuitively, even if the geothermal gradient is warmer, the area needs twice exhumation rather than if a colder geothermal gradient is used ( $0.2 \pm 0.1$  km/m.y. with a gradient of  $18^\circ\text{C}/\text{km}$ ). Ages and T-t paths are less reproducible and predicted thermochronological ages are, in most of the cases, younger than the observed data (Figure S45b and c). Consequently, the  $\sim 20^\circ\text{C}/\text{km}$  geotherm seems to be the most suitable gradient for this part of the Altiplano.

For the Eastern Cordillera block model, we explored exhumation rates for the entire crustal block between 50 Ma to present-day for values ranging from 0 to 5 km/m.y. At the same time, we inverted the timing for the Apurimac fault system activation (between 0 and 14 Ma) and the fault velocity (0 to 10 km/m.y.). These three parameters nicely converge to values of  $0.2 \pm 0.1$  km/m.y. (Figure S46a),  $7 \pm 1$  Ma and  $1.4 \pm 0.4$  km/m.y. respectively (Figure S46b). Exhumation rate for the entire crustal block with this warmer geotherm is identical with the one obtained with the  $18^\circ\text{C}/\text{km}$  gradient. The timing for faulting initiation is quite similar too ( $7 \pm 1$  Ma vs.  $5 \pm 2$  Ma). The fault velocity is, however, divided by  $\sim 2$  ( $1.4 \pm 0.4$  km/m.y. ( $30^\circ\text{C}/\text{km}$ ) vs.  $2.9 \pm 0.6$  ( $18^\circ\text{C}/\text{km}$ )), which is quite logical as the geothermal gradient is multiplied by  $\sim 2$ . Whatever the geothermal gradient imposed, tectonic is needed through the Apurimac fault system to reproduce the thermochronological ages (Figure S46c and d). The data reproducibility is, nevertheless, lower with the warmer geotherm and predicted ages are older than observed ones (Figure S46c), especially for the AHe system. The  $\sim 20^\circ\text{C}/\text{km}$  geotherm, in that case, seems to be the most suitable gradient for this part of the Eastern Cordillera.

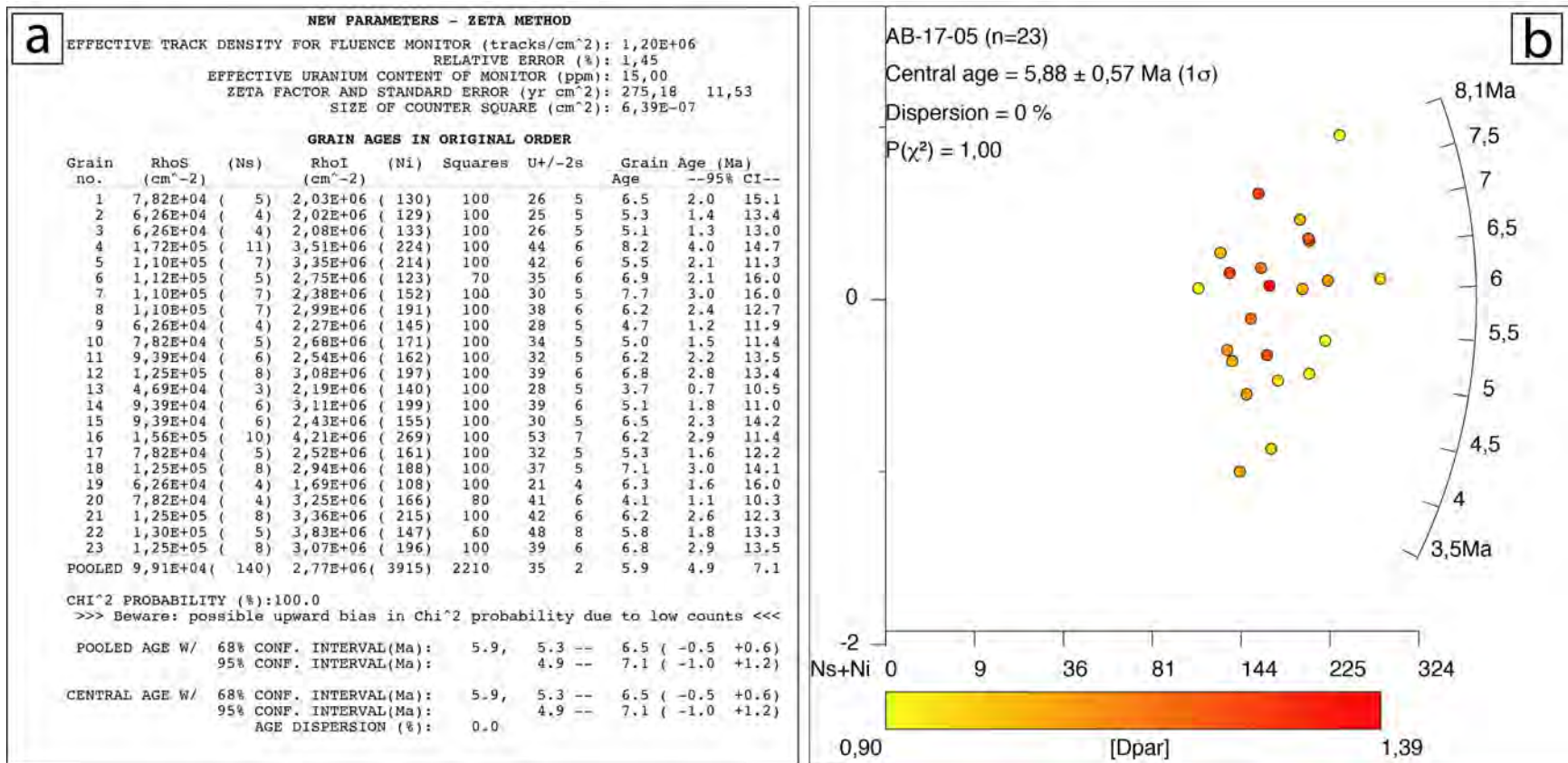


**Figure S1.** AFT single-grain data (a) and radial plots (b) for sample AB-17-05. See Figure S44 for location.



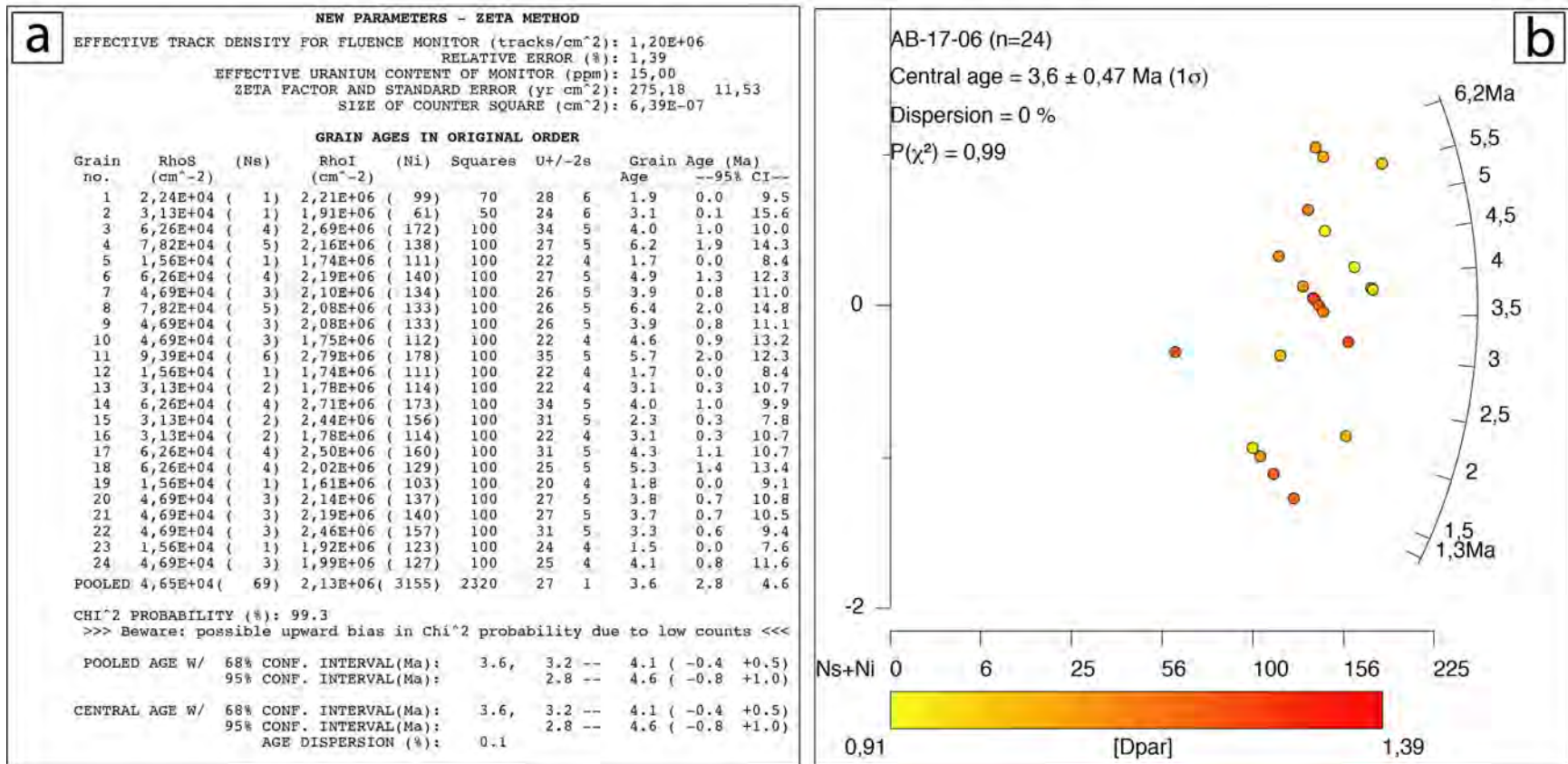


**Figure S2.** AFT single-grain data (a) and radial plots (b) for sample AB-17-06. See Figure S44 for location.

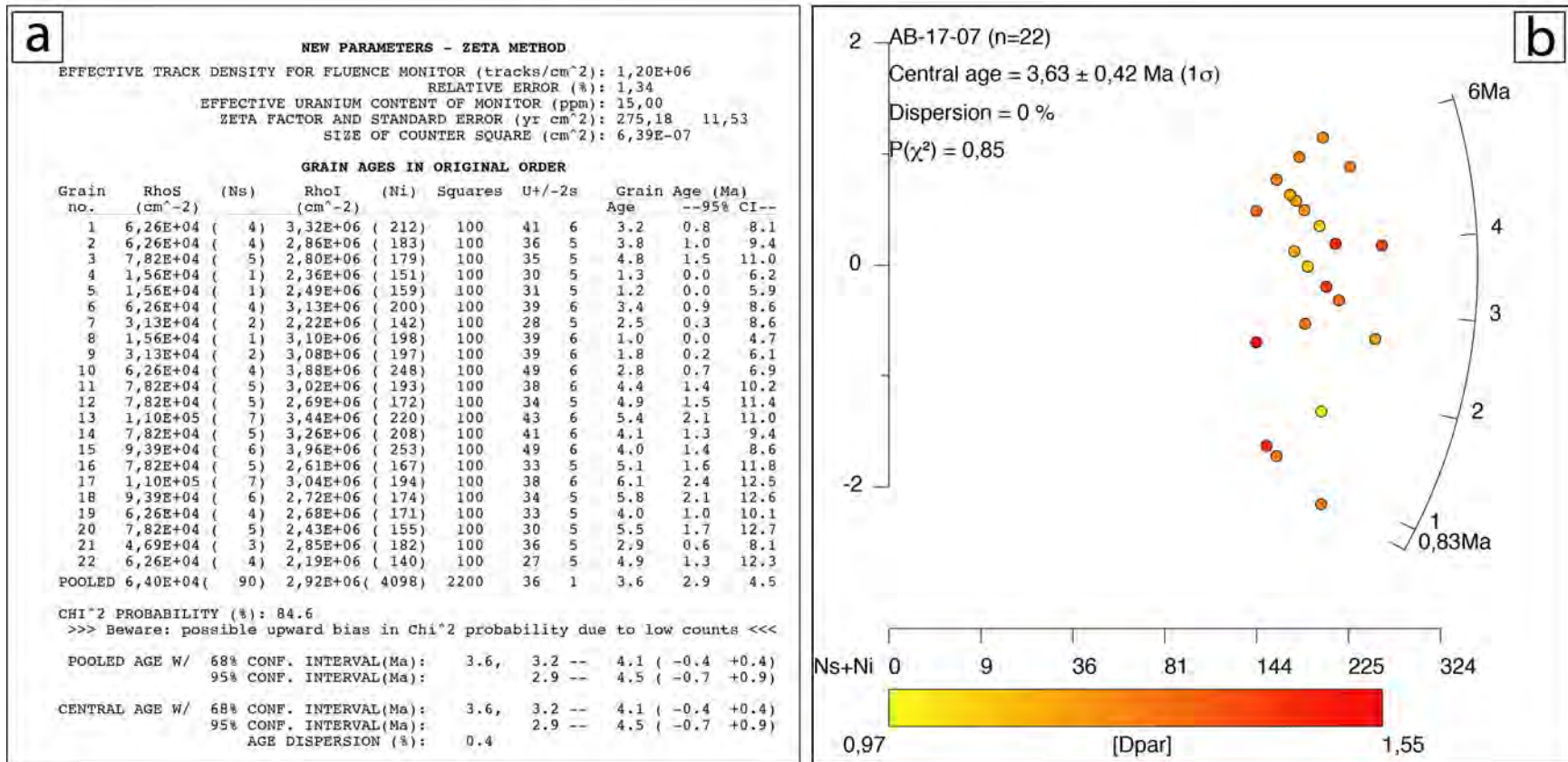


**Figure S3.** AFT single-grain data (a) and radial plots (b) for sample AB-17-07. See Figure S44 for location.

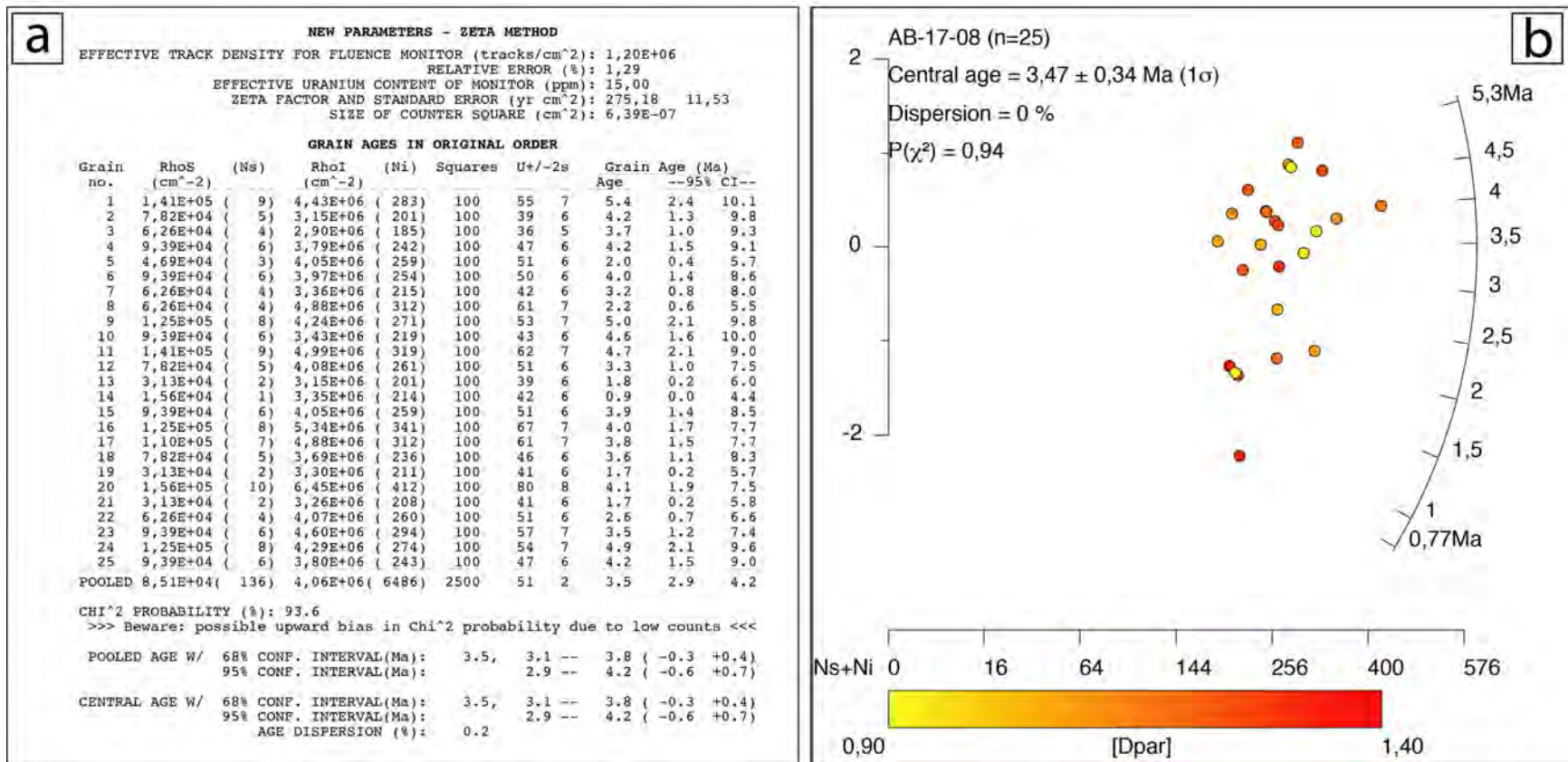


**Figure S4.** AFT single-grain data (a) and radial plots (b) for sample AB-17-08. See Figure S44 for location.

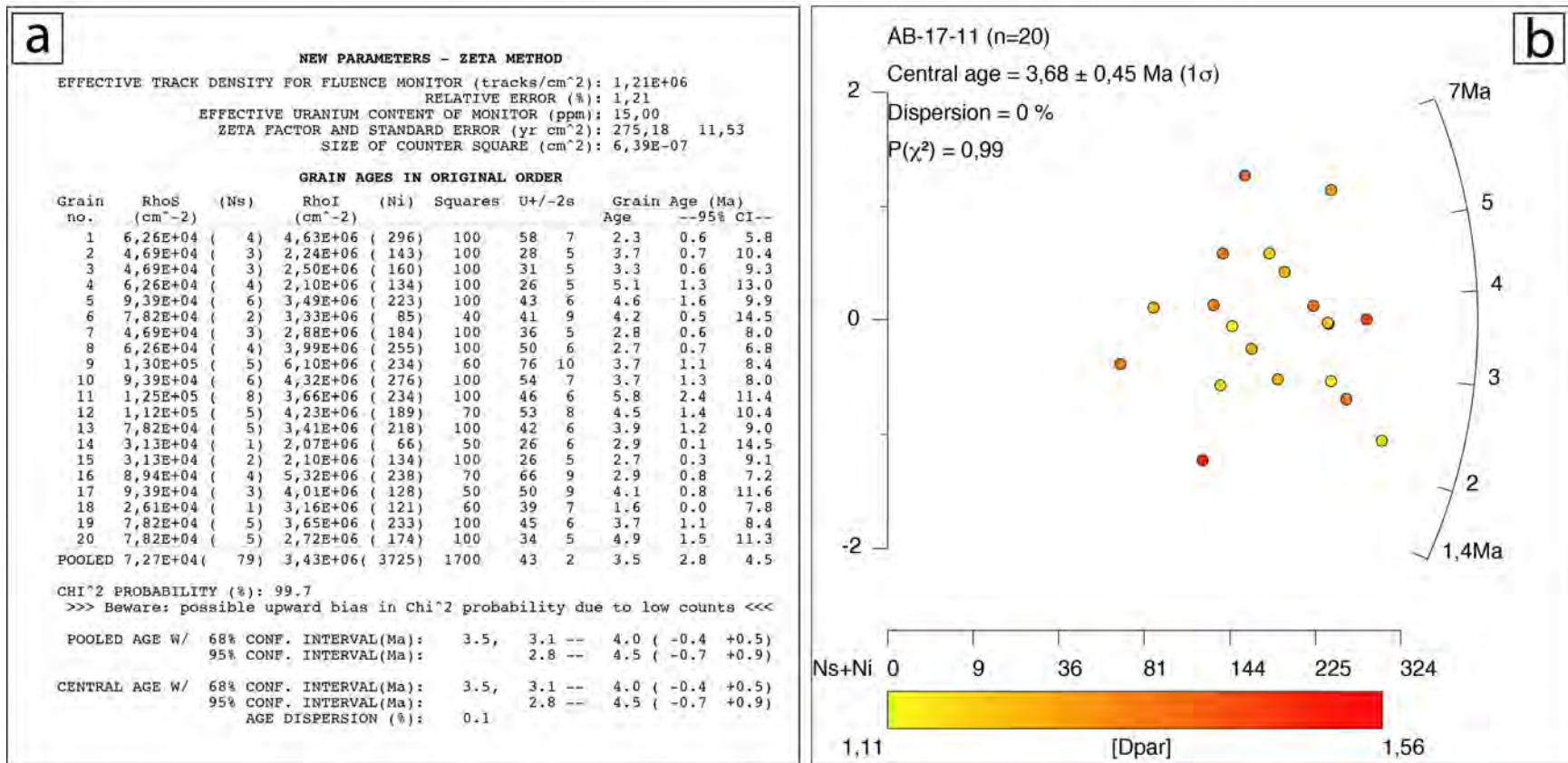


**Figure S5.** AFT single-grain data (a) and radial plots (b) for sample AB-17-11. See Figure S44 for location.

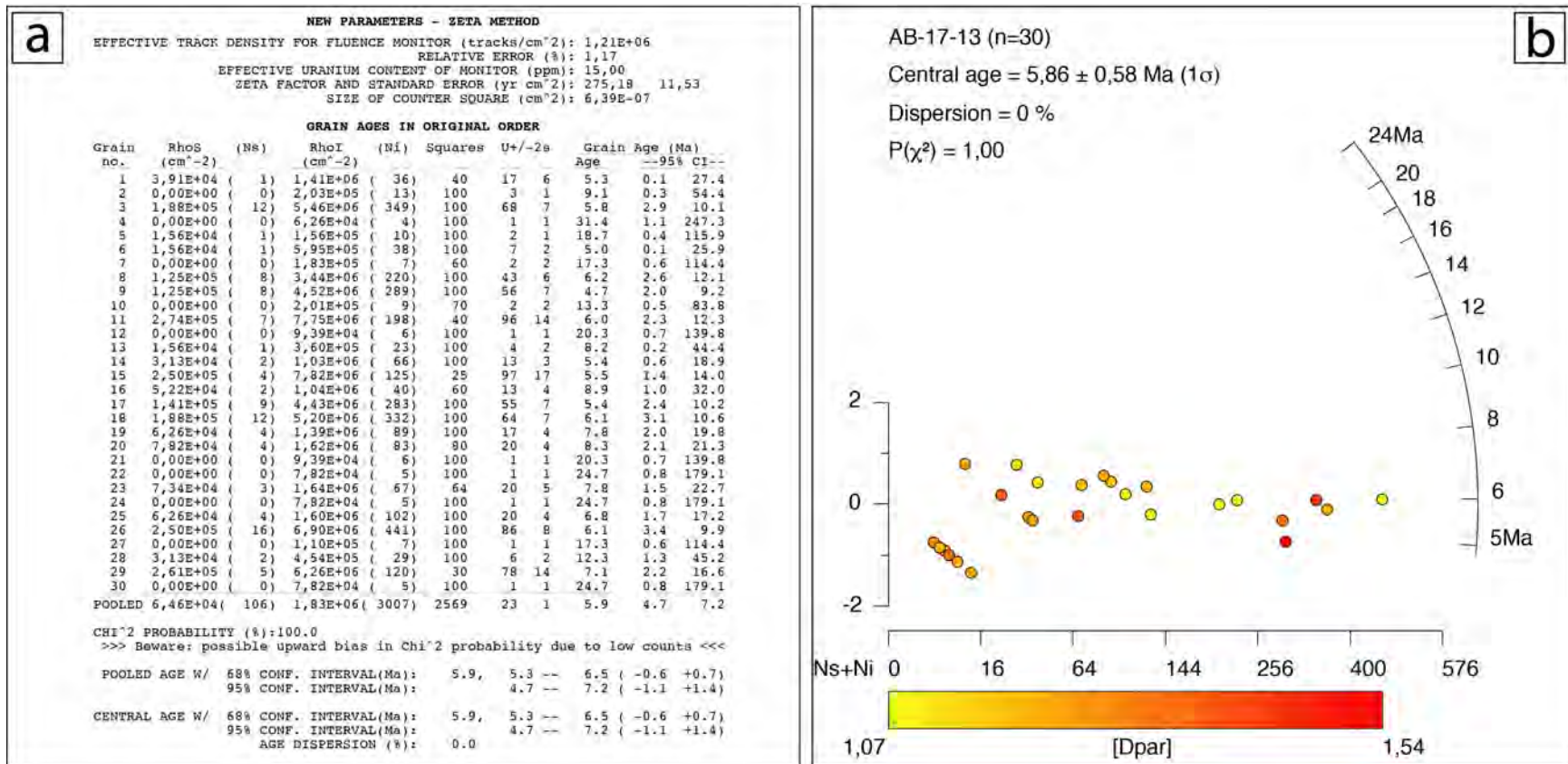


**Figure S6.** AFT single-grain data (a) and radial plots (b) for sample AB-17-13. See Figure S44 for location.

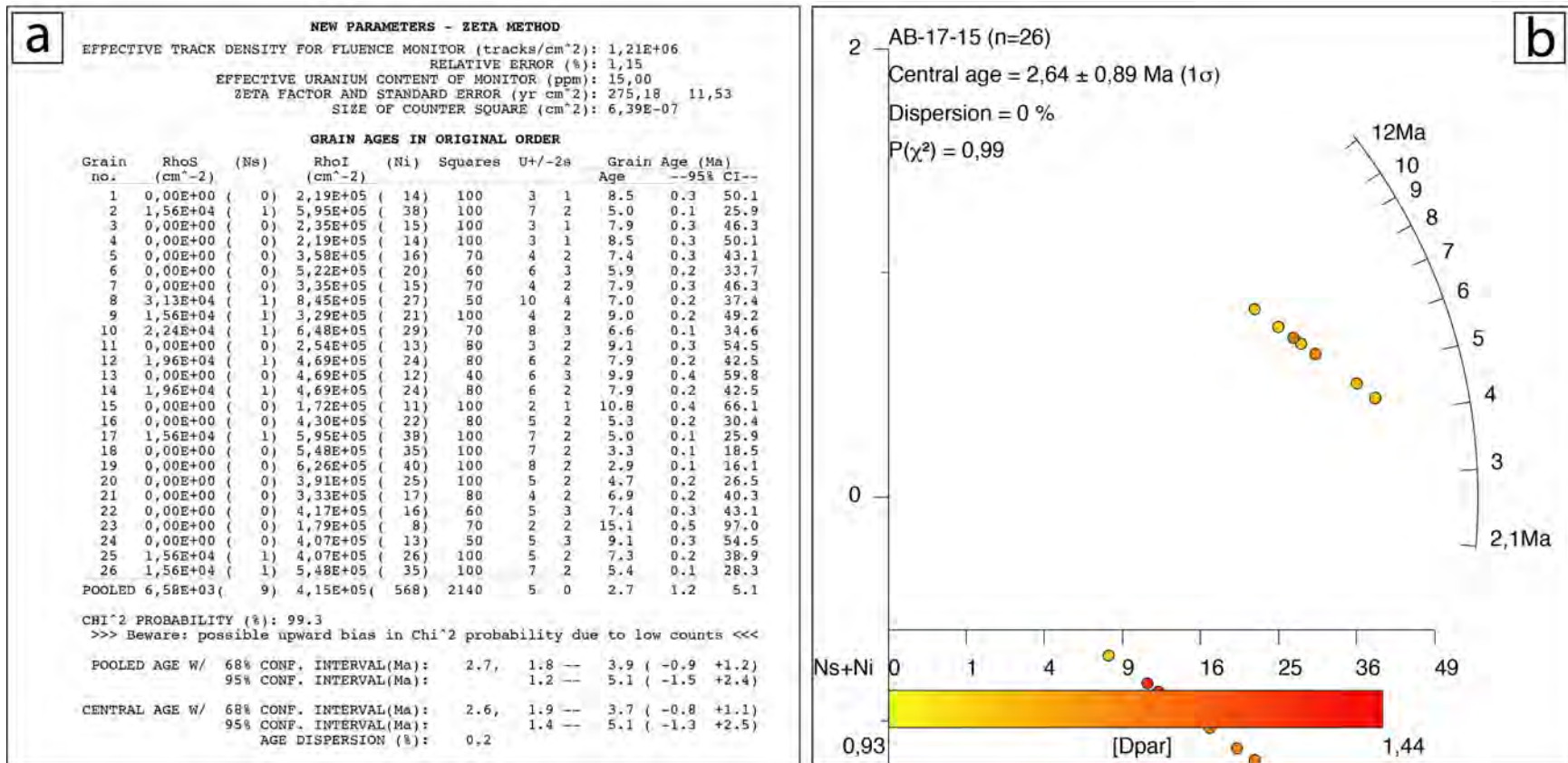


**Figure S7.** AFT single-grain data (a) and radial plots (b) for sample AB-17-15. See Figure S44 for location.

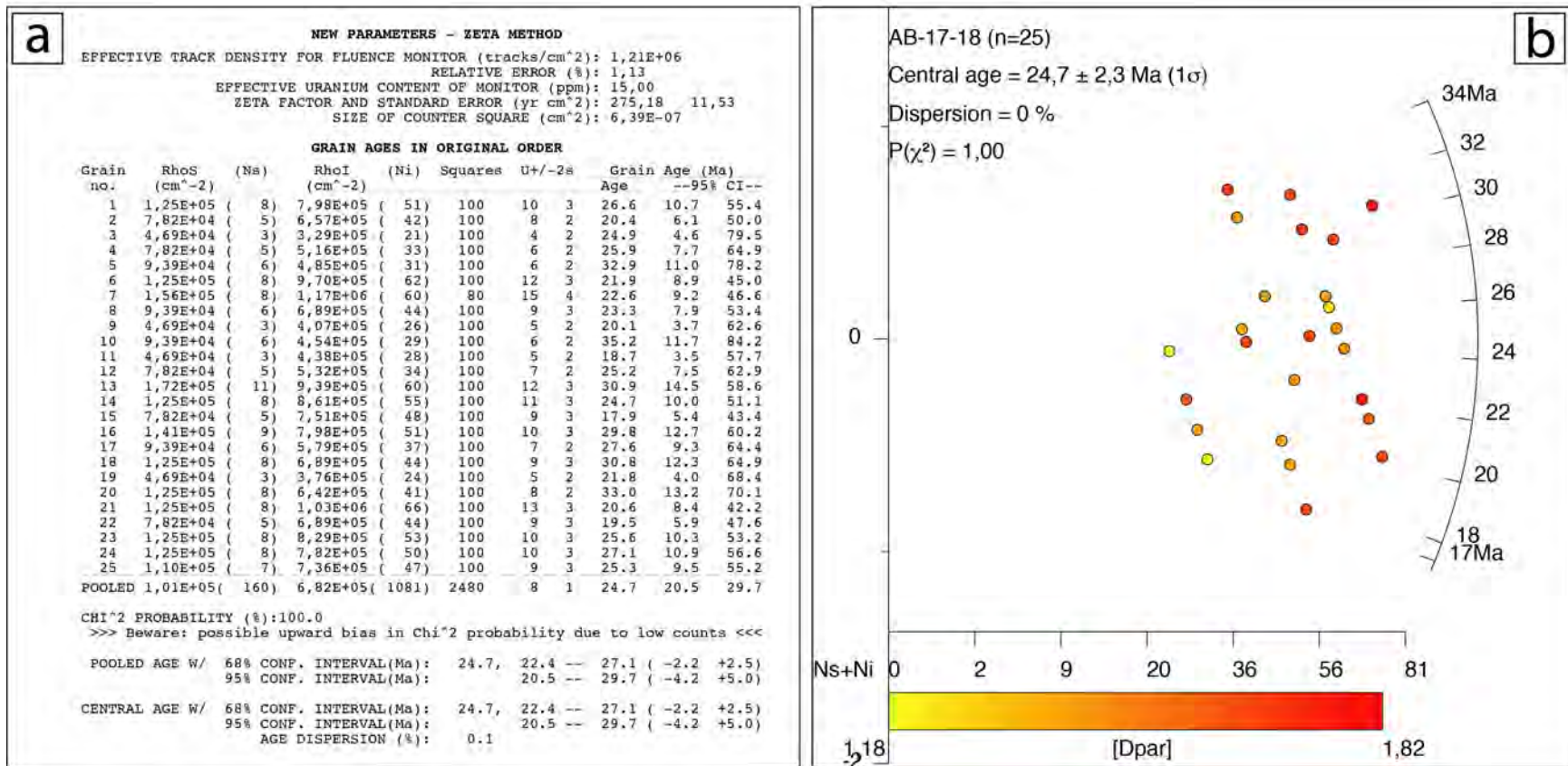


**Figure S8.** AFT single-grain data (a) and radial plots (b) for sample AB-17-18. See Figure S44 for location.

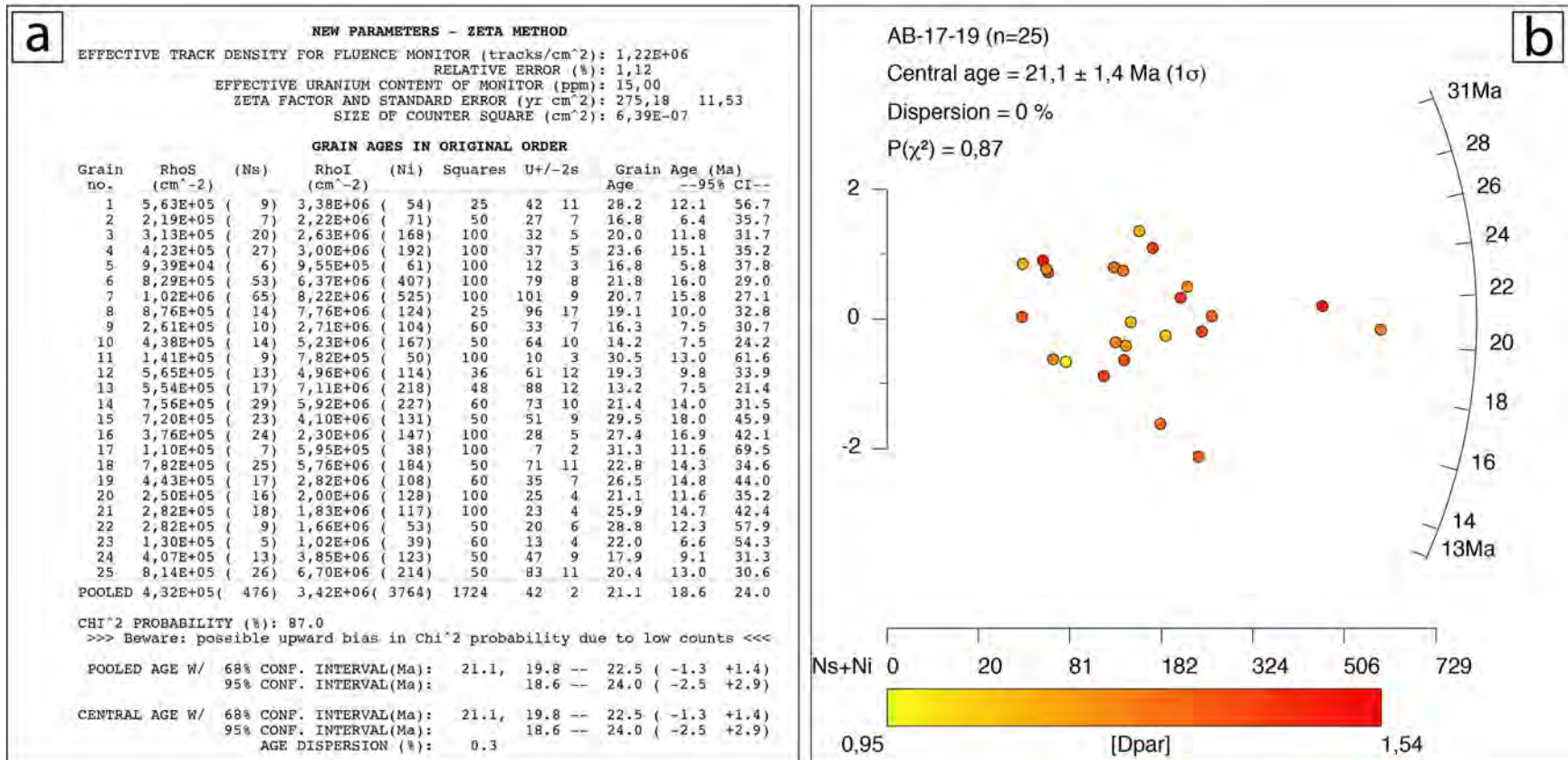


**Figure S9.** AFT single-grain data (a) and radial plots (b) for sample AB-17-19. See Figure S44 for location.



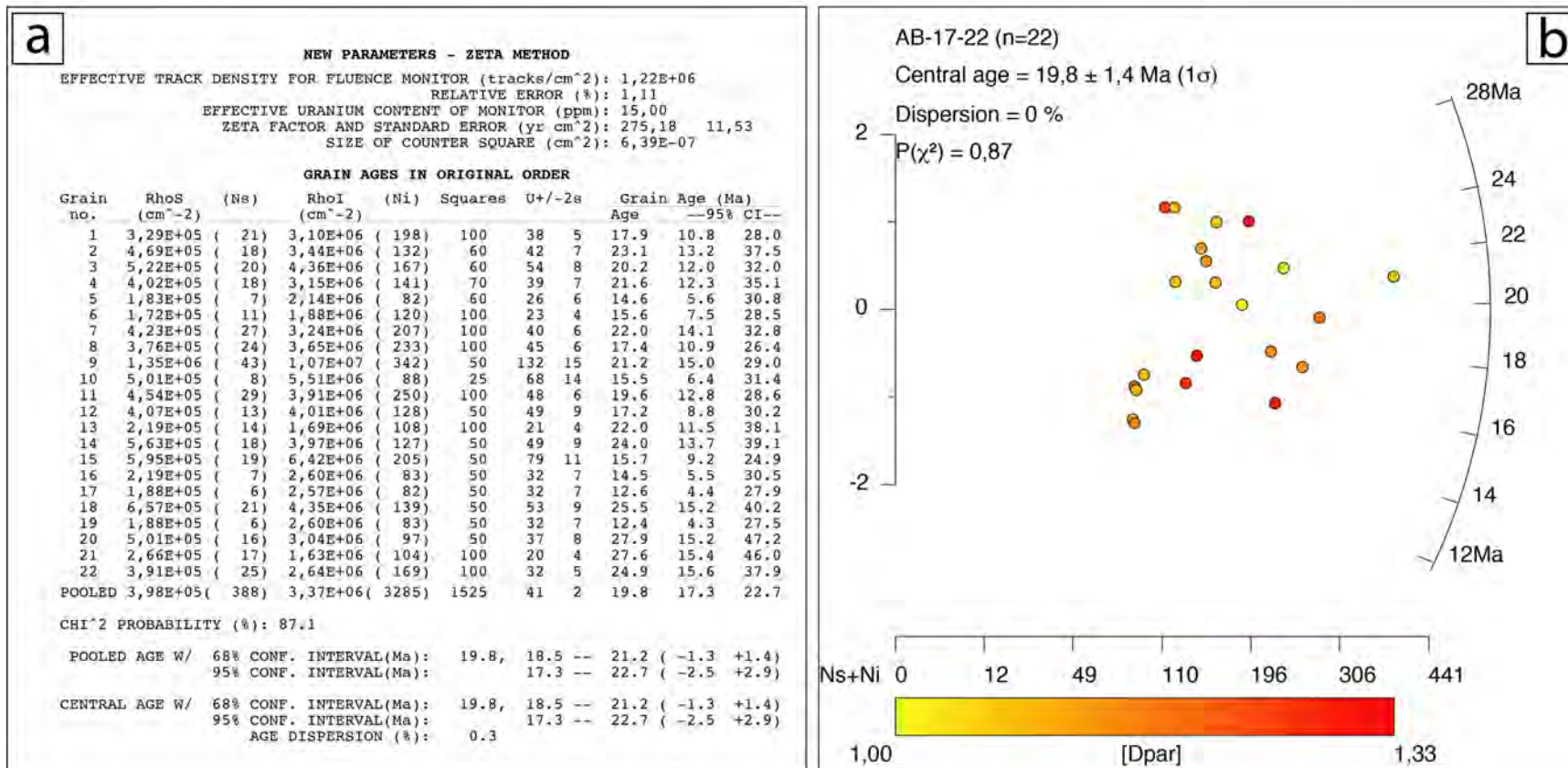


**Figure S10.** AFT single-grain data (a) and radial plots (b) for sample AB-17-22. See Figure S44 for location.

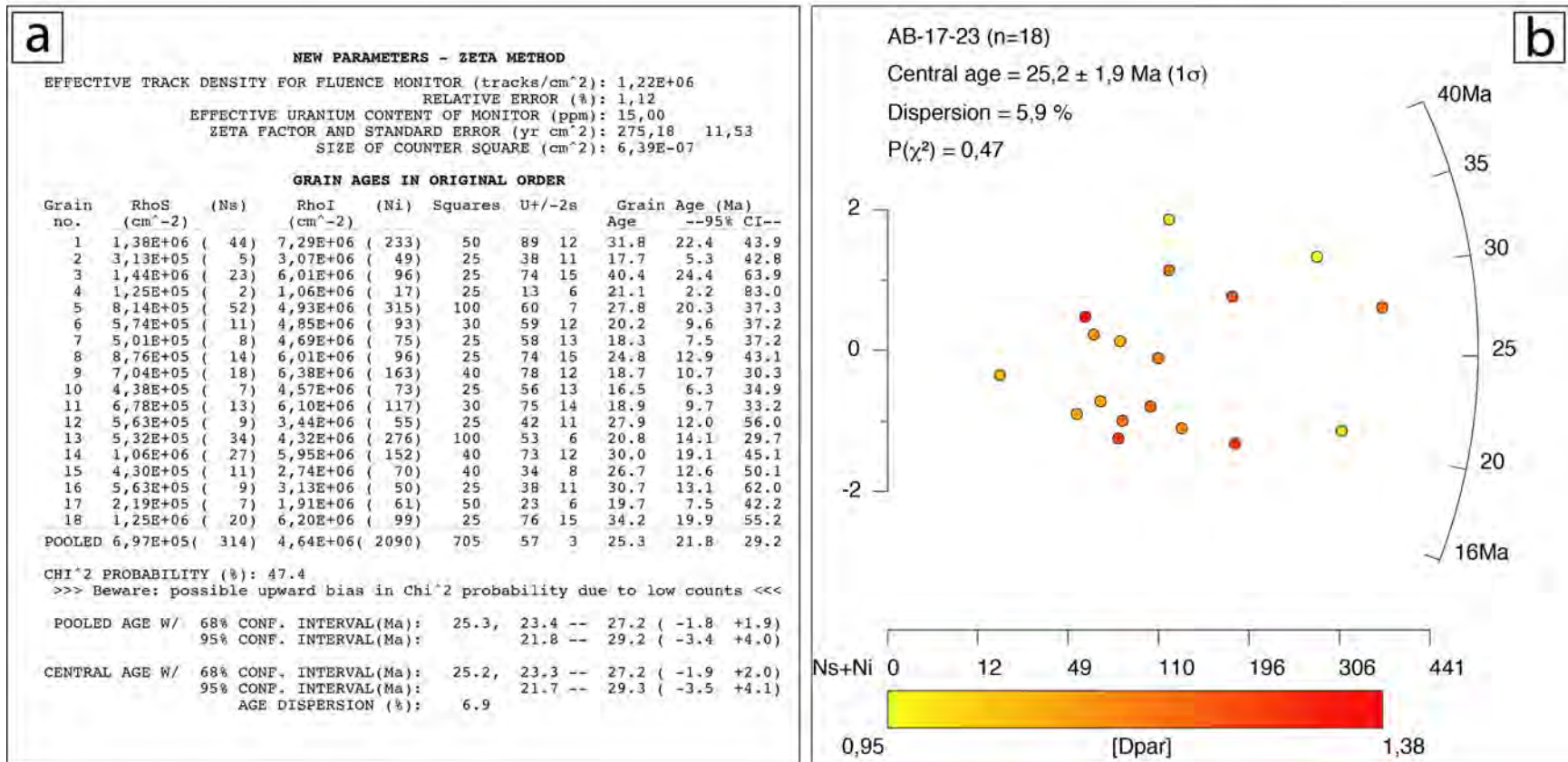


**Figure S11.** AFT single-grain data (a) and radial plots (b) for sample AB-17-23. See Figure S44 for location.

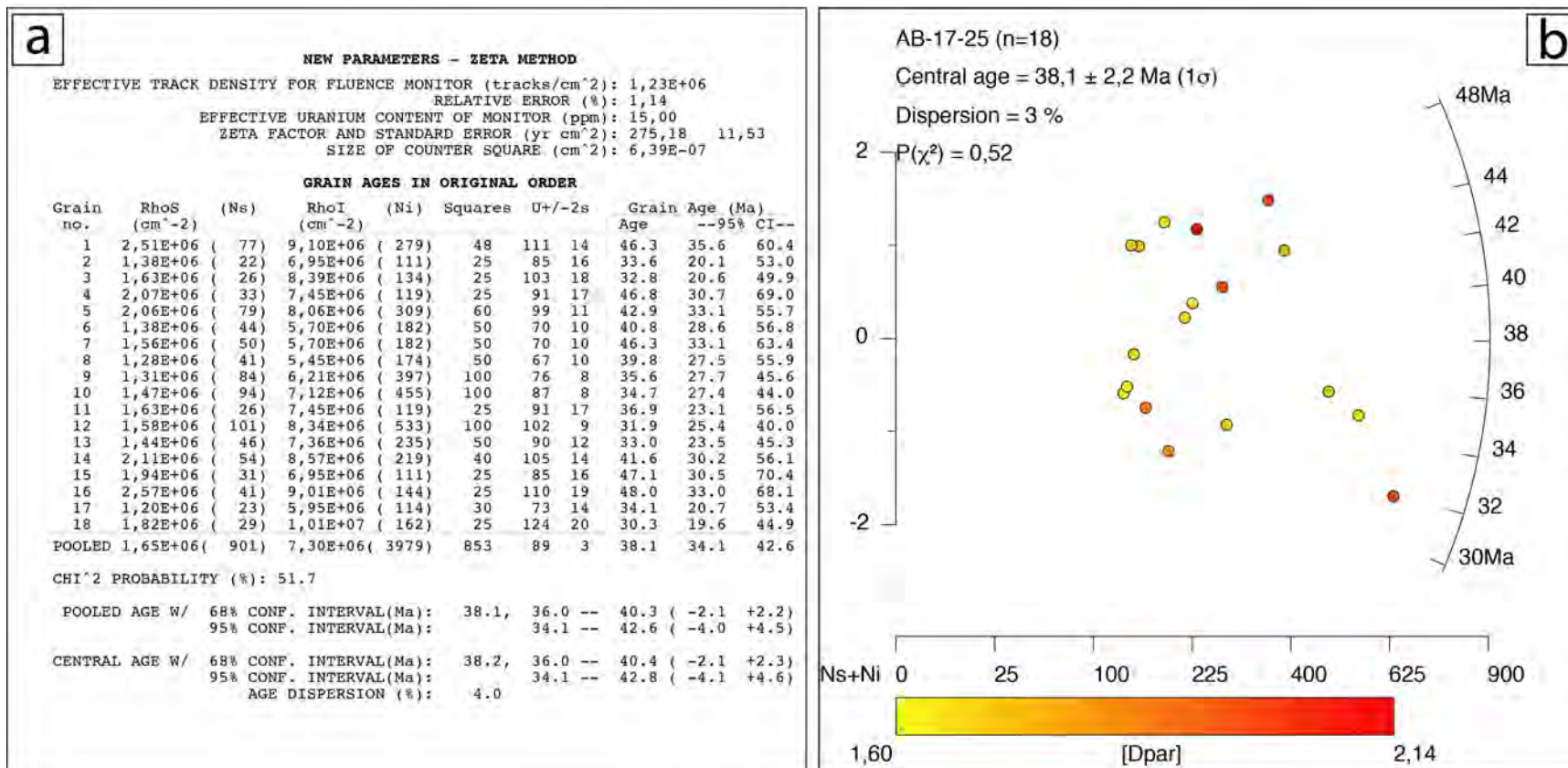


**Figure S12.** AFT single-grain data (a) and radial plots (b) for sample AB-17-25. See Figure S44 for location.

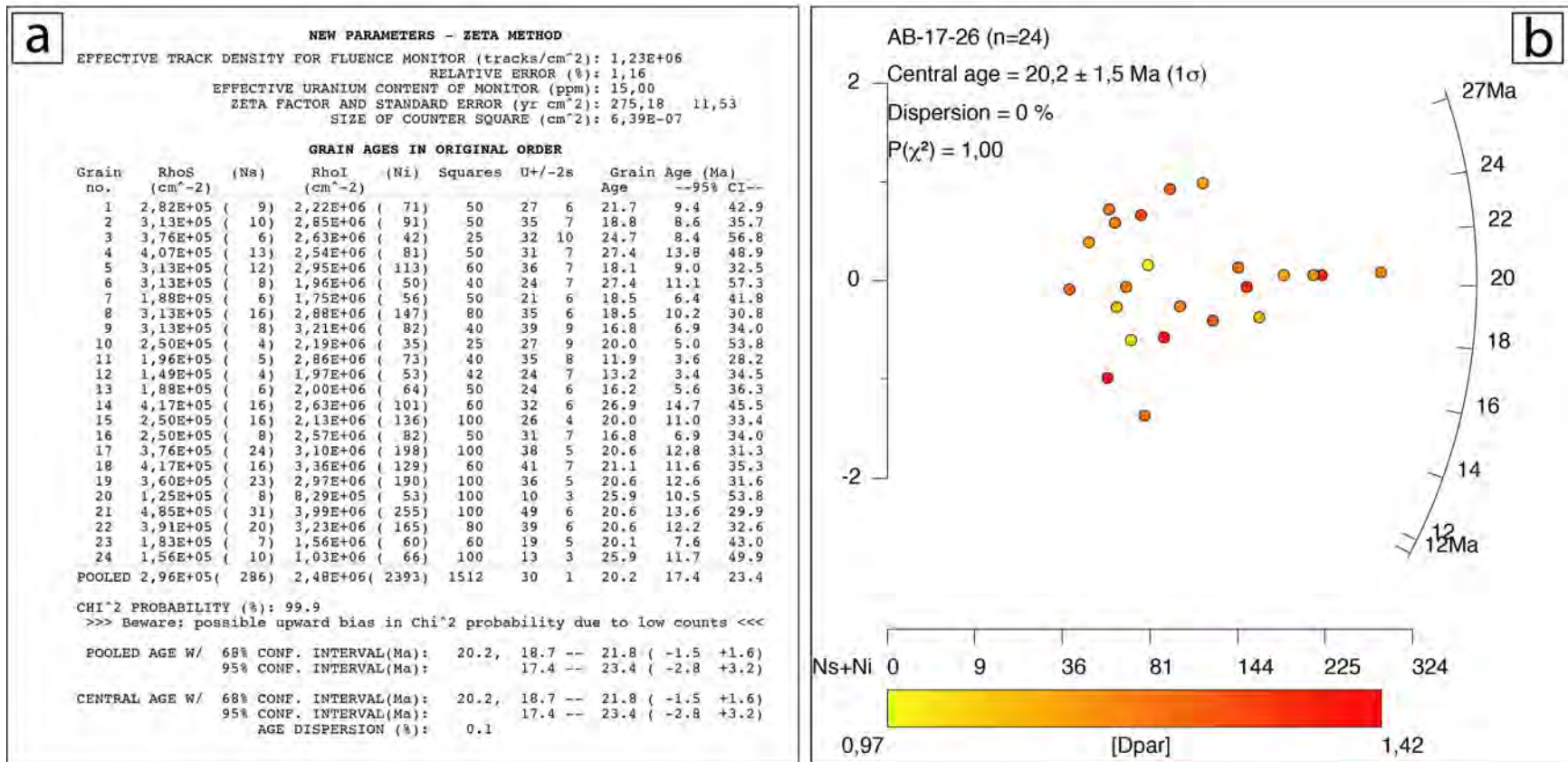


**Figure S13.** AFT single-grain data (a) and radial plots (b) for sample AB-17-26. See Figure S44 for location.

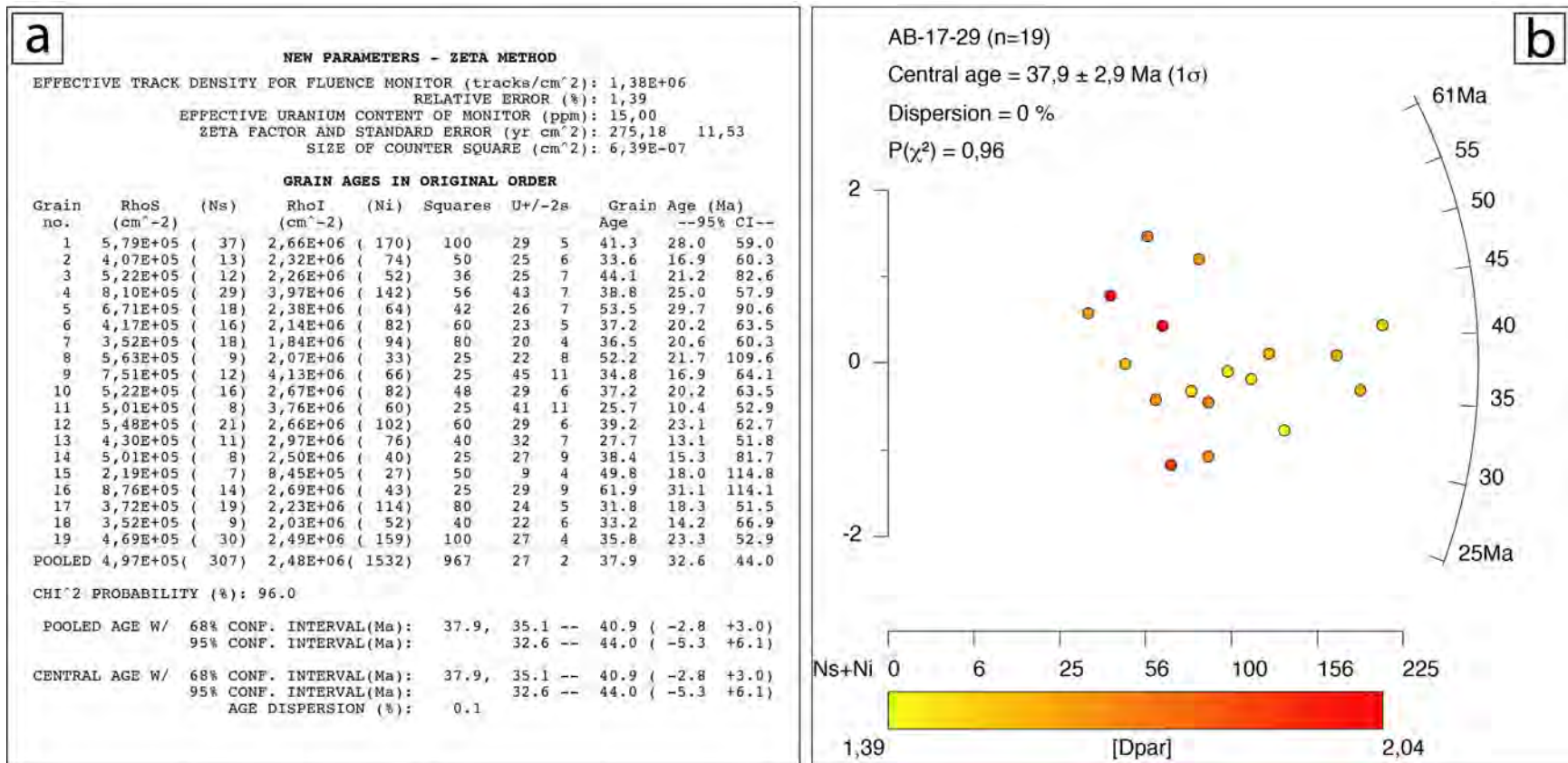


**Figure S14.** AFT single-grain data (a) and radial plots (b) for sample AB-17-29. See Figure S44 for location.

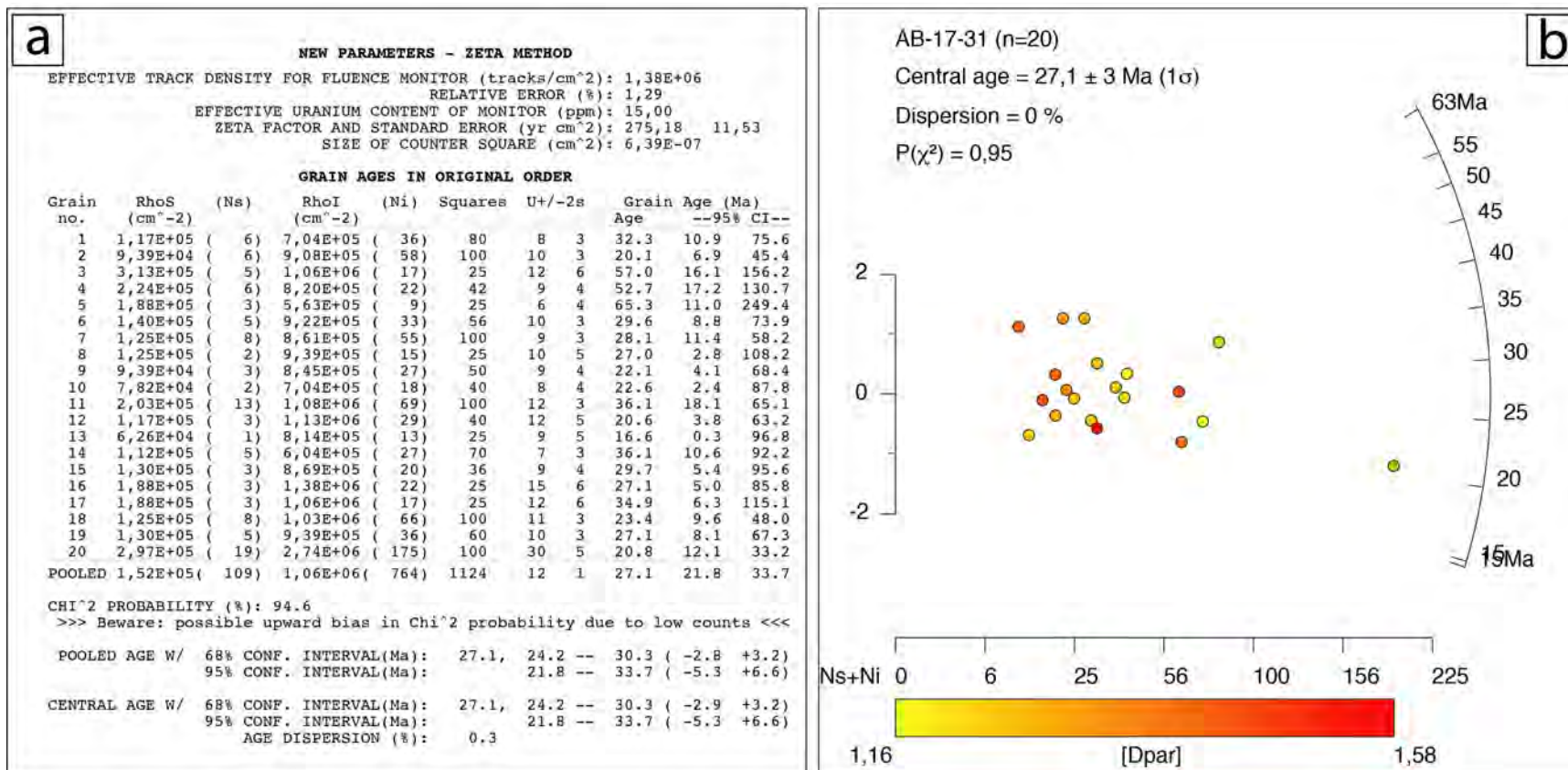


**Figure S15.** AFT single-grain data (a) and radial plots (b) for sample AB-17-31. See Figure S44 for location.

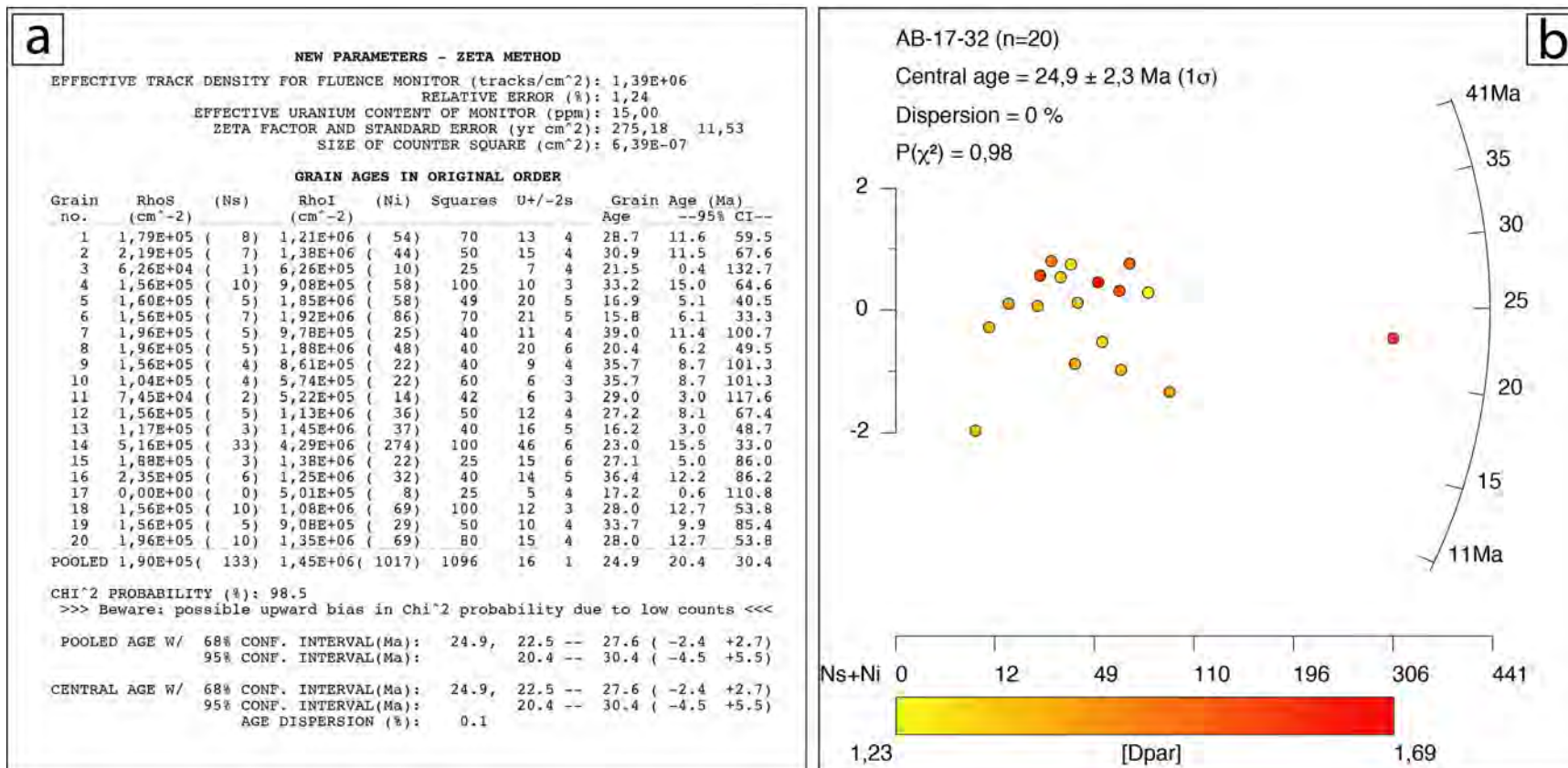


**Figure S16.** AFT single-grain data (a) and radial plots (b) for sample AB-17-32. See Figure S44 for location.

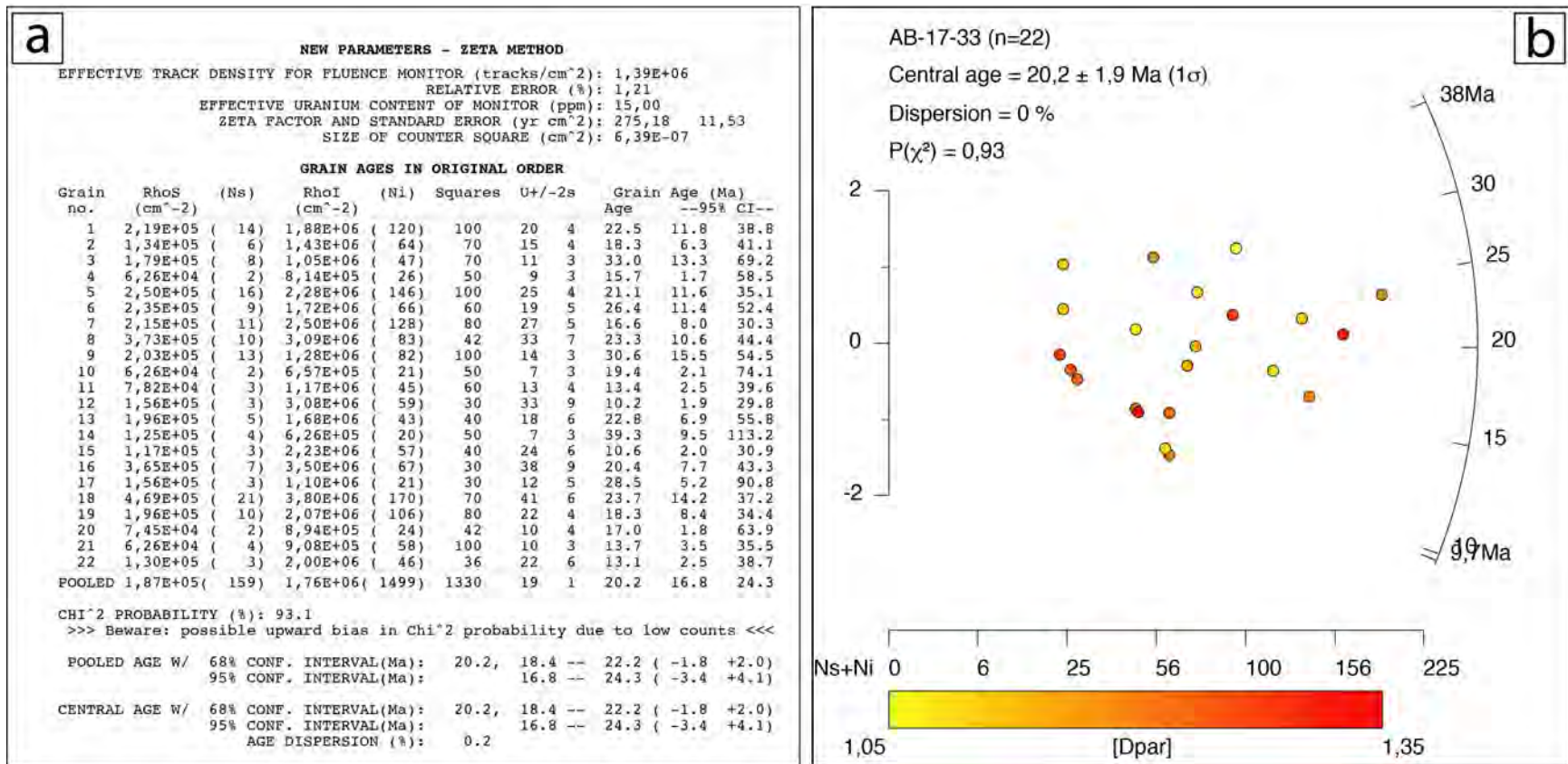


**Figure S17.** AFT single-grain data (a) and radial plots (b) for sample AB-17-33. See Figure S44 for location.



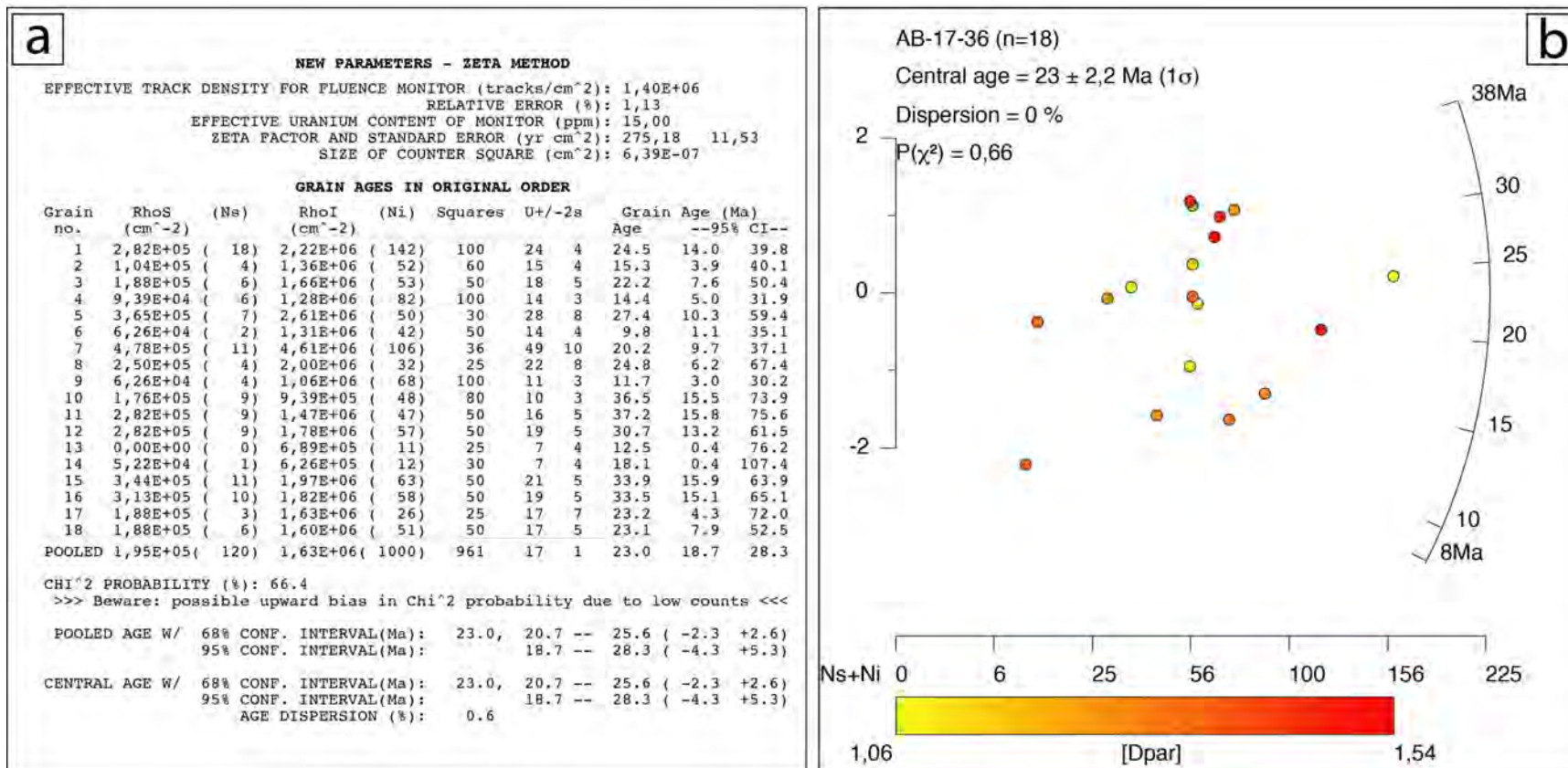


**Figure S18.** AFT single-grain data (a) and radial plots (b) for sample AB-17-36. See Figure S44 for location.

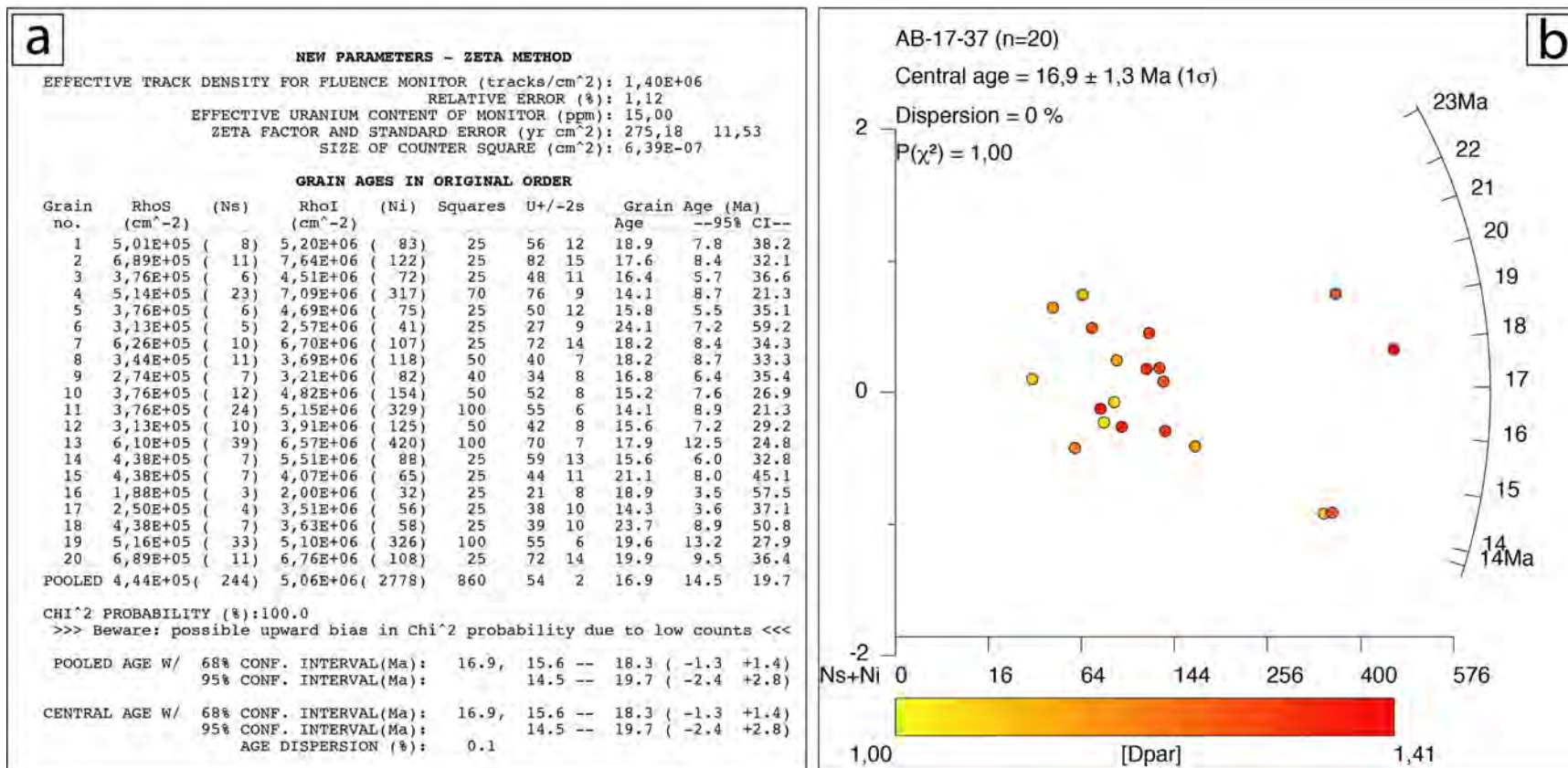


**Figure S19.** AFT single-grain data (a) and radial plots (b) for sample AB-17-37. See Figure S44 for location.

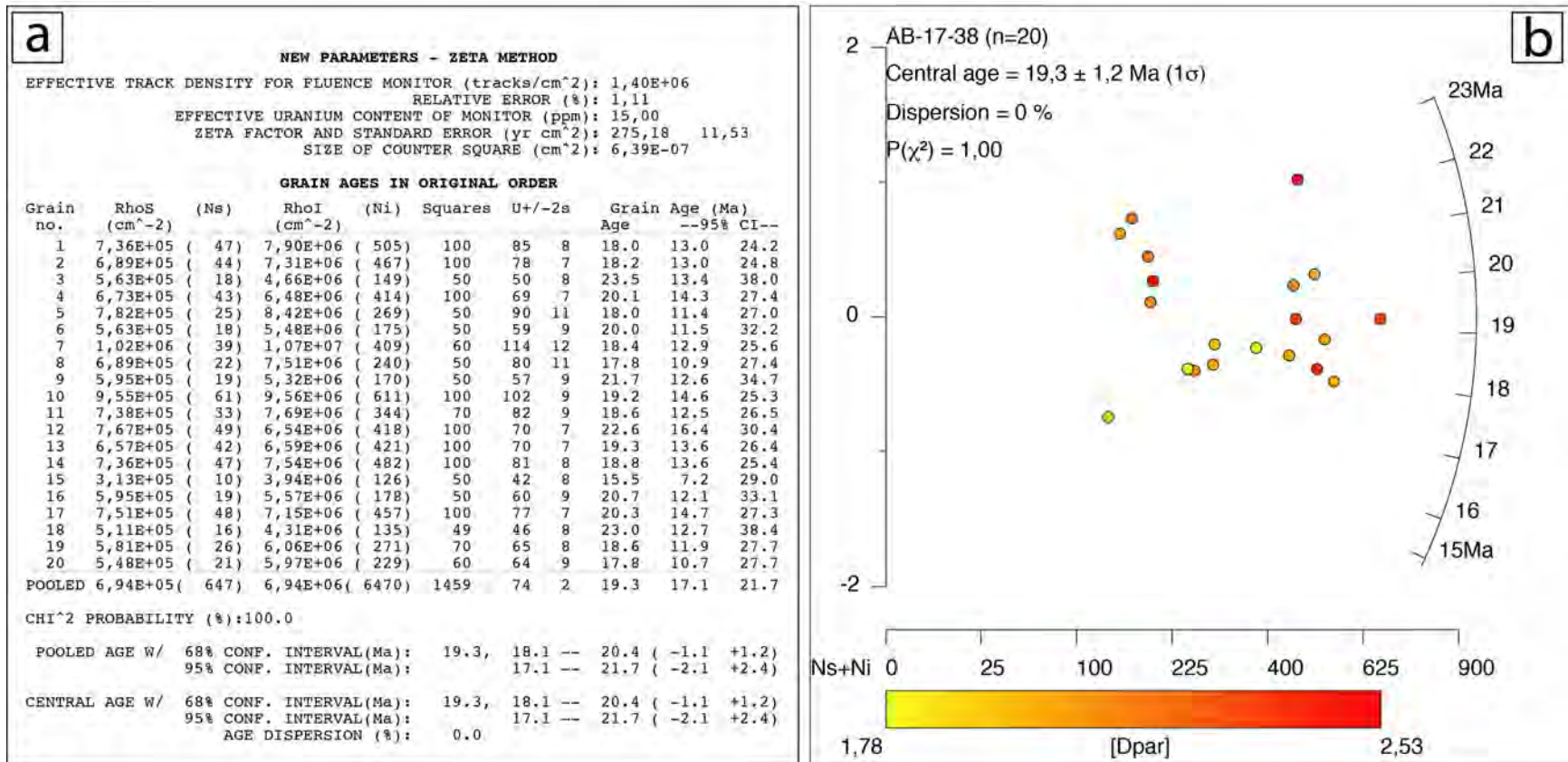


**Figure S20.** AFT single-grain data (a) and radial plots (b) for sample AB-17-38. See Figure S44 for location.

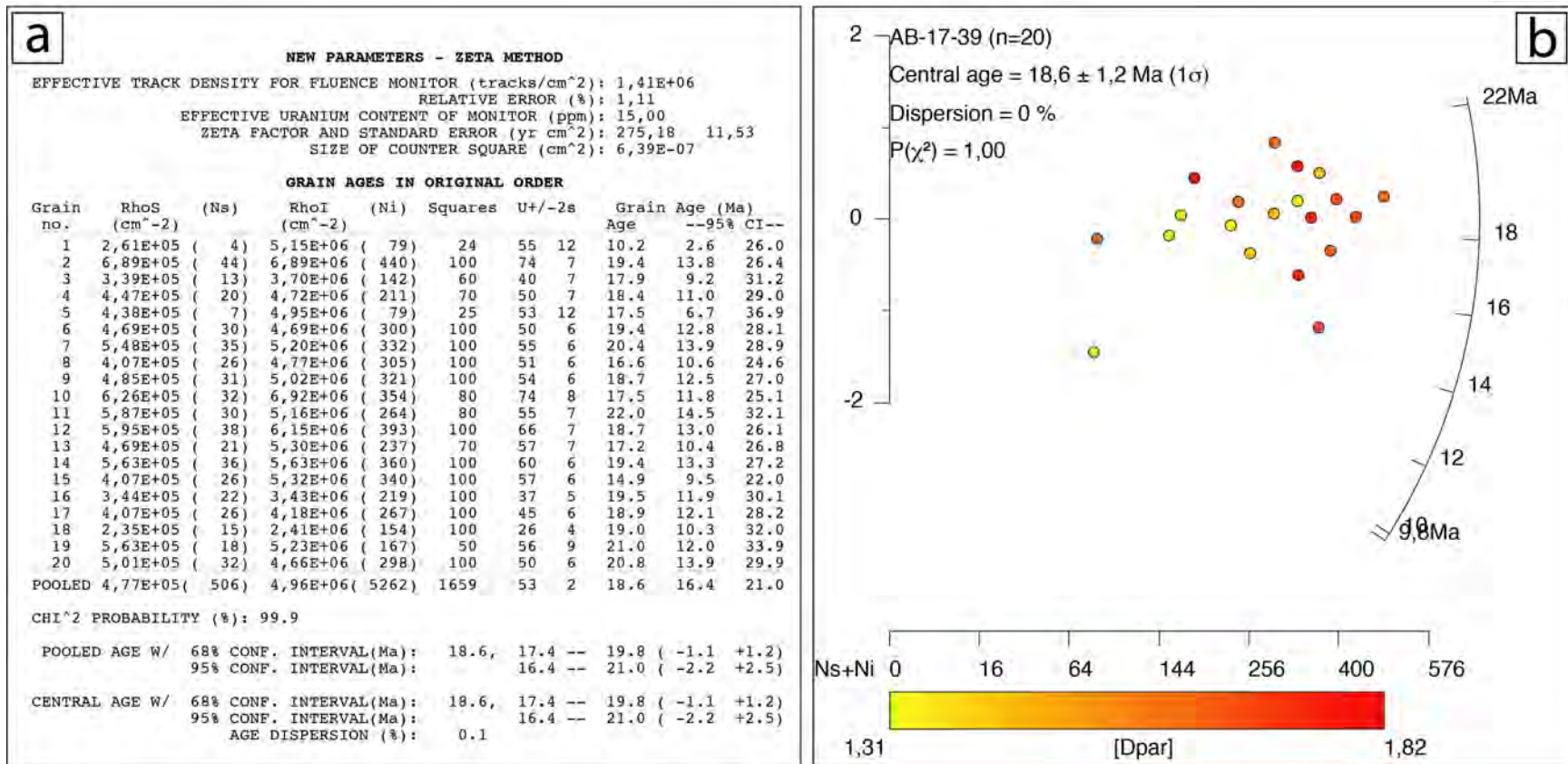


**Figure S21.** AFT single-grain data (a) and radial plots (b) for sample AB-17-39. See Figure S44 for location.

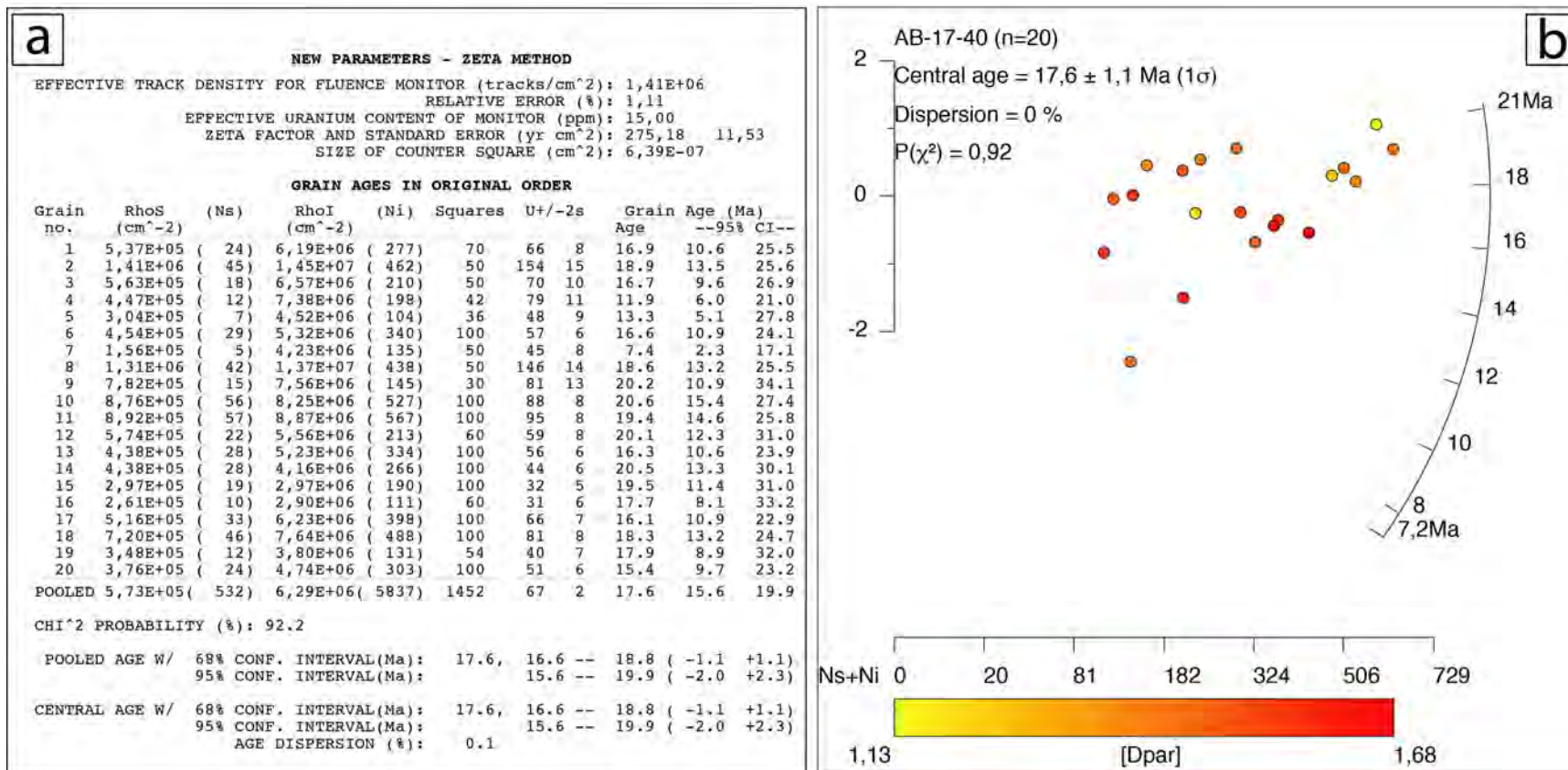


**Figure S22.** AFT single-grain data (a) and radial plots (b) for sample AB-17-40. See Figure S44 for location.

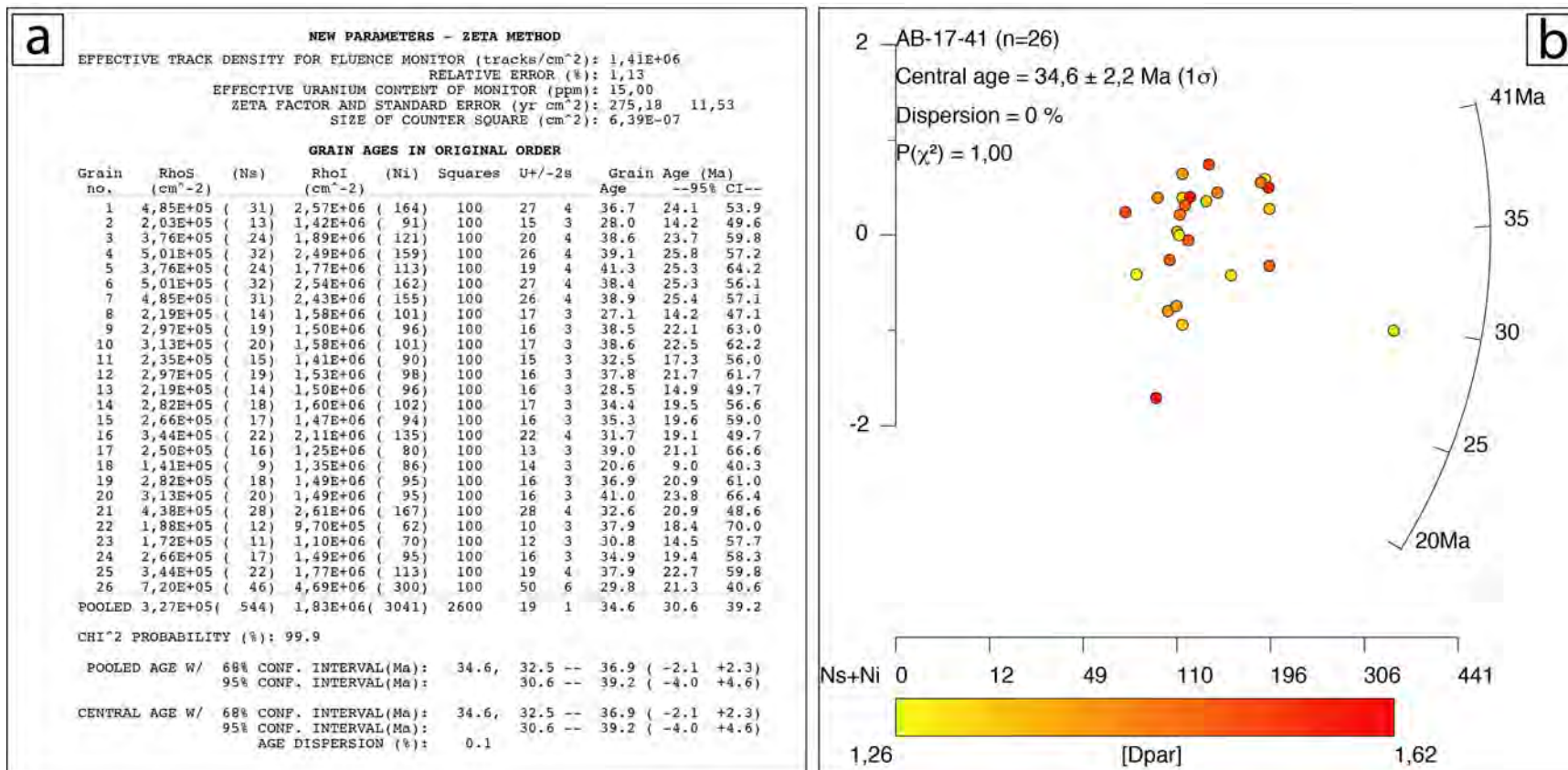


**Figure S23.** AFT single-grain data (a) and radial plots (b) for sample AB-17-41. See Figure S44 for location.

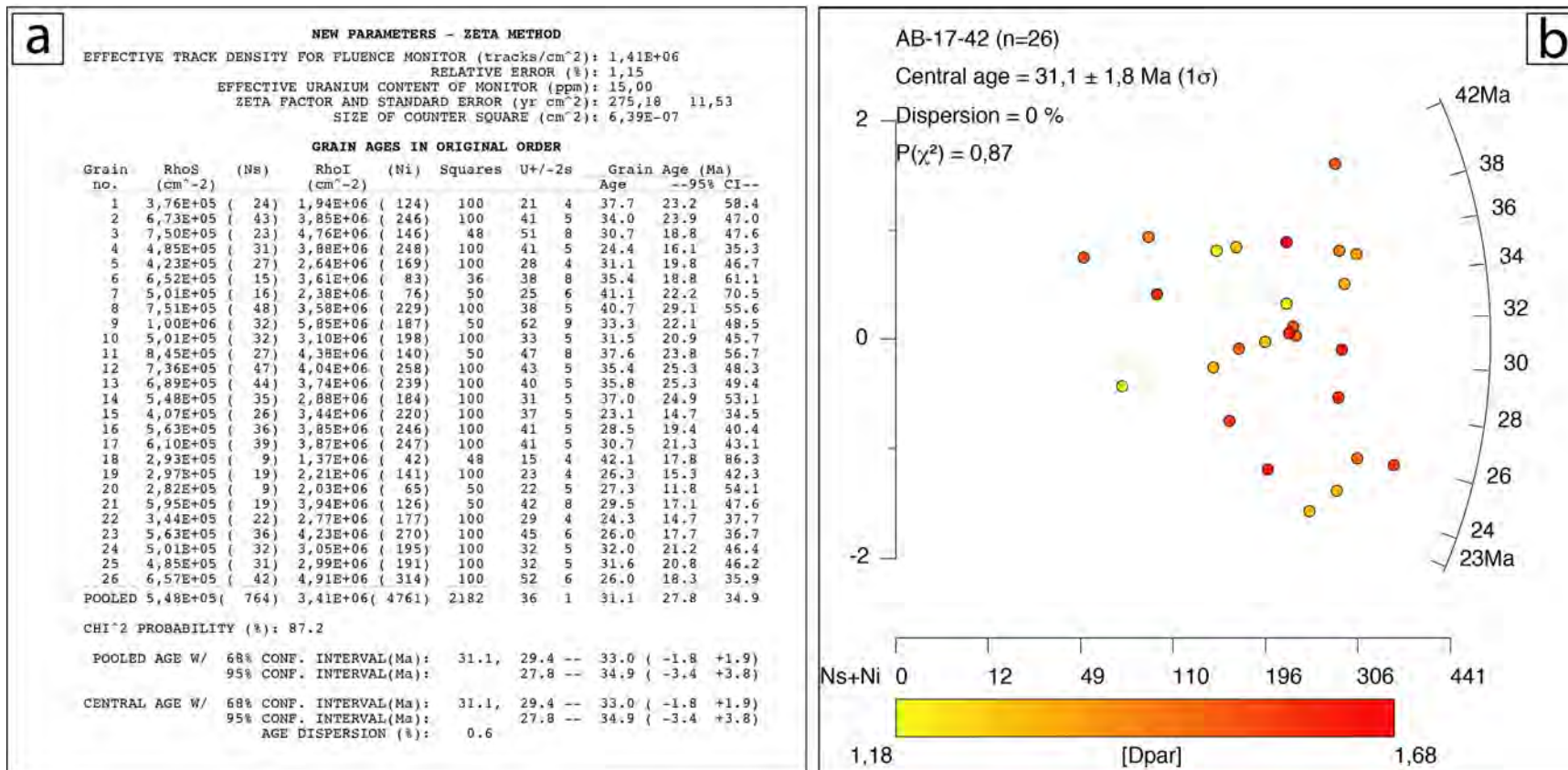


**Figure S24.** AFT single-grain data (a) and radial plots (b) for sample AB-17-42. See Figure S44 for location.

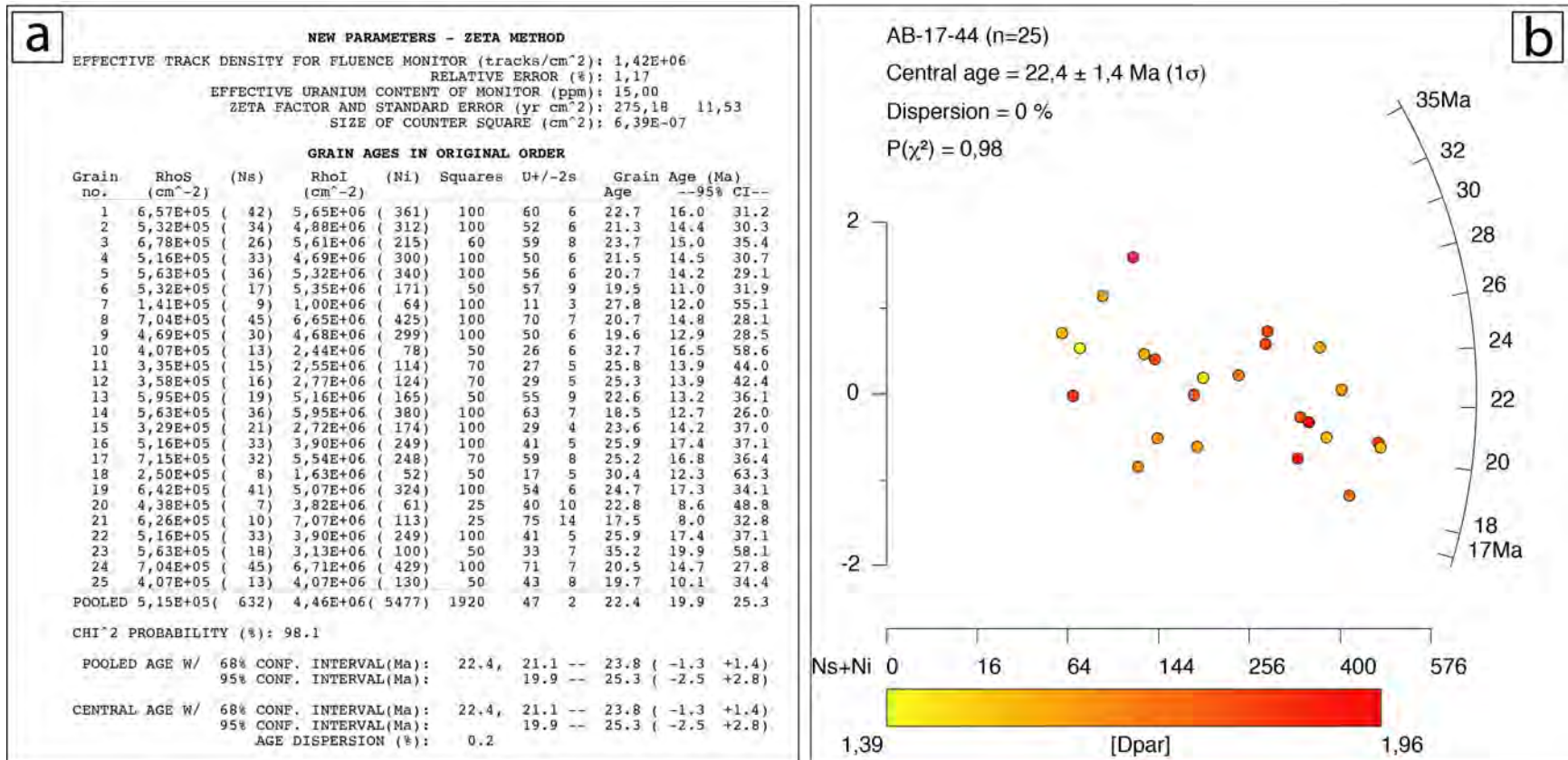


**Figure S25.** AFT single-grain data (a) and radial plots (b) for sample AB-17-44. See Figure S44 for location.



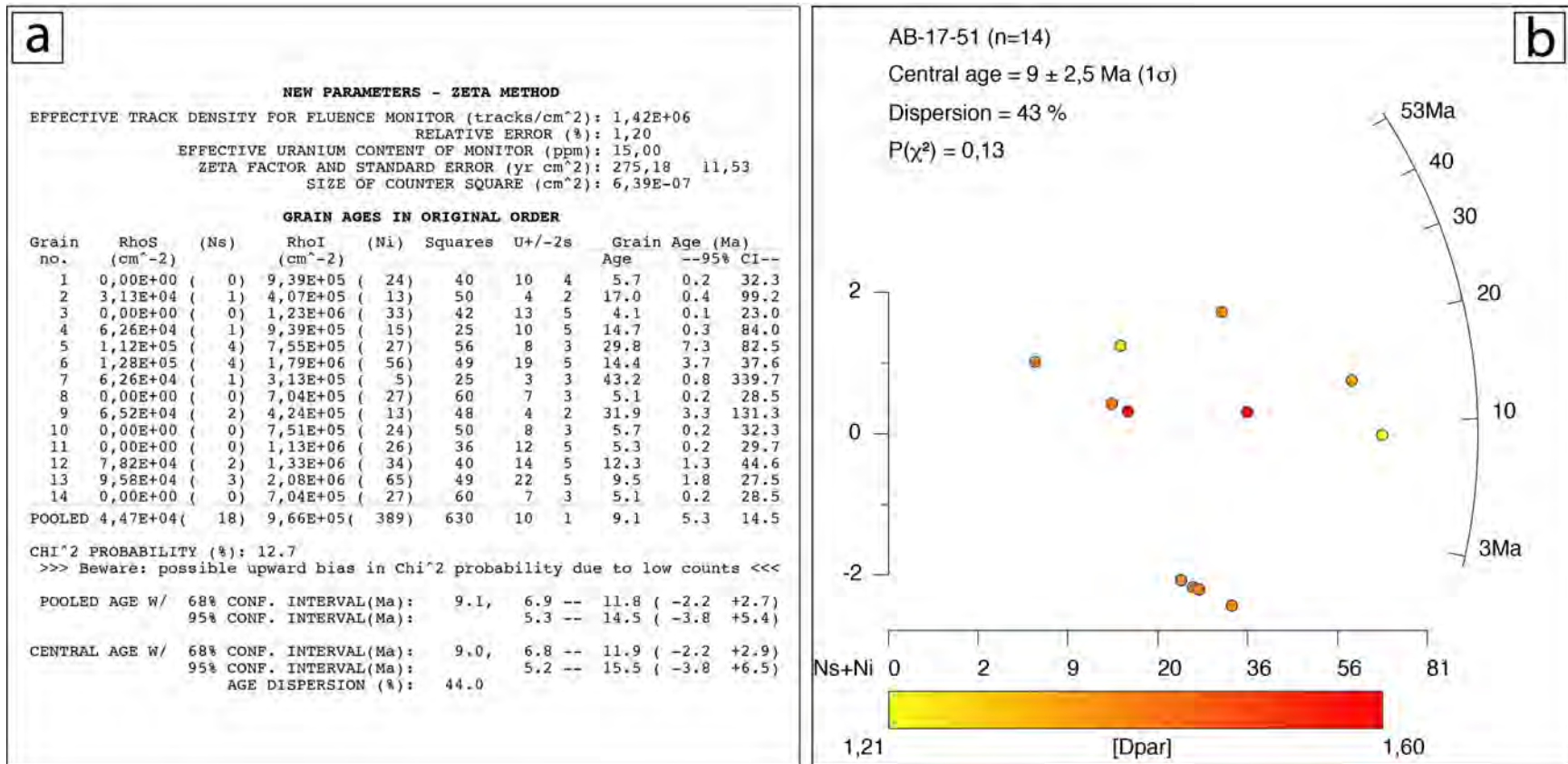


**Figure S26.** AFT single-grain data (a) and radial plots (b) for sample AB-17-51. See Figure S44 for location.

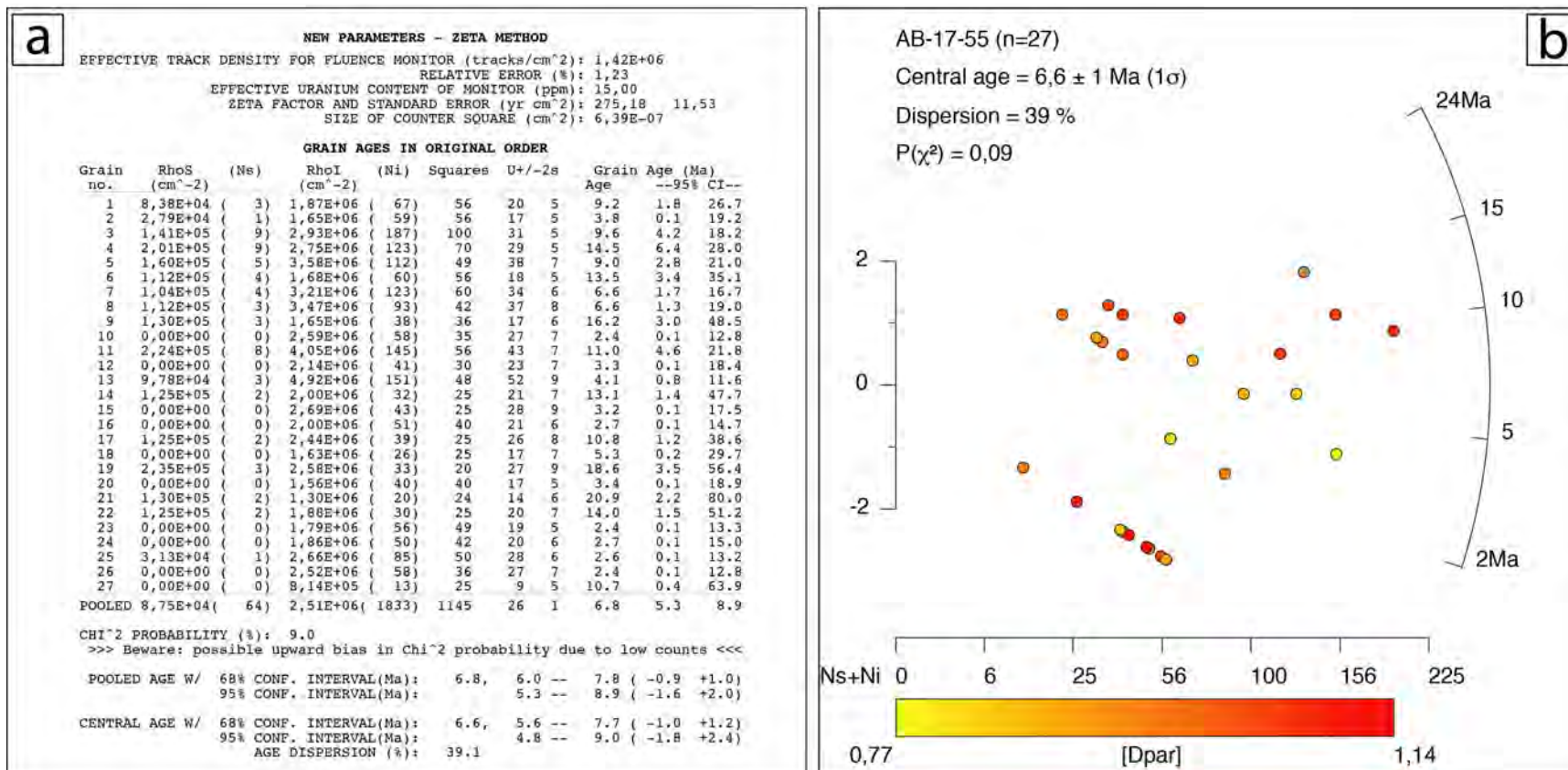


**Figure S27.** AFT single-grain data (a) and radial plots (b) for sample AB-17-55. See Figure S44 for location.

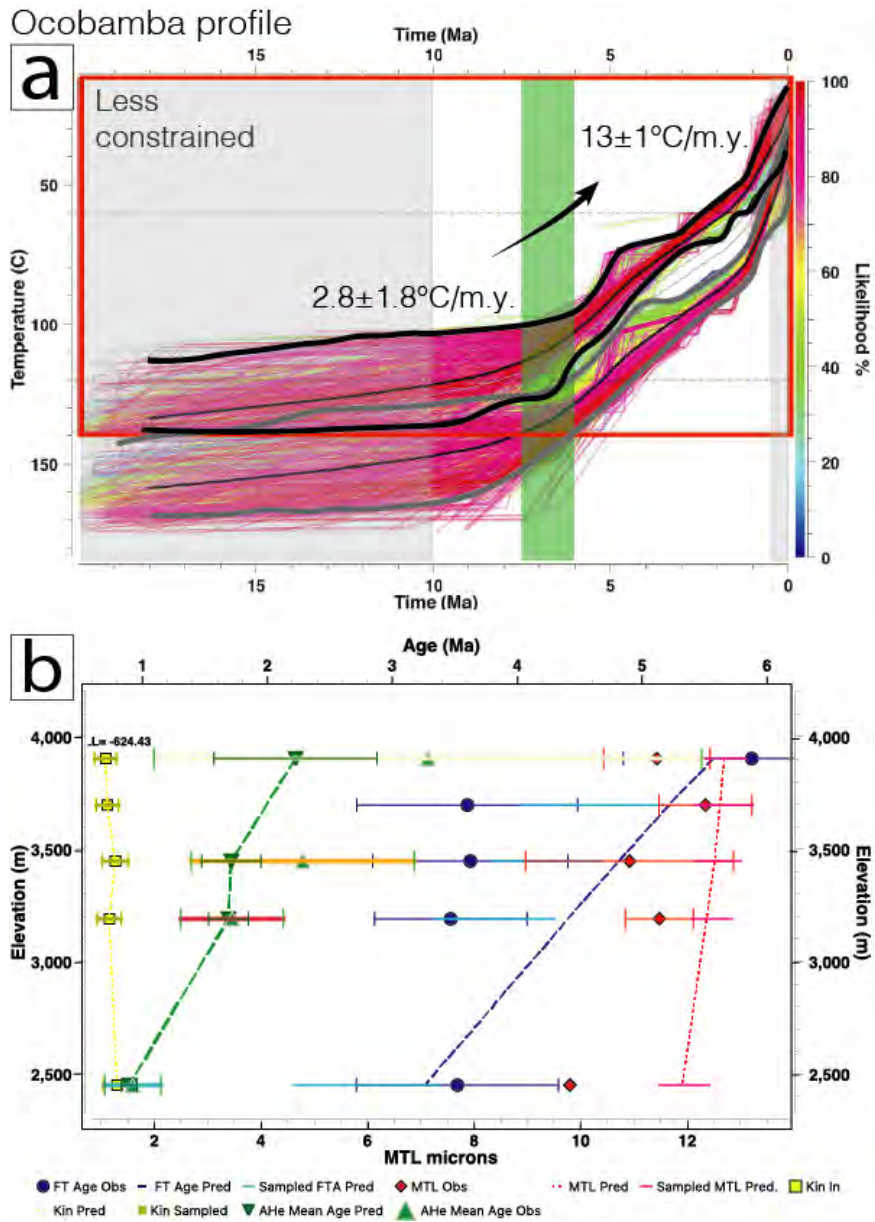


**Figure S28.** QTQt inversion results for the Ocobamba high-altitudinal profile. a) Time-temperature paths obtained by inversion of AHe and AFT thermochronology data from the Ocobamba age-elevation profile using QTQt (AB-17-05 to AB-17-11). The red square shows the explored time and temperature range for inversion. The colored lines show the T-t paths for the top and the bottom samples with their respective likelihood (see color scale on right). The solid black and grey lines show the expected model and its 95% reliable interval for the thermal histories of the top and bottom samples, respectively. The grey lines in between represent the expected cooling paths for the intermediate samples. The green vertical band indicates the well-constrained acceleration of cooling at ~6.5 Ma. Cooling rates derived from QTQt are indicated on the graph. b) Graph of observed vs. predicted data. Fit of best-fit model predictions to the data. FT: Fission Track; MTL: Mean Track Length; AHe: Apatite Helium; Obs: Observed; Pred: Predicted.

AB-17-13

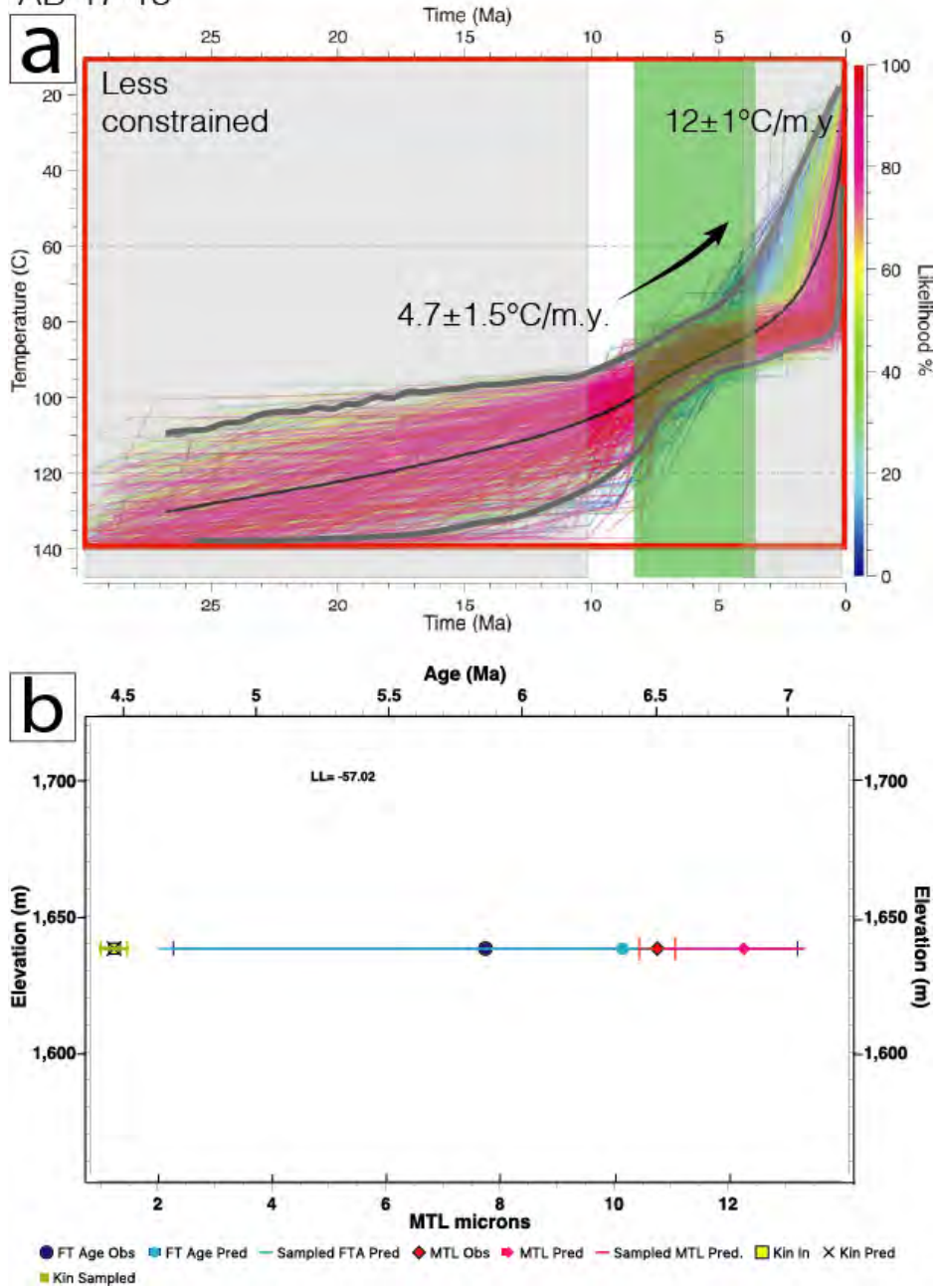


**Figure S29.** QTQt inversion results for the AB-17-13 sample. a) Time-temperature paths obtained by inversion of AFT data from the AB-17-13 sample using QTQt. The red square shows the explored time and temperature range for inversion. The colored lines show the T-t paths for the unique sample with its respective likelihood (see color scale on right). The solid grey lines show the expected model and its 95% reliable interval for the thermal histories of the sample. The green vertical band indicates the well-constrained acceleration of cooling at ~6 Ma. Cooling rates derived from QTQt are indicated on the graph. The apparent ~3–2 Ma cooling acceleration is a model bias and is not constrained by the data. b) Graph of observed vs. predicted data. Fit of best-fit model predictions to the data. FT: Fission Track; MTL: Mean Track Length; Obs: Observed; Pred: Predicted.

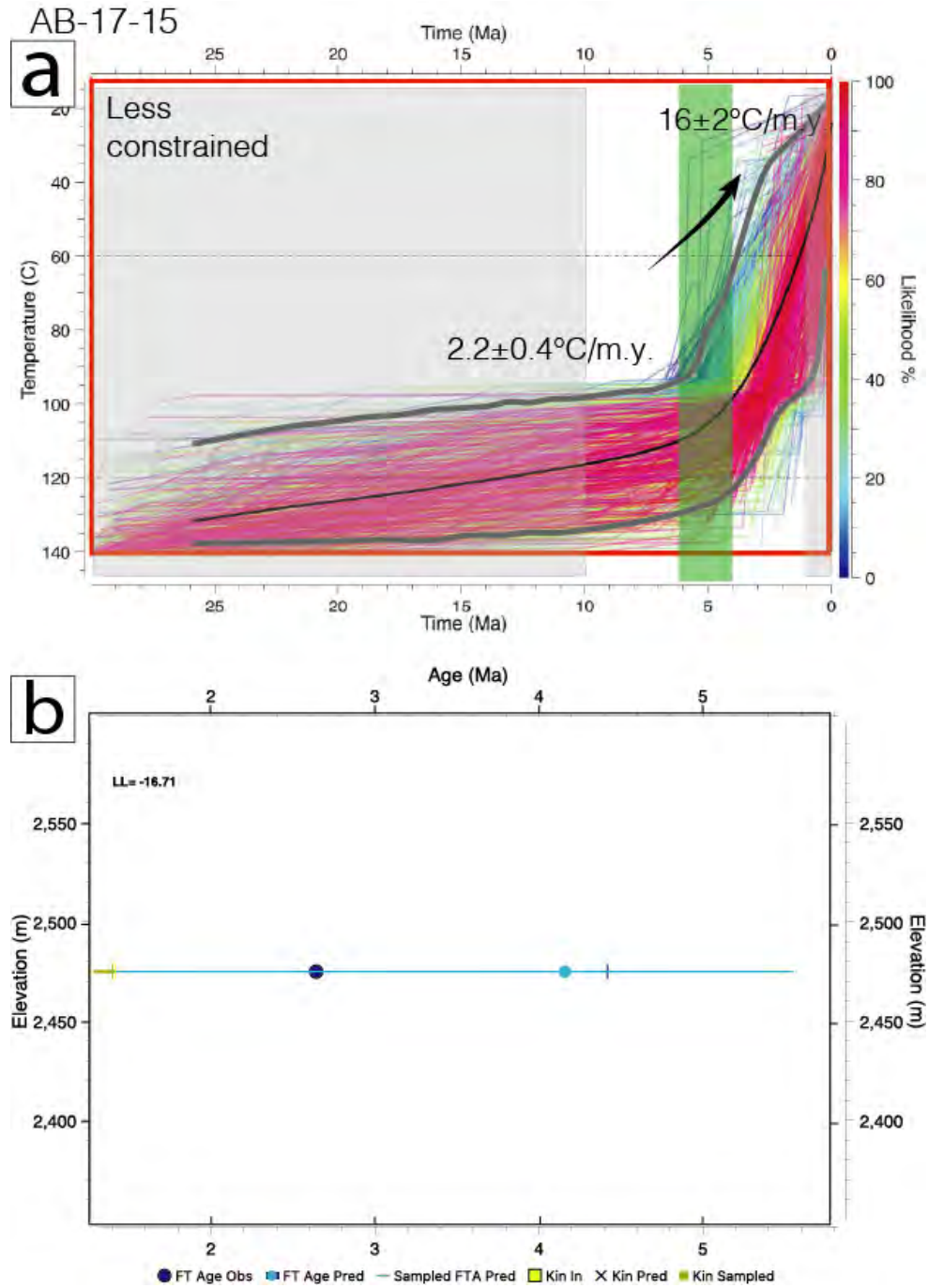


**Figure S30.** QTQt inversion results for the AB-17-15 sample. a) Time-temperature paths obtained by inversion of AFT data from the AB-17-15 sample using QTQt. The red square shows the explored time and temperature range for inversion. The colored lines show the T-t paths for the unique sample with its respective likelihood (see color scale on right). The solid grey lines show the expected model and its 95% reliable interval for the thermal histories of the sample. The green vertical band indicates the well-constrained acceleration of cooling at ~5 Ma. Cooling rates derived from QTQt are indicated on the graph. b) Graph of observed vs. predicted data. Fit of best-fit model predictions to the data. FT: Fission Track; Obs: Observed; Pred: Predicted.

AB-17-18

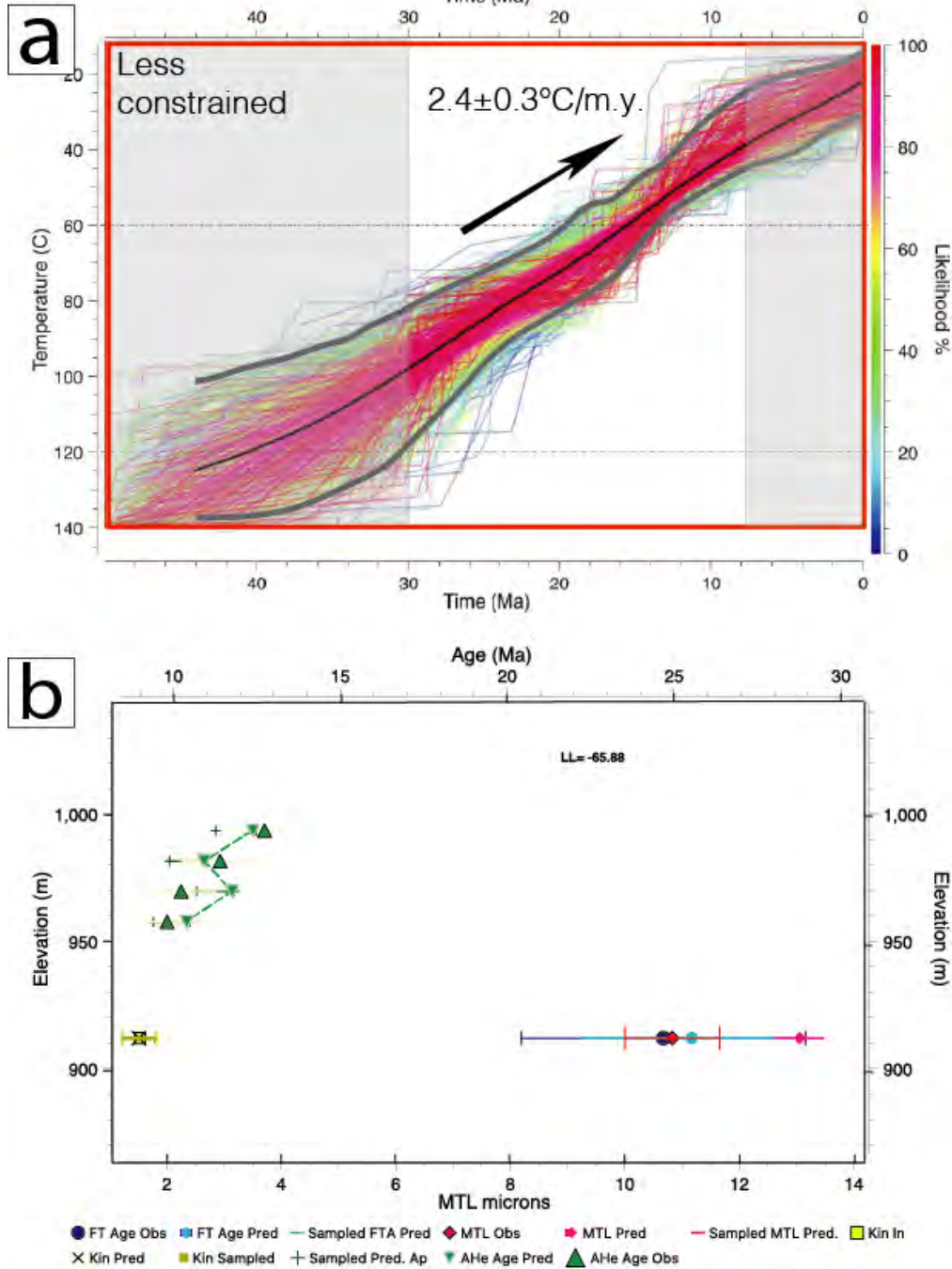


**Figure S31.** QTQt inversion results for the AB-17-18 sample. a) Time-temperature paths obtained by inversion of AHe and AFT data from the AB-17-18 sample using QTQt. The red square shows the explored time and temperature range for inversion. The colored lines show the T-t paths for the unique sample with its respective likelihood (see color scale on right). The solid grey lines show the expected model and its 95% reliable interval for the thermal histories of the sample. Cooling rate derived from QTQt is indicated on the graph. b) Graph of observed vs. predicted data. Fit of best-fit model predictions to the data. FT: Fission Track; MTL: Mean Track Length; AHe: Apatite Helium; Obs: Observed; Pred: Predicted.

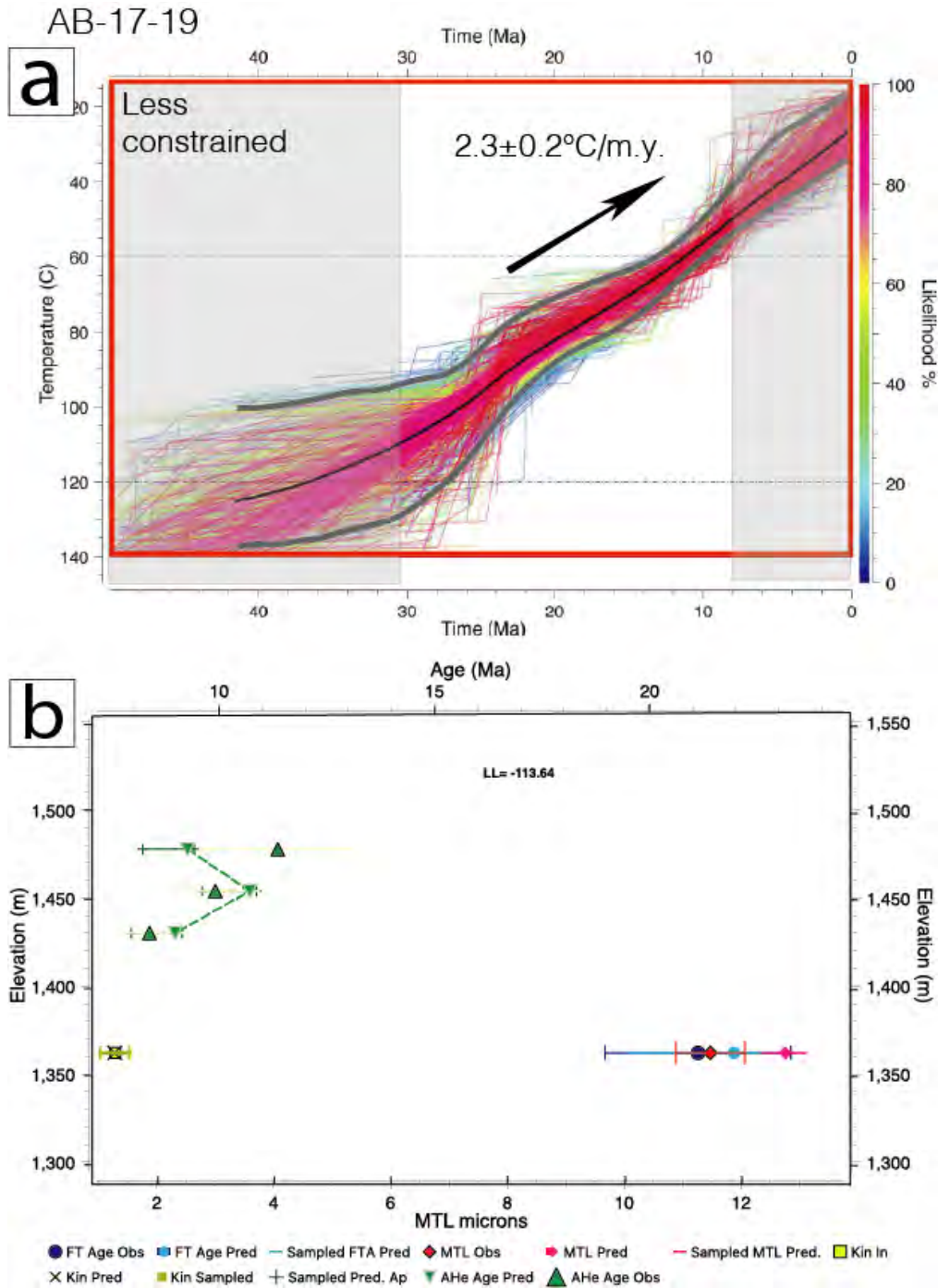


**Figure S32.** QTQt inversion results for the AB-17-19 sample. a) Time-temperature paths obtained by inversion of AHe and AFT data from the AB-17-19 sample using QTQt. The red square shows the explored time and temperature range for inversion. The colored lines show the T-t paths for the unique sample with its respective likelihood (see color scale on right). The solid grey lines show the expected model and its 95% reliable interval for the thermal histories of the sample. Cooling rate derived from QTQt is indicated on the graph. b) Graph of observed vs. predicted data. Fit of best-fit model predictions to the data. FT: Fission Track; MTL: Mean Track Length; AHe: Apatite Helium; Obs: Observed; Pred: Predicted.

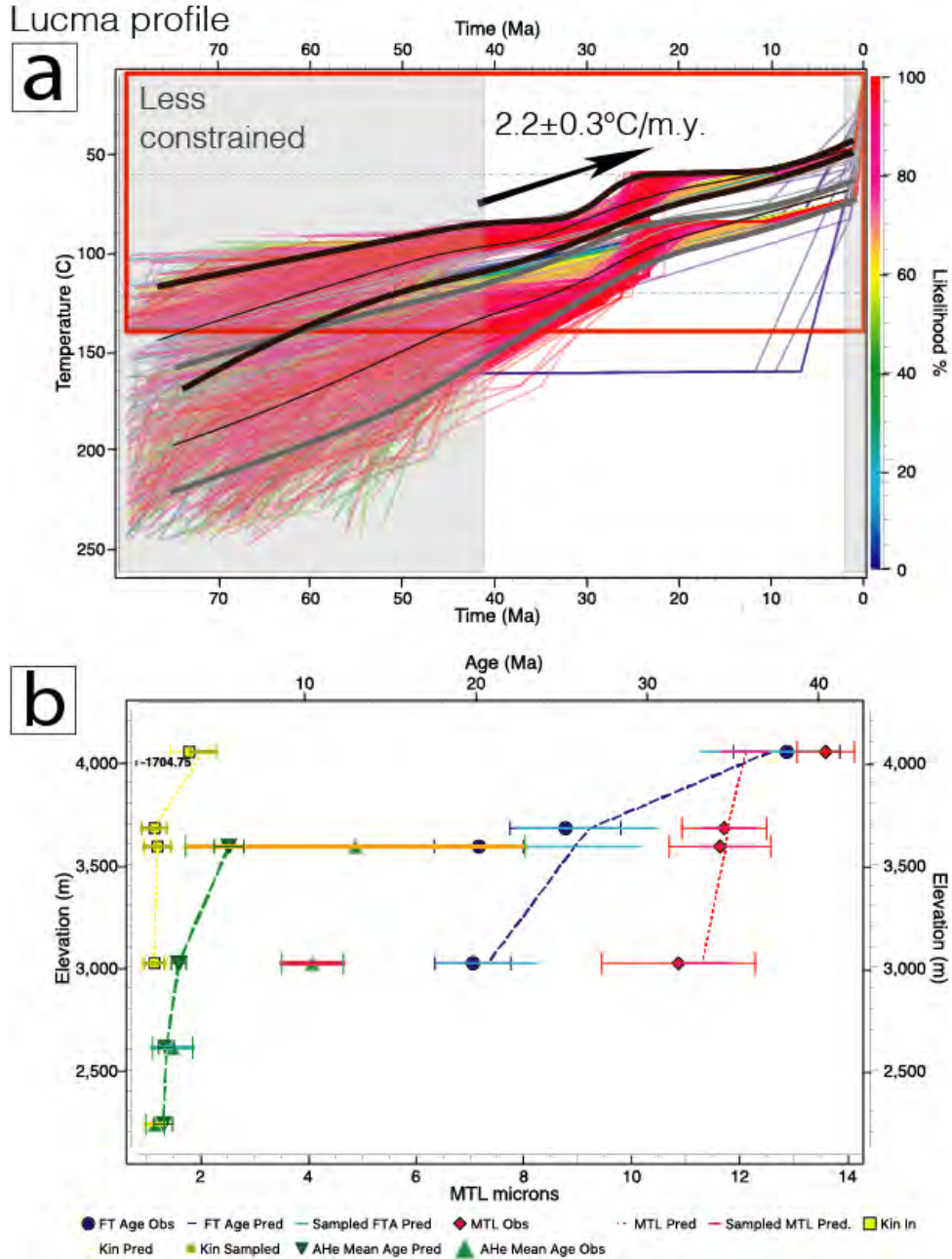


**Figure S33.** QTQt inversion results for the Lucma high-altitudinal profile. a) Time-temperature paths obtained by inversion of AHe and AFT thermochronology data from the Lucma age-elevation profile using QTQt (AB-17-21 to AB-17-28). The red square shows the explored time and temperature range for inversion. The colored lines show the T-t paths for the top and the bottom samples with their respective likelihood (see color scale on right). The solid black and grey lines show the expected model and its 95% reliable interval for the thermal histories of the top and bottom samples, respectively. The grey lines in between represent the expected cooling paths for the intermediate samples. Cooling rate derived from QTQt is indicated on the graph. b) Graph of observed vs. predicted data. Fit of best-fit model predictions to the data. FT: Fission Track; MTL: Mean Track Length; AHe: Apatite Helium; Obs: Observed; Pred: Predicted.



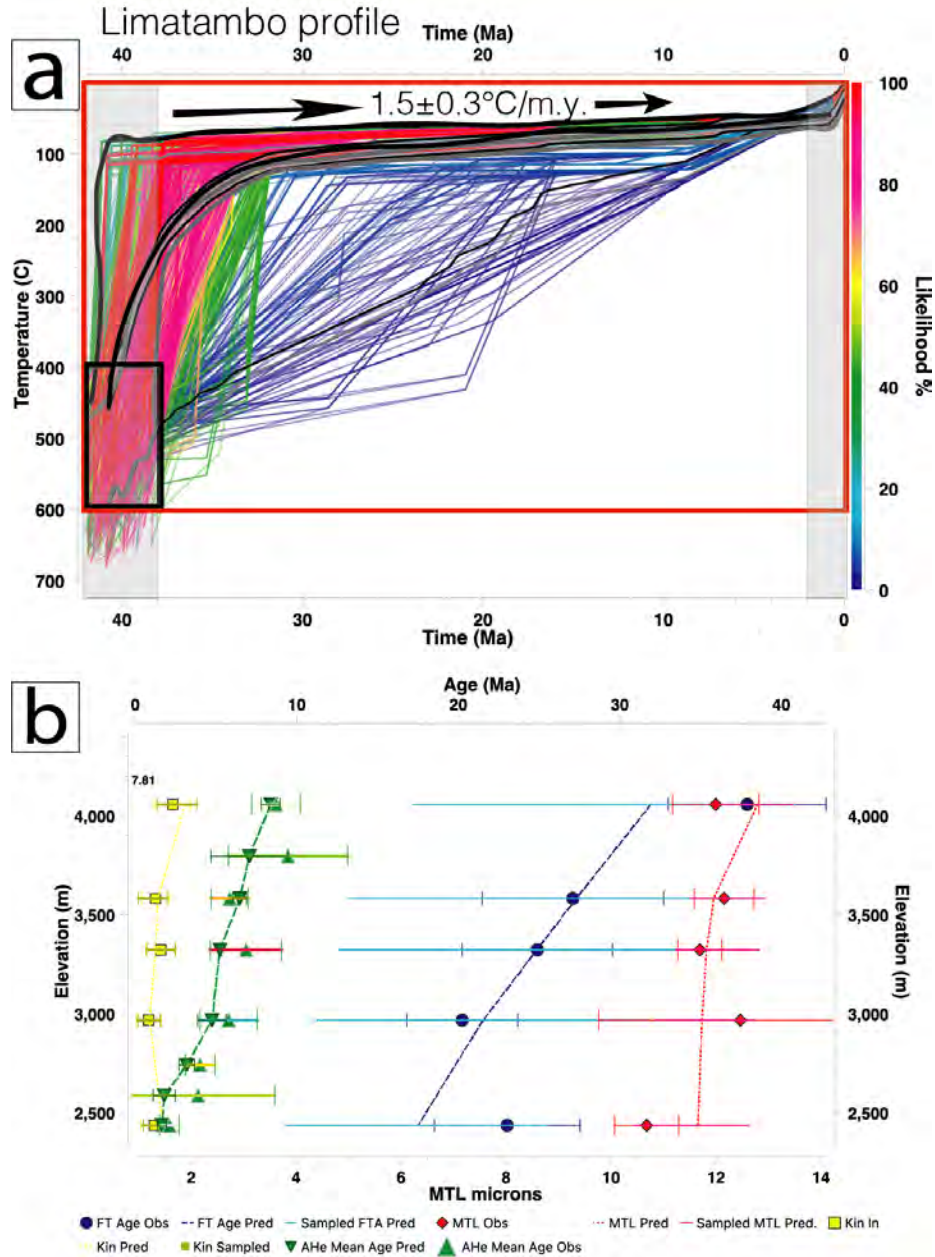


**Figure S34.** QTQt inversion results for the Limatambo high-altitudinal profile. a) Time-temperature paths obtained by inversion of AHe and AFT thermochronology data from the Limatambo age-elevation profile using QTQt (AB-17-29 to AB-17-36). The red square shows the explored time and temperature range for inversion. The black square corresponds to the pluton emplacement age and temperature constraints (Table S1). The colored lines show the T-t paths for the top and the bottom samples with their respective likelihood (see color scale on right). The solid black and grey lines show the expected model and its 95% reliable interval for the thermal histories of the top and bottom samples, respectively. The grey lines in between represent the expected cooling paths for the intermediate samples. Cooling rate derived from QTQt is indicated on the graph. b) Graph of observed vs. predicted data. Fit of best-fit model predictions to the data. FT: Fission Track; MTL: Mean Track Length; AHe: Apatite Helium; Obs: Observed; Pred: Predicted.

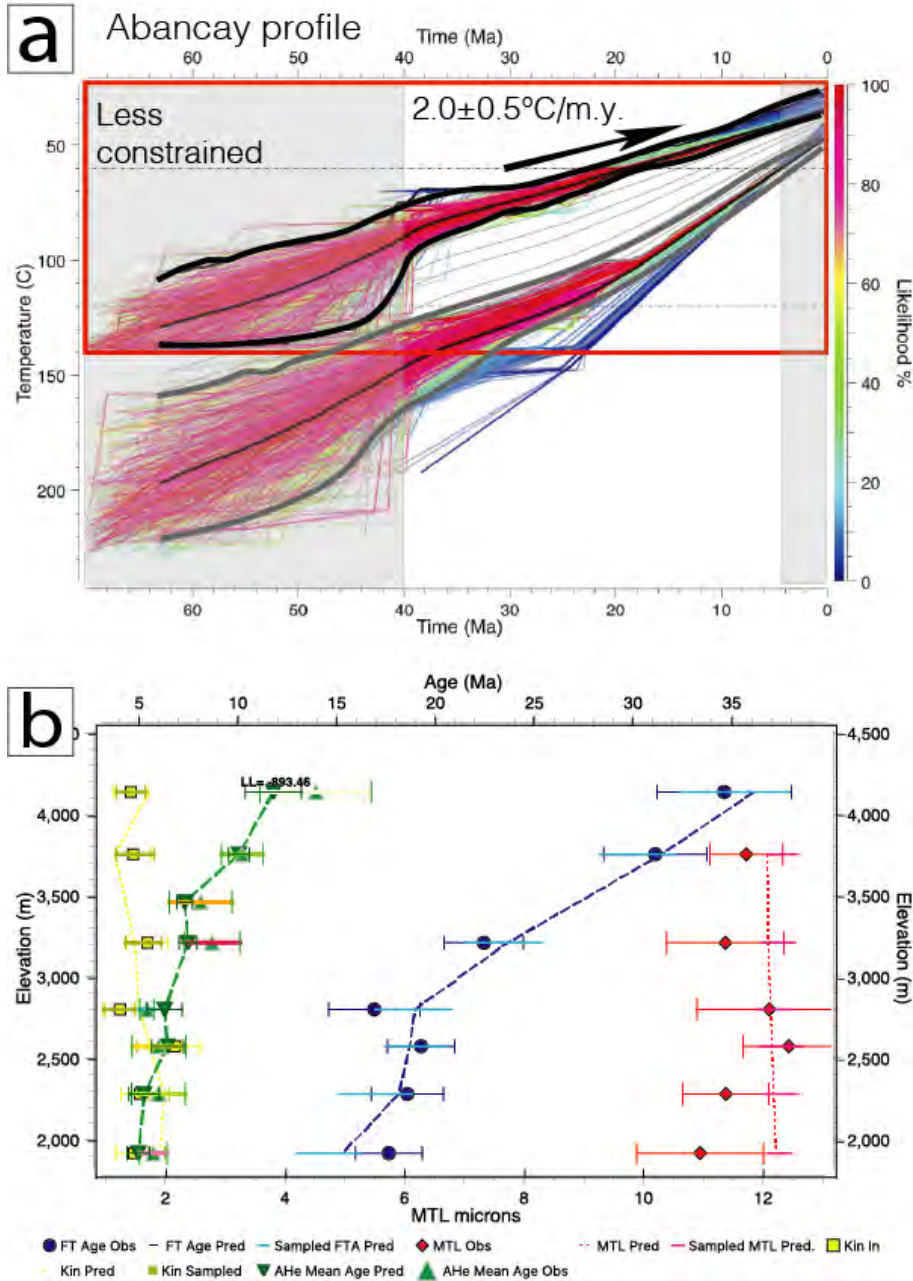


**Figure S35.** QTQt inversion results for the Abancay high-altitudinal profile. a) Time-temperature paths obtained by inversion of AHe and AFT thermochronology data from the Abancay age-elevation profile using QTQt (AB-17-37 to AB-17-44). The red square shows the explored time and temperature range for inversion. The colored lines show the T-t paths for the top and the bottom samples with their respective likelihood (see color scale on right). The solid black and grey lines show the expected model and its 95% reliable interval for the thermal histories of the top and bottom samples, respectively. The grey lines in between represent the expected cooling paths for the intermediate samples. Cooling rate derived from QTQt is indicated on the graph. b) Graph of observed vs. predicted data. Fit of best-fit model predictions to the data. FT: Fission Track; MTL: Mean Track Length; AHe: Apatite Helium; Obs: Observed; Pred: Predicted.

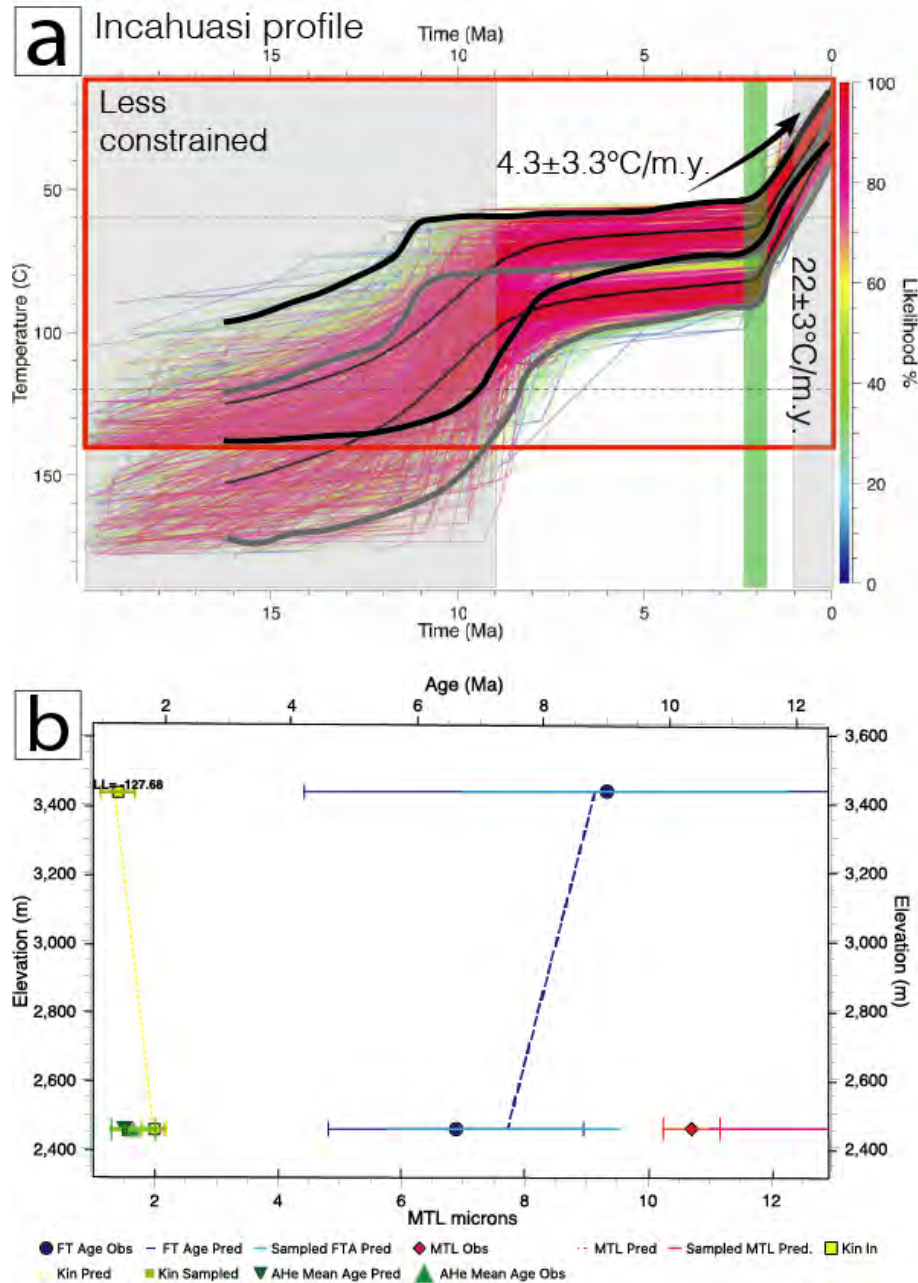


**Figure S36.** QTQt inversion results for the Incahuasi high-altitudinal profile. a) Time-temperature paths obtained by inversion of AHe and AFT thermochronology data from the Incahuasi age-elevation profile using QTQt (AB-17-51 and AB-17-55). The red square shows the explored time and temperature range for inversion. The colored lines show the T-t paths for the top and the bottom samples with their respective likelihood (see color scale on right). The solid black and grey lines show the expected model and its 95% reliable interval for the thermal histories of the top and bottom samples, respectively. The green vertical band indicates the well-constrained acceleration of cooling at ~2 Ma. Cooling rates derived from QTQt are indicated on the graph. b) Graph of observed vs. predicted data. Fit of best-fit model predictions to the data. FT: Fission Track; MTL: Mean Track Length; AHe: Apatite Helium; Obs: Observed; Pred: Predicted.

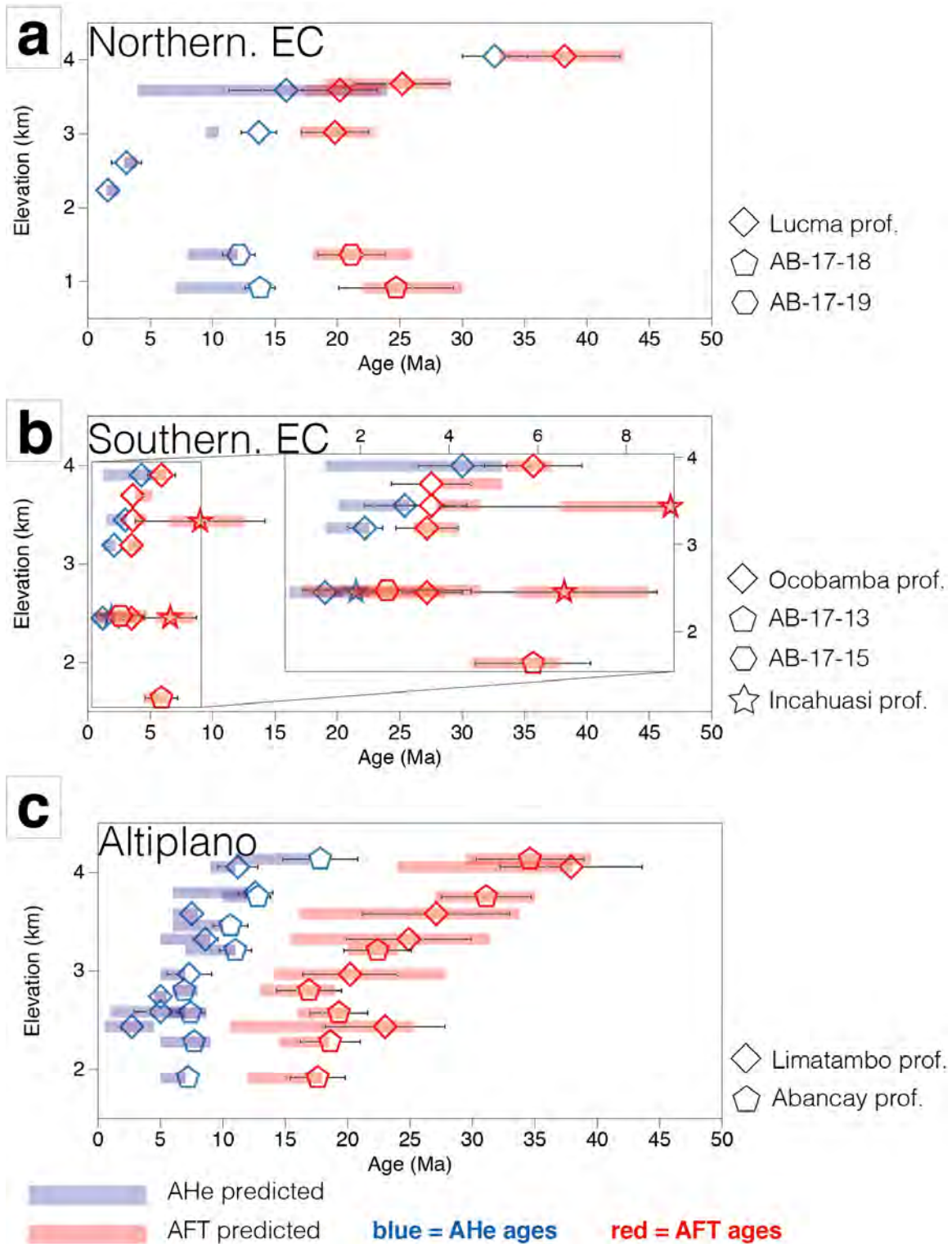
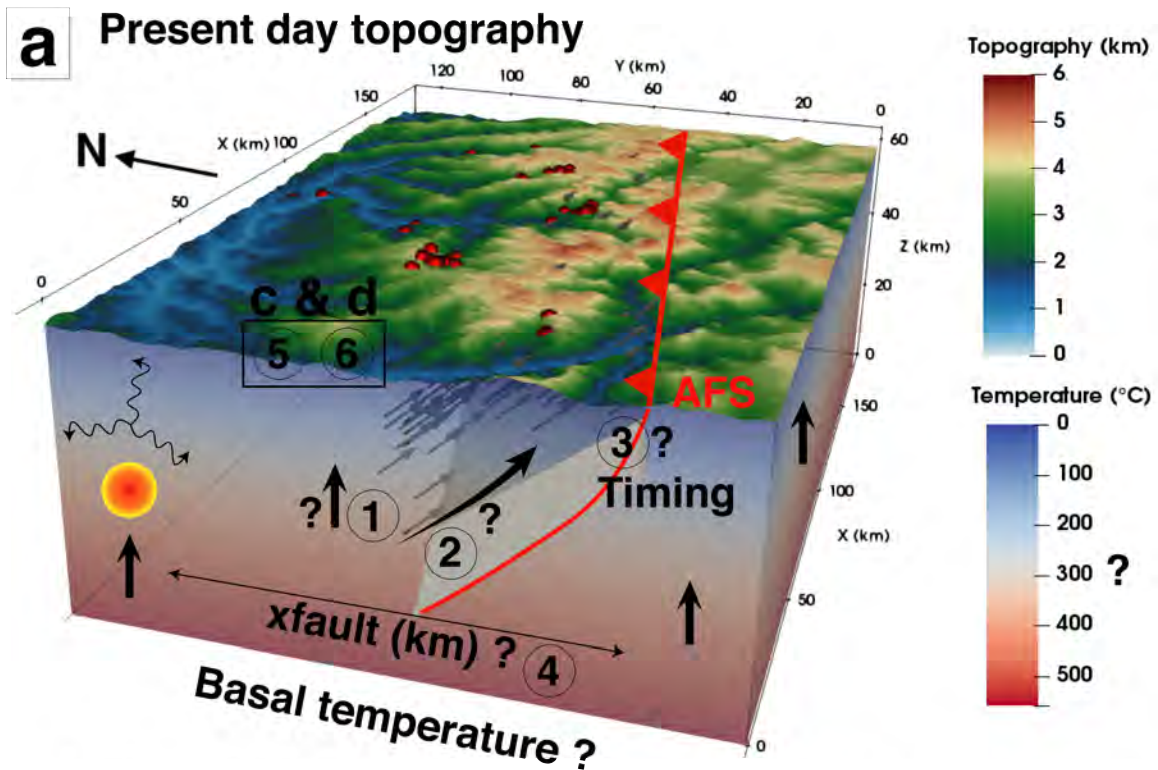


**Figure S37.** Observed vs. predicted thermochronological ages (AFT & AHe) modeled with QTQt. Panels a, b and c refer to the data associated to the northern Eastern Cordillera, the southern Eastern Cordillera and the Altiplano respectively (see Figure 4 for the location).



- Thermal diffusivity - fixed
- Heat production - fixed
- Crustal / Mantle density - fixed
- Lapse rate - fixed

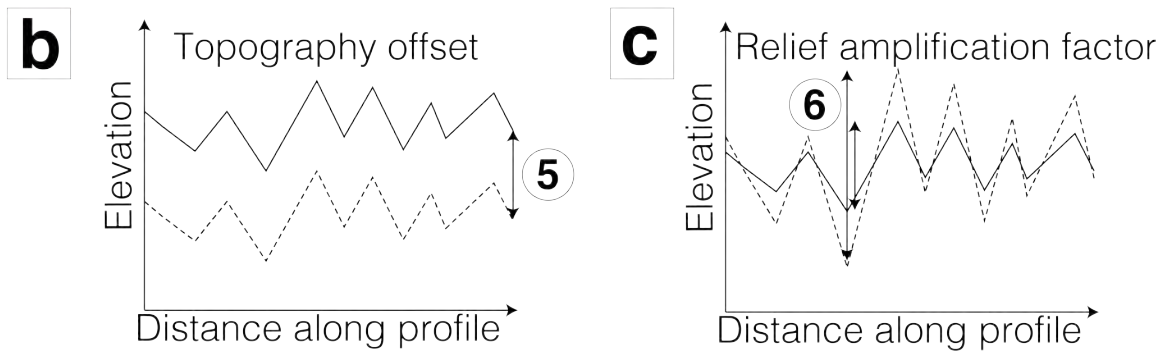
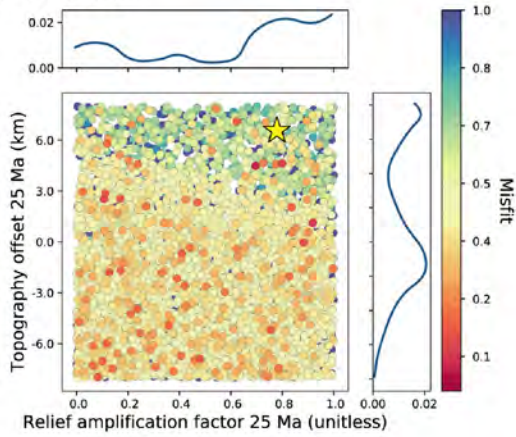


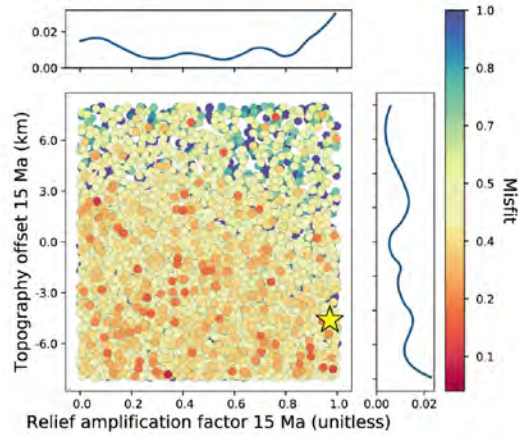
**Figure S38.** Parameters implemented and/or explored in Pecube through time. a) Example of the Eastern Cordillera crustal block (see Figure 2 for location). Red balls mark the location of the thermochronological data. Numbers and question marks refer to explored parameters. 1: Crustal block exhumation (km/Ma); 2: Fault velocity (km/Ma); 3: Timing of fault activation (Ma); 4:  $x$  fault (km), proxy for the fault geometry (fault dip). AFS: Apurimac fault system. b) Synthetic topographic profile presenting the topography-offset parameter evolution through time (5). c) Synthetic topographic profile presenting the relief amplification factor evolution through time (6).

# Altiplano

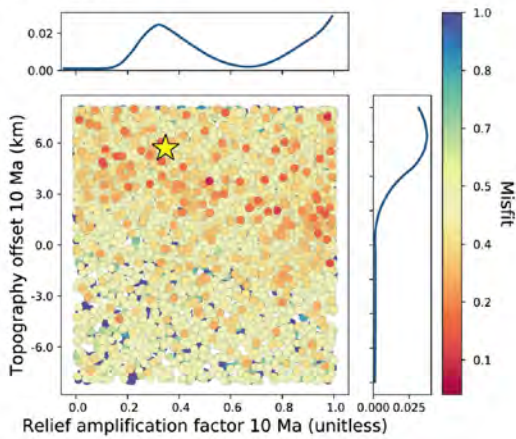
## 25 Ma



## 15 Ma



## 10 Ma



## 5 Ma

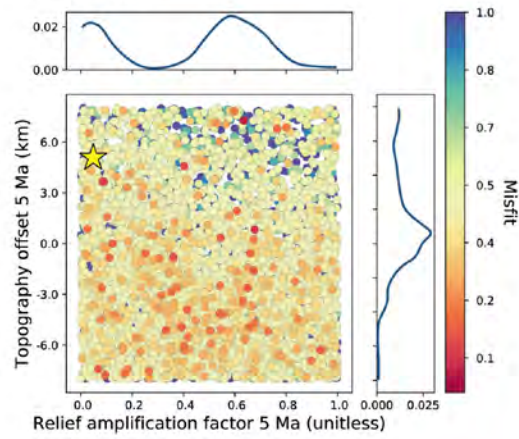
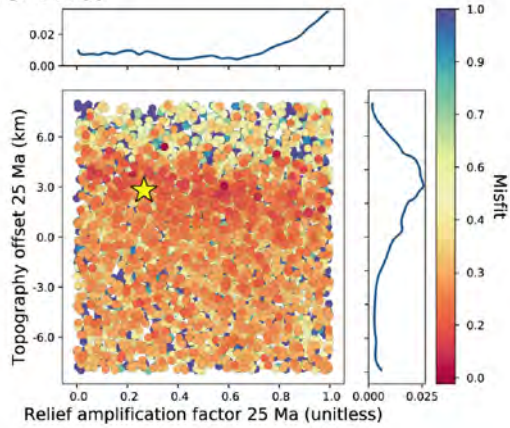
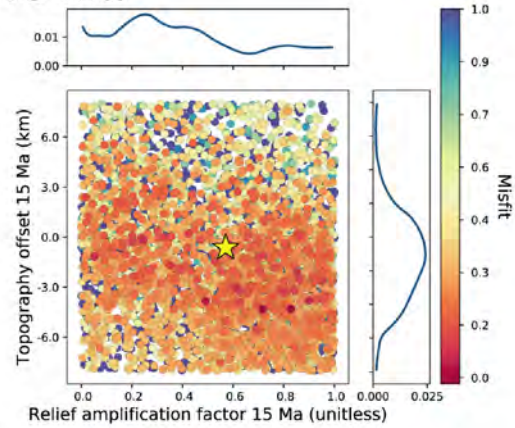


**Figure S39.** Pecube inversion results for landscape evolution parameters through time for the Altiplano block (performed using a 18°C/km geotherm). Y-axis is the topography-offset parameter; X-axis is the relief amplification factor. These outcomes correspond to a unique inversion with all the parameters free for each time period. These parameters do not converge toward a unique solution.

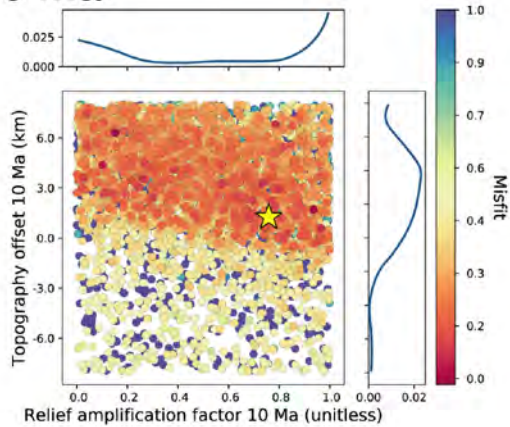
## Eastern Cordillera 25 Ma



## 15 Ma



## 10 Ma



## 5 Ma

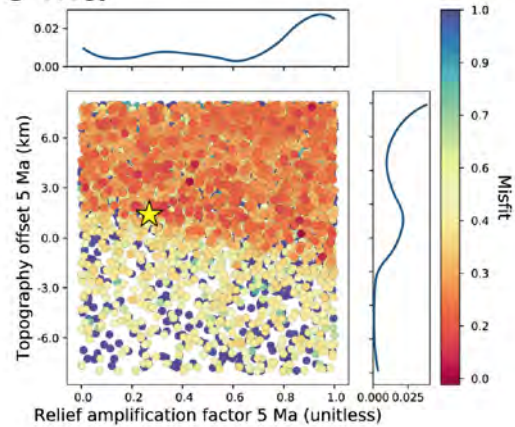


**Figure S40.** Pecube inversion results for landscape evolution parameters through time for the Eastern Cordillera block (performed using a 18°C/km geotherm). Y-axis is the topography-offset parameter; X-axis is the relief amplification factor. These outcomes correspond to a unique inversion with all the parameters free for each time period. These parameters do not clearly converge toward a unique solution.

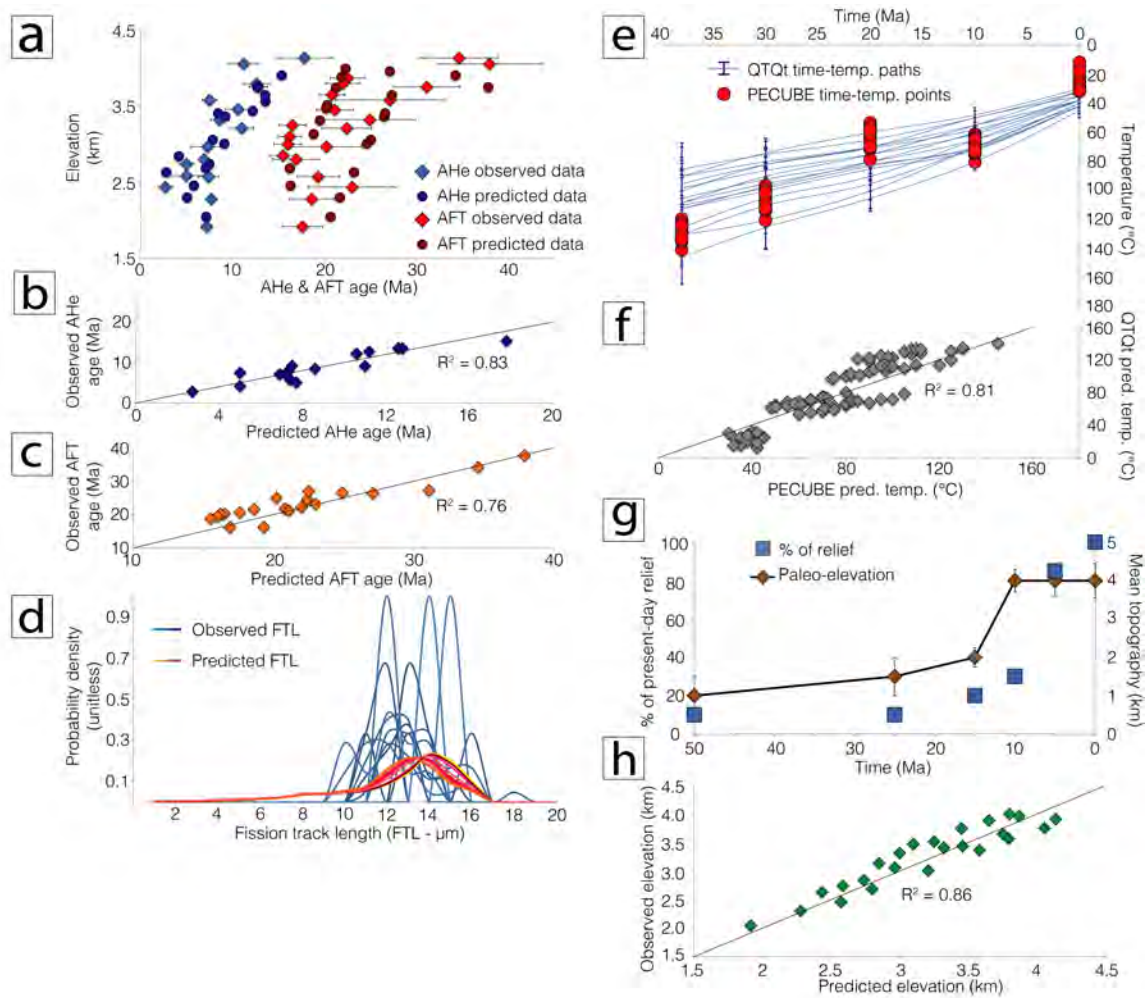


**Figure S41.** Observed data vs. predicted ones from Pecube best-fitting model for the Altiplano crustal block (performed using a 18°C/km geotherm). a) Age-elevation plot for observed AHe and AFT ages vs. predicted ones. b) Implemented AHe ages in function of predicted AHe ages. c) Implemented AFT ages in function of predicted AFT ages. d) Probability density function for implemented fission track length vs. predicted ones. e) Direct comparison of Time-temperature paths derived from QTQt modeling and T-t paths derived from Pecube. f) Implemented temperature (QTQt) in function of predicted ones computed with Pecube. g) Implemented modeled mean topography evolution (Sundell et al., 2019) and percentage of present-relief for forward modeling. h) Implemented topography (GTOPO30) in function of the predicted one by Pecube after landscape evolution computation. In any case, the data reproducibility is very satisfactory.



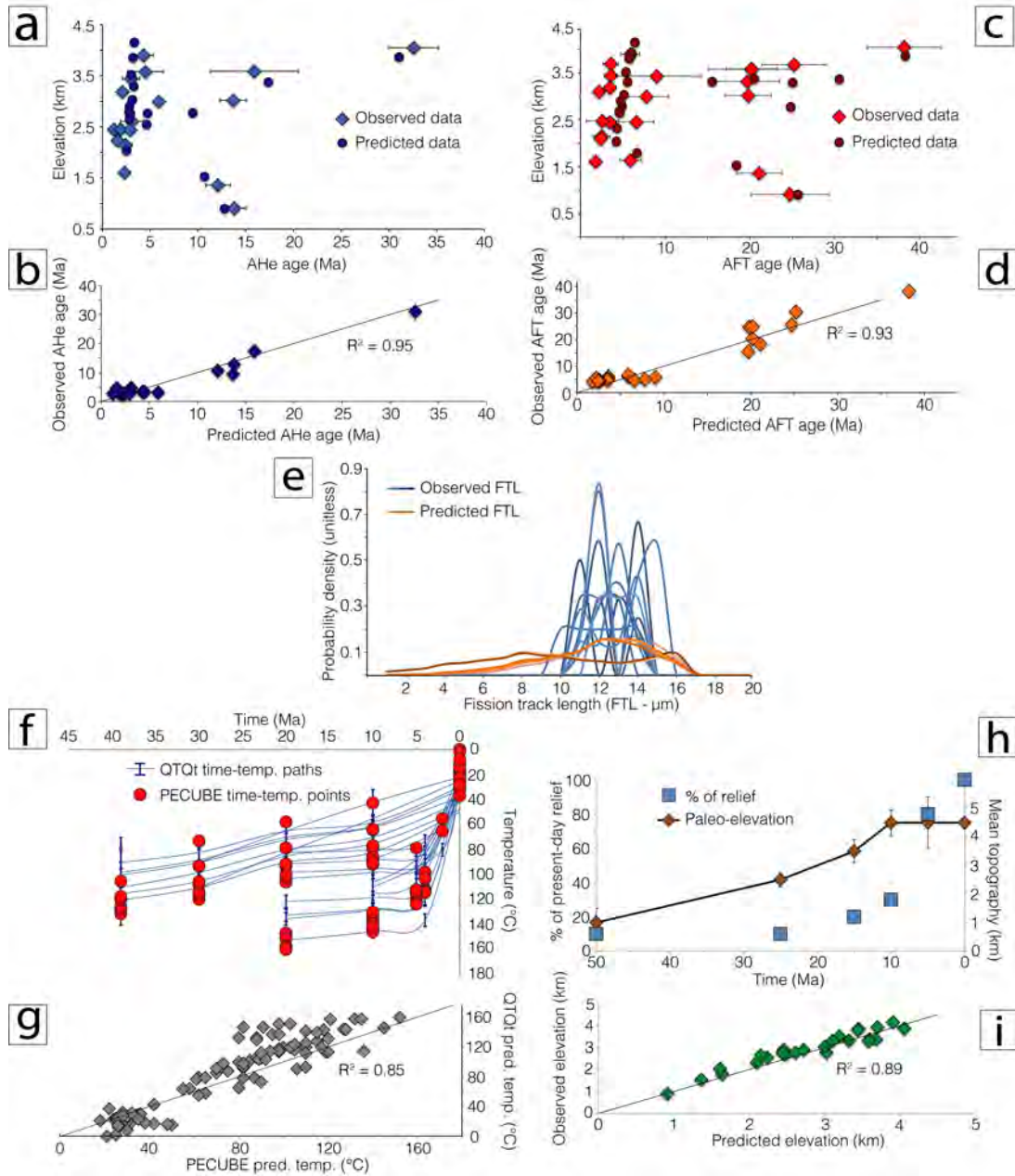


**Figure S42.** Observed data vs. predicted ones from Pecube best-fitting model for the Eastern Cordillera crustal block (performed using a 18°C/km geotherm). a) Age-elevation plot for observed AHe ages vs. predicted ones. b) Implemented AHe ages in function of predicted AHe ages. c) Age-elevation plot for observed AFT ages vs. predicted ones. d) Implemented AFT ages in function of predicted AFT ages. e) Probability density function for implemented fission track length vs. predicted ones. f) Direct comparison of Time-temperature paths derived from QTQt modeling and T-t paths derived from Pecube. g) Implemented temperature (QTQt) in function of predicted ones computed with Pecube. h) Implemented modeled mean topography evolution (Sundell et al., 2019) and percentage of present-relief for forward modeling. i) Implemented topography (GTOPO30) in function of the predicted one by Pecube after landscape evolution computation. In any case, the data reproducibility is very satisfactory.

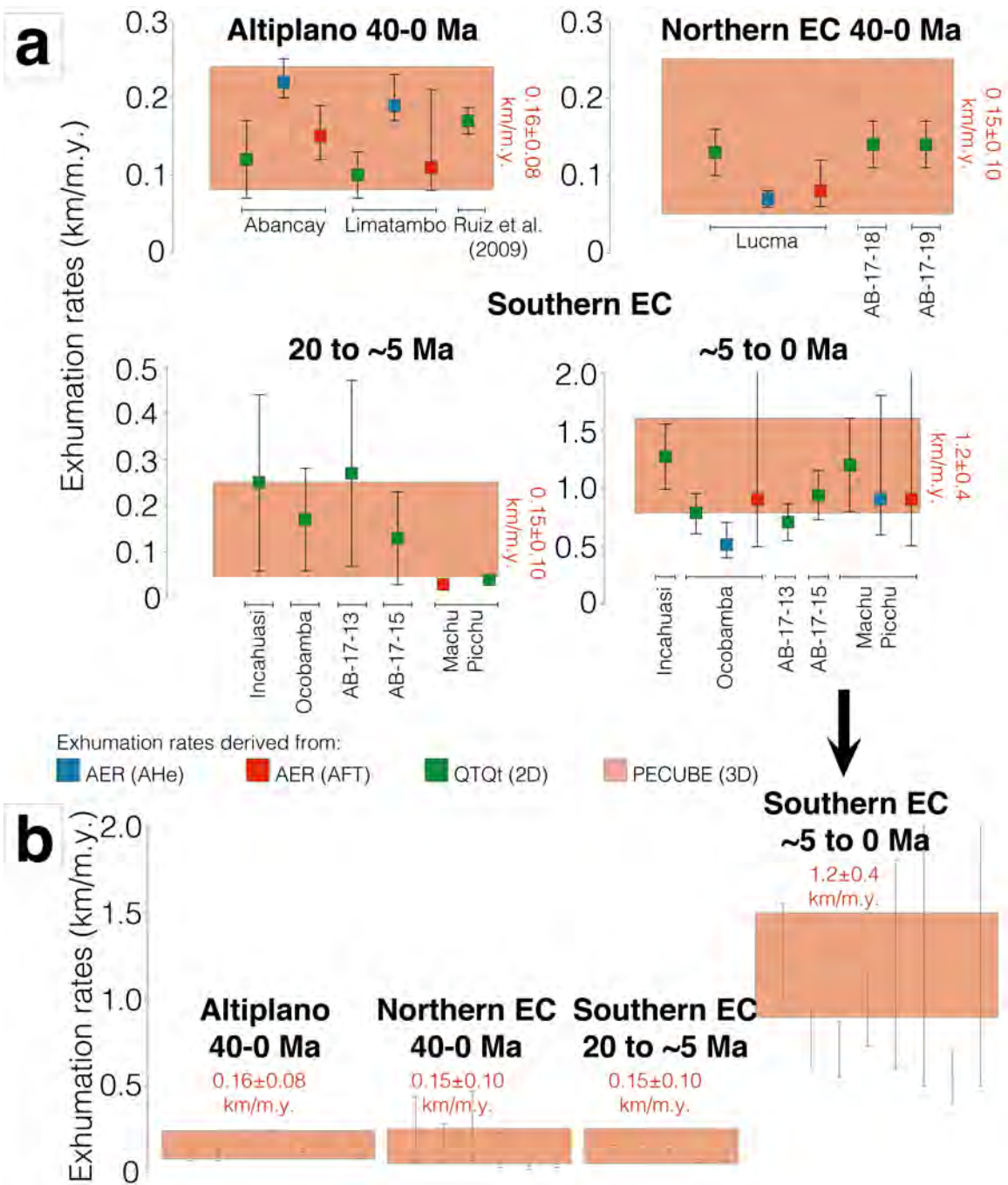


**Figure S43.** Exhumation rates derived from AER, QTQt and Pecube. a) Exhumation rate data per vertical profile and individual samples of the Abancay Deflection. b) Compilation of the data displayed in a.

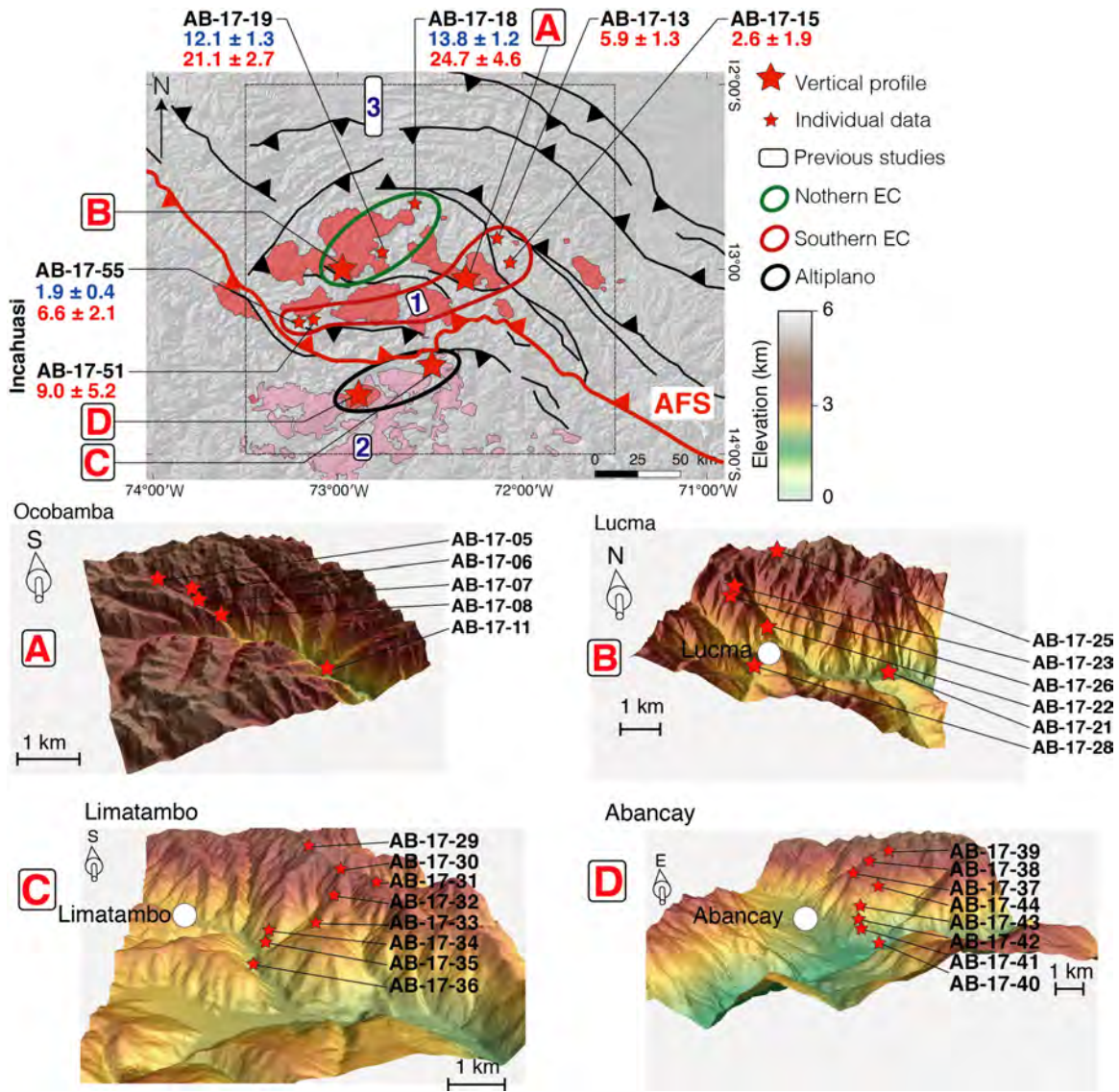


**Figure S44.** Sample locations within the Abancay Deflection. Red and pink polygons are respectively Permo-Triassic and Eocene plutons. Previous studies are: 1: Gérard et al. (in press) and Kennan (2008); 2: Ruiz et al. (2009); 3: Espurt et al. (2011) and Gautheron et al. (2013). Blue and red numbers below sample names refer to AHe mean ages and AFT central ages for individual samples and the two-sampled-point Incahuasi vertical profile. Red capital letters refer to the other sampled vertical profiles (A: Ocobamba profile; B: Lucma profile; C: Limatambo profile & D: Abancay profile). Green, red and black contours mark the latitudinal segmentation of the Abancay Deflection defining three areas according to thermal histories modeled with QTQt. The black dashed square frames the Abancay Deflection. AFT: Apurimac fault system; EC: Eastern Cordillera.

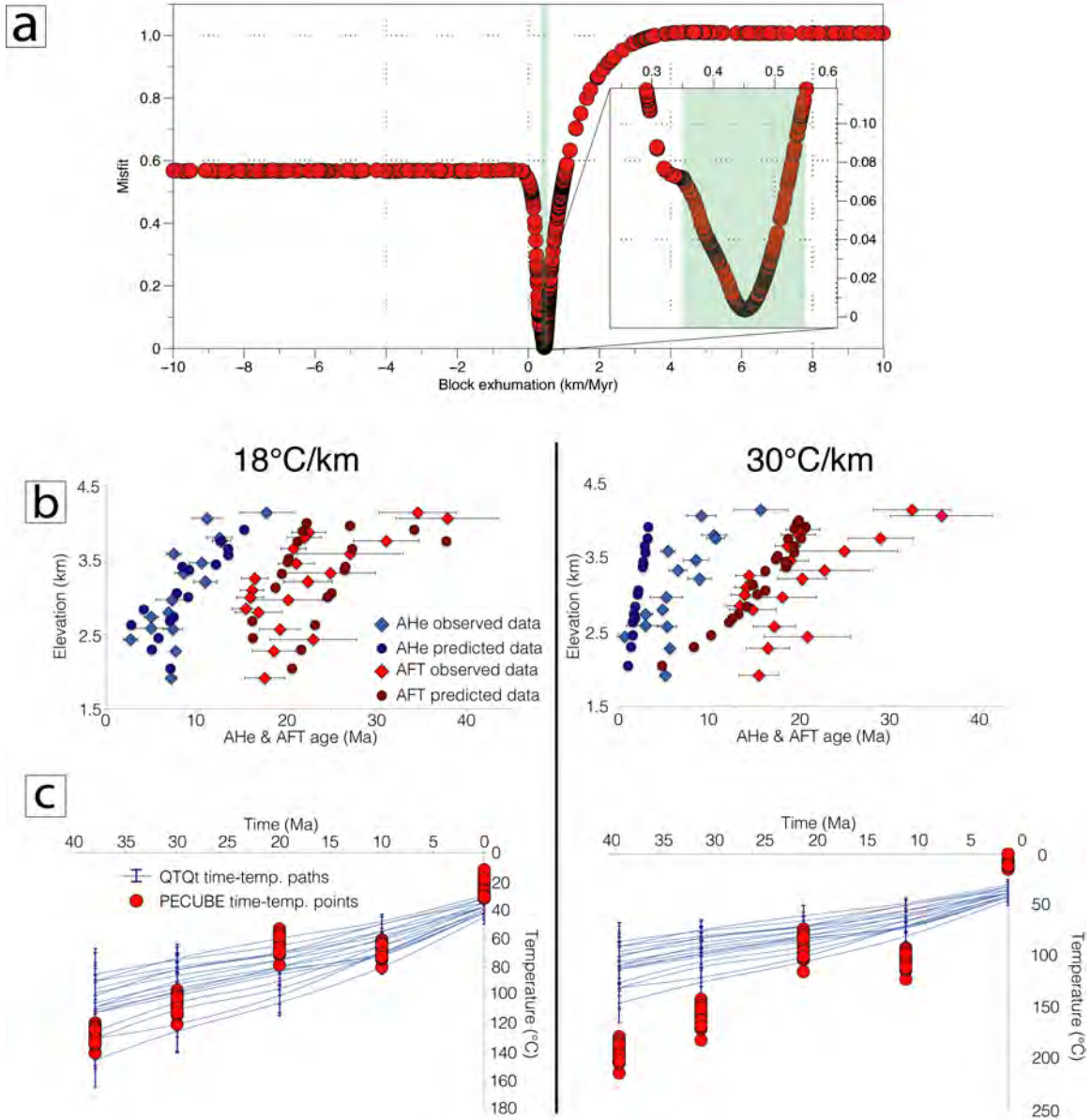


**Figure S45.** 3D Pecube inversion results for the Altiplano crustal block imposing a geothermal gradient of 30°C/km. The total sample size for inverse modeling is 1000. a) 1D parameter space and inversion results for crustal-block exhumation. Each point corresponds to one forward model. Lowest misfit value obtained corresponds to an exhumation rate of ~0.45 km/m.y. b and c) Observed data vs. predicted ones from Pecube best-fitting model for the Altiplano crustal block. A geothermal gradient of 18°C/km is imposed on left panels, while one of 30°C/km is implemented on right panels. b) Age-elevation plot for observed AHe and AFT ages vs. predicted ones. c) Direct comparison of time-temperature paths derived from QTQt and ones computed with Pecube best-fitting model. With a 30°C/km geothermal gradient, predicted ages are too young in most of cases for the Altiplano model.

**Figure S46.** 3D Pecube inversion results for the Eastern Cordillera crustal block imposing a geothermal gradient of 30°C/km. The total sample size for inverse modeling is 1000. a) 1D parameter space and inversion results for crustal-block exhumation. Each point corresponds to one forward model. Lowest misfit value obtained corresponds to an exhumation rate of ~0.2 km/m.y. b) 2D parameter space and inversion results for the fault velocity vs. activation timing of the Apurimac fault system. Each colored point corresponds to one forward model. Blue curves (up and right subpanels) are the probability density for each parameter. The

yellow stars in panels a and b are the best-fitting model. Models converge for values of  $7 \pm 1$  Ma for the fault activation timing and a fault velocity of  $1.4 \pm 0.4$  km/m.y since that time. c and d) Observed data vs. predicted ones from Pecube best-fitting model for the Eastern Cordillera crustal block. A geothermal gradient of  $18^\circ\text{C}/\text{km}$  is imposed on left panels, while one of  $30^\circ\text{C}/\text{km}$  is implemented on right panels. c) Direct comparison of observed thermochronological data (AHe and AFT) with ones predicted with Pecube best-fitting model. d) Direct comparison of time-temperature paths derived from QTQt and ones computed with Pecube best-fitting model. With a  $30^\circ\text{C}/\text{km}$  geothermal gradient, predicted ages are too old in most of cases for the Eastern Cordillera model.

Parameter	Value	Profile or individual data	Reference / Justification
Time explored (Ma)	0 - 20 0 - 30 0 - 30 0 - 50 0 - 50 0 - 80 0 - 42 0 - 70 0 - 20	Ocobamba AB-17-13 AB-17-15 AB-17-18 AB-17-19 Lucma Limatambo Abancay Incahuasi	Time interval with the age range extended to twice the oldest thermochronological age obtained to avoid a modeling bias. Except for Limatambo; the time interval explored is framed by the batholith crystallization age ( $40 \pm 2$ Ma; Perello et al., 2003). For the Limatambo profile, we imposed in QTQt a temperature ranging from $400^\circ\text{C}$ to $600^\circ\text{C}$ ( $\gg$ to the AHe and AFT closure temperature) between 42 and 38 m.y.
Explored temperature ( $^\circ\text{C}$ )	0 – 140 0 – 600	All except Limatambo Limatambo	Closure temperature for AHe and AFT systems (Ault et al., 2019). For Limatambo: temperature for pluton emplacement.
Explored $\delta T/\delta t$ ( $^\circ\text{C}/\text{My}$ )	1000	All	Maximum exploration – no constrains
Geothermal gradient ( $^\circ\text{C}/\text{km}$ )	$25 \pm 15$	All excepted individual data (AB-17-xx)	Geothermal exploration for common values in orogens. This range includes our computed gradient for the Abancay Deflection region ( $18 \pm 4^\circ\text{C}/\text{km}$ ) and accepted values for the Eastern Cordillera further south in Bolivia ( $26 \pm 8^\circ\text{C}/\text{km}$ ; Barnes et al., 2008).
Present-day temperature ( $^\circ\text{C}$ )	$25 \pm 10$	All	N.A.*
Lapse rate ( $^\circ\text{C}/\text{km}$ )	$6 \pm 2$	All	Estimated from Gonfiantini et al. (2001) and Klein et al. (1999).
Allow the geothermal gradient to vary over time	Yes	All	N.A.*
Reheating	No	All	No evidence for reheating (burial) of the samples.
Number of iteration	Prior = 100000 Post = 200000	All	N.A.*
Etchant	5.5 M	All	Analytical protocol
Annealing model (AFT)	N.A.*	All	Ketcham et al. (2007)
Radiation damage model (AHe)	N.A.*	All	Gautheron et al. (2009)
<i>Note:</i>			
*N.A. = not applicable.			

**Table S1.** QTQt parameters for thermochronological data modeling

Sample number	Arithmetic mean age (Ma)	Error - Standard deviation (Ma)
<u>Ocobamba profile</u>		
AB-17-05	4.3	1.0
AB-17-07	3.0	0.9
AB-17-08	2.1	0.4
AB-17-11	1.2	0.2
<u>Punctual data</u>		
AB-17-18	13.8	1.2
AB-17-19	12.1	1.3
<u>Lucma profile</u>		
AB-17-21	1.6	0.4
AB-17-22	13.7	1.4
AB-17-25	32.6	2.6
AB-17-26	15.9	4.6
AB-17-28	3.1	1.2
<u>Limatambo profile</u>		
AB-17-29	11.2	1.6
AB-17-30	12.6	1.4
AB-17-31	7.5	0.8
AB-17-32	8.6	1.0
AB-17-33	7.3	1.8
AB-17-34	5.0	0.8
AB-17-35	5.0	2.1
AB-17-36	2.7	0.8
<u>Abancay profile</u>		
AB-17-37	6.9	0.4
AB-17-38	7.4	1.1
AB-17-39	7.7	0.3
AB-17-40	7.2	0.6
AB-17-41	17.8	3.0
AB-17-42	12.8	1.0
AB-17-43	10.6	1.4
AB-17-44	11.0	1.3
<u>Incahuasi profile</u>		
AB-17-55	1.9	0.4

**Table S2.** Apatite (U-Th-Sm)/He data – Mean ages and errors for Pecube modeling



Parameter	Value	Reference
Crustal density (kg/m <sup>3</sup> )	<b>2721</b> ±65	Arndt et al. (1997) ; Waples and Waples (2004)
Mantle density (kg/m <sup>3</sup> )	<b>3095</b> ±147	Waples and Waples (2004)
Lapse rate (°C/km)	<b>6</b> ±1	Klein et al. (1999) ; Gonfiantini et al. (2001)
Heat flow (mW/m <sup>2</sup> )	<b>57</b> ±5	Henry and Pollack (1988) ; Davies (2013)
Thermal conductivity (W/m/°C)	<b>2.8</b> ±0.2	Henry and Pollack (1988)
Geothermal gradient (°C/km)	<b>18</b> ±4	This study
Heat production (mean for the crust; μW/m <sup>3</sup> )	<b>0.9</b>	Springer (1999)
Specific thermal capacity (J/kg/K)	<b>900</b> ±200	Arndt et al. (1997); Waples and Waples (2004)
Thermal diffusivity (km <sup>2</sup> /Ma)	<b>40</b> ±11	Arndt et al. (1997); Whittington et al. (2009)
Heat production through time (°C/Ma)	<b>6</b>	This study
Base model temperature (°C)	<b>560</b>	This study
Crust thickness (Moho depth; km)	<b>56</b> ±7	Mcglashan et al. (2008); Lloyd et al. (2010) Assumpção et al. (2013); Chulick et al. (2013); Ma and Clayton (2014); Bishop et al. (2017)
Elastic thickness (km)	<b>17.5</b> ±2.5	Pérez-Gussinyé et al. (2008)
Young modulus (Pa)	<b>1.10</b> <sup>11</sup>	Standard value
Poisson's coefficient (unitless)	<b>0.25</b>	Standard value

*Note:* Displayed results and errors were computed from the literature (Arithmetic mean and standard deviation). Pecube does not take into account these parameter values dispersion. Implemented values into Pecube are in bold.

**Table S3.** Thermal and rheological parameters for Pecube modeling.

Parameter	Range
<u>Altiplano model</u>	
Crustal block exhumation (km/m.y.)	0 – 5
Basal temperature - 56 km depth (°C)	400 – 800 (13°C/km – 26°C/km)
<u>Eastern Cordillera model</u>	
Crustal block exhumation (km/m.y.)	0 - 2
x fault – 25 km depth – proxy for fault dip (km)	-50 (26°) – 0 (vertical – 90°)
Fault velocity (km/m.y.)	0 – 5
Timing for fault activation (Ma)	0 – 10
<u>Common parameters explored for the Altiplano and the Eastern Cordillera</u>	
<u>Topography offset (km)</u>	
At 25 Ma	-6 – 6
At 15 Ma	-6 – 6
At 10 Ma	-6 – 6
At 5 Ma	-6 – 6
<u>Relief amplification factor (unitless)</u>	
At 25 Ma	0 – 1
At 15 Ma	0 – 1
At 10 Ma	0 – 1
At 5 Ma	0 – 1

*Note:* Pecube inversions were performed processing 12 successive iterations. The sample size for the first iteration is 984 and 480 for all other iterations. The number of resample cells is 288 (for n iteration) meaning a 60 % resampling of the previous best-fitting models (from n-1 iteration). The total sample size for inverse modeling is 6744 (Figures 8a, 9a and 9b).

**Table S4.** Explored parameters and ranges for thermochronological data inversion (Pecu modeling)

## References

- Arndt, J., Bartel, T., Scheuber, E., & Schilling, F. (1997). Thermal and rheological properties of granodioritic rocks from the Central Andes, North Chile. *Tectonophysics*, 271(1–2), 75–88. [https://doi.org/10.1016/S0040-1951\(96\)00218-1](https://doi.org/10.1016/S0040-1951(96)00218-1)
- Assumpção, M., Feng, M., Tassara, A., & Julià, J. (2013). Models of crustal thickness for South America from seismic refraction, receiver functions and surface wave tomography. *Tectonophysics*. Elsevier B.V. <https://doi.org/10.1016/j.tecto.2012.11.014>
- Ault, A. K., Gautheron, C., & King, G. E. (2019). Innovations in (U-Th)/He, fission track, and trapped charge thermochronometry with applications to earthquakes, weathering, surface mantle connections, and the growth and decay of mountains. *Tectonics*. <https://doi.org/10.1029/2018tc005312>
- Barnes, J. B., Ehlers, T. A., McQuarrie, N., O'Sullivan, P. B., & Tawackoli, S. (2008). Thermochronometer record of central Andean Plateau growth, Bolivia (19.5°S). *Tectonics*, 27(3). <https://doi.org/10.1029/2007TC002174>
- Bishop, B. T., Beck, S. L., Zandt, G., Wagner, L., Long, M., Antonijevic, S. K., et al. (2017). Causes and consequences of flat-slab subduction in southern Peru. *Geosphere*, 13(5), 1392–1407. <https://doi.org/10.1130/GES01440.1>
- Braun, J. (2003). Pecube: A new finite-element code to solve the 3D heat transport equation including the effects of a time-varying, finite amplitude surface topography. *Computers and Geosciences*, 29(6), 787–794. [https://doi.org/10.1016/S0098-3004\(03\)00052-9](https://doi.org/10.1016/S0098-3004(03)00052-9)
- Braun, J., van der Beek, P., & Batt, G. (2006). *Quantitative Thermochronology: Numerical Methods for the Interpretation of Thermochronological Data*. Cambridge: Cambridge Univ. Press.
- Braun, J., van der Beek, P., Valla, P., Robert, X., Herman, F., Glotzbach, C., et al. (2012). Quantifying rates of landscape evolution and tectonic processes by thermochronology and numerical modeling of crustal heat transport using PECUBE. *Tectonophysics*, 524–525, 1–28. <https://doi.org/10.1016/j.tecto.2011.12.035>
- Chulick, G. S., Detweiler, S., & Mooney, W. D. (2013). Seismic structure of the crust and uppermost mantle of South America and surrounding oceanic basins. *Journal of South American Earth Sciences*. Elsevier Ltd. <https://doi.org/10.1016/j.jsames.2012.06.002>
- Davies, J. H. (2013). Global map of solid Earth surface heat flow. *Geochemistry, Geophysics, Geosystems*, 14(10), 4608–4622. <https://doi.org/10.1002/ggge.20271>
- Espurt, N., Barbarand, J., Roddaz, M., Brusset, S., Baby, P., Saillard, M., & Hermoza, W. (2011). A scenario for late Neogene Andean shortening transfer in the Camisea Subandean zone (Peru, 12°S): Implications for growth of the northern Andean Plateau. *Bulletin of the Geological Society of America*, 123(9–10), 2050–2068. <https://doi.org/10.1130/B30165.1>
- Gallagher, K. (2012). Transdimensional inverse thermal history modeling for quantitative thermochronology. *Journal of Geophysical Research: Solid Earth*, 117(2), 1–16. <https://doi.org/10.1029/2011JB008825>
- Gautheron, C., Tassan-Got, L., Barbarand, J., & Pagel, M. (2009). Effect of alpha-damage annealing on apatite (U-Th)/He thermochronology. *Chemical Geology*,

- 266(3–4), 166–179. <https://doi.org/10.1016/j.chemgeo.2009.06.001>
- Gautheron, C., Espurt, N., Barbarand, J., Roddaz, M., Baby, P., Brusset, S., et al. (2013). Direct dating of thick- and thin-skin thrusts in the Peruvian Subandean zone through apatite (U-Th)/He and fission track thermochronometry. *Basin Research*, 25(4), 419–435. <https://doi.org/10.1111/bre.12012>
- Gérard, B., Audin, L., Robert, X., Gautheron, C., van der Beek, P., Bernet, M., et al. (2021). Pliocene river capture and incision of the northern Altiplano: Machu Picchu, Peru. *Journal of the Geological Society*.
- Gonfiantini, R., Roche, M.-A., Olivry, J.-C., Fontes, J.-C., & Zuppi, G. M. (2001). The altitude effect on the isotopic composition of tropical rains. *Chemical Geology*, 181, 147–167.
- van Heiningen, P. S., Carlotto, V., Zuloaga, A. D., Romero, L., & Andriessen, P. A. M. (2005). Oligocene to Pleistocene exhumation patterns across the Apurimac River drainage basin, southern Peru. *6th International Symposium on Andean Geodynamics (ISAG 2005, Barcelona)*, 763–766.
- Henry, S. G., & Pollack, H. N. (1988). Terrestrial heat flow above the Andean Subduction Zone in Bolivia and Peru. *Journal of Geophysical Research: Solid Earth*, 93(B12), 15153–15162. <https://doi.org/10.1029/jb093ib12p15153>
- Kennan, L. (2008). Fission track ages and sedimentary provenance studies in Peru, and their implications for andean paleogeographic evolution, stratigraphy and hydrocarbon systems. In *VI INGEPET, 13–17 October 2008* (p. 13). Lima, Peru. Retrieved from <http://www.agu.org/pubs/crossref/1988/JB093iB12p15153.shtml>
- Ketcham, R. A., Carter, A., Donelick, R. A., Barbarand, J., & Hurford, A. J. (2007). Improved modeling of fission-track annealing in apatite. *American Mineralogist*, 92(5–6), 799–810. <https://doi.org/10.2138/am.2007.2281>
- Klein, A. G., Seltzer, G. O., & Isacks, B. L. (1999). Modern and last local glacial maximum snowlines in the Central Andes of Peru, Bolivia, and Northern Chile. *Quaternary Science Reviews*, 18(1), 63–84. [https://doi.org/10.1016/S0277-3791\(98\)00095-X](https://doi.org/10.1016/S0277-3791(98)00095-X)
- Lloyd, S., Van Der Lee, S., França, G. S., Assumpção, M., & Feng, M. (2010). Moho map of South America from receiver functions and surface waves. *Journal of Geophysical Research: Solid Earth*, 115(11), 1–12. <https://doi.org/10.1029/2009JB006829>
- Ma, Y., & Clayton, R. W. (2014). The crust and uppermost mantle structure of Southern Peru from ambient noise and earthquake surface wave analysis. *Earth and Planetary Science Letters*, 395, 61–70. <https://doi.org/10.1016/j.epsl.2014.03.013>
- Mcglashan, N., Brown, L., & Kay, S. (2008). Crustal thickness in the central Andes from teleseismically recorded depth phase precursors. *Geophysical Journal International*, 175(3), 1013–1022. <https://doi.org/10.1111/j.1365-246X.2008.03897.x>
- Perello, J., Carlotto, V., Zarate, A., Ramos, P., Posso, H., Neyra, C., et al. (2003). Porphyry-Style Alteration and Mineralization of the Middle Eocene to Early Oligocene Andahuaylas-Yauri Belt, Cuzco Region, Peru. *Economic Geology*, 98, 1575–1605.
- Pérez-Gussinyé, M., Lowry, A. R., Phipps Morgan, J., & Tassara, A. (2008). Effective elastic thickness variations along the andean margin and their relationship to subduction geometry. *Geochemistry, Geophysics, Geosystems*, 9(2).

- <https://doi.org/10.1029/2007GC001786>
- Reiners, P. W., & Brandon, M. T. (2006). Using Thermochronology To Understand Orogenic Erosion. *Annual Review of Earth and Planetary Sciences*, 34(1), 419–466. <https://doi.org/10.1146/annurev.earth.34.031405.125202>
- Ruiz, G. M. H., Carlotto, V., Van Heiningen, P. V., & Andriessen, P. A. M. (2009). Steady-state exhumation pattern in the Central Andes – SE Peru. *Geological Society, London, Special Publications*, 324(1), 307–316. <https://doi.org/10.1144/SP324.20>
- Sambridge, M. (1999). Geophysical inversion with a neighbourhood algorithm –II. Appraising the ensemble. *Geophys. J. Int.*, 138, 727–746.
- Sambridge, Malcolm. (1999). Geophysical inversion with a neighbourhood algorithm - I. Searching a parameter space. *Geophysical Journal International*, 138(2), 479–494. <https://doi.org/10.1046/j.1365-246X.1999.00876.x>
- Springer, M. (1999). Interpretation of heat-flow density in the Central Andes. In *Tectonophysics* (Vol. 306, pp. 377–395). [https://doi.org/10.1016/S0040-1951\(99\)00067-0](https://doi.org/10.1016/S0040-1951(99)00067-0)
- Sundell, K. E., Saylor, J. E., Lapen, T. J., & Horton, B. K. (2019). Implications of variable late Cenozoic surface uplift across the Peruvian central Andes. *Scientific Reports*, 9(1), 1–12. <https://doi.org/10.1038/s41598-019-41257-3>
- Waples, D. W., & Waples, J. S. (2004). A review and evaluation of specific heat capacities of rocks, minerals, and subsurface fluids. Part 2: Fluids and porous rocks. *Natural Resources Research*. <https://doi.org/10.1023/B:NARR.0000032648.15016.49>
- Whittington, A. G., Hofmeister, A. M., & Nabelek, P. I. (2009). Temperature-dependent thermal diffusivity of the Earth’s crust and implications for magmatism. *Nature*, 458(7236), 319–321. <https://doi.org/10.1038/nature07818>

Locations and bedrock lithologies

Sample number	Latitude (°S)	Longitude (°W)	Elevation (m)	Lithology	Geologic unit
<u>Ocobamba profile*</u>					
AB-17-05	13.091198	72.26337	3903	Granite	Mesapelada pluton
AB-17-06	13.07867	72.27952	3696	Granite	Mesapelada pluton
AB-17-07	13.07128	72.2803	3447	Granite	Mesapelada pluton
AB-17-08	13.05875	72.28962	3190	Granite	Mesapelada pluton
AB-17-11	13.00978	72.3299	2450	Monzonite	Mesapelada pluton
<u>Individual data</u>					
AB-17-13	12.83221	72.14085	1638	Granite	Colca pluton
AB-17-15	12.9652	72.07252	2475	Granite	Colca pluton
AB-17-18	12.64752	72.55498	912	Granite	Quellotuno pluton
AB-17-19	12.89585	72.74471	1362	Granite	Kiteni pluton
<u>Lucma profile*</u>					
AB-17-21	13.04408	72.88454	2235	Granite	Kiteni pluton
AB-17-22	13.04171	72.93961	3020	Granite	Kiteni pluton
AB-17-23	13.02889	72.9593	3678	Granite	Kiteni pluton
AB-17-25	13.00124	72.9468	4050	Granite	Kiteni pluton
AB-17-26	13.03244	72.9577	3589	Granite	Kiteni pluton
AB-17-28	13.05984	72.9371	2609	Granite	Kiteni pluton
<u>Limatambo profile*</u>					
AB-17-29	13.5299	72.43471	4056	Diorite	Cotabamba pluton
AB-17-30	13.53367	72.45849	3795	Diorite	Cotabamba pluton
AB-17-31	13.5419	72.4688	3581	Diorite	Cotabamba pluton
AB-17-32	13.52771	72.4671	3322	Diorite	Cotabamba pluton
AB-17-33	13.51888	72.47569	2966	Diorite	Cotabamba pluton
AB-17-34	13.50543	72.4702	2740	Diorite	Cotabamba pluton
AB-17-35	13.50373	72.47325	2586	Diorite	Cotabamba pluton
AB-17-36	13.49839	72.48075	2435	Diorite	Cotabamba pluton
<u>Abancay profile*</u>					
AB-17-37	13.67147	72.89801	2800	Monzonite	Abancay orthogneiss
AB-17-38	13.67129	72.90512	2573	Diorite	Abancay orthogneiss
AB-17-39	13.6721	72.90939	2280	Gabbro	Abancay orthogneiss
AB-17-40	13.68018	72.91482	1916	Granite	Abancay orthogneiss
AB-17-41	13.68651	72.84196	4136	Granite	Abancay orthogneiss
AB-17-42	13.67414	72.85007	3753	Granite	Abancay orthogneiss
AB-17-43	13.66636	72.86651	3459	Granitic arena	Abancay orthogneiss
AB-17-44	13.6792	72.88035	3209	Granitic arena	Abancay orthogneiss
<u>Incahuasi profile*</u>					
AB-17-51	13.2918	73.15121	3434	Granite	Chucuito pluton
AB-17-55	13.30613	73.21085	2455	Granite	Chucuito pluton

*Note:* The Geologic unit and pluton period columns refer to the studies of Egeler & De Booy (1978), Mišković et al. (2009), Perello et al. (2003), Reitsma (2012) and the INGEMMET geologic map.

\* Profile names were given considering the main cities nearby the investigated area.

Pluton period	Pluton age (Ma)	Reference
Permian	277±2	Reitsma (2012)
Permian	277±2	Reitsma (2012)
Permian	277±2	Reitsma (2012)
Permian	277±2	Reitsma (2012)
Permian	277±2	Reitsma (2012)
Carboniferous	330±10	Lancelot et al. (1978)
Carboniferous	330±10	Lancelot et al. (1978)
Permian	282±1	Reitsma (2012)
Permian	279±2	Reitsma (2012)
Permian	257±3	Lancelot et al. (1978)
Permian	257±3	Lancelot et al. (1978)
Permian	257±3	Lancelot et al. (1978)
Permian	257±3	Lancelot et al. (1978)
Permian	257±3	Lancelot et al. (1978)
Permian	257±3	Lancelot et al. (1978)
Paleogene	40±2	Perello et al. (2003)
Paleogene	40±2	Perello et al. (2003)
Paleogene	40±2	Perello et al. (2003)
Paleogene	40±2	Perello et al. (2003)
Paleogene	40±2	Perello et al. (2003)
Paleogene	40±2	Perello et al. (2003)
Paleogene	40±2	Perello et al. (2003)
Paleogene	40±2	Perello et al. (2003)
Triassic	222±7	Lancelot et al. (1978)
Triassic	222±7	Lancelot et al. (1978)
Triassic	222±7	Lancelot et al. (1978)
Triassic	222±7	Lancelot et al. (1978)
Triassic	222±7	Lancelot et al. (1978)
Triassic	222±7	Lancelot et al. (1978)
Triassic	222±7	Lancelot et al. (1978)
Triassic	222±7	Lancelot et al. (1978)
Ordovician	475±5	Reitsma (2012)
Ordovician	475±5	Reitsma (2012)

061), Lancelot et al. Geological database.

## apatite (U-Th-Sm)/He data

Sample number	Morphology	Length ( $\mu\text{m}$ )	Width ( $\mu\text{m}$ )	Thickness ( $\mu\text{m}$ )	$R_s$ ( $\mu\text{m}$ )	Weight ( $\mu\text{g}$ )
<u>Ocobamba profile</u>						
AB-17-05A	2b	144	92	99	63	2.9
AB-17-05B	2py	201	128	115	61	4.1
AB-17-07A	1b + 1py	180	139	122	73	5.1
AB-17-07B	2b	118	125	79	54	2.1
AB-17-07C	2b	109	108	92	64	2.3
AB-17-07D	2b	194	128	115	79	6.2
AB-17-07E	1b + 1py	146	123	118	68	3.6
AB-17-08A	2b	198	112	114	76	5.8
AB-17-08B	1b + 1py	212	142	133	81	7.2
AB-17-08C	1b + 1py	168	117	122	69	4.2
AB-17-08D	1b + 1py	162	129	114	68	4.0
AB-17-08E	1b + 1py	182	164	157	89	7.7
AB-17-11A	1b + 1py	133	101	105	59	2.4
AB-17-11B	2b	171	99	93	64	3.5
AB-17-11C	1b + 1py	207	104	99	62	4.1
AB-17-11E	2b	191	119	99	69	4.7
<u>Individual data</u>						
AB-17-18A	2b	144	127	119	82	4.8
AB-17-18B	2b	146	93	96	63	2.9
AB-17-18C	2b	230	120	114	78	7.0
AB-17-18E	2b	128	128	99	69	3.2
AB-17-19A	2b	172	159	143	99	8.6
AB-17-19B	2b	158	129	93	65	3.7
AB-17-19I	2b	164	135	106	74	4.7
<u>Lucma profile</u>						
AB-17-21A	1b + 1py	169	126	112	68	4.1
AB-17-21C	2py	324	145	137	78	10.5
AB-17-21D	2b	207	141	118	82	7.2
AB-17-21E	1b + 1py	205	107	116	66	4.7
AB-17-22B	1b + 1py	205	100	98	61	3.9
AB-17-22C	2b	120	110	94	65	2.6
AB-17-22D	2b	130	119	108	74	3.6
AB-17-22E	1b + 1py	115	111	77	46	1.4
AB-17-25A	2b	102	137	84	56	2.0
AB-17-25C	2b	109	92	97	63	2.2
AB-17-25D	2b	145	125	80	54	2.6
AB-17-25E	1b + 1py	170	139	127	75	5.1
AB-17-26A	2b	217	111	105	72	5.6
AB-17-26C	2b	165	142	129	89	6.6
AB-17-28A	2py	218	94	84	49	2.8
AB-17-28B	2py	192	105	79	46	2.3



AB-17-28C	1b + 1py	228	117	89	57	4.1
AB-17-28D	2b	157	150	122	85	5.9
AB-17-28E	1b + 1py	146	101	94	57	2.4

Limatambo profile

AB-17-29A	2b	173	109	100	69	4.1
AB-17-29B	2b	151	132	114	79	4.8
AB-17-29C	1b + 1py	165	92	89	54	2.5
AB-17-29D	1b + 1py	140	116	103	61	2.8
AB-17-29E	1b + 1py	149	110	112	64	3.2
AB-17-30B	1b + 1py	148	92	84	52	2.1
AB-17-30C	1b + 1py	170	133	104	64	3.8
AB-17-31A	2b	189	104	114	72	4.9
AB-17-31C	1b + 1py	153	112	99	60	2.9
AB-17-31E	1b + 1py	185	103	100	61	3.6
AB-17-32A	2b	140	114	103	71	3.6
AB-17-32B	2b	140	111	106	73	3.7
AB-17-33A	2py	155	109	100	50	2.2
AB-17-33B	1b + 1py	161	152	175	85	6.4
AB-17-33C	2b	175	115	102	71	4.5
AB-17-33D	1b + 1py	234	118	103	66	5.2
AB-17-33E	2b	133	119	104	72	3.5
AB-17-34A	2b	154	118	113	77	4.6
AB-17-34B	2b	155	152	126	87	6.2
AB-17-34C	2b	179	127	134	87	6.7
AB-17-34D	1b + 1py	139	93	95	55	2.2
AB-17-34E	2b	180	104	97	67	4.0
AB-17-35D	1b + 1py	203	122	97	62	4.1
AB-17-35E	2b	142	104	96	66	3.1
AB-17-36A	1b + 1py	142	103	105	60	2.7
AB-17-36D	1b + 1py	160	108	100	60	3.0
AB-17-36E	1b + 1py	186	128	123	74	5.2

Abancay profile

AB-17-37A	2py	242	123	125	67	5.8
AB-17-37B	2b	117	113	102	70	2.9
AB-17-37C	1b + 1py	252	139	111	71	6.8
AB-17-37D	1b + 1py	189	132	100	57	3.5
AB-17-38A	1b + 1py	240	121	128	75	6.9
AB-17-38B	1b + 1py	254	132	144	82	8.8
AB-17-38C	2py	297	144	152	80	10.2
AB-17-38D	1b + 1py	260	133	149	83	9.3
AB-17-38E	1b + 1py	202	119	97	61	4.0
AB-17-39C	1b + 1py	190	129	132	77	5.8
AB-17-39D	2py	185	109	99	53	2.9
AB-17-40A	1b + 1py	237	118	124	73	6.6
AB-17-40B	2py	209	115	113	60	4.1
AB-17-40C	1b + 1py	247	128	137	79	8.0

AB-17-40D	2py	228	156	161	76	7.5
AB-17-40E	1b + 1py	197	128	104	65	4.5
AB-17-41A	1b + 1py	224	131	125	77	6.8
AB-17-41B	1b + 1py	115	103	95	55	1.8
AB-17-41C	2py	220	121	104	58	4.1
AB-17-41D	2b	160	111	134	77	4.9
AB-17-41E	1b + 1py	187	137	122	74	5.4
AB-17-42A	2b	180	128	122	83	6.3
AB-17-42B	2b	145	132	125	86	5.3
AB-17-42C	2py	216	109	113	59	4.1
AB-17-42D	1b + 1py	177	101	123	63	3.7
AB-17-43A	1b + 1py	166	108	90	56	2.8
AB-17-43C	2b	162	93	85	58	2.8
AB-17-43D	2b	197	92	100	63	3.9
AB-17-43E	2b	164	97	93	63	3.3
AB-17-44A	1b + 1py	214	112	101	63	4.5
AB-17-44B	1b + 1py	100	114	181	60	2.1
AB-17-44C	2b	184	139	114	79	6.0
AB-17-44D	1b + 1py	154	110	102	61	3.0
AB-17-44E	2b	136	110	110	74	3.7
<u>Incahuasi profile</u>						
AB-17-55A	1b + 1py	213	157	139	84	8.0
AB-17-55B	1b + 1py	198	117	110	68	4.7
AB-17-55C	2py	221	117	102	58	4.0
AB-17-55D	2b	183	129	125	85	6.6
AB-17-55E	1b + 1py	196	138	132	79	6.4

*Note:* Morphology refers to the apatite geometry. 2py: 2 hexagonal pyramids; 2b: 2 broken fa  
sphere equivalent radius of hexagonal crystal (Gautheron et al., 2012; Ketcham et al., 2011).

$F_T$	$^4\text{He}$ (nccSTP/g)	$^{238}\text{U}$ (ppm)	$^{232}\text{Th}$ (ppm)	$^{147}\text{Sm}$ (ppm)	Th/U	eU (ppm)
0.78	16932	29.3	21.5	80.5	0.7	35
0.77	14156	40.5	25.2	84.6	0.6	47
0.81	23568	65.6	41.9	98.1	0.6	76
0.74	22253	45.1	26.1	93.4	0.6	52
0.78	19309	58.3	35.4	107.4	0.6	67
0.82	7087	36.2	26.3	92.8	0.7	43
0.79	6820	32.2	20.5	82.4	0.6	38
0.81	12131	63.8	29.1	88.9	0.5	71
0.82	13951	70.6	18.7	89.3	0.3	76
0.80	14539	56.3	27.4	85.2	0.5	63
0.79	18175	59.2	19.0	81.6	0.3	64
0.84	8668	47.2	17.1	72.9	0.4	52
0.76	21106	111.0	213.5	89.7	1.9	163
0.78	13654	65.5	157.8	72.5	2.4	104
0.77	15283	107.9	190.1	76.6	1.8	154
0.79	3626	29.4	55.0	27.3	1.9	43
0.82	24984	10.8	39.4	40.9	3.6	21
0.78	42585	19.6	68.4	52.4	3.5	36
0.82	33557	12.0	41.1	37.7	3.4	22
0.79	20493	8.3	27.5	35.9	3.3	15
0.85	148729	122.7	5.9	55.9	0.1	124
0.78	108144	103.9	11.9	48.2	0.1	107
0.81	81674	58.3	4.8	32.2	0.1	60
0.79	5878	50.8	144.1	61.4	2.8	86
0.82	22398	55.6	290.9	91.1	5.2	126
0.82	10613	35.4	102.9	40.6	2.9	60
0.79	1580	4.7	15.7	5.3	3.3	9
0.77	109443	72.5	16.5	83.3	0.2	77
0.78	69585	47.1	87.0	103.1	1.8	68
0.81	89394	60.5	14.5	71.9	0.2	64
0.70	89806	71.4	14.5	56.4	0.2	75
0.75	129728	39.0	3.5	80.0	0.1	40
0.78	586257	183.9	18.4	104.7	0.1	189
0.74	266746	82.9	19.7	93.8	0.2	88
0.81	131857	47.2	7.5	43.2	0.2	49
0.80	37130	17.4	5.0	67.6	0.3	19
0.84	11233	9.0	3.3	42.7	0.4	10
0.72	15300	40.8	142.5	69.7	3.5	75
0.70	13444	23.5	90.8	55.5	3.9	46

0.75	11401	34.8	125.5	57.5	3.6	65
0.83	21690	93.9	77.5	56.6	0.8	113
0.75	31059	31.3	121.4	59.5	3.9	61
0.79	46518	37.9	83.0	7.5	2.2	58
0.82	44428	21.3	59.1	6.9	2.8	36
0.74	37896	19.2	54.1	11.9	2.8	32
0.77	42107	23.3	66.6	10.8	2.9	39
0.78	19662	13.4	31.7	8.7	2.4	21
0.73	31674	22.5	40.6	8.2	1.8	32
0.78	29403	14.2	35.4	8.8	2.5	23
0.80	12508	11.6	33.1	8.0	2.9	20
0.77	10929	11.0	23.3	4.8	2.1	17
0.77	14176	9.6	32.4	10.7	3.4	17
0.80	12686	9.6	32.4	4.5	3.4	17
0.80	17613	11.9	30.3	6.1	2.6	19
0.72	8244	7.4	19.0	7.0	2.6	12
0.83	13196	15.3	33.0	14.8	2.2	23
0.80	19221	36.9	31.1	5.6	0.8	44
0.78	25030	18.9	27.2	7.6	1.4	25
0.80	13308	11.2	21.8	11.5	1.9	16
0.81	12084	11.3	29.9	9.2	2.6	19
0.84	7372	7.6	27.1	7.7	3.6	14
0.83	7112	10.3	31.9	17.8	3.1	18
0.75	5905	8.1	19.5	5.5	2.4	13
0.79	5074	6.8	26.9	11.2	3.9	13
0.77	5720	15.3	25.9	8.9	1.7	22
0.78	12729	11.6	30.8	6.1	2.7	19
0.77	9698	23.5	41.8	8.5	1.8	34
0.77	5544	9.4	32.3	6.6	3.4	17
0.81	3274	12.6	37.8	10.5	3.0	22
0.79	70766	88.7	113.0	23.4	1.3	116
0.80	72471	82.8	104.3	22.2	1.3	108
0.80	51165	63.5	75.0	12.2	1.2	82
0.75	38099	44.3	45.9	18.3	1.0	56
0.81	53821	50.9	59.8	15.8	1.2	65
0.83	52415	52.3	56.4	16.8	1.1	66
0.82	67076	70.5	75.4	18.4	1.1	89
0.83	77615	74.9	87.9	19.9	1.2	96
0.77	13309	21.2	40.3	13.1	1.9	31
0.81	55767	61.8	41.0	27.6	0.7	72
0.74	95376	116.8	113.2	19.5	1.0	144
0.81	137948	171.0	73.7	33.9	0.4	189
0.77	50558	68.0	69.9	28.2	1.0	85
0.82	92739	112.4	67.5	28.2	0.6	129

0.81	103926	113.9	73.5	28.6	0.6	132
0.78	49030	70.7	42.0	14.7	0.6	81
0.81	25929	13.0	21.9	17.4	1.7	18
0.74	50384	18.0	17.6	10.3	1.0	22
0.76	40105	19.7	21.8	16.2	1.1	25
0.81	27300	10.1	26.9	17.6	2.7	17
0.81	37150	23.1	9.4	5.2	0.4	25
0.83	67778	44.1	34.7	13.7	0.8	52
0.83	25104	18.5	20.0	22.4	1.1	23
0.76	100130	68.3	52.9	14.8	0.8	81
0.77	72476	48.0	28.3	11.8	0.6	55
0.75	49427	40.8	7.3	12.7	0.2	43
0.76	35909	33.7	5.4	19.1	0.2	35
0.77	49624	45.3	25.0	20.1	0.6	52
0.78	43734	52.5	20.7	10.1	0.4	58
0.78	144444	129.5	14.1	13.7	0.1	133
0.76	86599	83.7	19.7	7.7	0.2	88
0.82	76257	76.9	12.9	9.1	0.2	80
0.77	94100	95.5	39.5	18.5	0.4	105
0.81	134264	88.5	52.8	17.6	0.6	101
0.83	5526	21.0	37.7	40.6	1.8	30
0.79	6030	28.8	47.5	47.3	1.6	40
0.76	10533	32.4	50.0	51.4	1.5	45
0.83	5988	21.5	36.6	52.4	1.7	31
0.82	4848	27.3	41.8	43.6	1.5	38

aces; 1b + 1py: 1 broken face & 1 hexagonal pyramid (Brown et al., 2013).  $F_T$  is the alpha eject

Age (Ma)	Corrected Age (Ma)	$\pm 1 \sigma$
4.1	5.2	0.4
2.5	3.3	0.3
2.6	3.2	0.3
3.6	4.9	0.4
2.4	3.1	0.2
1.4	1.7	0.1
1.5	1.9	0.2
1.4	1.7	0.1
1.5	1.9	0.1
1.9	2.4	0.2
2.4	3.0	0.2
1.4	1.7	0.1
1.1	1.4	0.1
1.1	1.4	0.1
0.8	1.1	0.1
0.7	0.9	0.1
10.2	12.4	1.0
9.8	12.7	1.0
12.8	15.6	1.3
11.4	14.4	1.2
9.9	11.6	0.9
8.4	10.7	0.9
11.3	14.0	0.8
0.6	0.7	0.1
1.5	1.8	0.1
1.5	1.8	0.1
1.6	2.0	0.2
11.8	15.4	1.2
8.5	10.9	0.9
11.5	14.3	1.1
9.9	14.2	1.1
26.9	35.8	2.9
25.7	33.2	2.7
25.2	34.0	2.7
22.2	27.4	2.2
16.4	20.5	1.6
9.5	11.3	0.9
1.7	2.4	0.2
2.5	3.5	0.3

1.5	1.9	0.2
1.6	1.9	0.2
4.3	5.7	0.5
6.7	8.4	0.7
10.4	12.7	1.0
9.8	13.2	1.1
8.9	11.6	0.9
7.8	10.0	0.8
8.2	11.2	0.9
10.8	13.9	1.1
5.3	6.7	0.5
5.5	7.1	0.4
6.8	8.8	0.5
6.1	7.6	0.6
7.6	9.5	0.8
5.7	7.9	0.5
4.7	5.6	0.3
3.6	4.5	0.3
8.2	10.4	0.6
6.7	8.3	0.5
5.4	6.7	0.5
4.4	5.2	0.4
3.3	4.0	0.3
3.8	5.1	0.4
3.2	4.0	0.3
2.2	2.9	0.2
5.6	7.1	0.6
2.4	3.1	0.3
2.7	3.5	0.3
1.3	1.6	0.1
5.1	6.4	0.5
5.6	7.0	0.6
5.2	6.5	0.5
5.7	7.6	0.6
6.8	8.5	0.7
6.6	8.0	0.6
6.3	7.6	0.6
6.7	8.1	0.6
3.6	4.6	0.4
6.4	7.9	0.6
5.5	7.4	0.6
6.1	7.5	0.6
4.9	6.5	0.5
6.0	7.3	0.6

6.5	8.1	0.6
5.0	6.4	0.5
11.8	14.5	1.2
18.8	25.3	2.0
13.3	17.6	1.4
13.7	16.8	1.3
12.1	15.0	1.2
10.7	12.9	1.0
8.9	10.7	0.9
10.2	13.4	1.1
10.9	14.1	1.1
9.6	12.8	1.0
8.5	11.2	0.9
8.0	10.3	0.8
6.3	8.1	0.6
9.0	11.6	0.9
8.1	10.6	0.8
7.9	9.6	0.8
7.4	9.6	0.8
11.0	13.6	1.1
1.5	1.8	0.1
1.2	1.6	0.1
2.0	2.6	0.2
1.6	2.0	0.2
1.1	1.3	0.1

---

tion correction factor and Rs is the

---



Apatite fission-track data

Sample number	n	$\rho_s$ ( $10^5 \text{ cm}^{-2}$ )	$N_s$	$\rho_i$ ( $10^5 \text{ cm}^{-2}$ )	$N_i$	$\rho_d$ ( $10^5 \text{ cm}^{-2}$ )
<u>Ocobamba profile</u>						
AB-17-05	23	0.99	140	27.7	3915	12.0
AB-17-06	24	0.47	69	21.3	3155	12.0
AB-17-07	22	0.64	90	29.2	4098	12.0
AB-17-08	25	0.85	136	40.6	6486	12.0
AB-17-11	20	0.73	79	34.3	3725	12.1
<u>Individual data</u>						
AB-17-13	30	0.65	106	18.3	3007	12.1
AB-17-15	26	0.07	9	4.15	568	12.1
AB-17-18	25	1.01	160	6.82	1081	12.1
AB-17-19	25	4.32	476	34.2	3762	12.2
<u>Lucma profile</u>						
AB-17-22	22	3.98	388	33.7	3285	12.2
AB-17-23	18	6.79	314	46.4	2090	12.2
AB-17-25	18	16.5	901	73.0	3979	12.3
AB-17-26	24	2.95	286	24.8	2393	12.3
<u>Limatambo profile</u>						
AB-17-29	19	4.97	307	24.8	1532	13.8
AB-17-31	20	1.52	109	10.6	764	13.8
AB-17-32	20	1.90	133	14.5	1017	13.9
AB-17-33	22	1.87	159	17.6	1499	13.9
AB-17-36	18	1.95	120	16.3	1000	14.0
<u>Abancay profile</u>						
AB-17-37	20	4.44	244	50.6	2778	14.0
AB-17-38	20	6.94	647	69.4	6470	14.0
AB-17-39	20	4.77	506	49.6	5262	14.1
AB-17-40	20	5.73	532	62.9	5837	14.1
AB-17-41	26	3.27	544	18.3	3041	14.1
AB-17-42	26	5.48	764	34.1	4761	14.1
AB-17-44	25	5.15	632	44.6	5477	14.2
<u>Incahuasi profile</u>						
AB-17-51	14	0.45	18	9.66	389	14.2
AB-17-55	27	0.88	64	25.1	1833	14.2
<u>Previous studies</u>						
LK95/200 <sup>†</sup>	30	N.R. <sup>§</sup>	N.R. <sup>§</sup>	N.R. <sup>§</sup>	N.R. <sup>§</sup>	N.R. <sup>§</sup>
LK95/202 <sup>†</sup>	30	N.R. <sup>§</sup>	N.R. <sup>§</sup>	N.R. <sup>§</sup>	N.R. <sup>§</sup>	N.R. <sup>§</sup>
Pi6.1 <sup>#</sup>	23	2.27	456	20.7	4159	11.0
Pi6.2 <sup>#</sup>	16	1.55	168	13.8	1491	10.9
Pi6.3 <sup>#</sup>	20	1.74	323	16.2	3005	10.8
Pi6.4 <sup>#</sup>	20	0.69	137	6.21	1242	10.7
Pi6.5 <sup>#</sup>	19	0.79	148	9.05	1701	10.6
Pi6.6 <sup>#</sup>	20	1.04	203	12.0	2354	10.5
Pi6.7 <sup>#</sup>	20	1.09	141	12.7	1637	10.4

Pi6.8<sup>#</sup>                      20                      0.86                      140                      10.2                      1662                      10.3

---

*Note:* Fission-track age is given as Central Age (Galbraith & Laslett, 1993). Tracks were counted using the FTStage 4.04 program at ISTerre. Ages were calculated with the BINOMFIT program. Dpar value, MTL = mean track lengths of horizontally confined tracks.

\*N.D. = no data

<sup>†</sup>Previous data (Kennan, 2008). For samples LK95/200 and LK95/202, elevations are respectively

<sup>§</sup>N.R. = not reported

<sup>#</sup> Previous data from Ruiz et al. (2009) for samples Pi6.1 (3.87 km); Pi6.2 (3.80 km); Pi6.3 (3.80 km)

---

$P(\chi^2)$	Dispersion (%)	Central age (Ma)	$\pm 2 \sigma$	U (ppm)	$\pm 1 \sigma$	n D <sub>par</sub>
100.0	0.0	5.9	1.1	35	2	88
99.3	0.1	3.6	0.9	27	1	82
84.6	0.4	3.6	0.8	36	1	68
93.6	0.2	3.5	0.7	51	2	106
99.7	0.1	3.5	0.8	43	2	96
100.0	0.0	5.9	1.3	23	1	66
99.3	0.2	2.6	1.9	5	0	52
100.0	0.1	24.7	4.6	8	1	109
87.0	0.3	21.1	2.7	42	2	139
87.1	0.3	19.8	2.7	41	2	115
47.4	6.9	25.2	3.8	57	3	92
51.7	4.0	38.2	4.4	89	3	121
99.9	0.1	20.2	3.0	30	1	117
96.0	0.1	37.9	5.7	27	2	96
94.6	0.3	27.1	5.9	12	1	116
98.5	0.1	24.9	5.0	16	1	151
93.1	0.2	20.2	3.8	19	1	117
66.4	0.6	23.0	4.8	17	1	70
100.0	0.1	16.9	2.6	54	2	103
100.0	0.0	19.3	2.3	74	2	113
99.9	0.1	18.6	2.4	53	2	102
92.2	0.1	17.6	2.2	67	2	80
99.9	0.1	34.6	4.3	19	1	118
87.2	0.6	31.1	3.6	36	1	137
98.1	0.2	22.4	2.7	47	2	146
12.7	44.0	9.0	5.2	10	1	32
9.0	39.1	6.6	2.1	26	1	108
46.5	N.R. <sup>§</sup>	2.2	0.5	N.R. <sup>§</sup>	N.R. <sup>§</sup>	N.R. <sup>§</sup>
97.0	N.R. <sup>§</sup>	2.4	0.5	N.R. <sup>§</sup>	N.R. <sup>§</sup>	N.R. <sup>§</sup>
10.0	N.R. <sup>§</sup>	22.5	N.R. <sup>§</sup>	23	2	40
100.0	N.R. <sup>§</sup>	22.0	N.R. <sup>§</sup>	17	2	20
99.5	N.R. <sup>§</sup>	20.8	N.R. <sup>§</sup>	18	1	44
98.0	N.R. <sup>§</sup>	21.1	N.R. <sup>§</sup>	7	2	28
100.0	N.R. <sup>§</sup>	16.5	N.R. <sup>§</sup>	10	2	43
87.0	N.R. <sup>§</sup>	16.2	N.R. <sup>§</sup>	14	1	31
93.0	N.R. <sup>§</sup>	16.0	N.R. <sup>§</sup>	16	2	23

93.0      N.R.<sup>§</sup>      15.5      N.R.<sup>§</sup>      12      2      17

---

nted and horizontally confined track lengths were measured dry at 1250x magnification under :  
n (Ehlers et al., 2005), using a zeta value of  $275.18 \pm 11.53$  and the IRMM 540 uranium glass s

tively 3.1 and 2.1 km.

3.65 km); Pi6.4 (3.45 km); Pi6.5 (3.25 km); Pi6.6 (3.10 km); Pi6.7 (3.00 km); and Pi6.8 (2.85 k

MDpar ( $\mu\text{m}$ )	n TL	MTL ( $\mu\text{m}$ )
1.09	6	11.43
1.12	3	12.34
1.27	5	10.92
1.16	12	11.48
1.30	1	9.8
1.24	5	10.76
1.18	N.D.*	N.D.*
1.53	3	10.83
1.29	10	11.48
1.15	5	10.87
1.16	7	11.72
1.80	7	13.59
1.21	7	11.64
1.65	8	11.99
1.32	3	12.15
1.42	2	11.69
1.19	3	12.46
1.30	3	10.68
1.24	3	12.10
2.15	18	12.43
1.57	5	11.38
1.47	7	10.94
1.42	N.D.*	N.D.*
1.46	7	11.72
1.70	21	11.37
1.41	N.D.*	N.D.*
0.98	6	10.71
N.R. <sup>§</sup>	N.R. <sup>§</sup>	N.R. <sup>§</sup>
N.R. <sup>§</sup>	N.R. <sup>§</sup>	N.R. <sup>§</sup>
2.68	41	11.21
2.78	31	13.40
2.87	37	14.04
2.37	46	12.76
2.55	34	13.13
2.61	21	13.36
2.72	35	12.89

2.98

30

12.45

---

an Olympus BX51 optical microscope,  
standard (15 ppm U). MDpar = mean

m).

---